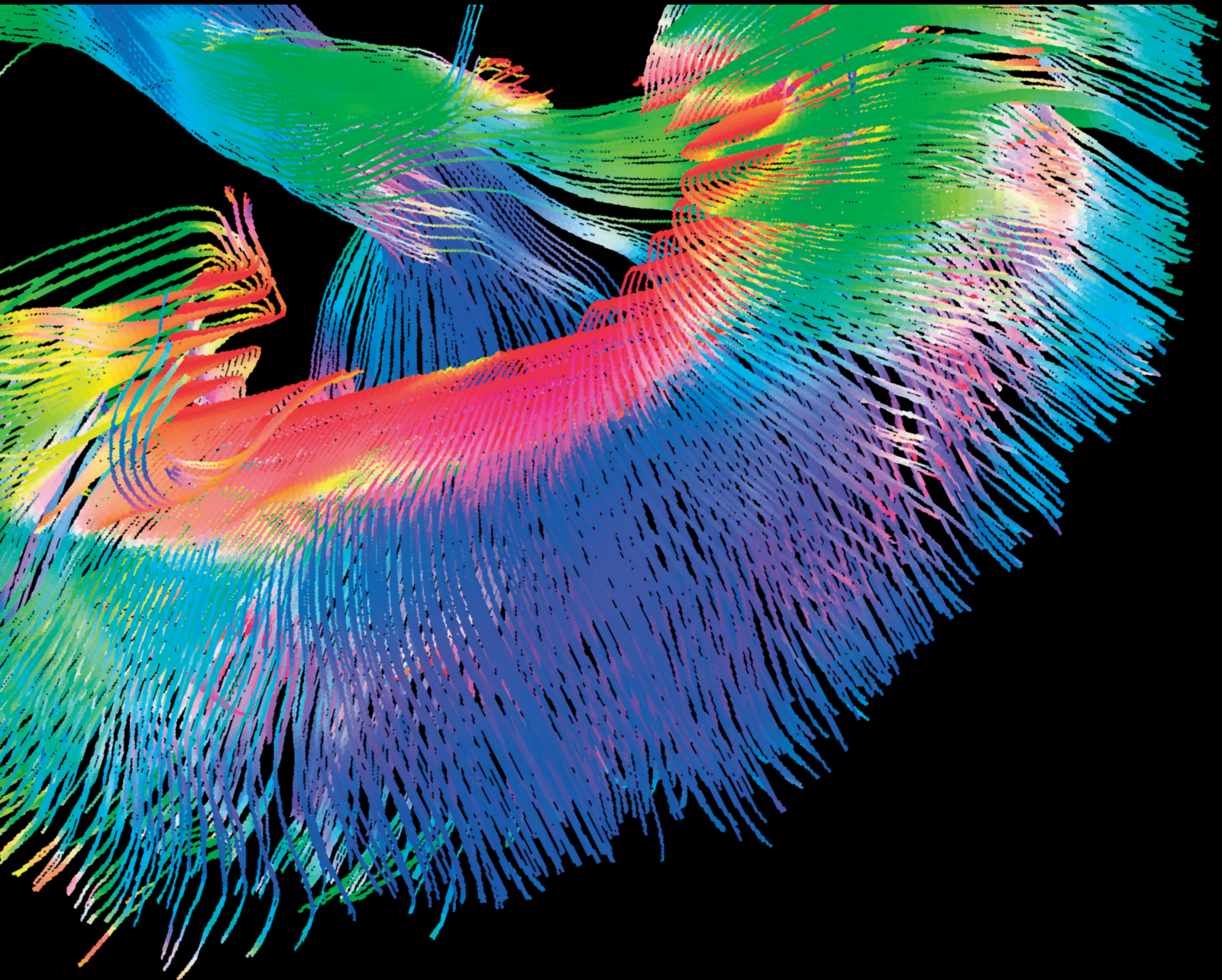


Contrast Media & Molecular Imaging

Imaging Biomarkers in Translational Small Animal Models

Lead Guest Editor: Pablo Aguiar

Guest Editors: Anxo Fernández-Ferreiro, Charalampos Tsoumpas,
and Filippo Galli





Imaging Biomarkers in Translational Small Animal Models

Contrast Media & Molecular Imaging

Imaging Biomarkers in Translational Small Animal Models

Lead Guest Editor: Pablo Aguiar

Guest Editors: Anxo Fernández-Ferreiro, Charalampos Tsoumpas,
and Filippo Galli



Copyright © 2019 Hindawi. All rights reserved.

This is a special issue published in “Contrast Media & Molecular Imaging.” All articles are open access articles distributed under the Creative Commons Attribution License, which permits unrestricted use, distribution, and reproduction in any medium, provided the original work is properly cited.

Editorial Board

Ali Azhdarinia, USA
Peter Bannas, Germany
Giorgio Biasiotto, Italy
André L. B. de Barros, Brazil
Dinesh K. Deelchand, USA
Paul Edison, UK
Michael J. Evans, USA
Samer Ezziddin, Germany
G. Ferro-Flores, Mexico
Luca Filippi, Italy
Filippo Galli, Italy
María L. García-Martín, Spain

Alexander R. Haug, Germany
Hao Hong, USA
Alexey P. Kostikov, Canada
Françoise Kraeber-Bodéré, France
Kuo-Shyan Lin, Canada
Gaurav Malviya, UK
Barbara Palumbo, Italy
Giancarlo Pascali, Australia
Maria Joao Ribeiro, France
Laurent M. Riou, France
Anne Roivainen, Finland
Pedro Rosa-Neto, Canada

Giuseppe Rubini, Italy
Barbara Salvatore, Italy
Ralf Schirmacher, Canada
Enza Torino, Italy
Giorgio Treglia, Switzerland
Reza Vali, Canada
Mattia Veronese, UK
Changning Wang, USA
Habib Zaidi, Switzerland
Luc Zimmer, France

Contents

Imaging Biomarkers in Translational Small Animal Models

Pablo Aguiar , Anxo Fernández-Ferreiro, Filippo Galli , and Charalampos Tsoumpas 
Editorial (2 pages), Article ID 9469041, Volume 2019 (2019)

Preclinical Imaging Biomarkers for Postischaemic Neurovascular Remodelling

Richa Gandhi  and Charalampos Tsoumpas 
Review Article (21 pages), Article ID 3128529, Volume 2019 (2019)

Hybrid PET/MR Kernelised Expectation Maximisation Reconstruction for Improved Image-Derived Estimation of the Input Function from the Aorta of Rabbits

Daniel Deidda , Nicolas A. Karakatsanis, Philip M. Robson, Claudia Calcagno, Max L. Senders, Willem J. M. Mulder, Zahi A. Fayad, Robert G. Aykroyd , and Charalampos Tsoumpas 
Research Article (12 pages), Article ID 3438093, Volume 2019 (2019)

Sensitivity of Multiphase Pseudocontinuous Arterial Spin Labelling (MP pCASL) Magnetic Resonance Imaging for Measuring Brain and Tumour Blood Flow in Mice

Jessica Buck , James R. Larkin , Manon A. Simard , Alexandre A. Khrapitchev , Michael A. Chappell , and Nicola R. Sibson 
Research Article (11 pages), Article ID 4580919, Volume 2018 (2019)

Image-Guided Neutron Capture Therapy Using the Gd-DO3A-BTA Complex as a New Combinatorial Treatment Approach

Ki-Hye Jung , Ji-Ae Park , Jung Young Kim , Mi Hyun Kim, Seyoung Oh, Hee-Kyung Kim, Eun-Ji Choi, Han-Jun Kim, Sun Hee Do , Kyo Chul Lee, Kyeong Min Kim , Yong Jin Lee , and Yongmin Chang 
Research Article (9 pages), Article ID 3727109, Volume 2018 (2019)

Multimodal PET/MRI Imaging Results Enable Monitoring the Side Effects of Radiation Therapy

Noémi Kovács, Krisztián Szigeti , Nikolett Hegedűs , Ildikó Horváth, Dániel S Veres , Michael Bachmann, Ralf Bergmann, and Domokos Máthé 
Research Article (9 pages), Article ID 5906471, Volume 2018 (2019)

Quantification of Nanoparticle Enhancement in Polarized Breast Tumor Macrophage Deposits by Spatial Analysis of MRI and Histological Iron Contrast Using Computer Vision

Avigdor Leftin  and Jason A. Koutcher
Research Article (9 pages), Article ID 3526438, Volume 2018 (2019)

How to Modulate Tumor Hypoxia for Preclinical In Vivo Imaging Research

Sven De Bruycker , Christel Vangestel, Steven Staelens, Tim Van den Wyngaert, and Sigrid Stroobants 
Review Article (17 pages), Article ID 4608186, Volume 2018 (2019)

MT1-MMP as a PET Imaging Biomarker for Pancreas Cancer Management

Miguel Ángel Morcillo, Ángel García de Lucas, Marta Oteo, Eduardo Romero, Natalia Magro, Marta Ibáñez, Alfonso Martínez, Guillermo Garaulet, Alicia G. Arroyo, Pedro Pablo López-Casas, Manuel Hidalgo, Francisca Mulero , and Jorge Martínez-Torrecuadrada 
Research Article (13 pages), Article ID 8382148, Volume 2018 (2019)

Early Imaging Biomarker of Myocardial Glucose Adaptations in High-Fat-Diet-Induced Insulin Resistance Model by Using ^{18}F -FDG PET and [$\text{U-}^{13}\text{C}$]glucose Nuclear Magnetic Resonance Tracer

Yi-Hsiu Chung, Kuan-Ying Lu, Shao-Chieh Chiu, Chi-Jen Lo, Li-Man Hung, Jiung-Pang Huang, Mei-Ling Cheng, Chao-Hung Wang , Cheng-Kun Tsai, Yu-Chun Lin , Shang-Hung Chang, and Gigin Lin 

Research Article (10 pages), Article ID 8751267, Volume 2018 (2019)

Positron Emission Tomography Imaging of Macrophages in Atherosclerosis with ^{18}F -GE-180, a Radiotracer for Translocator Protein (TSPO)

Sanna Hellberg , Heidi Liljenbäck, Olli Eskola, Veronique Morisson-Iveson, Matthew Morrison, William Trigg, Pekka Saukko, Seppo Ylä-Herttuala , Juhani Knuuti, Antti Saraste, and Anne Roivainen 

Research Article (11 pages), Article ID 9186902, Volume 2018 (2019)

Editorial

Imaging Biomarkers in Translational Small Animal Models

Pablo Aguiar ^{1,2}, **Anxo Fernández-Ferreiro**,³ **Filippo Galli** ⁴,
and Charalampos Tsoumpas ^{5,6,7}

¹*Molecular Imaging Group, Nuclear Medicine Dept., Health Research Institute of Santiago de Compostela (IDIS), 15706 Santiago de Compostela, Spain*

²*Molecular Imaging and Medical Physics Group, Radiology Dept., University of Santiago de Compostela, Santiago de Compostela, Spain*

³*Clinical Pharmacology Group, Health Research Institute of Santiago de Compostela (IDIS), 15706 Santiago de Compostela, Spain*

⁴*Nuclear Medicine Unit, Faculty of Medicine and Psychology, Department of Medical-Surgical Sciences and Translational Medicine, "Sapienza" University, Roma, Italy*

⁵*Biomedical Imaging Science Department, Leeds Institute of Cardiovascular and Metabolic Medicine, School of Medicine, University of Leeds, Leeds, UK*

⁶*Research & Development, Invicro, London, UK*

⁷*Translational Molecular Imaging Institute, Mount Sinai, New York, NY, USA*

Correspondence should be addressed to Pablo Aguiar; pablo.aguiar.fernandez@sergas.es

Received 8 January 2019; Accepted 9 January 2019; Published 4 February 2019

Copyright © 2019 Pablo Aguiar et al. This is an open access article distributed under the Creative Commons Attribution License, which permits unrestricted use, distribution, and reproduction in any medium, provided the original work is properly cited.

Preclinical molecular imaging has become an essential tool in translating the scientific understanding that has been gained by studying and developing the animal models of multiple human diseases to the clinic [1]. Today, several of the current clinical imaging techniques are already available for use in preclinical imaging models. It has allowed that same parameters can be derived from preclinical and clinical images, which has meant a swift translational trajectory for many clinical trials in oncology [2], neurology [3] or inflammation [4], or cardiology [5]. These parameters can be considered as imaging biomarkers because they represent objective physical and biological characteristics of tissues, tumours, or organs, and they can help to identify normal or pathogenic processes and treatment response. Nevertheless, the use of preclinical molecular imaging is still limited due to the lack of efficient and standardized methods for extracting accurate and reproducible imaging biomarkers for each particular disease model. The translational benefit of preclinical molecular imaging will substantially increase by improving the reliability of the collected data [6]. In this regard, a key challenge in translational molecular imaging is to define appropriate imaging biomarkers for each disease for prediction of therapeutic outcome and follow-up of new

treatments. This will help in swift and successful translation of studies from small animal models to patients and consequently reduce the cost of drug discovery portfolio. This special issue focuses on the recent advances in quantitative imaging biomarkers that can be used for translational research. In particular, it promotes the discussion of the various methods that benefit from the use of markers derived from preclinical imaging techniques that can be directly transferred to clinical imaging.

This special issue contains both review (2) and original articles (8), and its focus is to provide insights into the methodologies to investigate new imaging biomarkers in translational small animal models. An open call for papers was announced in December 2017, and the submission deadline was in August 2018. In total, 20 articles were submitted, and 10 articles were accepted for publication. In terms of imaging modality, all articles used magnetic resonance imaging (MRI) (7 articles) and/or positron emission tomography (PET) (7 articles), of which 3 articles utilised both MRI and PET. Only one of the review articles included other imaging techniques, but even in that case, PET and MRI were the predominant imaging techniques. Therefore, it seems that both PET and MRI are efficient research tools in

the domain of translational preclinical imaging. In terms of disease animal models, the clinical conditions were mainly oncology (brain, breast, and pancreatic cancer) and cardiovascular diseases (cardiovascular dysfunction and atherosclerosis) and other clinical fields such as radiotherapy (neutron capture and high energy photons). Obviously, the articles included in this special issue represent only a small part of the uses of translational molecular imaging in animal models, but we believe that they can be representative in relative terms. The predominance of PET and MRI could be interpreted as the consequence of their higher translational potential if compared with optical imaging or ultrasound.

In brief, the published papers on oncology show biomarkers for monitoring therapies such as radiation treatment and its side effects. S. De Bruycker et al. reviewed the different approaches to generate hypoxic in vivo cancer models directly related to PET imaging. N. Kovács et al. in their original paper performed a study to monitor the dose-limiting organs in patients undergoing radiotherapy. They report that conventional SUV values derived from brain PET and apparent diffusion coefficients from DWI can be considered as biomarkers for the follow-up of the health status after radiation therapy.

Among the other research articles, some were focused on new tracers and contrast agents. A. Leftin and J. A. Koutcher showed that tumour-associated macrophages can be accurately estimated in a mouse model of breast cancer by focusing on spatial distributions of iron deposits rather than ROI averages. They found that the polarization status of the iron⁺ populations is affected by contrast-agent injection, which has broad implications for nanoparticle-enhanced biomedical imaging. The paper by K.-H. Jung et al. was focused on the use of new agents for theragnostic approaches based on MRI and neutron capture therapies, showing increased MRI signal in the tumour after therapy. Also, new radiolabelled peptides and antibodies were proposed by M. A. Morcillo et al. as novel PET biomarkers for the diagnosis and prognosis of pancreatic ductal adenocarcinoma. Finally, J. Buck et al. described a novel arterial spin labelling MRI method to perform accurate and robust measurements of cerebral blood flow.

In metabolism and cardiology, different PET and MRI biomarkers were proposed by Y. H. Chung et al. for measuring the myocardial glucose adaptations in high-fat-diet-induced insulin resistance, and novel PET tracers were proposed by S. Hellberg et al. to improve characteristics for imaging atherosclerotic plaque inflammation. In neurology, R. Gandhi et al. reported in their systematic review different uses of preclinical imaging techniques of postischaemia neurovascular remodeling. Finally, a technical research article by D. Deidda et al. proposes a novel PET image reconstruction algorithm by utilizing MRI information. This approach offers the opportunity to extract the time-activity curve from the images so that kinetic information can be calculated without the potential need of continuous arterial blood sampling from animals. All ten articles illustrate that the value of predominantly PET and MRI biomarkers in different animal models offers useful biological information in various clinical applications. It is interesting to note that

hybrid PET/MRI imaging was performed only in the technical article, whereas in the others, only PET or MRI was used. Thus, it remains to be seen if this powerful machine can become a mainstream multimodality imaging tool to offer substantially improved information than standalone PET and MRI [7].

We envision the scientific findings and knowledge printed in this special issue demonstrate the importance of PET and MRI imaging biomarkers in preclinical investigations as well as the need for standardisation of the imaging biomarkers of each particular disease model and for the follow-up of new treatments and drugs from the small animal model to the patient.

Finally, we would like to thank the reviewers for their valuable review comments, improving greatly the quality of all submitted papers.

Conflicts of Interest

On behalf of the Guest Editors, we declare that there are no conflicts of interest regarding the publication of this article.

Pablo Aguiar
Anxo Fernández-Ferreiro
Filippo Galli
Charalampos Tsoumpas

References

- [1] R. Weissleder, M. C. Schwaiger, S. S. Gambhir, and H. Hricak, "Imaging approaches to optimize molecular therapies," *Science Translational Medicine*, vol. 8, no. 355, article 355ps16, 2016.
- [2] M. de Jong, S. Mather, and T. Maina, "Preclinical in vivo cancer, straightway to patients?," *Quarterly Journal of Nuclear Medicine and Molecular Imaging*, vol. 61, no. 2, pp. 145–152, 2017.
- [3] Z. T. Kincses, A. Király, D. Veréb, and L. Vécsei, "Structural magnetic resonance imaging markers of Alzheimer's disease and its retranslation to rodent models," *Journal of Alzheimer's Disease*, vol. 47, no. 2, pp. 277–290, 2015.
- [4] E. Kaaru, A. Bianchi, A. Wunder, V. Rasche, and D. Stiller, "Molecular imaging in preclinical models of IBD with nuclear imaging techniques: state-of-the-art and perspectives," *Inflammatory Bowel Diseases*, vol. 22, no. 10, pp. 2491–2498, 2016.
- [5] S. G. Nekolla, C. Rischpler, A. Paschali, and C. Anagnostopoulos, "Cardiovascular preclinical imaging," *Quarterly Journal of Nuclear Medicine and Molecular Imaging*, vol. 61, no. 1, pp. 48–59, 2017.
- [6] J. G. Mannheim, F. Kara, J. Doorduyn et al., "Standardization of small animal imaging—current status and future prospects," *Molecular Imaging and Biology*, vol. 20, no. 5, pp. 716–731, 2017.
- [7] M. Schwaiger, K. Kunze, C. Rischpler, and S. G. Nekolla, "PET/MR: yet another Tesla?," *Journal of Nuclear Cardiology*, vol. 24, no. 3, pp. 1019–1031, 2016.

Review Article

Preclinical Imaging Biomarkers for Postischaemic Neurovascular Remodelling

Richa Gandhi  and Charalampos Tsoumpas 

Department of Biomedical Imaging Science, Leeds Institute of Cardiovascular and Metabolic Medicine, University of Leeds, Leeds LS2 9NL, West Yorkshire, UK

Correspondence should be addressed to Richa Gandhi; mnrg@leeds.ac.uk

Received 22 August 2018; Revised 22 November 2018; Accepted 4 December 2018; Published 3 February 2019

Academic Editor: Barbara Palumbo

Copyright © 2019 Richa Gandhi and Charalampos Tsoumpas. This is an open access article distributed under the Creative Commons Attribution License, which permits unrestricted use, distribution, and reproduction in any medium, provided the original work is properly cited.

In the pursuit of understanding the pathological alterations that underlie ischaemic injuries, such as vascular remodelling and reorganisation, there is a need for recognising the capabilities and limitations of *in vivo* imaging techniques. Thus, this review presents contemporary published research of imaging modalities that have been implemented to study postischaemic neurovascular changes in small animals. A comparison of the technical aspects of the various imaging tools is included to set the framework for identifying the most appropriate methods to observe postischaemic neurovascular remodelling. A systematic search of the PubMed® and Elsevier's Scopus databases identified studies that were conducted between 2008 and 2018 to explore postischaemic neurovascular remodelling in small animal models. Thirty-five relevant *in vivo* imaging studies are included, of which most made use of magnetic resonance imaging or positron emission tomography, whilst various optical modalities were also utilised. Notably, there is an increasing trend of using multimodal imaging to exploit the most beneficial properties of each imaging technique to elucidate different aspects of neurovascular remodelling. Nevertheless, there is still scope for further utilising noninvasive imaging tools such as contrast agents or radiotracers, which will have the ability to monitor neurovascular changes particularly during restorative therapy. This will facilitate more successful utility of the clinical imaging techniques in the interpretation of neurovascular reorganisation over time.

1. Introduction

Oxygen is essential for the survival and basic functioning of biological systems. A stable equilibrium between the supply and usage of oxygen in biological systems generates oxygen gradients, wherein areas with low concentrations of oxygen (i.e., hypoxic regions) are situated relatively distant from the central vasculature. These oxygen gradients contribute to a healthy and functioning physiology, and their disturbance—for example, due to injury or disease—can confer debilitating effects on the functioning physiology [1]. Neural ischaemia is typically a hypoxic phenomenon, usually the result of some kind of traumatic injury or vascular disruption, developing from a deficiency in blood flow to brain tissue. This interrupted circulatory flow then triggers changes in the brain's metabolic processes [2]. Immediately following ischaemic injury, a series of biochemical reactions

ensue within the brain, which are collectively termed the ischaemic cascade. The ischaemic cascade involves biochemical energy depletion and the inability to maintain ionic gradients across cell membranes due to the restriction in blood supply. This eventually triggers cytotoxic and vasogenic oedema, as well as apoptotic and necrotic processes, which ultimately result in the deterioration of healthy brain tissue [3–5]. This cascade is elicited in patients who experience ischaemic stroke (Figure 1) [6].

One of the outcomes of an ischaemic stroke is the structural alteration of blood vessels to accommodate for the changes in haemodynamic conditions. This remodelling of the vasculature involves alterations in angiogenesis, the development of new blood vessels from preexisting ones; angioneurosis, the death of blood vessels or of the walls of blood vessels; migration of cells that compose blood vessels; and production and/or degradation of the

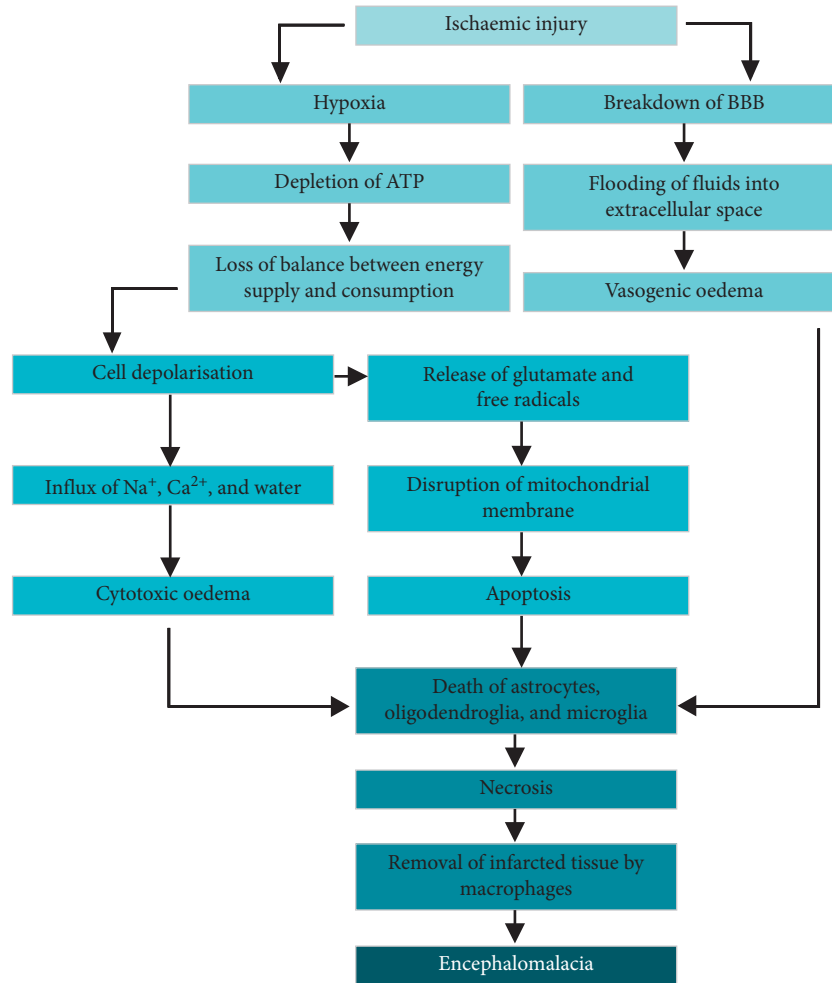


FIGURE 1: Ischaemic cascade. The cascade involves a series of events that follow ischaemic injury to the brain, such as that due to stroke. Eventually, this results in the softening or loss of brain tissue (i.e., encephalomalacia). BBB, blood-brain barrier; ATP, adenosine triphosphate.

extracellular matrix. Essentially, vascular remodelling is dependent on an interplay of haemodynamic stimuli, growth factors, and vasoactive substances [7]. As a result of the inclusion of a wide range of processes, it is essential to briefly address that the terminology of vascular “remodelling” may be used interchangeably with “alterations,” “plasticity,” “reorganisation,” “rearrangement,” or other similar keywords in the literature. The biological process involving this interplay is described in Figure 2, wherein the detection and relay of haemodynamic signals ultimately lead to vascular reorganisation.

Knowledge of the overall neurovasculature is useful for distinguishing the blood vessel or group of vessels that may be associated with an ischaemic stroke; unusual vascular patterns can then be attributed to other diseases, such as seizures, intracerebral haemorrhage, or brain tumours [8]. The functional deficits resulting from an ischaemic stroke are dependent on the cerebral arteries—and thus the brain regions—that are disrupted [6]. The cerebral hemispheres are each supplied by the posterior, middle, and anterior cerebral arteries. The posterior cerebral arteries originate from the basilar artery and supply the medial and posterior regions of the temporal

and occipital lobes, as well as the thalamus and brainstem regions. The middle cerebral arteries, which originate from the supraclinoid internal carotid, supply the anterior and lateral regions of the temporal lobes and lateral regions of the parietal and frontal lobes. The anterior cerebral arteries also originate from the supraclinoid internal carotid and supply the anterior regions of the basal ganglia, as well as the medial regions of the parietal and frontal lobes [9].

Imaging techniques play a significant role in clinical research; they are crucial for enhanced visualisation to better understand biological processes. The world’s first images of human brain metabolism were acquired via continuous inhalation of positron-emitting radioactive oxygen ($[^{15}\text{O}]$) to study the neurovascular distribution and accumulation of oxygen [10, 11]. Since then, our understanding of neurovascular dynamics has significantly progressed; various neuroimaging techniques with additional advantages, such as improved spatial resolution and the capacity for longitudinal imaging, are implemented in preclinical research and clinical practice. Neuroimaging (i.e., the use of imaging for neurological structures) can serve two purposes: (1) to differentiate amongst various morphological structures and (2) to visualise

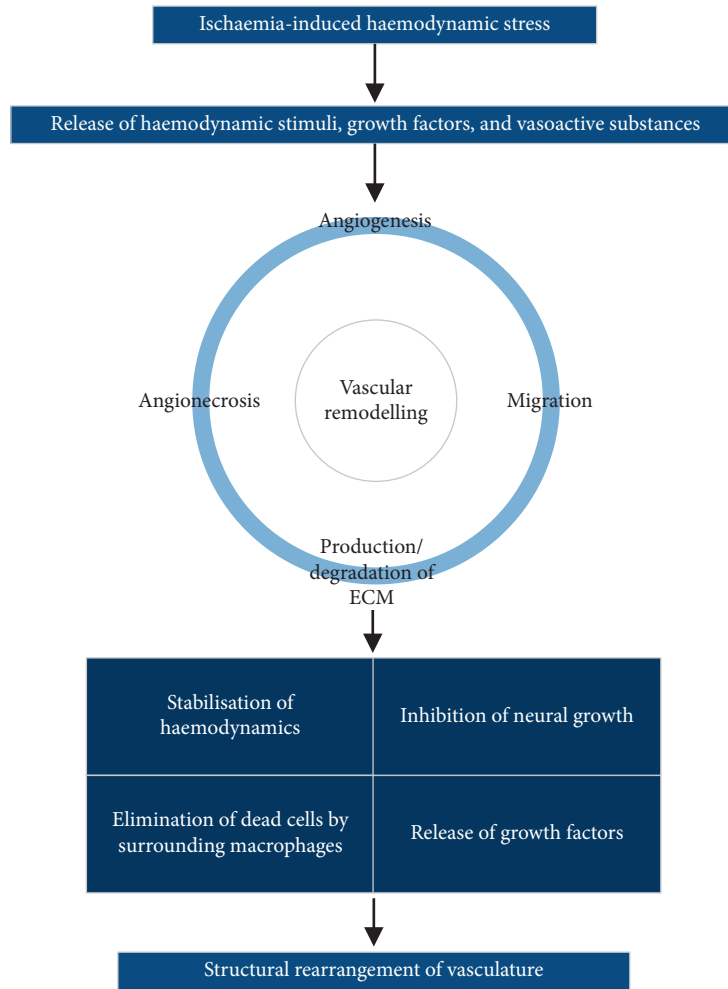


FIGURE 2: Biological process of vascular remodelling. Angiogenesis, migration of vascular cells, production and degradation of the ECM, and angioneclerosis constitute the major pathological hallmarks of vascular remodelling. ECM, extracellular matrix.

functional changes in neural plasticity following injury [6]. One such example involves imaging patients immediately after the onset of a stroke and posttraumatically at regular intervals. It is well established that patients who experience ischaemic stroke subsequently undergo vascular remodelling within the brain [2, 5, 7]. Studies of stroke in humans are limited because of the difficulties in collecting postmortem tissue samples when neuronal death occurs. Thus, neural ischaemia research is largely built upon information gathered from studies of animal models. When ischaemia is induced in experimental rodent models, for example, blood flow is disrupted to restrict the delivery of oxygen and glucose to neurons, eventually causing a depletion in biochemical energy [1, 12].

The aim of this review is to provide a guide to current imaging techniques being used to explore neurovascular remodelling in a preclinical in vivo setting. This review will contribute to the following:

- (i) Identify and distinguish preclinical imaging options used in the last 10 years
- (ii) Compare these techniques across common parameters

- (iii) Explore the potential applications of novel advances in imaging technologies
- (iv) Discuss how these imaging techniques could be translated to improve the medical management of ischaemic stroke

2. Materials and Methods

2.1. Search Strategy. The PubMed® and Elsevier’s Scopus online databases were used to retrieve journal papers. Titles, keywords, and abstracts were scanned for the search terminology using the search engines. The citations and references of any retrieved papers were also scanned for any relevant literature that may have been missed in the initial search. Boolean operating search strings were employed to ensure that the most suitable papers were retrieved. Table 1 outlines the search strategy that was implemented for literature retrieval.

2.2. Eligibility Criteria. Applying inclusion and exclusion parameters to the literature search process facilitated the

TABLE 1: Literature search strategy.

Initial search terminology	Synonyms and related terminology	Truncations and wildcards
ischaemic	ischaemia	isch?emia ischaemi* ischemi* hypoxi*
	low blood	
	low blood flow	
	low oxygen	
	hypoxia stroke	
neuro	brain	neuro* cerebro*
	cerebral neurological	
vascular	vasogenic	vascular* arteri*
	blood vessels arteries	
remodelling	rearrangement	remodel?ing remodel* reorgani?ation
	reorganisation	
imaging	scanning	imag* scan* observ* assess* measur* monitor* detect*
	observing	
	assessing	
	measuring	
	monitoring	
	detecting	

The initial search terminology stemmed from the wording of the overall aim of the review. The inclusion of alternative terminology and truncation and wildcard operators helped to uncover a wider range of papers from the databases. Some searches were also conducted with the exclusion of “remodelling” to assess whether imaging methods could potentially be implemented for this purpose.

retrieval of the most appropriate papers. Search results were restricted to papers published in English within the last 10 years (i.e., between 2008 and 2018, inclusive), as the translation of papers published in non-English languages may have distorted the understanding of the research. In vivo studies of small animals were included, and several papers discussing the same imaging technology were not disregarded, as these would only strengthen any common conclusions formed from these studies. Only primary research papers were included in the final analysis; other secondary or tertiary publications such as reviews, books, conference proceedings, presentations, and abstracts were only referred to for background or follow-up information and are cited accordingly in the discussion.

2.3. Quality Appraisal. The Preferred Reporting Items for Systematic Reviews and Meta-Analyses (PRISMA) guidelines were followed to ensure that the most appropriate research papers were included in this review. The PRISMA guidelines were established by David Moher and colleagues to conceptually represent the progressions within the field of systematic literature reviews. The papers that were retrieved from the search process following this model were systematically categorised according to their significance in helping to answer the overall aim of this research [13].

2.4. Data Collection and Analysis. Each of the retrieved papers from the literature search focussed on one or more imaging techniques. The next step involved assessing these

imaging techniques based on relevant parameters to evaluate whether they could be implemented to observe neurovascular remodelling following ischaemic injury. Accordingly, the following details were extracted from each of the retrieved papers, where available: imaging technique, purpose of the study, animal model used, spatial resolution or field of view, duration of scanning, contrast agent or molecular probe utilised, safety considerations for implementation in humans, and considerations for modality-specific image interpretation.

Although an effective imaging technique may offer excellent image resolution with minimal patient invasiveness, it may not be considered optimal for the purposes of clinical translation if the acquired data are exceedingly difficult and time-consuming to acquire and even process. By analysing and discussing comparisons between different technical characteristics and across a variety of imaging techniques, appropriate strategies to employ for postischaemic imaging can then be determined.

3. Results

The PRISMA model, as outlined in the previous section, was used to select the literature for this review. The articles’ filtering process is presented in Figure 3.

The results of the literature search essentially revealed a number of imaging parameters for each imaging technique that may be relevant for the imaging of neural vasculature, particularly following ischaemic trauma. These relevant parameters, along with a brief overview of the imaging techniques, are presented in Table 2.

The distribution of the selected publications per year is presented in Figure 4. There evidently appears to have been peaks of relevant research published in 2009, 2014–2015, and 2017 in relation to the search queries for this review, which may indicate a marginally increasing trend in studies of postischaemic neurovascular remodelling in the last 5 years.

4. Discussion

4.1. Rationale. Neurovascular remodelling is a process that establishes an ideal biological environment for neurological healing. Proceeding after an ischaemic injury, neurovascular remodelling acts to restore the haemodynamic stability of the brain, inhibit neural degeneration, eliminate any dead cells by surrounding macrophages, and facilitate the release of growth factors. Many signalling compounds and chemokines are involved in cell–cell interactions to facilitate attempts to salvage surviving neural tissue and reorganise the vasculature following ischaemic injury [17, 49]. A better understanding of these remodelling processes can enhance clinical diagnostics and restorative therapy options; thus, improved visualisation of this vascular reorganisation within the brain is beneficial. These biological pathways involve some of the same molecules that have already been used to inform the development of probes and tracers for the clinical study, such as the glucose analogue [^{18}F]FDG. Nonetheless, there remains a knowledge gap about the biological processes of neurovascular remodelling that can be answered by imaging the regions in which

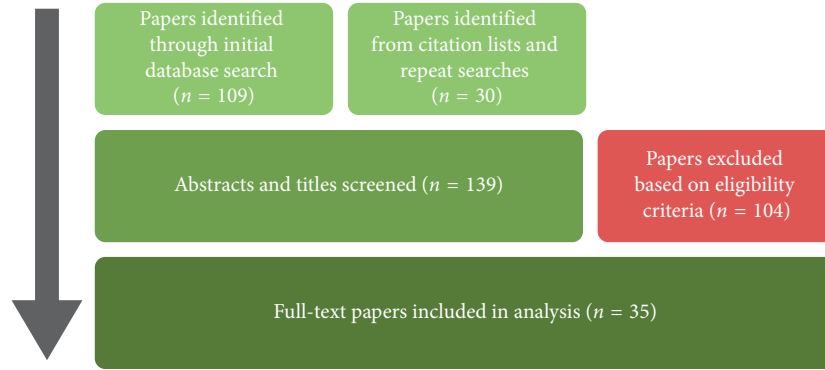


FIGURE 3: The Preferred Reporting Items for Systematic Reviews and Meta-Analyses model, as implemented for this systematic review. A final total of 35 papers were included in the literature analysis (adapted from [13]).

TABLE 2: Literature search results and extracted data.

Reference	Method and application (models)	Imaging parameters	Contrast agent or molecular probe	Safety considerations for clinical translation	Applications
Bosomtwi et al. [14]	MRI to observe poststroke vascular changes (rats)	FOV: 32 mm	Feridex	Noninvasive	Tissues can be monitored long term through stages of angiogenesis enabling evaluation of vascular remodelling
Bosomtwi et al. [15]	MRI in combination with LSCM to visualise postischaemic changes in vasculature (rats)	FOV: 32 mm	MIONs	Noninvasive; high doses of intravascular agent are required	LSCM can be used to validate MRI data; poststroke vascular remodelling can be three-dimensionally quantified
Brunner et al. [16]	fUS to measure postischaemic cerebral blood volume (rats)	Resolution: 100 μm , FOV: 12.8 \times 9 mm^2 , duration: approx. 3 min	None	No contrast agent injections are required	Stroke longitudinally studied across all stages; can image whilst in motion, as the probe is implanted on the head
Cai et al. [17]	PET to observe VEGFR expression in poststroke angiogenesis (rats)	—	^{64}Cu -DOTA-VEGF ₁₂₁	—	Some cellular VEGFRs may be visualised, resulting in the potential to observe poststroke reorganisation and plasticity
Deddens et al. [18]	MRI to detect vascular remodelling after cerebral ischaemia (mice)	FOV: 1 \times 1.2 \times 2 cm^3	PECAM-1-targetted FeO _x microparticles	—	PECAM-1 can be used to assess poststroke vascular remodelling
Ding et al. [19]	MRI to visualise poststroke cerebral angiogenesis (rats)	FOV: 32 \times 32 \times 16 mm^3	Gd-DTPA	Noninvasive	Detect angiogenesis and determine the temporal profile of angiogenic processes
Errico et al. [20]	Ultrafast US localisation microscopy to visualise neurovasculature and quantify haemodynamic characteristics (rats)	Resolution: 12.5 \times 2.5 \times 1 μm^3	Inert perfluorocarbon-filled microbubbles	Microbubbles are clinically approved contrast agents	Even slight haemodynamic changes in neurovasculature can be monitored; the resolution can be enhanced by localising microbubbles directly from radiofrequency data; motion correction algorithms needed

TABLE 2: Continued.

Reference	Method and application (models)	Imaging parameters	Contrast agent or molecular probe	Safety considerations for clinical translation	Applications
Figueiredo et al. [21]	CTA	Resolution: $16^3 \mu\text{m}^3$, duration: 20–40 s	Iomeprol	Injection of contrast agent is required	Can detect changes in the diameter of vasculature
	MRA	To observe cerebral vascular anatomy and blood flow (mice)	None	No ionising radiation	—
	Digital subtraction angiography	Resolution: $14 \times 14 \mu\text{m}^2$, duration: 3 s	Iomeprol	Low injection volume and dose of radiation, although much more invasive than CTA and MRA	Can detect changes in intracerebral blood flow
Gramer et al. [22]	PET, LSI, and RGB reflectometry to measure CBF, blood oxygenation, and glucose metabolism (rats)	Resolution (PET): 1.3 mm (FWHM), FOV: $12 \times 7 \text{ mm}^2$	^{18}F FDG	Thin-skull preparation is required	Can be used to quantify metabolic activity of neurovasculature in real time making it suitable for studying pathological conditions. Partial volume is an issue
Horton et al. [23]	Triphoton fluorescence microscopy to visualise hippocampal vasculature (mice)	Resolution: $4.4 \mu\text{m}$ (axial, FWHM)	Dextran-coupled Texas Red dye	—	Overcomes the limitations of two-photon microscopy, such as signal-to-background ratio of excitation in scattering tissues and lack of fluorescent labels that can be used
Howles et al. [24]	Contrast-enhanced MRA to visualise neurovasculature (mice)	Resolution: $52 \times 52 \times 100 \mu\text{m}^3$, FOV: $20 \times 20 \times 8 \text{ mm}^3$, duration: approx. 12 min	SC-Gd liposomal nanoparticles	—	SC-Gd allows for high contrast-to-noise ratio; useful to visualise very small vascular structures
Hu et al. [25]	Optical-resolution PAM to study micro-haemodynamic activities (rodents)	Resolution: $5 \times 15 \mu\text{m}^2$	—	Noninvasive	Can help quantify changes in metabolic parameters
Huang et al. [26]	MRI to assess vascular reactivity and functionality during postischaemic proangiogenic vascular remodelling (rats)	FOV: $2.56 \times 2.56 \text{ cm}^2$	—	—	Anaesthesia protocols must be optimised to minimise physiological disturbance
Jimenez-Xarrie et al. [27]	MRI to assess postischaemic cerebrovascular damage	FOV: $32 \times 32 \text{ mm}$, duration: 9 min 17 s	None	Isoflurane anaesthesia can affect stroke outcomes and evaluation of vascular changes	Long-term vascular consequences of ischaemia with coincident hypertension can be studied
Kolodziej et al. [28]	SPECT to study CBF (mice)	Resolution: 0.7 mm (FWHM), FOV: 20.9 mm (axial), duration: approx. 2 h	$^{99\text{m}}\text{Tc}$ -HMPAO	$^{99\text{m}}\text{Tc}$ -HMPAO is lipophilic and is quickly cleared from the plasma	Uses pinhole imaging for higher resolution

TABLE 2: Continued.

Reference	Method and application (models)	Imaging parameters	Contrast agent or molecular probe	Safety considerations for clinical translation	Applications
Lake et al. [29]	MRI to assess poststroke brain morphology and vascular function (rats)	Resolution: $0.1 \times 0.1 \text{ mm}^2$, duration: <12 min	—	Propofol anaesthesia induces 20–60% regional vasoconstriction, which may influence vascular studies	Functional MRI can be used to measure resting blood flow and cerebrovascular reactivity; structural MRI may have limited sensitivity to detect subtle changes in tissue morphology
Lecoq et al. [30]	Two-photon phosphorescence lifetime microscopy to measure the partial pressure of oxygen and blood flow (mice)	Resolution: $<1 \mu\text{m}$ (lateral)	Phosphorescent nanoprobe PtP-C343	Minimally invasive; the probe is neither toxic nor phototoxic	Oxygen gradients in microvascular networks can be distinguished; this is particularly useful for postischaemia imaging
Letourneur et al. [31]	Two-photon laser scanning microscopy to longitudinally image vascular development (mice)	Duration: 50–150 s	Fluorescein-conjugated dextran and Texas Red-dextran	Requires thinning of the skull; head must be immobilised	Can longitudinally image the same areas over many days; can measure flow dynamics over time in relation to changes in vessel diameter
Li et al. [32]	LSI to study neurovasculature (rats)	Resolution: $6.7 \times 6.7 \mu\text{m}^2$	None	Requires thinning of the skull	Different circulatory dynamics can be observed at different spatial locations
Liao et al. [33]	Functional PAM to study functional changes in total haemoglobin concentration, cerebral blood volume, and haemoglobin O_2 saturation in cerebral blood vessels (rats)	Resolution: $36 \times 65 \mu\text{m}^2$	None	—	Can be complemented with other imaging modalities for label-free visualisation of neurovasculature
Lin et al. [34]	3D ΔR_2 -based microscopy of MRA to visualise poststroke changes in neurovasculature (rats)	Resolution: $54 \times 54 \times 72 \mu\text{m}^3$, FOV: $2.8 \times 2.8 \times 1.4 \text{ cm}^3$, duration: 76 min	MIONs	Greater magnetic fields may be needed to visualise smaller vessels	Can simultaneously visualise microvascular morphology and reveal physiological properties of microvascular cerebral blood volume
Luckl et al. [35]	LSI and imaging of intrinsic signals to study CBF dynamics during ischaemia (rats)	Resolution: $140 \mu\text{m}$ every 2 s, FOV: $5 \times 5 \text{ mm}^2$	Erythrosin B dye	Requires thinning of the skull for better observation	Vascular changes in metabolism can be quantified
Miao et al. [36]	LSI to study angiogenesis (rats)	FOV: $4.7 \times 4.7 \text{ mm}^2$	None	Requires thinning of the skull	CBF under various pathological states can be analysed, and smaller vessels can be enhanced; results can be affected by motion artefacts
Nagaraja et al. [37]	MRI to visualise poststroke changes in the BBB (rats)	FOV: 32 mm	Gd-DTPA and Gd-DTPA linked to bovine serum albumin and Evans blue dye	Noninvasive	Different measurements are obtained with different contrast agents; quantifying BBB permeability can help in understanding the progression of ischaemic injury

TABLE 2: Continued.

Reference	Method and application (models)	Imaging parameters	Contrast agent or molecular probe	Safety considerations for clinical translation	Applications
Sakadžić et al. [38]	Two-photon phosphorescence lifetime microscopy to measure partial pressure of oxygen in cortical microvasculature under hypoxic conditions (rats, mice)	—	Phosphorescent nanoprobe PtP-C343	Minimally invasive with low doses of the probe required; no detected leakage of the probe into interstitial spaces	The partial pressure of oxygen can be simultaneously assessed at various positions and depths, making it more feasible to functionally study transient changes in oxygen levels
Schambach et al. [39]	Volume-CTA to visualise cerebral vessels (mice)	Duration: 40 s	Iodinated contrast agent	Large dose of contrast agent is required	Changes in vessel diameter can be monitored
Schroeter et al. [40]	PET	To observe postischaemic vascular changes (rats) Duration: up to 60 min	$[^{18}\text{F}]\text{FDG}$ and $[^{11}\text{C}]\text{PK11195}$	Noninvasive	Characterise neuroinflammation and metabolic disruptions repeatedly over time. Can help localise areas of infarction
	MRI	FOV: 3.0 cm	—	Noninvasive	
Seo et al. [41]	Contrast-enhanced μCT to visualise poststroke changes in cerebral vasculature (rats)	Duration: approx. 2 min	Iopromide	High doses of iodinated contrast agent are needed	Images are subject to blurring due to physiological motion
Stein et al. [42]	PAM to study blood oxygenation dynamics of hypoxic cerebral vasculature (mice)	Resolution: $70 \times 54 \mu\text{m}^2$	None; monitors “endogenous” haemodynamics	Noninvasive	Single blood vessels can be noninvasively assessed in real time
Struys et al. [43]	PET	To characterise acute and long-term vascular and metabolic effects of unilateral common carotid artery occlusion (mice) Resolution: 1.35 mm (transaxial, FWHM), duration: 10 min	$[^{15}\text{O}]\text{H}_2\text{O}$ and $[^{18}\text{F}]\text{FDG}$	—	Can be used to monitor short-term/long-term perfusion and vascular remodelling in ischaemic stroke models
	MRI	Resolution: $98 \times 98 \mu\text{m}^2$, FOV: $2.5 \times 2.5 \text{ cm}^2$	—	—	
Tsukada et al. [44]	PET to study postischaemic changes (monkeys)	Duration: 91 min	$[^{18}\text{F}]\text{flurpiridaz}$ and $[^{18}\text{F}]\text{BCPP-EF}$	Surgical procedures are invasive and require anaesthesia	Study metabolic properties and distinguish inflammatory processes
Yanev et al. [45]	Steady-state contrast-enhanced MRI to assess the changes in cerebral blood volume and microvascular density after transient stroke (rats)	FOV: $30 \times 30 \text{ mm}^2$, duration: approx. 135 min	Ultrasmall iron oxide particles	—	Changes in cerebral blood volume and microvascular density can be observed at least 3 months after stroke; only perfused (and therefore functional) vessels can be detected
Yoon et al. [46]	Multiphoton luminescence to visualise morphological changes in cortical vasculature over time (mice)	—	PEG-GNPs	PEG-GNPs are highly biocompatible	Long circulation time of PEG-GNPs enables vascular imaging for several hours, making them suitable to observe remodelling

TABLE 2: Continued.

Reference	Method and application (models)	Imaging parameters	Contrast agent or molecular probe	Safety considerations for clinical translation	Applications
Yu et al. [47]	Spectral Doppler OCT to quantitatively assess dynamic blood flow before and after stroke (mice)	Duration: approx. 20 min	Rose bengal	—	Mimics ischaemic conditions by reducing CBF in microvasculature; the pulsatility of CBF is quantified; changes in heart rate due to anaesthesia wearing off and being readministered must be considered
Zhang et al. [48]	SR-PCI to visualise neural microvasculature (rats)	Resolution: <math><10 \mu\text{m}</math>, FOV: approx. 3 mm	None	High doses of ionising radiation	Vascular architecture and volume can be visualised and quantified; FOV is limited

External sources were not consulted to fill in missing details at this stage in the research. Abbreviations: FOV, field of view; MRI, magnetic resonance imaging; LSCM, laser scanning confocal microscopy; MION, monocrystalline iron oxide nanoparticle; fUS, functional ultrasound; PET, positron emission tomography; VEGFR, vascular endothelial growth factor receptor; PECAM, platelet endothelial cell adhesion molecule; Gd-DTPA, gadolinium-diethylenetriaminepentaacetate; US, ultrasound; CTA, computed tomography-angiography; MRA, magnetic resonance angiography; LSI, laser speckle imaging; RGB, red-green-blue; CBF, cerebral blood flow; FWHM, full width at half maximum; [^{18}F]FDG, [^{18}F]fluorodeoxyglucose; SC-Gd, surface-conjugated gadolinium; PAM, photoacoustic microscopy; SPECT, single-photon emission computed tomography; $^{99\text{m}}\text{Tc}$ -HMPAO, $^{99\text{m}}\text{Tc}$ -hexamethylpropyleneamineoxime; BBB, blood-brain barrier; μCT , microcomputed tomography; PEG-GNP, polyethylene glycosylated gold nanoparticle; OCT, optical coherence tomography; SR-PCI, synchrotron radiation phase contrast imaging.

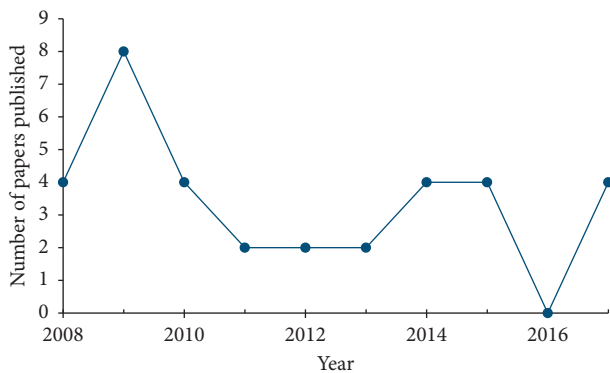


FIGURE 4: Number of publications fulfilling the search criteria per year.

the neurovascular changes occur. Consequently, this review purports itself to identify current imaging technologies being used in neurovascular research to observe postischaemic neurovascular remodelling in small animals. Various techniques were revealed in the published literature and evaluated against a set of properties and common measures in image analysis that were deemed relevant for vascular imaging in the brain. The imaging techniques have been categorised to help identify when certain modalities may be more appropriate for the given purpose. This review provides guidance in the identification of imaging modalities for different translational applications.

4.2. *Animal Models of Ischaemia.* Small animals play a valuable role in elucidating the mechanisms underlying ischaemia. The use of small animal models allows for greater

control and reproducibility to precisely evaluate ischaemic pathophysiology, compared to human cases that involve heterogeneous manifestations and causal factors. Invasive techniques can also be implemented in small animals for direct access to the brain vasculature, although they are undesirable in the context of clinical translatability. Furthermore, animal models allow for the study of immediate postischaemic changes, providing insights into early-stage mechanisms [50]. Some common rodent models of stroke include the (a) middle cerebral artery (MCA) occlusion (MCAo) model, which involves temporarily or permanently disrupting blood flow in the MCA and associated vascular branches that are predominantly affected in human stroke; (b) craniotomy model, which involves craniectomy and removal of a section of dura mater to access the MCA; (c) embolic stroke model, which involves the application of micro/macrospheres or clots to induce ischaemic lesions; (d) endothelin-1 (ET-1) model, which involves the application of ET-1 to a neural region of interest (often the MCA) to act as a vasoconstrictor and thus induce ischaemia; and (e) photothrombosis model, which involves targeted photo-oxidation to generate precise ischaemic lesions [50–54]. The most commonly reported ischaemia models in the papers identified in this review were the embolic stroke, MCAo, and craniotomy models (Figure 5). Different stroke models have different advantages and may provide information on different aspects of postischaemic changes; therefore, it is useful to consider the type of information that is desired when designing an imaging study.

4.3. *Fundamentals.* Neurovascular remodelling undergoes several phases in its process of ultimately establishing fully functional vasculature. To better understand postischaemic

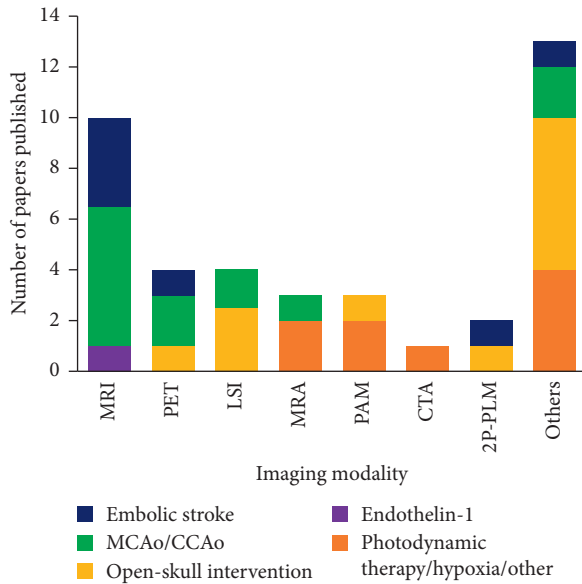


FIGURE 5: Frequency distribution of imaging modalities amongst papers retrieved through the literature search, with further distinction of the ischaemia induction models implemented. Magnetic resonance imaging and positron emission tomography were the most common techniques employed for *in vivo* preclinical studies of postischaemic neurovasculature. Other modalities included one instance each of multiphoton luminescence, optical coherence tomography, ultrafast ultrasound localisation microscopy, synchrotron radiation phase contrast imaging, digital subtraction angiography, microcomputed tomography, red-green-blue reflectometry, single-photon emission computed tomography, functional ultrasound, laser scanning confocal microscopy, three-photon fluorescence microscopy, and two-photon laser scanning microscopy. The MCAo/CCAO model was used most commonly across all the imaging modalities. Open-skull intervention included craniotomy, thinning of the skull, and electrode or optic fibre implantation. MRI, magnetic resonance imaging; PET, positron emission tomography; LSI, laser speckle imaging; MRA, magnetic resonance angiography; PAM, photoacoustic microscopy; CTA, computed tomography angiography; 2P-PLM, two-photon phosphorescence lifetime microscopy; MCAo, middle cerebral artery occlusion; CCAo, common carotid artery occlusion.

changes, studying neurovascular remodelling in its individual stages is ideal. The individual characteristics of these phases can be measured to provide a better understanding of the postischaemic reorganisation that occurs. Firstly, a cellular cascade instigated by endothelial cells causes heightened permeability of vessels due to the deterioration of key vascular junctions. This, in turn, enables the extravasation of plasma proteins, which helps construct a framework for the development of new vessels. Thereafter, the growth of new vasculature leads to fluctuations in haemodynamic properties, such as cerebral blood flow and volume, as well as in vessel density, whilst the vascular network continues to develop. The remapping of the vascular network in response to ischaemia is an important aspect of appreciating neurovascular outcomes [55, 56].

Therefore, it might be of considerable value to utilise small nanometre-scale intravascular contrast agents that could trace this extravasation to signal the generation of new

vasculature. Agents of different sizes could help detect different levels of permeability in different areas at different intervals, whilst enhanced opacification could ideally be achieved by utilising a higher density contrast. Ideally, an imaging approach would enable the dynamic visualisation of both large and small vessels as postischaemic angiogenesis proceeds for a more complete picture of the vascular microanatomy, although studying microvascular changes might offer significant information about the earliest postischaemic processes. Hence, to distinguish individual vessels, the image resolution should complement the range of vessel diameters. An imaging resolution of at least 0.5 mm would confer the greatest benefit if the biological tracer being utilised is nonspecific to the vasculature, since cerebral arteries are larger in diameter than this, although a more precise range may be necessary to observe the remodelling of microvessels [57–59]. Nevertheless, neurovascular remodelling is not a one-off event; thus, the capacity to obtain repeated measurements over time (i.e., longitudinal imaging) is also desirable in an ideal imaging approach, thereby circumventing the need for more invasive methods. By visualising early processes, studies can infer postischaemic remodelling changes from an earlier time point. This would be valuable in a twofold manner. Firstly, experiments could retain a larger sample size, given the survival durations after ischaemia. Secondly, studying earlier fundamental processes using imaging would allow for better correlations with later outcomes in studies of neurovascular outcomes.

4.4. General Overview of Imaging Modalities. A wide array of imaging techniques have been implemented within the last 10 years in preclinical small animal models specifically for *in vivo* visualisation of vascular changes following ischaemic injury. Magnetic resonance imaging (MRI) and positron emission tomography (PET) remain the predominant modalities of choice to study postischaemic neurovascular changes, despite the advent of numerous other modalities being implemented over the last 10 years (Figure 5). According to a survey ($n = 173$) conducted amongst UK and non-UK university researchers and UK National Health Service personnel, MRI is amongst the topmost researched areas [60].

Well-established modalities such as computed tomography (CT), MRI, and PET were expectedly found in the literature; in addition, several other methods have been developed and introduced relatively recently. These include ultrafast ultrasound localisation microscopy (uULM), which incorporates the use of inert gas microbubbles for precise visualisation of cortical vessel branching; synchrotron radiation phase contrast imaging (SR-PCI), which does not require the administration of a contrast agent, but it involves high doses of ionising radiation; the use of gold-coated nanoparticles in multiphoton luminescence to allow for repeated imaging over time (Figure 6); and functional ultrasound (fUS), which can be implemented in freely moving models without the use of contrast agents [16, 20, 46, 48]. Each new imaging modality improves on singular aspects of imaging vascular disease and may likely serve as an adjunct

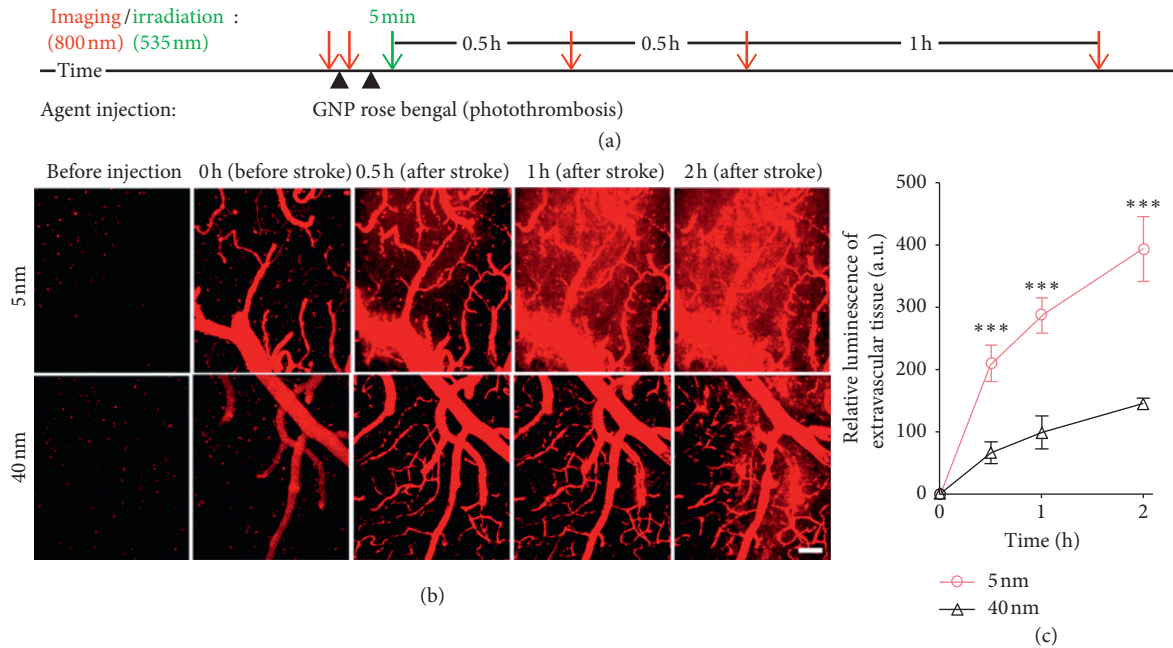


FIGURE 6: In vivo multiphoton luminescence imaging using PEG-GNPs of cerebral vasculature in murine stroke models. (a) Experimental timeline, prior to which an open-skull cranial window was generated in a live mouse. Photothrombosis was induced within the vessels to generate the mouse model. (b) Multiphoton luminescence images of neurovasculature before and after induction of photothrombotic stroke with 5 and 40 nm sized PEG-GNPs. Scale bar, 100 μm . (c) Relative luminescence of extravascular tissues following photothrombosis. *** $P < 0.001$, one-tailed t -test, $n = 3$; values are mean with standard deviation. PEG-GNP, polyethylene glycosylated gold nanoparticle (republished with permission from the Royal Society of Chemistry [46]; permission conveyed through Copyright Clearance Center, Inc).

to existing clinical imaging modalities. Given the general accessibility of PET and MRI and their preexisting use in patients, these well-established techniques are likely to persist and receive the bulk of the relevant research focus. Nonetheless, much like PET/CT being a widely available hybrid system, continued study of neurovascular remodeling is likely to rely on more than one technique to develop our understanding and help fine-tune the output data from these large-scale techniques. These novel methods show promise for neurovascular imaging, and it would be of interest to follow any future work involving these methods.

4.5. Imaging Specifications Representing Limitations to Overcome. Multiphoton microscopy is a fluorescence technique that effectively merges laser scanning microscopy with pulsatile multiphoton excitation to image tissues that have been labelled with fluorophores [61]. This approach has been actively employed to investigate the mechanisms of neurovascular reorganisation following ischaemic injury [62]. Despite the high spatial resolution from targeted imaging, this technique suffers from slow imaging times, limited fields of view, and depth of tissue penetration. For example, live imaging in small rodents requires a cranial window—an opening in the skull for optical access to the parenchyma—to be created in the model being tested. This functionally limits the field of view available. In rats, a large cranial window (e.g., $4 \times 6 \text{ mm}^2$ in size) is usually created, involving removal of the overlying bone and resection of the dura mater, to enable the insertion of devices, such as

cannulae and electrodes. This step is complicated by the need to reseal the window to reestablish intracranial pressure and reduce motion artefacts [63]. Mice, on the contrary, are a good alternative because cranial window generation is less invasive than that in rats; the thin skull of mice can remain intact and only requires thinning for a resulting cranial window (e.g., $2 \times 2 \text{ mm}^2$ in size), which produces limited disruptions in intracranial pressure and decreased inflammation [64]. Therefore, animal choice forms a key part of designing such imaging experiments.

PET and single-photon emission computed tomography (SPECT) are molecular imaging techniques that track biological target-specific changes in function with high sensitivity. Nonetheless, their relatively poor resolution (around 0.8 mm for PET and 0.3 mm for SPECT) prevents anatomically specific imaging and presents as a limiting factor, which may also augment partial volume effects and influence the measurement of vascular parameters. Partial volume effects are a direct response to multiple tissue types present within a single voxel, hence generating image blurring. Partial volume effects refer to the difference between actual and obtained image intensity values and typically occur when more than one type of tissue is contained within individual voxels, ultimately influencing the quantification of key parameters. Larger voxels have a greater probability of containing various tissue types in comparison to smaller voxels. The consequential blurring effects are essentially the result of the interplay between low spatial resolution and limited tissue sampling. Methods to correct for partial volume effects in PET imaging represent an active field of

research [65–67]. The biggest advantage of using these nuclear medicine techniques despite the poor anatomical definition is that dynamic, real-time imaging becomes possible. Dynamic imaging offers considerable diagnostic information that may not be accessible from static imaging by overcoming the bias presumed by static imaging, in which a single time frame is selected to reflect the overall tracer metabolism without correcting for variabilities in distribution and activity [68]. This advantage of dynamic imaging is important for neurovascular studies when studying absolute blood flow dynamics and the remodelling process.

If anatomical detail is required, MRI provides a complement of both real-time imaging and high spatial resolution without the use of ionising radiation [3]. Access to MRI systems incorporating ultrahigh magnetic fields (i.e., greater than 9.4 T) can allow for the acquisition of images with higher spatial resolution [69]. This enhancement of resolution, however, comes at the cost of increased scan durations. With lengthier scans, the probability of involuntary movements (e.g., cyclic respiration) increases, thus resulting in lower-quality images [57]. An apparently missing imaging technique from the preclinical imaging investigations is functional MRI (fMRI). In patients, these limitations in resolution and real-time imaging have been increasingly overcome by fMRI. Even if this is perhaps one of the most successful imaging modalities in the clinic, its fundamental principle of operation and practical aspects make it largely incompatible for standard imaging of small animals [70].

In general, particularly high-resolution parameters for vascular imaging may be achieved by the newer uULM (Figure 7) and SR-PCI techniques ($<10\ \mu\text{m}$), but also by SPECT ($<1\ \text{mm}$), photon excitation microscopy ($<1\ \mu\text{m}$), and angiography ($<20\ \mu\text{m}$); however, the applications of these may come at the cost of longer scanning durations, the use of contrast agents, cranial window generation, or high ionising radiation doses [20, 21, 28, 30, 48, 62]. On the contrary, when a technique is minimally invasive to the subject, the resolution is compromised, as noted with MRI (0.1 mm, $<30\ \text{mm}$) and functional photoacoustic microscopy (fPAM; $<30\ \mu\text{m}$) [14, 15, 19, 33, 37, 40, 42, 71, 72]. Researchers have many imaging modalities available to them; however, it is important to understand the limitations of each technology and design experiments based on the limitations of the modalities.

4.6. Contrast Agents and Molecular Probes. Imaging with molecular probes is useful for studying active biological processes at cellular and subcellular levels. Most molecular probes are radionuclide tracers and are used because of their ability to emit radiation from within the body including cells in which these tracers are taken up. As a result, radionuclide imaging offers both qualitative and quantitative data on dynamic biological processes [17, 73]. Meanwhile, contrast agents also emit signals that can enable the collection of qualitative data on the vascular architecture, although there have been discussions regarding their potential side effects [74, 75].

PET is well established as a valuable method to visualise the interplay between changes in cerebral blood flow and the metabolic needs of ischaemic tissues. The effectiveness of PET in understanding different aspects of postischaemic vascular processes depends largely on the types of tracers utilised. For example, [^{15}O]-radiolabelled tracers offer the ability to quantify a number of haemodynamic characteristics, such as cerebral blood flow, cerebral blood volume, cerebral metabolic rate of oxygen, oxygen extraction, and energy metabolism [3]. The most common tracer used in PET imaging is [^{18}F]FDG, although other tracers such as [^{18}F]MISO, [^{18}F]BCPP-EF, and [^{11}C]PK11195 have been utilised as well for different applications [22, 40, 44, 76].

Different molecular factors, such as vascular endothelial growth factor (VEGF), trigger angiogenesis as a component of vascular remodelling, and these processes are regulated by the interplay between components of extracellular matrices and adhesion molecules. VEGF, associated adhesion molecules (e.g., integrins), and microvessel density can thus be useful targets to detect and visualise angiogenesis using probes that are specific to radionuclide imaging techniques [17, 73, 77]. The use of [^{15}O]H₂O as a PET tracer was also noted. Although blood oxygen level-dependent fMRI confers better spatial and temporal resolution and reduced radiation exposure, [^{15}O]H₂O PET benefits include quantitative data output and the capacity for longitudinal imaging [78]. Accordingly, few [^{15}O]H₂O PET studies have been conducted to evaluate cerebral blood flow and other haemodynamics in small animals primarily due to the short half-life of ^{15}O and its potentially high-energy emitted positron, which render the PET images noisier and of lower resolution. Nevertheless, the development of [^{15}O]H₂O-based imaging in small animals is an increasing focus of recent research, and the aforementioned challenges may be technically addressed in the near future (more information is available on the website of the project Small Animal Fast MRI Insert at <https://safir.ethz.ch>) [43, 79–82].

Despite the high resolution of MRI, it generally does not require intravenous contrast agent injections; however, MRI may be enhanced by effective contrast agents for visualisation or quantitative analysis, and this can be facilitated by monocrySTALLINE iron oxide nanoparticles (MIONs). MIONs are useful contrast agents because they are relatively cost-effective to produce, nontoxic, biocompatible, and both chemically and physically stable [83]. Although they are able to depict the vascular architecture clearly, it is important to note that utilising MIONs or any intravascular MRI contrast agents may cause difficulties in evaluating vessels with large diameters due to the contrast agent particles reducing the baseline intravascular signals from larger vessels. This suggests that there may exist an upper threshold in studying vascular remodelling using contrast-enhanced MRI and that only small-vessel changes may reliably be observed. This might be an important aspect to consider when assessing vascular remodelling that includes larger vessel sizes and densities [15, 34, 57, 84].

CT methods, such as micro-CT (μCT) and CT angiography, offer detailed images of the neurovascular

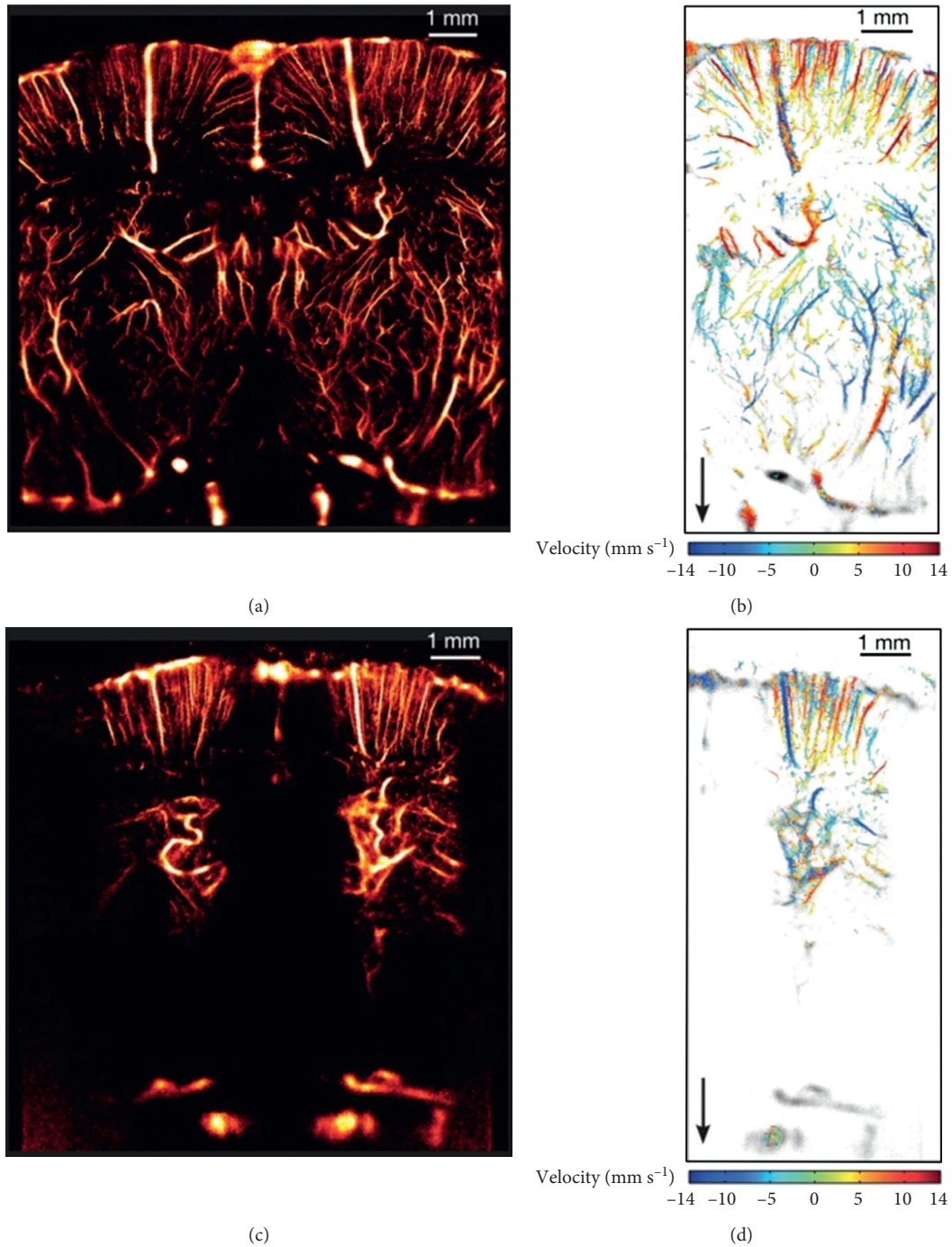


FIGURE 7: (a) Coronal-view image of uULM performed through a thinned-skull window, conferring a resolution of $10 \times 8 \mu\text{m}^2$. (b) In-plane velocity map of some vessels from (a). (c) Coronal-view image of uULM performed through an intact skull, conferring a resolution of $12.5 \times 1 \mu\text{m}^2$. (d) In-plane velocity map of some vessels from (c). uULM, ultrafast ultrasound localisation microscopy [20] (reprinted with permission from Copyright Clearance Center, Inc. [20]).

architecture. Their strengths are reflected in their ability to rapidly generate high-resolution images at relatively low costs [9, 85]. CT angiography involves the administration of an intravenous contrast agent to visualise the vasculature on thin-section images in any plane. Moreover, these detailed images can be obtained in short time frames of approximately less than a minute [21, 39]. Whilst CT does not offer

the same degree of soft-tissue resolution as MRI, CT scans are not contraindicated when metal is present. This is uniquely beneficial because animals with implants or devices can still be imaged. For qualitative data on structural changes in the neurovasculature, CT may be a more practical choice of imaging modality, which may require supplementation by other imaging modalities for quantification.

This systematic literature review also revealed a number of techniques that do not require the administration of contrast agents or tracer molecules; these include fUS, photoacoustic microscopy (PAM), fPAM, laser speckle imaging (LSI), and SR-PCI [16, 32, 33, 36, 42, 48]. Evidently, evading the need for intravenous injections would render these techniques as attractive and ideal for translation to clinical practice. LSI has already been implemented to assess systemic microvascular function in patients with and without cardiovascular disease [86]. Meanwhile, PAM has been used previously to evaluate vascular profiles and oxygen saturation in patients with complex regional pain syndrome, as well as to visualise the microvasculature and changes in vascular networks in patients with and without acral melanoma [87, 88].

4.7. Safety Considerations in Small Animals. Depending on the type of study being designed, there are different safety issues to consider. Some optical imaging modalities involve directly exposing cerebral tissue via thinning of the skull or creation of a cerebral window, after which intravascular labels can be monitored as close to the surface as possible [61]. Because of the invasiveness required, in addition to offering comparatively small fields of view due to minimal penetration of tissue, they are commonly employed in small animal preclinical studies [63, 69]. Alternatively, other optical approaches such as fluorescence microscopy offer the ability for repeated imaging longitudinally in the same animals, which circumvents two major problems: (1) needing to sacrifice animals after critical time intervals in a study and (2) using different cohorts of animals for different time points [89]. In this way, noninvasive imaging techniques may allow for longer experiments over a span of several days, weeks, or months with minimal interruption to the animals whilst monitoring dynamic processes like neurovascular remodelling after ischaemic stroke.

Dose-equivalent radiation is another concern. The performance of μ CT is influenced by the X-ray source utilised. In preclinical applications, μ CT involves significantly lower photon output than that used in clinical CT scanners. Long (e.g., around 50 min) average scan durations may thus be required for preclinical μ CT to achieve comparable noise levels to those in clinical CT [90]. Maintaining recovery anaesthesia, restricting movements, and minimising ionising radiation doses over longer periods then become major procedural concerns [39]. The effects of large doses of radiation on such small animals must also be considered. However, a recent study that evaluated X-ray doses and their corresponding biological effects in experimental animals that underwent cone-beam μ CT scans demonstrated no significant radiation damage in the animals used [91].

Imaging system design may sometimes dictate animal handling. For example, in MRI studies, no items comprising ferromagnetic metals should be present within an MRI suite; this inflicts limitations on equipment that may be needed for small animals in a given investigation, such as monitoring probes, catheters, needles, metal-containing sutures, or

implants. Although shielding from magnetic penetration may be implemented for certain tools, MRI-compatible alternatives are available for instruments that must be present within the MRI suite and within close proximity to the MRI unit [92].

Functional imaging modalities, which reveal physiological changes in response to experimental interventions, mandate stable homeostasis. The administration of anaesthesia may influence key parameters, such as blood volume, flow, and oxygenation; therefore, these changes must be acknowledged and compensated for when administering anaesthetics, analgesics, fluids, body temperature control, blood pressure regulation, or artificial ventilation [27, 93–95]. Other considerations when using small animal models arise simply from their small size, which imposes the need for specialised equipment. In experimental models, it is important for stroke to be stimulated under sterile and hygienic conditions to minimise the occurrence of wound infections. It is crucial to verify that any neuroinflammation that is identified using imaging techniques stems from ischaemia, rather than inadequate aseptic methods [96]. Administering sufficient anaesthesia for the duration of the imaging scan, sustaining metabolic homeostasis via dedicated monitoring equipment, and restricted access to the animal during the imaging scan are also prominent aspects that require consideration to ensure that the instruments utilised do not generate image distortions or hazards to the animals or researchers [92].

4.8. Potential Limitations in Imaging Vascular Remodelling. Improving the interpretation of imaging data is an active field of research to overcome the functional limitations present in various imaging techniques. For example, PET produces high-resolution images that are subject to background noise in the data that must be corrected for. Imaging vascular changes using contrast-enhanced methods experiences similar issues. Contrast-enhanced imaging methods rely on the distribution of molecules throughout the vasculature to be visualised. In ischaemic injury, vessel disruption directly affects the distribution of contrast. Acutely, this absence of contrast agents may contribute to the diagnosis of ischaemia; however, in long-term settings, the remodelling itself may contribute to the absence of contrast agents by means of vessel occlusion, haemostasis, or sub-threshold quantities of contrast in these vessels, thus limiting detection on image acquisition. This disruption in blood flow is certainly not uncommon in ischaemic injury, and this phenomenon has been previously demonstrated with the use of ultrafast Doppler angiography to study coronary blood flow dynamics [97]. Cerebral blood volume is another concern when assessing neurovascular remodelling because an increase can represent either neoangiogenesis or vessel dilatation [14]. Lack of definition is also an issue to consider when imaging vasculature after injury. The damaged vessels may also allow the contrast agent to leak into the interstitial space around the vessels, which can inevitably distort the resulting images obtained by generating blurred images [98]. Thus, in such cases, certain types of noise in the data could

potentially represent vascular leakage or, comprising a more positive outlook, could provide information on changes in postinjury blood flow dynamics.

One overarching aspect that may be worth considering when interpreting images from the translation of preclinical research to its application to humans is the age of animal models used. In general, younger animal models are used for research purposes simply because they are easier to manage and incur lower laboratory costs; older animals would need to be maintained for several months until the equivalent “old age.” However, ischaemic injury in the form of stroke is a much more common occurrence in elderly individuals amongst humans. The ischaemic penumbra also varies in measurements of size and its incorporation into the ischaemic core over time between young and old animals [96]. As a result, it may be worth imaging small animals at various time points into “older” age to inform the interpretation of imaging results in preclinical models. Whether the physiology and pathology of younger preclinical models provide a sufficient platform to develop effective treatments in older humans is a point to consider in future research.

4.9. Future Prospects. The current trends in preclinical imaging are progressing towards synergistic methods, allowing for the simultaneous extraction of the beneficial characteristics of each individual modality, a broader range of information that can be obtained from resulting images, and thus, optimisation of diagnosis. It is difficult to establish a single imaging technique that is optimal in all cases, as this will likely require a trade-off between different parameters; instead, multimodal techniques can be employed to take advantage of the most optimal parameters. Furthermore, with the data obtained from multiple imaging techniques, a greater number of parameters may be integrated into or used to confirm mathematical models to shed further light on physiological and pathological information [69, 73].

A multimodal imaging system with the ability to perform SPECT, bioluminescence imaging, and fluorescence imaging—referred to as the U-SPECT-BioFluo system—was introduced to elucidate physiological and anatomical information within the body, specifically to target tumours. To achieve this, mouse models were administered with both a fluorescent optical dye and radioactive agent to visualise their molecular-level interactions within the body. This imaging system was originally introduced with specific relevance to study tumourigenic angiogenesis, and similarly, such a system could be employed to study the vascular changes (which also involve angiogenesis, amongst other cellular processes) following ischaemic injury (Figure 8) [99]. On a similar note, another group developed a hexamodal imaging system that exploited a unique porphyrin-phospholipid-coated type of nanoparticle. These nanoparticulate agents can be utilised to retrieve information from six different imaging modalities that comprise this system: upconversion, fluorescence, photoacoustic, PET, CT, and Cherenkov luminescence imaging [100]. Highly integrated systems such as this show great promise and

feasibility for providing information that may not be achievable with single or dual imaging modalities. Multimodal neuroimaging hence represents the foundation for advancing postischaemic restorative therapies. Combinatorial techniques can ultimately be implemented to achieve a more needs-based and personalised approach in medicine and healthcare.

Novel tracers that target different molecular pathways and can be utilised with existing imaging systems are also continuously under investigation. For example, the newly characterised PET tracer [^{18}F]glycoprotein-1 ([^{18}F]GP1) has been demonstrated to elucidate regions of platelet aggregation and thrombi in cynomolgus monkeys. Small venous and arterial thrombi were clearly and simply visualised in real time, and the tracer exhibited rapid blood clearance, raising the possibility of imaging ischaemia-related vascular changes in humans using [^{18}F]GP1 (Figure 9) [101]. In addition, another group demonstrated the feasibility of a dual optical and PET/CT tracer for (a) noninvasive in vivo imaging of activated macrophages and vascular inflammatory activity in atherosclerotic plaques in mouse models and (b) visualisation of activated macrophages in human carotid plaque tissues, based on the activity of cysteine cathepsins [102].

Developments in MRI systems that may be useful in cases of ischaemia are also worth mentioning here. Four-dimensional (4D) flow MRI has been demonstrated to be useful for the evaluation of neurovascular haemodynamics and cerebral blood flow [103, 104]. Although long acquisition times (approx. 5–20 min) and a spatial resolution that is insufficient to capture small-vessel haemodynamics represent considerable technical limitations, 4D flow MRI comes with the benefit of evading the necessity for gadolinium contrast agents [105]. To achieve superior image contrast, MRI-based quantitative susceptibility-weighted imaging offers a way to facilitate the delineation of neural structures with the added advantage of quantification of magnetic properties in the brain [83]. Ultimately, preclinical imaging is performed with the aim of translating findings to clinical practice. Given the fact that the most common preclinical imaging techniques are MRI followed by PET, as identified in this systematic literature review, their direct combination in dedicated PET/MRI systems can prove to be advantageous for providing complementary functional and structural data. This would be advantageous for studying ongoing vascular changes; however, technical developments are warranted to facilitate accurate quantification and improved spatiotemporal resolution [106, 107].

Through its wide-ranging applications, preclinical imaging generously lends itself to translational approaches from small animals to humans. The ability to visualise tissues and organs influences the precision and accuracy of diagnosis, staging, treatment planning, and treatment response evaluation. MRI, PET, SPECT, CT, and ultrasound are commonly used in clinical practice for various imaging purposes. Although optical imaging modalities are relatively not as frequently implemented in the clinic, they are increasingly garnering attention for clinical translation [108]. The Network for Translational Research: Optical Imaging in

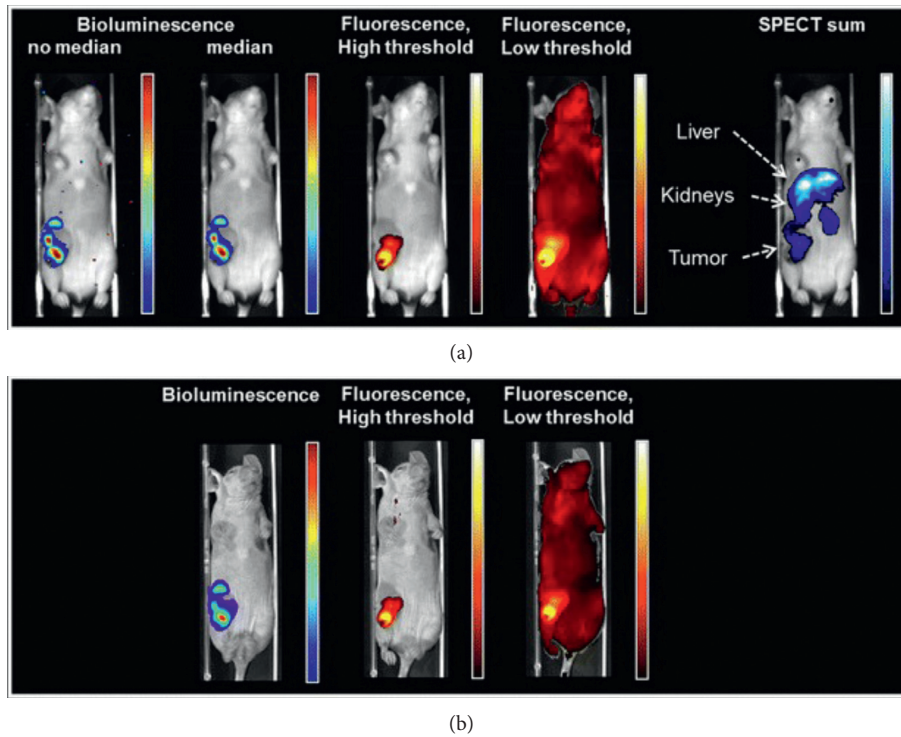


FIGURE 8: Images of a mouse with a 4T1-luc + tumour. Bioluminescence images were acquired following D-luciferin injections; fluorescence and SPECT images were acquired following multimodal tracer $[^{111}\text{In}]\text{-RGD-MSAP}$ injections. (a) U-SPECT-BioFluo bioluminescence images with and without median filter applied, fluorescence images with high and low threshold applied, and SPECT image. (b) IVIS bioluminescence and fluorescence images. SPECT, single-photon emission computed tomography; IVIS, in vivo imaging system. This figure is published in [99], which is distributed under the terms of the Creative Commons Attribution 4.0 International License (<http://creativecommons.org/licenses/by/4.0>).

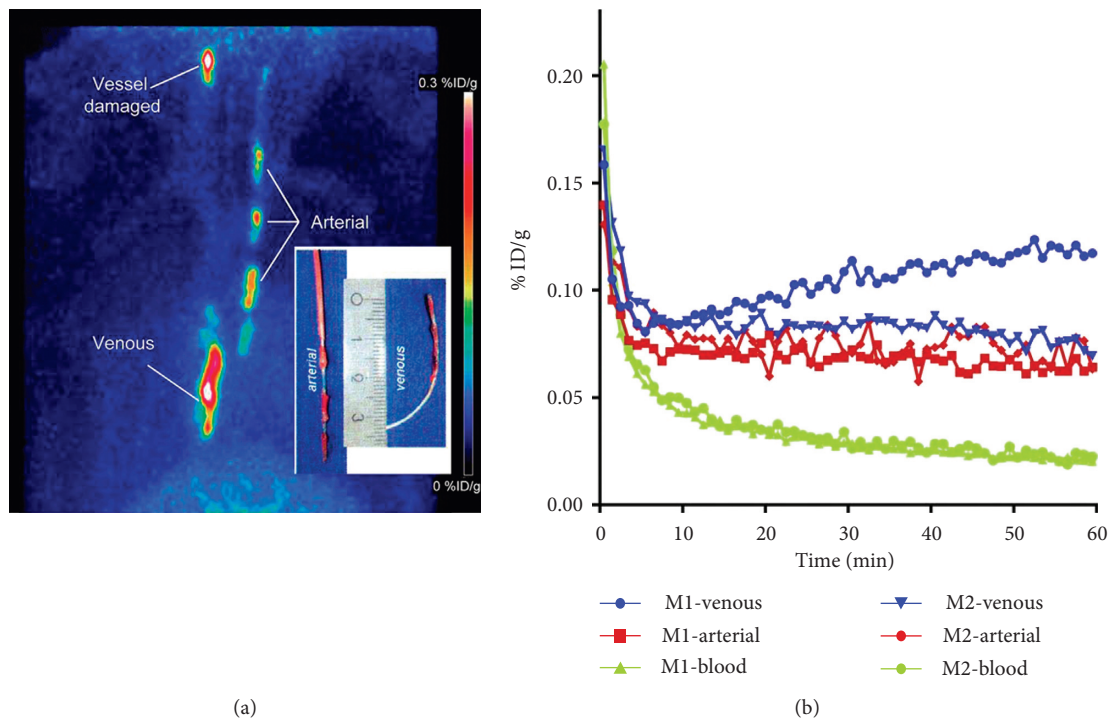


FIGURE 9: (a) $[^{18}\text{F}]\text{GP1}$ PET image of cynomolgus monkeys with arterial and venous catheters that were inserted in the right carotid artery and vena cava, respectively (maximum-intensity projection 0–60 min). Both arterial and venous thrombi exhibited tracer uptake. (b) $[^{18}\text{F}]\text{GP1}$ time-activity curves of thrombus uptake and blood clearance in monkeys 1 (displayed in (a)) and 2. $[^{18}\text{F}]\text{GP1}$, $[^{18}\text{F}]\text{glycoprotein-1}$; PET, positron emission tomography; M1, monkey 1; M2, monkey 2; %ID/g, percentage injected dose per gram. This research was originally published by Lohrke et al. [101].

Multimodal Platforms is a programme dedicated to developing, optimising, and validating imaging methods for rapid clinical translation. In particular, this network focusses on early-stage imaging using multiple common modalities in combination with an optical imaging modality; this combination may facilitate a quicker progression of optical imaging modalities to clinical trials [109, 110].

Furthermore, multidisciplinary collaboration can prove to enhance the value of imaging technology in translating preclinical animal models to clinical settings. For example, point-of-care technology is emerging as the future direction for clinical applications of imaging to enhance patients' experiences and decrease associated expenses. The most significant advantage of point-of-care medical imaging is the capacity to provide instant information to guide immediate clinical management decisions, as it acts as a first-line tool to screen for acute medical problems, particularly in resource-limited settings [60]. Ultimately, optimal medical and molecular imaging methods may contribute to more accurate diagnoses at earlier disease stages and prior to and during surgical operations; in due course, these methods are anticipated to enhance therapeutic outcomes in patients.

5. Conclusions

The field of neuroimaging has augmented our understanding of the mechanisms of ischaemic trauma, and a variety of imaging techniques are particularly helpful for observing subsequent vascular remodelling within the brain. Appropriate combinations of imaging modalities incorporating biomarkers of blood flow, energy fluctuations, and neurovascular breakdown can potentially elucidate optimal perspectives of postischaemic reorganisation.

This review is a systematic study and analysis of the literature published between 2008 and 2018 regarding preclinical in vivo imaging biomarkers for postischaemia neurovascular remodelling. The search identified 35 peer-reviewed research articles, which predominantly reported on the use of MRI or PET, although other imaging modalities were also utilised. There remain critical gaps in our knowledge within the field of restorative therapy for neurological pathologies, such as traumatic brain injury and ischaemia; amongst them, being able to detect vascular remodelling noninvasively and observe its evolution through stages of vascular recovery is an important aspect. The push towards molecular imaging has promoted the development of biological target-specific tracers to reveal the physiological and pathological mechanisms within the brain. Concurrently, the prospect of multimodality clinical imaging with its unification of anatomical and functional information holds superior potential in expanding our understanding of neurovascular organisation and disease activity.

Conflicts of Interest

The authors have no conflicts of interest to disclose, and they reported all papers that satisfied the specified relevant criteria; however, if some papers are missing, this was not

intentional and they wish to proactively apologise to any corresponding authors.

Acknowledgments

This study was supported by the Engineering and Physical Sciences Research Council (EPSRC) Center for Doctoral Training in Tissue Engineering and Regenerative Medicine (EP/L014823/1).

References

- [1] E. Taoufik and L. Probert, "Ischemic neuronal damage," *Current Pharmaceutical Design*, vol. 14, no. 33, pp. 3565–3573, 2008.
- [2] K. Arai, G. Jin, D. Navaratna, and E. H. Lo, "Brain angiogenesis in developmental and pathological processes: neurovascular injury and angiogenic recovery after stroke," *FEBS Journal*, vol. 276, no. 17, pp. 4644–4652, 2009.
- [3] P. Barber, "Magnetic resonance imaging of ischemia viability thresholds and the neurovascular unit," *Sensors*, vol. 13, no. 6, pp. 6981–7003, 2013.
- [4] A. Sachdev, R. Sharma, and D. Gupta, "Cerebrovascular complications in pediatric intensive care unit," *Indian Journal of Critical Care Medicine*, vol. 14, no. 3, pp. 129–140, 2010.
- [5] Y. Xiong, A. Mahmood, and M. Chopp, "Angiogenesis, neurogenesis and brain recovery of function following injury," *Current Opinion in Investigational Drugs*, vol. 11, no. 3, pp. 298–308, 2010.
- [6] J. Boltze, C. Kleinschnitz, K. G. Reymann et al., "Neurovascular pathophysiology in cerebral ischemia, dementia and the ageing brain—current trends in basic, translational and clinical research," *Experimental & Translational Stroke Medicine*, vol. 4, no. 1, p. 14, 2012.
- [7] A. Popa-Wagner, D. Pirici, E. Bogdan Petcu et al., "Pathophysiology of the vascular wall and its relevance for cerebrovascular disorders in aged rodents," *Current Neurovascular Research*, vol. 7, no. 3, pp. 251–267, 2010.
- [8] K. S. Kamalian S, D. J. Boulter, M. H. Lev, R. G. Gonzalez, and P. W. Schaefer, "Stroke differential diagnosis and mimics: part 1," *Applied Radiology*, vol. 44, no. 11, pp. 26–39, 2015.
- [9] A. Dorr, J. G. Sled, and N. Kabani, "Three-dimensional cerebral vasculature of the CBA mouse brain: a magnetic resonance imaging and micro computed tomography study," *Neuroimage*, vol. 35, no. 4, pp. 1409–1423, 2007.
- [10] R. S. J. Frackowiak, G.-L. Lenzi, T. Jones, and J. D. Heather, "Quantitative measurement of regional cerebral blood flow and oxygen metabolism in man using ^{15}O and positron emission tomography," *Journal of Computer Assisted Tomography*, vol. 4, no. 6, pp. 727–736, 1980.
- [11] T. Jones, D. A. Chesler, and M. M. Ter-Pogossian, "The continuous inhalation of oxygen-15 for assessing regional oxygen extraction in the brain of man," *British Journal of Radiology*, vol. 49, no. 580, pp. 339–343, 1976.
- [12] H.-Y. Wey, V. R. Desai, and T. Q. Duong, "A review of current imaging methods used in stroke research," *Neurological Research*, vol. 35, no. 10, pp. 1092–1102, 2013.
- [13] D. Moher, A. Liberati, J. Tetzlaff, D. G. Altman, and for the PRISMA Group, "Preferred reporting items for systematic reviews and meta-analyses: the PRISMA statement," *BMJ*, vol. 339, no. 1, article b2535, 2009.

- [14] A. Bosomtwi, Q. Jiang, G. L. Ding et al., "Quantitative evaluation of microvascular density after stroke in rats using MRI," *Journal of Cerebral Blood Flow & Metabolism*, vol. 28, no. 12, pp. 1978–1987, 2008.
- [15] A. Bosomtwi, M. Chopp, L. Zhang et al., "Mean microvessel segment length and radius after embolic stroke: comparison of magnetic resonance imaging (MRI) and laser scanning confocal microscopy (LSCM)," *Brain Research*, vol. 1381, pp. 217–227, 2011.
- [16] C. Brunner, C. Isabel, A. Martin et al., "Mapping the dynamics of brain perfusion using functional ultrasound in a rat model of transient middle cerebral artery occlusion," *Journal of Cerebral Blood Flow & Metabolism*, vol. 37, no. 1, pp. 263–276, 2017.
- [17] W. Cai, R. Guzman, A. R. Hsu et al., "Positron emission tomography imaging of poststroke angiogenesis," *Stroke*, vol. 40, no. 1, pp. 270–277, 2009.
- [18] L. H. Deddens, G. A. van Tilborg, A. van der Toorn, H. E. de Vries, and R. M. Dijkhuizen, "PECAM-1-targeted micron-sized particles of iron oxide as MRI contrast agent for detection of vascular remodeling after cerebral ischemia," *Contrast Media & Molecular Imaging*, vol. 8, no. 5, pp. 393–401, 2013.
- [19] G. Ding, Q. Jiang, L. Li et al., "Angiogenesis detected after embolic stroke in rat brain using magnetic resonance T2*WI," *Stroke*, vol. 39, no. 5, pp. 1563–1568, 2008.
- [20] C. Errico, J. Pierre, S. Pezet et al., "Ultrafast ultrasound localization microscopy for deep super-resolution vascular imaging," *Nature*, vol. 527, no. 7579, pp. 499–502, 2015.
- [21] G. Figueiredo, C. Brockmann, H. Boll et al., "Comparison of digital subtraction angiography, micro-computed tomography angiography and magnetic resonance angiography in the assessment of the cerebrovascular system in live mice," *Clinical Neuroradiology*, vol. 22, no. 1, pp. 21–28, 2012.
- [22] M. Gramer, D. Feuerstein, A. Steimers et al., "Device for simultaneous positron emission tomography, laser speckle imaging and RGB reflectometry: validation and application to cortical spreading depression and brain ischemia in rats," *Neuroimage*, vol. 94, pp. 250–262, 2014.
- [23] N. G. Horton, K. Wang, D. Kobat et al., "In vivo three-photon microscopy of subcortical structures within an intact mouse brain," *Nature Photonics*, vol. 7, no. 3, pp. 205–209, 2013.
- [24] G. P. Howles, K. B. Ghaghada, Y. Qi, S. Mukundan, and G. A. Johnson, "High-resolution magnetic resonance angiography in the mouse using a nanoparticle blood-pool contrast agent," *Magnetic Resonance in Medicine*, vol. 62, no. 6, pp. 1447–1456, 2009.
- [25] S. Hu, K. Maslov, and L. V. Wang, "Noninvasive label-free imaging of microhemodynamics by optical-resolution photoacoustic microscopy," *Optics Express*, vol. 17, no. 9, pp. 7688–7693, 2009.
- [26] C.-H. Huang, Y.-Y. Ian Shih, T.-Y. Siow et al., "Temporal assessment of vascular reactivity and functionality using MRI during postischemic proangiogenic vascular remodeling," *Magnetic Resonance Imaging*, vol. 33, no. 7, pp. 903–910, 2015.
- [27] E. Jimenez-Xarrie, B. Perez, A. P. Dantas et al., "Uric acid treatment after stroke prevents long-term middle cerebral artery remodeling and attenuates brain damage in spontaneously hypertensive rats," *Translational Stroke Research*, 2018, In press.
- [28] A. Kolodziej, M. Lippert, F. Angenstein et al., "SPECT-imaging of activity-dependent changes in regional cerebral blood flow induced by electrical and optogenetic self-stimulation in mice," *Neuroimage*, vol. 103, pp. 171–180, 2014.
- [29] E. M. R. Lake, P. Bazzigaluppi, J. Mester et al., "Neurovascular unit remodelling in the subacute stage of stroke recovery," *Neuroimage*, vol. 146, pp. 869–882, 2017.
- [30] J. Lecoq, A. Parpaleix, E. Roussakis et al., "Simultaneous two-photon imaging of oxygen and blood flow in deep cerebral vessels," *Nature Medicine*, vol. 17, no. 7, pp. 893–898, 2011.
- [31] A. Letourneur, V. Chen, G. Waterman, and P. J. Drew, "A method for longitudinal, transcranial imaging of blood flow and remodeling of the cerebral vasculature in postnatal mice," *Physiological Reports*, vol. 2, no. 12, article e12238, 2014.
- [32] N. Li, X. Jia, K. Murari et al., "High spatiotemporal resolution imaging of the neurovascular response to electrical stimulation of rat peripheral trigeminal nerve as revealed by in vivo temporal laser speckle contrast," *Journal of Neuroscience Methods*, vol. 176, no. 2, pp. 230–236, 2009.
- [33] L. D. Liao, C. T. Lin, Y. Y. Shih et al., "Investigation of the cerebral hemodynamic response function in single blood vessels by functional photoacoustic microscopy," *Journal of Biomedical Optics*, vol. 17, no. 6, article 061210, 2012.
- [34] C. Y. Lin, M. H. Lin, W. M. Cheung et al., "In vivo cerebro-microvasculature visualization using 3D DeltaR2-based microscopy of magnetic resonance angiography (3DDeltaR2-mMRA)," *Neuroimage*, vol. 45, no. 3, pp. 824–831, 2009.
- [35] J. Luckl, W. Baker, Z.H. Sun, T. Durduran, A. G. Yodh, and J. H. Greenberg, "The biological effect of contralateral forepaw stimulation in rat focal cerebral ischemia: a multispectral optical imaging study," *Frontiers in Neurogenetics*, vol. 2, p. 19, 2010.
- [36] P. Miao, A. Rege, N. Li, N. V. Thakor, and S. Tong, "High resolution cerebral blood flow imaging by registered laser speckle contrast analysis," *IEEE Transactions on Biomedical Engineering*, vol. 57, no. 5, pp. 1152–1157, 2010.
- [37] T. N. Nagaraja, K. Karki, J. R. Ewing, R. L. Croxen, and R. A. Knight, "Identification of variations in blood-brain barrier opening after cerebral ischemia by dual contrast-enhanced magnetic resonance imaging and T1sat measurements," *Stroke*, vol. 39, no. 2, pp. 427–432, 2008.
- [38] S. Sakadžić, E. Roussakis, M. A. Yaseen et al., "Two photon imaging of the oxygen partial pressure in cerebral microvasculature," *Nature Methods*, vol. 7, no. 9, pp. 755–759, 2010.
- [39] S. J. Schambach, S. Bag, V. Steil et al., "Ultrafast high-resolution in vivo volume-CTA of mice cerebral vessels," *Stroke*, vol. 40, no. 4, pp. 1444–1450, 2009.
- [40] M. Schroeter, M. A. Dennin, M. Walberer et al., "Neuroinflammation extends brain tissue at risk to vital peri-infarct tissue: a double tracer [11C]PK11195- and [18F]FDG-PET study," *Journal of Cerebral Blood Flow & Metabolism*, vol. 29, no. 6, pp. 1216–1225, 2009.
- [41] Y. Seo, T. Hashimoto, Y. Nuki, and B. H. Hasegawa, "In vivo microCT imaging of rodent cerebral vasculature," *Physics in Medicine & Biology*, vol. 53, no. 7, pp. N99–N107, 2008.
- [42] E. W. Stein, K. Maslov, and L. V. Wang, "Noninvasive, in vivo imaging of blood-oxygenation dynamics within the mouse brain using photoacoustic microscopy," *Journal of Biomedical Optics*, vol. 14, no. 2, article 020502, 2009.
- [43] T. Struys, K. Govaerts, W. Oosterlinck et al., "In vivo evidence for long-term vascular remodeling resulting from chronic cerebral hypoperfusion in mice," *Journal of Cerebral Blood Flow & Metabolism*, vol. 37, no. 2, pp. 726–739, 2017.

- [44] H. Tsukada, H. Ohba, S. Nishiyama et al., "PET imaging of ischemia-induced impairment of mitochondrial complex I function in monkey brain," *Journal of Cerebral Blood Flow & Metabolism*, vol. 34, no. 4, pp. 708–714, 2014.
- [45] P. Yanev, P. R. Seevinck, U. S. Rudrapatna et al., "Magnetic resonance imaging of local and remote vascular remodelling after experimental stroke," *Journal of Cerebral Blood Flow & Metabolism*, vol. 37, no. 8, pp. 2768–2779, 2017.
- [46] H.-J. Yoon, E.-S. Lee, M. Kang, Y. Jeong, and J.-H. Park, "In vivo multi-photon luminescence imaging of cerebral vasculature and blood-brain barrier integrity using gold nanoparticles," *Journal of Materials Chemistry B*, vol. 3, no. 15, pp. 2935–2938, 2015.
- [47] L. Yu, E. Nguyen, G. Liu, B. Choi, and Z. Chen, "Spectral Doppler optical coherence tomography imaging of localized ischemic stroke in a mouse model," *Journal of Biomedical Optics*, vol. 15, no. 6, article 066006, 2010.
- [48] M. Q. Zhang, L. Zhou, Q. F. Deng et al., "Ultra-high-resolution 3D digitalized imaging of the cerebral angioarchitecture in rats using synchrotron radiation," *Scientific Reports*, vol. 5, article 14982, 2015.
- [49] D. M. Hermann, A. M. Buga, and A. Popa-Wagner, "Neurovascular remodeling in the aged ischemic brain," *Journal of Neural Transmission*, vol. 122, no. 1, pp. S25–S33, 2015.
- [50] F. Fluri, M. K. Schuhmann, and C. Kleinschnitz, "Animal models of ischemic stroke and their application in clinical research," *Drug Design, Development and Therapy*, vol. 9, p. 3445, 2015.
- [51] F. Liu and L. D. McCullough, "Middle cerebral artery occlusion model in rodents: methods and potential pitfalls," *Journal of Biomedicine and Biotechnology*, vol. 2011, article 464701, 9 pages, 2011.
- [52] M. Walberer and M. A. Rueger, "The macrosphere model—an embolic stroke model for studying the pathophysiology of focal cerebral ischemia in a translational approach," *Annals of Translational Medicine*, vol. 3, no. 9, p. 123, 2015.
- [53] H. C. S. Abeysinghe, L. Bokhari, G. J. Dusting, and C. L. Roulston, "Brain remodelling following endothelin-1 induced stroke in conscious rats," *PLoS One*, vol. 9, no. 5, Article ID e97007, 2014.
- [54] A. B. Uzdensky, "Photothrombotic stroke as a model of ischemic stroke," *Translational Stroke Research*, vol. 9, no. 5, pp. 437–451, 2017.
- [55] P. Carmeliet, "Mechanisms of angiogenesis and arteriogenesis," *Nature Medicine*, vol. 6, no. 4, pp. 389–395, 2000.
- [56] M. A. Font, A. Arboix, and J. Krupinski, "Angiogenesis, neurogenesis and neuroplasticity in ischemic stroke," *Current Cardiology Reviews*, vol. 6, no. 3, pp. 238–44, 2010.
- [57] P. J. Bolan, E. Yacoub, M. Garwood, K. Ugurbil, and N. Harel, "In vivo micro-MRI of intracortical neurovasculature," *Neuroimage*, vol. 32, no. 1, pp. 62–69, 2006.
- [58] R. Gupta, S. E. Jones, E. A. Q. Mooyaart, and S. R. Pomerantz, "Computed tomographic angiography in stroke imaging: fundamental principles, pathologic findings, and common pitfalls," *Seminars in Ultrasound, CT and MRI*, vol. 27, no. 3, pp. 221–242, 2006.
- [59] M. A. Stefani, F. L. Schneider, A. C. H. Marrone, A. G. Severino, A. P. Jackowski, and M. C. Wallace, "Anatomic variations of anterior cerebral artery cortical branches," *Clinical Anatomy*, vol. 13, no. 4, pp. 231–236, 2000.
- [60] EPSRC, *Report of the Medical Imaging Technology Working Group*, EPSRC, Swindon, UK, 2012.
- [61] P. Yanev and R. M. Dijkhuizen, "In vivo imaging of neurovascular remodeling after stroke," *Stroke*, vol. 43, no. 12, pp. 3436–3441, 2012.
- [62] C. E. Brown, P. Li, J. D. Boyd, K. R. Delaney, and T. H. Murphy, "Extensive turnover of dendritic spines and vascular remodeling in cortical tissues recovering from stroke," *Journal of Neuroscience*, vol. 27, no. 15, pp. 4101–4109, 2007.
- [63] A. Y. Shih, J. D. Driscoll, P. J. Drew et al., "Two-photon microscopy as a tool to study blood flow and neurovascular coupling in the rodent brain," *Journal of Cerebral Blood Flow & Metabolism*, vol. 32, no. 7, pp. 1277–1309, 2012.
- [64] P. J. Drew, A. Y. Shih, J. D. Driscoll et al., "Chronic optical access through a polished and reinforced thinned skull," *Nature Methods*, vol. 7, no. 12, pp. 981–984, 2010.
- [65] E. Kim, M. Shidahara, C. Tsoumpas et al., "Partial volume correction using structural-functional synergistic resolution recovery: comparison with geometric transfer matrix method," *Journal of Cerebral Blood Flow & Metabolism*, vol. 33, no. 6, pp. 914–920, 2013.
- [66] M. Soret, S. L. Bacharach, and I. Buvat, "Partial-volume effect in PET tumor imaging," *Journal of Nuclear Medicine*, vol. 48, no. 6, pp. 932–945, 2007.
- [67] J. Tohka, "Partial volume effect modeling for segmentation and tissue classification of brain magnetic resonance images: a review," *World Journal of Radiology*, vol. 6, no. 11, pp. 855–864, 2014.
- [68] M. Muzi, F. O'Sullivan, D. A. Mankoff et al., "Quantitative assessment of dynamic PET imaging data in cancer imaging," *Magnetic Resonance Imaging*, vol. 30, no. 9, pp. 1203–1215, 2012.
- [69] A. P. Pathak, E. Kim, J. Zhang, and M. V. Jones, "Three-dimensional imaging of the mouse neurovasculature with magnetic resonance microscopy," *PLoS One*, vol. 6, no. 7, Article ID e22643, 2011.
- [70] A. Van der Linden, N. Van Camp, P. Ramos-Cabrer, and M. Hoehn, "Current status of functional MRI on small animals: application to physiology, pathophysiology, and cognition," *NMR Biomedicine*, vol. 20, no. 5, pp. 522–545, 2007.
- [71] Q. Jiang, Z. G. Zhang, G. L. Ding et al., "Investigation of neural progenitor cell induced angiogenesis after embolic stroke in rat using MRI," *Neuroimage*, vol. 28, no. 3, pp. 698–707, 2005.
- [72] R. Weber, S. Wegener, P. Ramos-Cabrer, D. Wiedermann, and M. Hoehn, "MRI detection of macrophage activity after experimental stroke in rats: new indicators for late appearance of vascular degradation?," *Magnetic Resonance in Medicine*, vol. 54, no. 1, pp. 59–66, 2005.
- [73] L. W. Dobrucki and A. J. Sinusas, "PET and SPECT in cardiovascular molecular imaging," *Nature Reviews Cardiology*, vol. 7, no. 1, pp. 38–47, 2010.
- [74] S. P. Lin and J. J. Brown, "MR contrast agents: physical and pharmacologic basics," *Journal of Magnetic Resonance Imaging*, vol. 25, no. 5, pp. 884–899, 2007.
- [75] E. Hernandez-Torres, N. Kassner, N. D. Forkert et al., "Anisotropic cerebral vascular architecture causes orientation dependency in cerebral blood flow and volume measured with dynamic susceptibility contrast magnetic resonance imaging," *Journal of Cerebral Blood Flow & Metabolism*, vol. 37, no. 3, pp. 1108–1119, 2017.
- [76] M. Takasawa, J. S. Beech, T. D. Fryer et al., "Imaging of brain hypoxia in permanent and temporary middle cerebral artery occlusion in the rat using 18F-fluoromisonidazole and

- positron emission tomography: a pilot study," *Journal of Cerebral Blood Flow & Metabolism*, vol. 27, no. 4, pp. 679–689, 2007.
- [77] A. Surov, H. J. Meyer, and A. Wienke, "Standardized uptake values derived from (18)F-FDG PET may predict lung cancer microvessel density and expression of KI 67, VEGF, and HIF-1 α but not expression of cyclin D1, PCNA, EGFR, PD L1, and p53," *Contrast Media & Molecular Imaging*, vol. 2018, article 9257929, 10 pages, 2018.
- [78] M. Kameyama, K. Murakami, and M. Jinzaki, "Comparison of [(15)O] H₂O positron emission tomography and functional magnetic resonance imaging in activation studies," *World Journal of Nuclear Medicine*, vol. 15, no. 1, pp. 3–6, 2016.
- [79] T. Temma, M. Yamazaki, J. Miyanojima et al., "Sequential PET estimation of cerebral oxygen metabolism with spontaneous respiration of (15)O-gas in mice with bilateral common carotid artery stenosis," *Journal of Cerebral Blood Flow & Metabolism*, vol. 37, no. 10, pp. 3334–3343, 2017.
- [80] G. Horitsugi, T. Watabe, Y. Kanai et al., "Oxygen-15 labeled CO(2), O(2), and CO PET in small animals: evaluation using a 3D-mode microPET scanner and impact of reconstruction algorithms," *EJNMMI Research*, vol. 7, no. 1, p. 91, 2017.
- [81] M. Kobayashi, T. Mori, Y. Kiyono et al., "Cerebral oxygen metabolism of rats using injectable (15)O-oxygen with a steady-state method," *Journal of Cerebral Blood Flow & Metabolism*, vol. 32, no. 1, pp. 33–40, 2012.
- [82] X. Zhang, Y. Petibon, A. Sitek et al., "In-vivo simultaneous DCE-MRI/O-15-water-PET," *Journal of Nuclear Medicine*, vol. 56, no. 3, p. 644, 2015.
- [83] H. Wei, L. Xie, R. Dibb et al., "Imaging whole-brain cytoarchitecture of mouse with MRI-based quantitative susceptibility mapping," *Neuroimage*, vol. 137, pp. 107–115, 2016.
- [84] N. Harel, J. Lin, S. Moeller, K. Ugurbil, and E. Yacoub, "Combined imaging-histological study of cortical laminar specificity of fMRI signals," *Neuroimage*, vol. 29, no. 3, pp. 879–887, 2006.
- [85] S. J. Schambach, S. Bag, C. Groden, L. Schilling, and M. A. Brockmann, "Vascular imaging in small rodents using micro-CT," *Methods*, vol. 50, no. 1, pp. 26–35, 2010.
- [86] J. P. Borges, G. O. Lopes, V. Verri et al., "A novel effective method for the assessment of microvascular function in male patients with coronary artery disease: a pilot study using laser speckle contrast imaging," *Brazilian Journal of Medical and Biological Research*, vol. 49, no. 10, article e5541, 2016.
- [87] C. P. Favazza, O. Jassim, L. A. Cornelius, and L. V. Wang, "In vivo photoacoustic microscopy of human cutaneous microvasculature and a nevus," *Journal of Biomedical Optics*, vol. 16, no. 1, article 016015, 2011.
- [88] Y. Zhou, X. Yi, W. Xing et al., "Microcirculatory changes identified by photoacoustic microscopy in patients with complex regional pain syndrome type I after stellate ganglion blocks," *Journal of Biomedical Optics*, vol. 19, no. 8, article 086017, 2014.
- [89] Y. Tomita, N. Kubis, Y. Calando et al., "Long-term in vivo investigation of mouse cerebral microcirculation by fluorescence confocal microscopy in the area of focal ischemia," *Journal of Cerebral Blood Flow & Metabolism*, vol. 25, no. 7, pp. 858–867, 2005.
- [90] D. P. Clark and C. T. Badea, "Micro-CT of rodents: state-of-the-art and future perspectives," *Physica Medica*, vol. 30, no. 6, pp. 619–634, 2014.
- [91] N. Miyahara, T. Kokubo, Y. Hara et al., "Evaluation of X-ray doses and their corresponding biological effects on experimental animals in cone-beam micro-CT scans (R-mCT2)," *Radiological Physics and Technology*, vol. 9, no. 1, pp. 60–68, 2016.
- [92] L. A. Colby and B. J. Morenko, "Clinical considerations in rodent bioimaging," *Comparative Medicine*, vol. 54, no. 6, pp. 623–630, 2004.
- [93] C. Broux, I. Tropres, O. Montigon et al., "The effects of sustained hyperventilation on regional cerebral blood volume in thiopental-anesthetized rats," *Anesthesia & Analgesia*, vol. 95, no. 6, pp. 1746–1751, 2002.
- [94] J. N. Lorenz, "A practical guide to evaluating cardiovascular, renal, and pulmonary function in mice," *American Journal of Physiology-Regulatory, Integrative and Comparative Physiology*, vol. 282, no. 6, pp. R1565–1582, 2002.
- [95] A. H. Moore, C. L. Osteen, A. F. Chatziioannou, D. A. Hovda, and S. R. Cherry, "Quantitative assessment of longitudinal metabolic changes in vivo after traumatic brain injury in the adult rat using FDG-microPET," *Journal of Cerebral Blood Flow & Metabolism*, vol. 20, no. 10, pp. 1492–1501, 2000.
- [96] I. M. Macrae, "Preclinical stroke research--advantages and disadvantages of the most common rodent models of focal ischaemia," *British Journal of Pharmacology*, vol. 164, no. 4, pp. 1062–1078, 2011.
- [97] D. Maresca, M. Correia, O. Villemain et al., "Noninvasive imaging of the coronary vasculature using ultrafast ultrasound," *JACC: Cardiovascular Imaging*, vol. 11, no. 6, pp. 798–808, 2018.
- [98] Y. Zhao, I. J. C. MacCormick, D. G. Parry et al., "Automated detection of leakage in fluorescein angiography images with application to malarial retinopathy," *Scientific Reports*, vol. 5, article 10425, 2015.
- [99] M. N. van Oosterom, R. Kreuger, T. Buckle et al., "U-SPECT-BioFluo: an integrated radionuclide, bioluminescence, and fluorescence imaging platform," *EJNMMI Research*, vol. 4, no. 1, p. 56, 2014.
- [100] J. Rieffel, F. Chen, J. Kim et al., "Hexamodal imaging with porphyrin-phospholipid-coated upconversion nanoparticles," *Advanced Materials*, vol. 27, no. 10, pp. 1785–1790, 2015.
- [101] J. Lohrke, H. Siebeneicher, M. Berger et al., "(18)F-GP1, a novel PET tracer designed for high-sensitivity, low-background detection of thrombi," *Journal of Nuclear Medicine*, vol. 58, no. 7, pp. 1094–1099, 2017.
- [102] N. P. Withana, T. Saito, X. Ma et al., "Dual-modality activity-based probes as molecular imaging agents for vascular inflammation," *Journal of Nuclear Medicine*, vol. 57, no. 10, pp. 1583–1590, 2016.
- [103] F. Schuchardt, L. Schroeder, C. Anastopoulos et al., "In vivo analysis of physiological 3D blood flow of cerebral veins," *European Radiology*, vol. 25, no. 8, pp. 2371–2380, 2015.
- [104] E. M. Schrauben, K. M. Johnson, J. Huston et al., "Reproducibility of cerebrospinal venous blood flow and vessel anatomy with the use of phase contrast-very undersampled isotropic projection reconstruction and contrast-enhanced MRA," *American Journal of Neuroradiology*, vol. 35, no. 5, pp. 999–1006, 2014.
- [105] S. Schnell, C. Wu, and S. A. Ansari, "Four-dimensional MRI flow examinations in cerebral and extracerebral vessels—ready for clinical routine?," *Current Opinion in Neurology*, vol. 29, no. 4, pp. 419–428, 2016.

- [106] J. H. Jung, Y. Choi, and K. C. Im, "PET/MRI: technical challenges and recent advances," *Nuclear Medicine and Molecular Imaging*, vol. 50, no. 1, pp. 3–12, 2016.
- [107] C. Tsoumpas, D. Visvikis, and G. Loudos, "Innovations in small-animal PET/MR imaging instrumentation," *PET Clinics*, vol. 11, no. 2, pp. 105–118, 2016.
- [108] B. Laviña, "Brain vascular imaging techniques," *International Journal of Molecular Sciences*, vol. 18, no. 1, p. 70, 2016.
- [109] N. C. Institute, "Network for translational research (NTR): optical imaging in multimodality platforms," 2016, https://imaging.cancer.gov/programs_resources/specialized_initiatives/ntroi.htm.
- [110] E. M. Sevick-Muraca, W. J. Akers, B. P. Joshi et al., "Advancing the translation of optical imaging agents for clinical imaging," *Biomedical Optics Express*, vol. 4, no. 1, pp. 160–170, 2013.

Research Article

Hybrid PET/MR Kernelised Expectation Maximisation Reconstruction for Improved Image-Derived Estimation of the Input Function from the Aorta of Rabbits

Daniel Deidda ^{1,2}, **Nicolas A. Karakatsanis**,^{3,4} **Philip M. Robson**,³ **Claudia Calcagno**,³ **Max L. Senders**,³ **Willem J. M. Mulder**,³ **Zahi A. Fayad**,³ **Robert G. Aykroyd** ², and **Charalampos Tsoumpas** ^{1,3}

¹Biomedical Imaging Science Department, University of Leeds, Leeds, UK

²Department of Statistics, University of Leeds, Leeds, UK

³Translational and Molecular Imaging Institute (TMII), Department of Radiology, Icahn School of Medicine at Mount Sinai, New York, NY, USA

⁴Division of Radiopharmaceutical Sciences, Department of Radiology, Weill Cornell Medical College, Cornell University, New York, NY, USA

Correspondence should be addressed to Daniel Deidda; daniel.deidda@npl.co.uk

Received 28 June 2018; Revised 15 November 2018; Accepted 21 November 2018; Published 16 January 2019

Academic Editor: Anne Roivainen

Copyright © 2019 Daniel Deidda et al. This is an open access article distributed under the Creative Commons Attribution License, which permits unrestricted use, distribution, and reproduction in any medium, provided the original work is properly cited.

Positron emission tomography (PET) provides simple noninvasive imaging biomarkers for multiple human diseases which can be used to produce quantitative information from single static images or to monitor dynamic processes. Such kinetic studies often require the tracer input function (IF) to be measured but, in contrast to direct blood sampling, the image-derived input function (IDIF) provides a noninvasive alternative technique to estimate the IF. Accurate estimation can, in general, be challenging due to the partial volume effect (PVE), which is particularly important in preclinical work on small animals. The recently proposed hybrid kernelised ordered subsets expectation maximisation (HKEM) method has been shown to improve accuracy and contrast across a range of different datasets and count levels and can be used on PET/MR or PET/CT data. In this work, we apply the method with the purpose of providing accurate estimates of the aorta IDIF for rabbit PET studies. In addition, we proposed a method for the extraction of the aorta region of interest (ROI) using the MR and the HKEM image, to minimise the PVE within the rabbit aortic region—a method which can be directly transferred to the clinical setting. A realistic simulation study was performed with ten independent noise realisations while two, real data, rabbit datasets, acquired with the Biograph Siemens mMR PET/MR scanner, were also considered. For reference and comparison, the data were reconstructed using OSEM, OSEM with Gaussian postfilter and KEM, as well as HKEM. The results across the simulated datasets and different time frames show reduced PVE and accurate IDIF values for the proposed method, with 5% average bias (0.8% minimum and 16% maximum bias). Consistent results were obtained with the real datasets. The results of this study demonstrate that HKEM can be used to accurately estimate the IDIF in preclinical PET/MR studies, such as rabbit mMR data, as well as in clinical human studies. The proposed algorithm is made available as part of an open software library, and it can be used equally successfully on human or animal data acquired from a variety of PET/MR or PET/CT scanners.

1. Introduction

[¹⁸F]-based PET imaging has been successfully used as a noninvasive imaging biomarker of different human diseases. [¹⁸F]-Sodium fluoride ([¹⁸F]-NaF) has been associated with calcium molecular metabolism, and it has been used to study benign osseous diseases such as osteoporosis, vascular

calcification, osteoarthritis, and rheumatoid arthritis [1–6]. [¹⁸F]-Fluorodeoxyglucose ([¹⁸F]-FDG) is the most commonly used in clinical practice and particularly for the detection, quantification, staging, and therapy evaluation of cancerous lesions, as well as in cardiovascular and neurological diseases [7–12].

Accurate and precise quantitative biomarkers can be obtained by exploiting the pharmacokinetic information in

the measured data [13]. This requires the estimation of the radiotracer concentration in the arterial blood plasma (input function). The gold standard for such measurement is blood sampling during the PET acquisition, via arterial cannulation [14]. Unfortunately, this technique is invasive and can be complicated, as it requires arterial blood samples in specific quantities and at precise times with corrections for delay and dispersion to account for the distance between the sampling site and the regions of interest (ROIs) [15].

A noninvasive technique is the image-derived input function (IDIF) [16] which uses a region of interest (ROI) to measure the uptake in the vessel over time. The IDIF is a simple way to calculate activity over time; however, it is challenging due to image-related issues. Firstly, the choice of the ROI has a very important impact, and nonaccurate ROIs will affect the measurement [17, 18]. Other challenges are related to the use of MR images to extract the ROI because a potentially inaccurate registration between PET and MR images can lead to erroneous estimates of the activity in the chosen arterial ROI. With a hybrid PET/MR scanner, the problem of coregistration is expected to be minimised.

The aforementioned problems are mostly related to the ordered subsets expectation maximisation (OSEM) method [19] which is usually followed by postreconstruction Gaussian filtering due to the high noise levels expected for the very short-time frames used for the IDIF estimation. OSEM with or without postfiltering has been shown to produce inaccurate values of IDIF with bias up to 30% propagating through the kinetic constant calculations [20]. In preclinical experiments, these issues can be even more challenging [13, 21] because of the smaller size of animal vessel tissue, such as rabbit aortas, especially when they are performed with clinical scanners designed for larger human subjects. In this case, the PVE can be significant, as the diameter of the rabbit aorta is about 5 mm which is the same order of magnitude as the PET resolution.

Different studies have proposed methods for the use of IDIF by correcting or avoiding PVE [22–26]. Zanotti-Fregonella et al. [16] have shown in their comparison between cannulation-based and image-derived input functions that the use of high-resolution PET images is often not sufficient to avoid the need of cannulation to obtain a reliable IDIF. Moreover, the accuracy of the IDIF may vary between radiotracers and scanners. MR-guided techniques have been proposed and discussed [15], showing that erroneous registration between the PET and the MR images, as well as erroneous MR segmentation, can introduce an error in the IDIF estimation. The problem of PET/MR misalignment has been discussed for the kernel by Deidda et al. [27]. In this study, we apply a PET/MR-guided image reconstruction algorithm, hybrid kernelised expectation maximisation (HKEM) [28], to minimise PVE during the reconstruction step so that we can obtain more accurate IDIF estimates. In addition, to minimise the PET/MR misalignment, the HKEM-reconstructed image at the peak activity frame was used together with the MR image to extract the ROI to be used for the estimation of the input function. In this way, only a percentage of the maximum value is included in the ROI avoiding low-value voxels outside the carotid in case of PET/MR misalignment.

The kernel method [29], which was first introduced in PET image reconstruction by Wang and Qi [30] and Hutchcroft et al. [31, 32], makes use of only one prior information image, MR or PET, respectively. Furthermore, many other studies showing promising performances have appeared in the literature [33–39]. In contrast, the HKEM method, which we recently developed in the open-source STIR library [40], exploits both the PET and the MR coregistered images to derive PET information iteration after iteration.

The HKEM algorithm was introduced by Deidda et al. [28] as a method for improving PET image resolution and uptake recovery in PET/MR phantom experiments, as well as contrast and quantification of atherosclerotic plaque lesions in carotid arteries in clinical PET/MR studies—which could also be applied in PET/CT studies. In addition, it is a robust and stable method which gives consistent results across different datasets using the same parameter settings. In this paper, we focus on the quantification of the aorta IDIF of rabbits using ^{18}F -based radiotracers such as [^{18}F]-FDG and [^{18}F]-NaF, to extend the applicability and usefulness of our novel reconstruction algorithm. Here, we assume that if HKEM can recover the uptake while retaining satisfactory noise suppression for low-count PET acquisitions, it will also be capable of providing accurate IDIF estimates using a wide range of dynamic PET frame durations.

The paper is structured as follows: Section 2 describes the datasets used to study image reconstruction, list mode (LM) subsampling, and the experimental methodology. Section 3 presents the results of the proposed method and comparison with different standard algorithms. The results are discussed in Section 4, and conclusions are drawn in Section 5.

2. Methods and Materials

2.1. Simulation. A realistic simulation was created using a model derived from real [^{18}F]-NaF rabbit data [41] and utilities implemented in the STIR library. The real data were acquired with the Siemens Biograph mMR scanner at Mount Sinai Hospital, NY, USA. The voxel size for the simulated image was $1.56 \times 1.56 \times 2.031$ mm. The rabbit was a healthy subject and was anaesthetised before the scan. It was injected with [^{18}F]-NaF 170 MBq and scanned for 90 minutes. Different organs and tissues were segmented from the acquired MR UTE sequence, using 0.07 ms echo time. The original voxel size is $1.56 \times 1.56 \times 1.56$ mm. It is then aligned to the PET field of view (FOV) and resliced to match the PET native voxel size, $1.56 \times 1.56 \times 2.031$ mm³, and FOV size, $344 \times 344 \times 127$ voxels. The same image is also used for the calculation of the kernel matrix. In particular, the abdominal aorta, kidneys, bladder, myocardium, lungs, stomach, and background were extracted as independent images. Each tissue type was segmented using a semiautomatic segmentation method in ITK-SNAP based on thresholding [39], and it was then used as a ROI in the real PET data to estimate the activity concentration over 45 frames organised as follows: 17×6 s, 4×15 s, 4×30 s, 4×60 s, 4×180 s, and 12×300 s.

The measured values were then assigned to every tissue in the simulation.

In order to create the projection data, each simulated image is forward projected into the sinogram space. The attenuation sinogram is estimated using the attenuation coefficient, μ , map obtained from a Dixon MR sequence [42–45], and the precalculated hardware attenuation coefficients for the bed and coils. The projection data containing random events were estimated as a uniform sinogram containing 20% of the total number of events in the simulated acquisition sinogram. In order to estimate the scattered events, the Watson single scatter simulation was applied [46], and a mask obtained from the μ map was used for the tail fitting. At this point, the random and scatter sinograms were combined as an additive term in the emission sinogram to create the modelled prompts projection data. The final step was the simulation of Poisson noise from the prompts events.

The above steps were repeated for each simulated frame image, and 10 noise realisations were created.

2.2. Real Rabbit Data. The acquisition was carried out using the Siemens Biograph mMR at Mount Sinai Hospital, NY, USA. The rabbit was a healthy subject and was anaesthetised during the scan. It was injected with [^{18}F]-NaF 170 MBq for the first study and [^{18}F]-FDG 133 MBq for the second, both scanned for 90 minutes. The attenuation images were obtained from the scanner, which included the attenuation coefficient for bed and coils. The LM data were divided into smaller frames, to permit calculation of the input function. The tracer was injected during the first seconds of the scan. The MR part of the kernel matrix was obtained from a MR UTE sequence with 0.07 ms echo time, and the original voxel size was $1.56 \times 1.56 \times 1.56$ mm. It was then aligned to the PET field of view (FOV) and resliced to match the PET native z voxel size, $1.56 \times 1.56 \times 2.031$ mm³, and FOV size, 344×127 voxels.

2.3. Reconstruction Setup. All the datasets were reconstructed using HKEM with 21 subsets and 10 iterations. The PET image voxel, λ_j , using the HKEM can be written as

$$\lambda_j = \sum_{f=1}^{N_j} \alpha_f k_{fj}, \quad (1)$$

where k_{fj} is the f j^{th} element of the kernel, N_j is the number of feature vectors related to voxel j , and α_f is the kernel coefficient to be estimated iteratively as follows:

$$\alpha_f^{(n+1)} = \frac{\alpha_f^{(n)}}{\sum_j k_{fj}^{(n)} \sum_i p_{fi}} \sum_j k_{fj}^{(n)} \sum_i p_{ij} \frac{1}{\sum_l p_{il} \sum_f k_{fl}^{(n)} \alpha_f^{(n)} + s_i}, \quad (2)$$

with p_{ij} being the system matrix and s_i the additive term. The f j^{th} element of the kernel consists in two components, and it can be written as follows:

$$k_{fj}^{(n)} = k_m(\mathbf{v}_f, \mathbf{v}_j) \cdot k_p(\mathbf{z}_f^{(n)}, \mathbf{z}_j^{(n)}), \quad (3)$$

where

$$k_m(\mathbf{v}_f, \mathbf{v}_j) = \exp\left(-\frac{\|\mathbf{v}_f - \mathbf{v}_j\|^2}{2\sigma_m^2}\right) \exp\left(-\frac{\|\mathbf{x}_f - \mathbf{x}_j\|^2}{2\sigma_{dm}^2}\right), \quad (4)$$

is the kernel derived from the MR image and

$$k_p(\mathbf{z}_f^{(n)}, \mathbf{z}_j^{(n)}) = \exp\left(-\frac{\|\mathbf{z}_f^{(n)} - \mathbf{z}_j^{(n)}\|^2}{2\sigma_p^2}\right) \exp\left(-\frac{\|\mathbf{x}_f - \mathbf{x}_j\|^2}{2\sigma_{dp}^2}\right), \quad (5)$$

is the kernel component derived from the updated PET image. The Gaussian kernel functions have been modulated by the distance between voxels in the image space. The quantity \mathbf{x}_j is the coordinate of the j^{th} voxel, n is the subiteration number, $\mathbf{z}_j^{(n)}$ and \mathbf{v}_j are the feature vectors that are calculated from the n^{th} updated PET image and the MR image, respectively, and σ_m , σ_p , σ_{dm} , and σ_{dp} are the scaling parameters for the distances in (4) and (5). Note that the HKEM uses a voxel-wise kernel. This means that the feature vector assigned for each voxel contains only one nonzero element with the same voxel value.

The kernel parameters were chosen in order to obtain the minimum RMSE in the aorta. The values of the kernel parameters were set as follows: $N = 27$, $\sigma_m = 1$, $\sigma_{dm} = 3$, $\sigma_p = 1$, and $\sigma_{dp} = 3$ (the last two are only used by HKEM).

For comparison, the same datasets have been reconstructed also with 21 subsets and 10 iterations of OSEM with and without 3 mm FWHM Gaussian postfilter. These methods are denoted as OSEM+G and OSEM, respectively, in this study. The selected number of subsets and the application of the Gaussian post-filter are considered as standard settings in clinical routine. All datasets were reconstructed using span 1.

Scatter correction was performed with the method described by Tsoumpas et al. [47] and Polycarpou et al. [48]. Randoms were estimated from singles, which were calculated from delayed events [49]. The procedures for these evaluations, including attenuation and normalisation corrections [50], make use of STIR.

2.4. Image Analysis. The comparison was carried out in terms of the mean value for all of the short frames and datasets, and the bias was estimated for the simulation to assess the accuracy of the proposed method. The ROI was obtained using the HKEM-reconstructed image and the MR image as follows (Figure 1):

- (i) The aorta was segmented from the MR image using the semiautomatic segmentation method in ITK-SNAP based on thresholding [51]
- (ii) The obtained mask is multiplied with the HKEM-reconstructed PET image to obtain the segmented aorta, A^s , from the the PET image

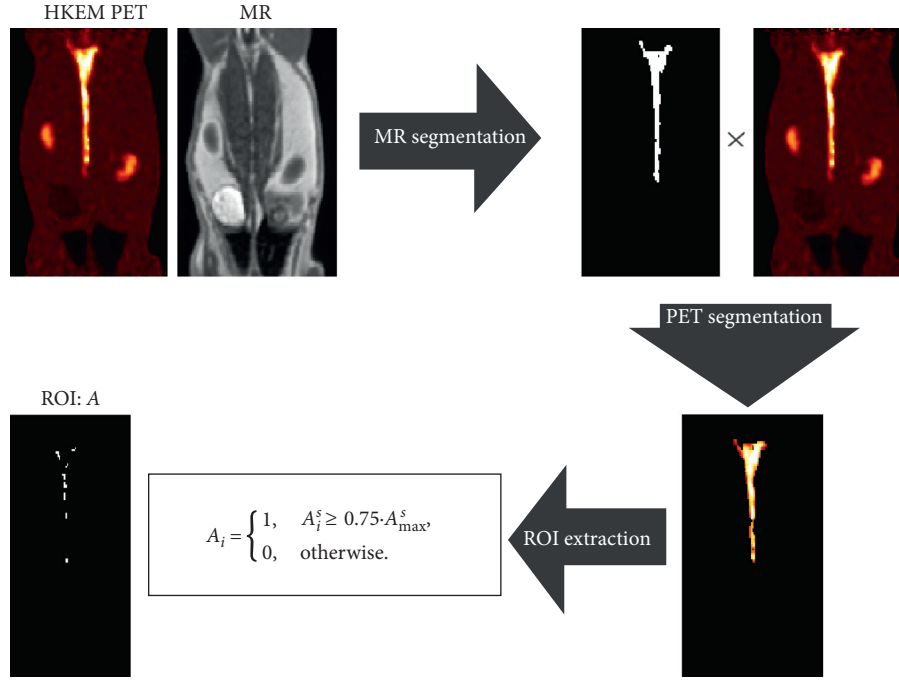


FIGURE 1: Schematic representation of the extraction of the region of interest (ROI), A , of the aorta using the PET and MR images as the input.

- (iii) The ROI, A , is obtained by taking into account only the voxels with a value bigger than 75% of the maximum in order to optimize those affected by PVE

$$A_i = \begin{cases} 1, & A_i^s \geq 0.75 \cdot A_{\max}^s, \\ 0, & \text{otherwise,} \end{cases} \quad (6)$$

where I is the index of the voxel. Quantitative comparison between algorithms was performed using the following figures of merit:

$$\text{mean}_k = t_k = \frac{\sum_{j=1}^V t_{jk}}{V}, \quad (7)$$

$$\text{bias}_k = \frac{|t_k - A_k^T|}{A_k^T} \cdot 100, \quad (8)$$

$$\text{CoV}_k = \frac{\sqrt{1/(V-1) \sum_{j=1}^V (t_{jk} - t_k)^2}}{t_k} \times 100, \quad (9)$$

where t_k is the mean value of the target ROI at frame k , t_{jk} is the value of voxel j within the ROI at frame k , and V is the number of voxels within the ROI. The ROIs obtained with the proposed method are shown for each dataset in Figure 2.

3. Results

3.1. Simulation. The IDIF estimates for the simulated rabbit data and the early and late frames for the IDIF are illustrated

in Figure 3. In the same figure, the reconstructed images with OSEM, OSEM+G, KEM, and HKEM, at the peak frame (24–30 s), are shown. Figure 4 presents the line profile of the aorta estimated for the images, as reconstructed with all investigated methods, at two different positions (LP1 and LP2), while Figure 5 reports the median IDIF estimated over the ten noise realisations using the HKEM. The shaded region is the range of possible values over the 10 simulated datasets, and the dashed line is the true IDIF. Finally, Table 1 reports the percentage value of the mean, maximum, and minimum absolute bias over the frames and the noise realisations.

A voxel-wise analysis example is reported in Figure 6, where the 10 peak frame images were combined to extract the bias and the SD images for each algorithm.

3.2. NaF Study. Figure 7 shows the comparison, on the bottom row, between the initial 200 s of the input function on the left, and the later section of the IDIF on the right. Moreover, to give an idea of the image quality, the reconstructed ^{18}F -NaF images for the peak time are shown on the top. Figure 8 reports the line profile of the aorta in two different positions (LP1 and LP2) for the ^{18}F -NaF peak images reconstructed with the investigated methods to illustrate in detail the differences between the images reconstructed with different techniques. Figure 9 gives an example of fused PET/MR image quality for all the reconstruction techniques.

3.3. FDG Study. The IDIF was estimated for a ^{18}F -FDG study in order to assess the method on a different tracer.

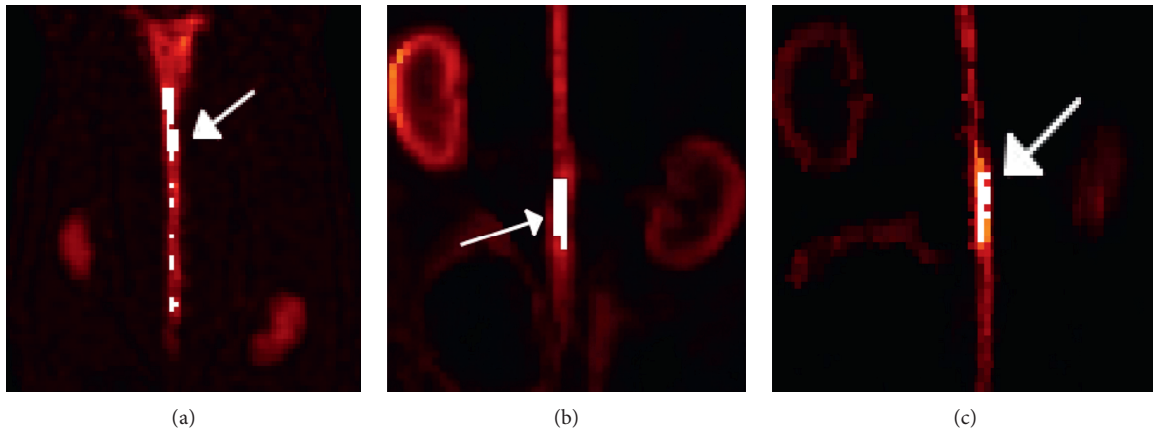


FIGURE 2: Regions of interest (ROIs) chosen for this study, defined by the white regions. The target ROIs for the (a) aorta in the simulation, (b) $[^{18}\text{F}]\text{-NaF}$ rabbit study, and (c) $[^{18}\text{F}]\text{-FDG}$ rabbit study. The target ROIs are indicated by the white arrows.

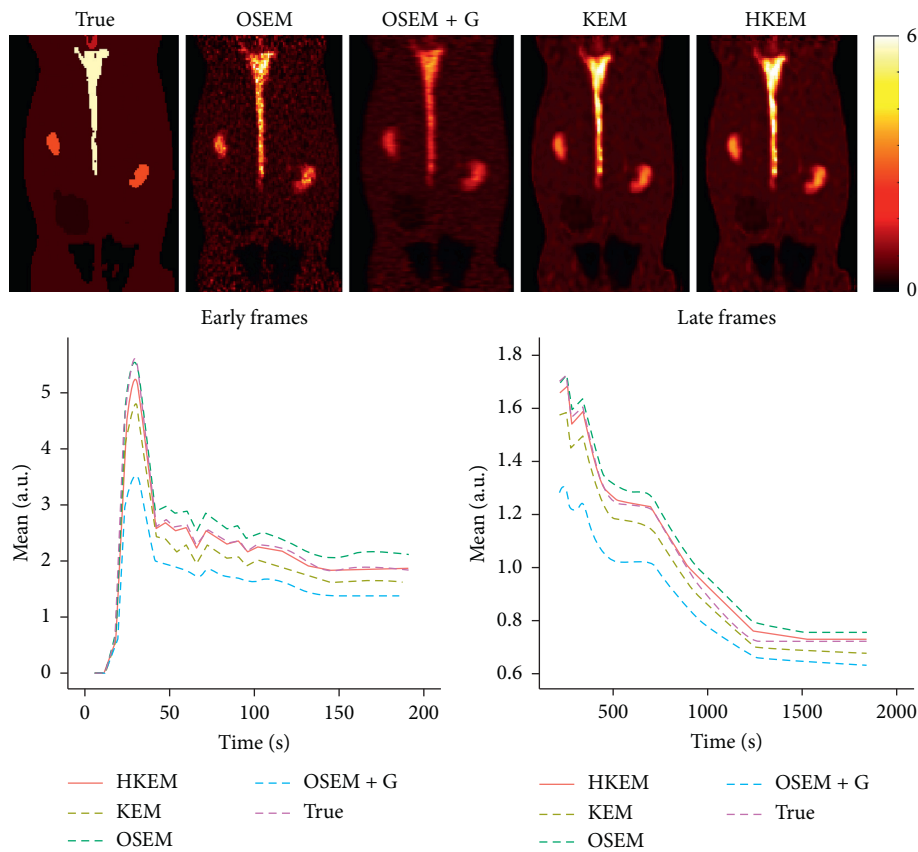


FIGURE 3: A comparison between the true and the measured IDIF values over time, as obtained from the reconstructed image with HKEM, KEM, OSEM, and OSEM+G. On the top, the peak frame (24–30 s) images are also shown.

Figure 10 shows a comparison among the different algorithms in terms of image quality at the $[^{18}\text{F}]\text{-FDG}$ peak activity frame, input function values. On the bottom row, we can see the initial 200 s of the input function on the left and the remaining part of the IDIF on the right, while on the top, the reconstructed images for the peak frame are shown. Figure 11 reports the line profile of the aorta in two different positions (LP1 and LP2) for the $[^{18}\text{F}]\text{-FDG}$ peak images reconstructed with all the investigated methods.

4. Discussion

In this study, we have proposed the use of our recently developed hybrid kernelised reconstruction algorithm HKEM, for the estimation of the IDIF in the aorta artery of rabbits having undergone $[^{18}\text{F}]\text{-FDG}$ and $[^{18}\text{F}]\text{-NaF}$ PET/MR studies using a clinical PET/MR scanner. The study was driven by the fact that many applications, where dynamic PET is used to extract more accurate and precise kinetic

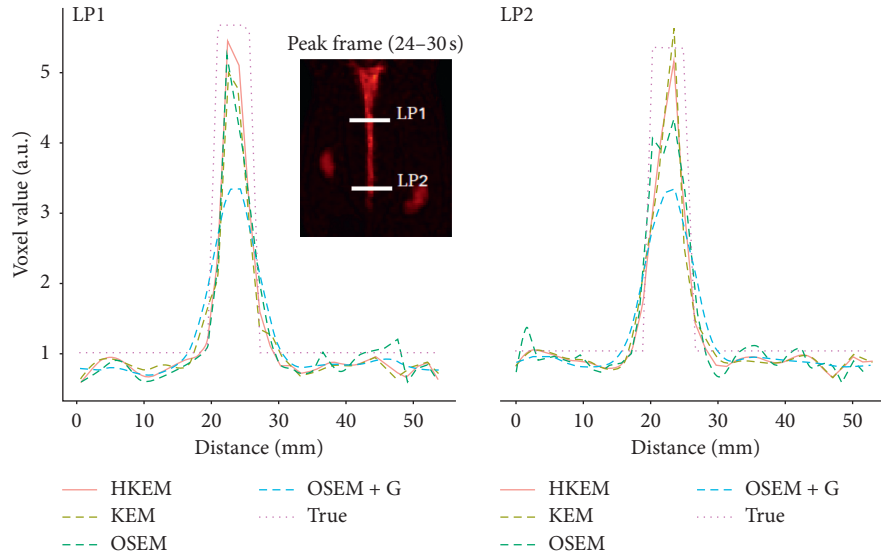


FIGURE 4: A comparison between the true line profiles, LP1 and LP2, and the ones obtained from the reconstructed image with OSEM, OSEM+G, KEM, and HKEM.

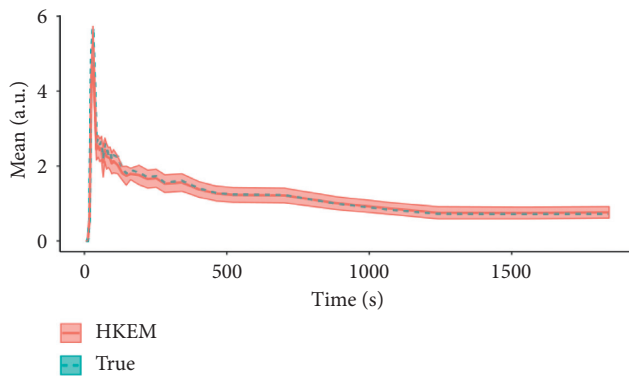


FIGURE 5: Median IDIF estimated over the ten noise realisations using the HKEM. The shaded region is the range of possible values over the 10 simulated datasets, and the dashed line is the true IDIF.

TABLE 1: Absolute bias (%) and CoV (%) estimation over the 45 frames.

	Mean bias	Max. bias	Min. bias	Mean CoV	Max. CoV	Min. CoV
OSEM	6.3	20.8	0.1	52.0	75.6	31.5
OSEM+G	23.32	39.2	4.4	16.2	34.9	10.1
KEM	12.8	30.2	7.7	19.3	30.4	10.9
HKEM	5.0	19.3	0.8	19.9	32.8	10.7

imaging biomarkers, rely on the estimation of the IDIF which is problematic in preclinical studies due to extensive PVE. As a consequence, it is relevant to propose a method which provides accurate estimates of IDIF. The results in Figure 3 show that the proposed reconstruction method and ROI extraction provide accurate results for all time points. The mean, maximum, and minimum bias were also calculated over the frames and the ten noise realisations (Table 1).

We were able to obtain a mean bias of 5% using the HKEM with the maximum value being 16.1%. Note that due to the applied threshold in the definition of the ROI, the OSEM also provided accurate results although the dynamic PET image frames were very noisy, and thus it becomes challenging to accurately delineate the appropriate aortic input function ROI, which is crucial for the IDIF calculation. In addition, a 52% averaged CoV over noise realisations means that there is a probability of about 68% that the repeated measure will have a value within $\pm 52\%$ around the mean. As a consequence, values with high bias are very likely with OSEM. The results suggest that MR information can provide substantial improvement in terms of PVE and noise suppression. Nevertheless, the inclusion of the PET functional information allows better accuracy at similarly low noise levels (Table 1), compared to KEM. Figure 4 shows the line profiles in two different points of the carotid for the image corresponding to the peak. Here, we can notice the better delineation of the aorta for both the KEM and HKEM MR-guided techniques, thanks to the broader smoothness applied in the background tissue regions. It is also important to highlight that the extraction of the ROI from the OSEM image in Figure 1 would not be accurate, as the maximum value was very high due to noise. Thus, the 75% thresholding would only extract very few voxels, therefore causing up to 100% bias in the OSEM IDIF values despite being associated with high accuracy estimates. Figure 5 illustrates the median full IDIF estimate over the 10 realisations, and it is possible to notice the accuracy over time compared to the true values. A voxel-wise analysis example is reported in Figure 6, where it can be seen the better image quality of KEM and HKEM, with lower bias in the aorta and low SD overall. The ROI analysis was also performed on this image. The results reported in Table 2 are in agreement with the ROI analysis performed with all the frames. Due to the optimized ROI, OSEM gives a similar bias value to HKEM on the peak

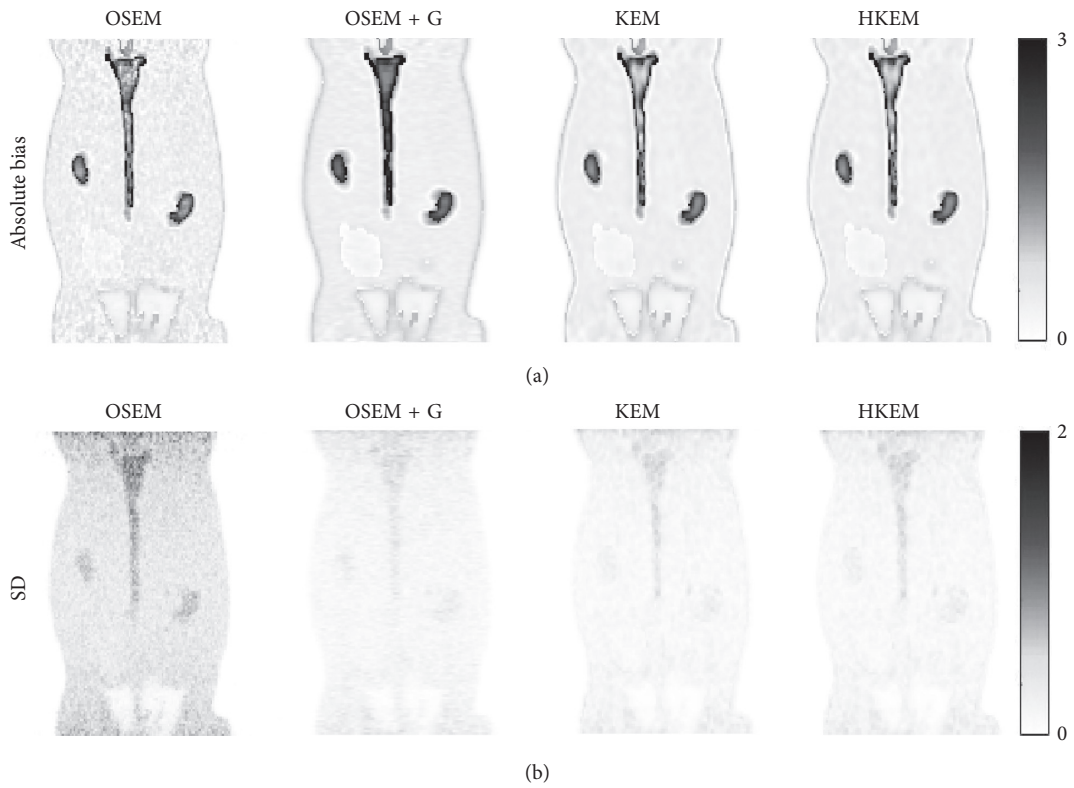


FIGURE 6: Voxel-wise image analysis over the ten noise realisations using the peak frame. The top row shows the average absolute bias, and the bottom row shows the SD over the ten noise realisations.

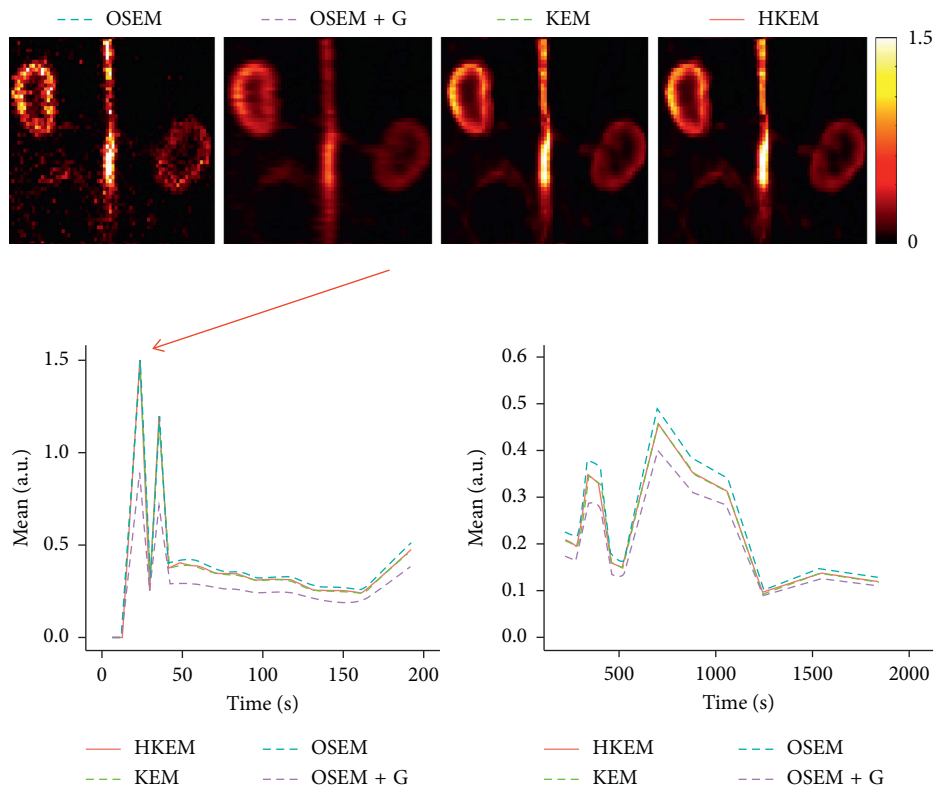


FIGURE 7: Comparison between the $[^{18}\text{F}]\text{-NaF}$ IDIF values over time, after reconstructing with OSEM, OSEM+G, KEM, and HKEM methods. On the top, the peak frame (30–36 s) images are also shown.

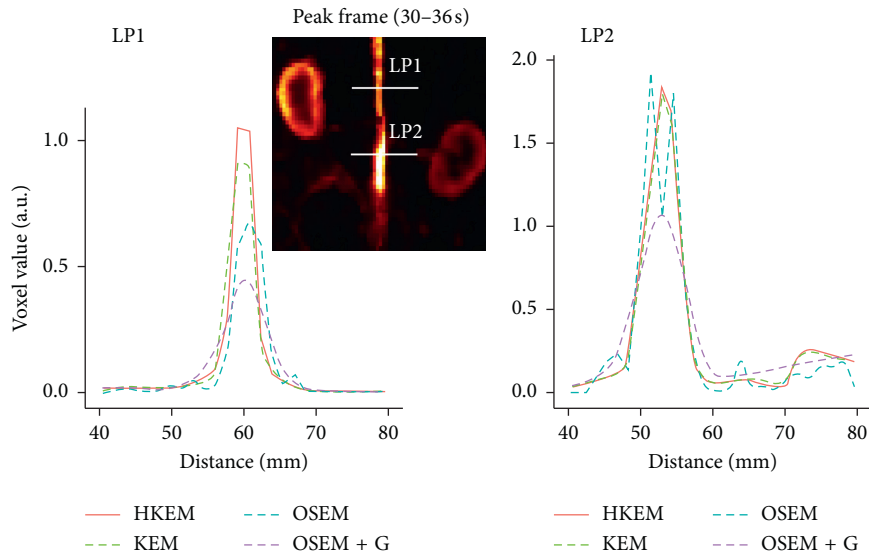


FIGURE 8: Comparison between the line profiles, LP1 and LP2, for the $[^{18}\text{F}]$ -NaF study, after reconstructing with HKEM, KEM, OSEM, and OSEM+G methods.

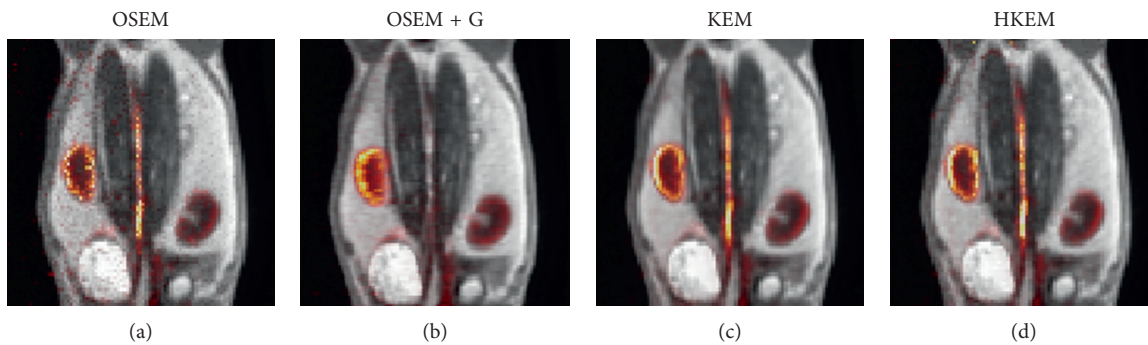


FIGURE 9: Comparison between reconstructed images with (a) OSEM, (b) OSEM+G, and (c) KEM using only MR and (d) the proposed HKEM fused with the MR UTE image for the $[^{18}\text{F}]$ -NaF rabbit data.

frame; however, the repeatability of the measure is around 3 times worse. When Gaussian filter is applied, the value is extremely biased with similar CoV to HKEM and KEM.

The same analysis was applied to two real PET/MR rabbit datasets acquired with the Biograph mMR scanner, using $[^{18}\text{F}]$ -NaF or $[^{18}\text{F}]$ -FDG radiotracers. Figure 7 shows consistent results for the IDIF plots. The reconstructed images using the real data show regions of high uptake only in some places of the aorta, thereby demonstrating the benefit in contrast and resolution of exploiting a hybrid PET/MR kernel matrix. Figure 8 presents the line profiles obtained with the different methods, showing the good resolution of the aorta when using the HKEM method and the poor quality of the postfiltered OSEM which is highly affected by the PVE. In Figure 9, the fused PET/MR image is illustrated for each technique, confirming the better alignment of the aorta region between the PET and the MR images and the resulting higher PET image resolution and aortic contrast. Moreover, the comparison between the $[^{18}\text{F}]$ -FDG and $[^{18}\text{F}]$ -NaF PET/MR studies allowed to assess the feasibility and performance of HKEM in estimating the aorta IDIF for

two of the most commonly employed radiotracers in oncology and cardiology. From the results in Figure 10, the benefit of the synergistic PET/MR information encoded in the kernel matrix is visible especially in the IDIF plot. These results are also supported by the line profiles in Figure 11 showing a clear definition of the aorta for the proposed method and minimum spill-out of activity from the aorta. It is worth noticing that, for the real data, there are two peaks in the early frames IDIF; this is probably due to the fact that the injection was not continuous during the scan but there was a sudden stop making the uptake rate drop down in that specific time frame. We could show the IDIF with one peak by summing the frame associated with the first peak and the frame having low uptake; however, we think it is interesting to show the effect of a noncontinuous injection on the IDIF estimation. The input function represents a very crucial data component when estimating kinetic parameters, and its accurate estimation can become extremely challenging for small animal imaging due to the very small sizes of the associated aortic vessels. In this study, we proposed the use of PET/MR synergistic information for the more accurate

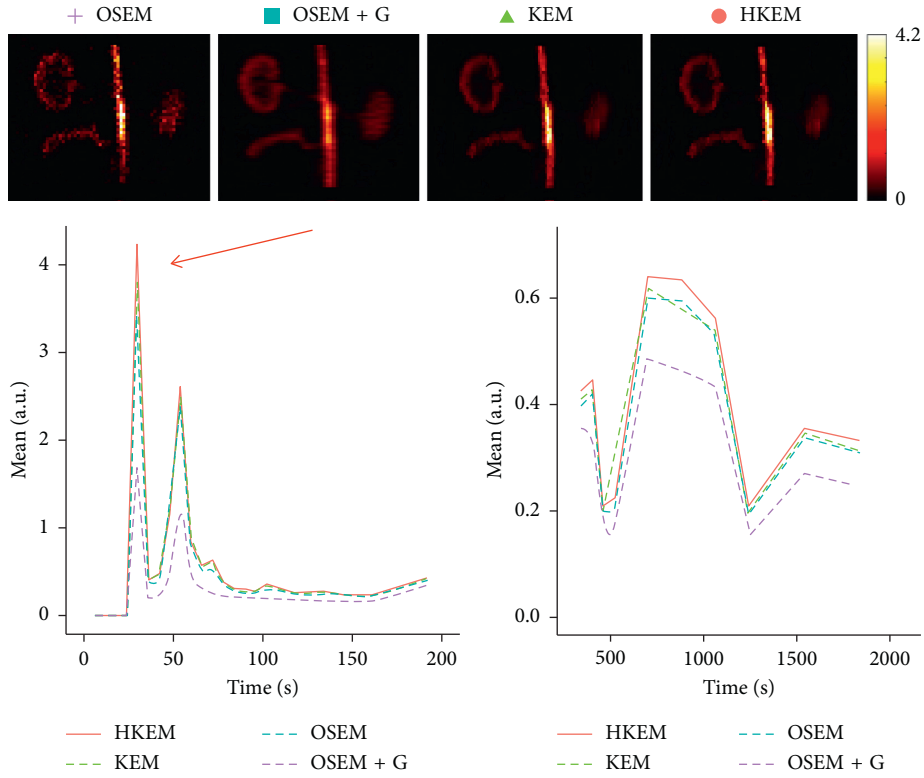


FIGURE 10: Comparison between the IDIF values over time, after reconstructing with OSEM, OSEM+G, KEM, and HKEM methods for the $[^{18}\text{F}]$ -FDG rabbit data. On the top, the peak frame (30–36 s) images are also shown.

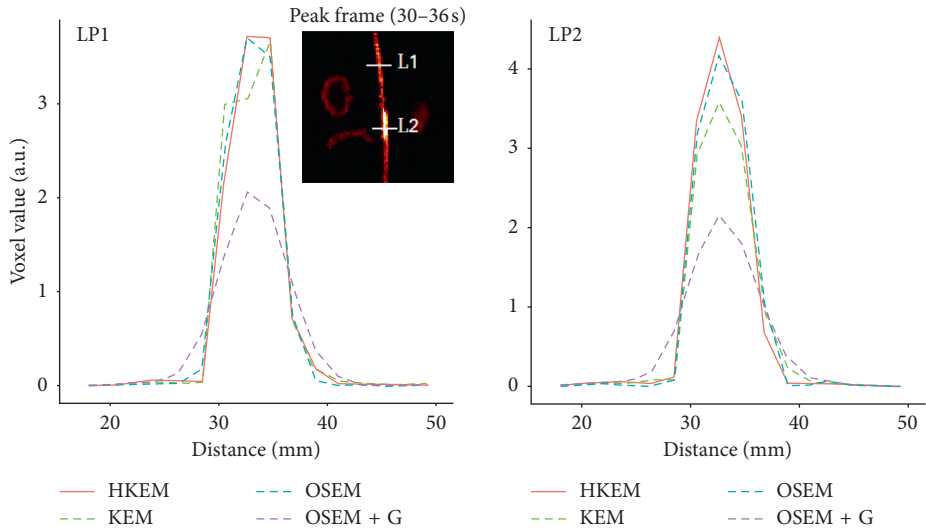


FIGURE 11: Comparison between the line profiles, LP1 and LP2, after reconstructing with OSEM, OSEM+G, KEM, and HKEM methods for the $[^{18}\text{F}]$ -FDG rabbit data.

TABLE 2: Bias (%) and CoV (%) estimation over the 10 noise realisations at the peak frame.

	Bias	Mean CoV
OSEM	19.3	15.4
OSEM+G	40.4	3.5
KEM	20.2	4.3
HKEM	19.3	4.6

and precise extraction of the aortic ROI and IDIF estimation in the framework of the HKEM method. We demonstrated that, despite the small size of the rabbit aorta, it is feasible and promising to employ the HKEM method for the extraction of an aorta IDIF estimate of improved accuracy and reduced PVE even when using a clinical PET/MR scanner. In addition, the method described to extract the ROI is easy to use and implement as it only involves trivial mathematics

between matrices. It is worth mentioning that, although this study was performed with PET/MR data, it could also work with PET-CT data especially if the CT image to use as anatomical information is a CT angiography image.

5. Conclusion

In this investigation, we demonstrated that the HKEM method allows the more accurate extraction of the aortic ROI for improved IDIF estimation even when using a human hybrid scanner, compared to conventional OSEM or anatomically guided KEM reconstruction. Our findings were validated with both 10 simulated [^{18}F]-NaF PET/MR datasets as well as 2 real rabbit PET/MR studies. Further, the methodology can be applied to most of the available radiotracers and with PET-CT without any major modification. This technique can enhance the use of dynamic PET in the context of imaging biomarkers with direct pharmacokinetic information.

Data Availability

A demonstrative code for the creation of the simulated study, reconstruction, and ROI extraction is available in CODE OCEAN at <https://doi.org/10.24433/CO.bde84e0c-4c73-47fa-8ba5-81fb8bd2af77>. The real rabbit data used to support the findings of this study, however, have not been made available because the Translational and Molecular Imaging Institute Group, who provided the data, retains the right to publish the data before making them generally available.

Conflicts of Interest

The authors declare that there are no conflicts of interest regarding the publication of this paper.

Acknowledgments

This work was undertaken on MARC1, part of the High Performance Computing and Leeds Institute for Data Analytics (LIDA) facilities at the University of Leeds, UK. The authors thank the Collaborative Computational Project in PET-MR Imaging (CCP-PET-MR), funded with EP/M022587/1 grant, for enabling PET-MR reconstruction and for funding Daniel Deidda's participation in an exchange programme at the University College of London (UCL). Part of this research was funded by the EPSRC Collaborative Computational Flagship Project (EP/P022200/1). This work was supported by the University Research Scholarship, University of Leeds, and the research grant NIH/NHLBI R01HL071021. Dr. Tsoumpas was sponsored by a Royal Society Industry Fellowship (IF170011).

References

- [1] W. Raynor, S. Houshmand, S. Gholami et al., "Evolving role of molecular imaging with 18f-sodium fluoride PET as a biomarker for calcium metabolism," *Current Osteoporosis Reports*, vol. 14, no. 4, pp. 115–125, 2016.
- [2] Y. Li, G. R. Berenji, W. F. Shaba, B. Tafti, E. Yevdayev, and S. Dadparvar, "Association of vascular fluoride uptake with vascular calcification and coronary artery disease," *Nuclear Medicine Communications*, vol. 33, no. 1, pp. 14–20, 2012.
- [3] Y. Wang, A. J. Yee, C. Sirard, S. Landau, N. Rajee, and U. Mahmood, "Sodium fluoride PET imaging as a quantitative pharmacodynamic biomarker for bone homeostasis during anti-DKK1 therapy for multiple myeloma," *Blood Cancer Journal*, vol. 7, no. 10, p. e615, 2017.
- [4] G. J. R. Cook, G. M. Blake, P. K. Marsden, B. Cronin, and I. Fogelman, "Quantification of skeletal kinetic indices in paget's disease using Dynamic18F-fluoride positron emission tomography," *Journal of Bone and Mineral Research*, vol. 17, no. 5, pp. 854–859, 2002.
- [5] M. L. Frost, A. E. Moore, M. Siddique et al., "18f-fluoride PET as a noninvasive imaging biomarker for determining treatment efficacy of bone active agents at the hip: a prospective, randomized, controlled clinical study," *Journal of Bone and Mineral Research*, vol. 28, no. 6, pp. 1337–1347, 2013.
- [6] U. Simoncic, S. Perlman, G. Liu, M. J. Staab, J. E. Straus, and R. Jeraj, "Comparison of NaF and FDG PET/CT for assessment of treatment response in castration-resistant prostate cancers with osseous metastases," *Clinical Genitourinary Cancer*, vol. 13, no. 1, pp. e7–e17, 2015.
- [7] C. Wu, F. Li, G. Niu, and X. Chen, "PET imaging of inflammation biomarkers," *Theranostics*, vol. 3, no. 7, pp. 448–466, 2013.
- [8] J. P. O'connor, E. O. Aboagye, J. E. Adams et al., "Imaging biomarker roadmap for cancer studies," *Nature Reviews Clinical Oncology*, vol. 14, no. 3, p. 169, 2017.
- [9] A. R. Seyal, K. Parekh, Y. S. Velichko, R. Salem, and V. Yaghmai, "Tumor growth kinetics versus RECIST to assess response to locoregional therapy in breast cancer liver metastases," *Academic Radiology*, vol. 21, no. 8, pp. 950–957, 2014.
- [10] A. R. Seyal, K. Parekh, A. Arslanoglu et al., "Performance of tumor growth kinetics as an imaging biomarker for response assessment in colorectal liver metastases: correlation with FDG PET," *Abdominal Imaging*, vol. 40, no. 8, pp. 3043–3051, 2015.
- [11] M. Alenezi, M. Bentourkia, F. A. A. Slimani, and A. Khalil, "Segmentation and kinetic modeling of human arteries in PET/CT imaging," in *Proceedings of 2016 IEEE NSS/MIC/RTSD*, pp. 1–3, Sydney, Australia, November 2016.
- [12] L. Jødal, S. B. Jensen, O. L. Nielsen et al., "Kinetic modelling of infection tracers [^{18}F] FDG, [^{68}Ga] ga-citrate, [^{11}C] methionine, and [^{11}C] donepezil in a porcine osteomyelitis model," *Contrast Media and Molecular Imaging*, vol. 2017, pp. 2017–18.
- [13] F. A. Kotasidis, C. Tsoumpas, and A. Rahmim, "Advanced kinetic modelling strategies: towards adoption in clinical PET imaging," *Clinical and Translational Imaging*, vol. 2, no. 3, pp. 219–237, 2014.
- [14] M. H. Bentourkia, "Determination of the input function at the entry of the tissue of interest and its impact on PET kinetic modeling parameters," *Molecular Imaging and Biology*, vol. 17, no. 6, pp. 748–756, 2015.
- [15] E. K. Fung and R. E. Carson, "Cerebral blood flow with [15O] water PET studies using an image-derived input function and MR-defined carotid centerlines," *Physics in Medicine and Biology*, vol. 58, no. 6, pp. 1903–1923, 2013.
- [16] P. Zanotti-Fregonara, K. Chen, J.-S. Liow, M. Fujita, and R. B. Innis, "Image-derived input function for brain pet studies: many challenges and few opportunities," *Journal of*

- Cerebral Blood Flow and Metabolism*, vol. 31, no. 10, pp. 1986–1998, 2011.
- [17] R. Boellaard, N. C. Krak, O. S. Hoekstra, and A. A. Lammertsma, “Effects of noise, image resolution, and ROI definition on the accuracy of standard uptake values: a simulation study,” *Journal of Nuclear Medicine*, vol. 45, no. 9, pp. 1519–1527, 2004.
- [18] M. Sattarivand, C. Caldwell, I. Poon, H. Soliman, and K. Mah, “Effects of ROI placement on PET-based assessment of tumor response to therapy,” *International Journal of Molecular Imaging*, vol. 2013, Article ID 132804, 9 pages, 2013.
- [19] H. M. Hudson and R. S. Larkin, “Accelerated image reconstruction using ordered subsets of projection data,” *IEEE Transactions on Medical Imaging*, vol. 13, no. 4, pp. 601–609, 1994.
- [20] R. Boellaard, A. Van Lingen, and A. A. Lammertsma, “Experimental and clinical evaluation of iterative reconstruction (OSEM) in dynamic PET: quantitative characteristics and effects on kinetic modeling,” *Journal of Nuclear Medicine*, vol. 42, no. 5, pp. 808–817, 2001.
- [21] C. Tsoumpas, D. Visvikis, and G. Loudos, “Innovations in small-animal PET/MR imaging instrumentation,” *PET clinics*, vol. 11, no. 2, pp. 105–118, 2016.
- [22] G. Germano, B. C. Chen, S.-C. Huang, S. S. Gambhir, E. J. Hoffman, and M. E. Phelps, “Use of the abdominal aorta for arterial input function determination in hepatic and renal PET studies,” *Journal of Nuclear Medicine*, vol. 33, no. 4, pp. 613–620, 1992.
- [23] R. Laforest, T. L. Sharp, J. A. Engelbach et al., “Measurement of input functions in rodents: challenges and solutions,” *Nuclear Medicine and Biology*, vol. 32, no. 7, pp. 679–685, 2005.
- [24] K.-P. Lin, S.-C. Huang, Y. Choi, R. C. Brunken, H. R. Schelbert, and M. E. Phelps, “Correction of spillover radioactivities for estimation of the blood time-activity curve from the imaged LV chamber in cardiac dynamic FDG PET studies,” *Physics in Medicine and Biology*, vol. 40, no. 4, pp. 629–642, 1999.
- [25] J.-E. Litton, “Technical note. Input function in PET brain studies using MR-defined arteries,” *Journal of Computer Assisted Tomography*, vol. 21, no. 6, pp. 907–909, 1997.
- [26] P. Zanotti-Fregonara, J.-S. Liow, M. Fujita et al., “Image-derived input function for human brain using high resolution PET imaging with [¹¹C](R)-rolipram and [¹¹C] PBR28,” *PLoS One*, vol. 6, no. 2, Article ID e17056, 2011.
- [27] D. Deidda, N. Karakatsanis, N. Karakatsanis et al., “Effect of PET-MR inconsistency in the kernel image reconstruction method,” *IEEE Transactions on Radiation and Plasma Medical Sciences*, pp. 1–13, 2018.
- [28] “Hybrid PET-MR list-mode kernelized expectation maximization reconstruction for quantitative PET images of the carotid arteries,” in *Proceedings of 2017 NSS/MIC*, Atlanta, GA, USA, September 2017.
- [29] T. Hoffman, B. Scholkopf, and A. Smola, “Kernel methods in machine learning,” *Annals of Statistics*, vol. 36, pp. 1171–1220, 2008.
- [30] G. Wang and J. Qi, “PET image reconstruction using kernel method,” *IEEE Transactions on Medical Imaging*, vol. 34, pp. 61–71, 2015.
- [31] W. Hutchcroft, G. Wang, and J. Qi, “Anatomical-image aided PET reconstruction by the kernel method,” *Journal of Nuclear Medicine*, vol. 55, no. 1, 2014.
- [32] W. Hutchcroft, G. Wang, K. T. Chen, C. Catana, and J. Qi, “Anatomically-aided PET reconstruction using the kernel method,” *Physics in Medicine and Biology*, vol. 61, no. 18, pp. 6668–6683, 2016.
- [33] P. Novosad and A. J. Reader, “MR-guided dynamic PET reconstruction with the kernel method and spectral temporal basis functions,” *Physics in Medicine and Biology*, vol. 61, no. 12, pp. 4624–4644, 2016.
- [34] S. Ellis and A. Reader, “Kernelised EM image reconstruction for dual-dataset PET studies,” in *Proceedings of NSS/MIC*, pp. 1–3, Strasburg, France, October 2016.
- [35] K. Gong, J. Cheng-Liao, G. Wang, K. T. Chen, C. Catana, and J. Qi, “Direct patlak reconstruction from dynamic PET data using the kernel method with MRI information based on structural similarity,” *IEEE Transactions on Medical Imaging*, vol. 37, no. 4, pp. 955–965, 2018.
- [36] J. Bland, A. Mehranian, M. A. Belzunze et al., “MR-guided kernel em reconstruction for reduced dose PET imaging,” *IEEE Transactions on Radiation and Plasma Medical Sciences*, vol. 2, no. 3, pp. 235–243, 2017.
- [37] B. Spencer and G. Wang, “Statistical image reconstruction for shortened dynamic PET using a dual kernel method,” in *Proceedings of NSS/MIC*, Atlanta, GA, USA, September 2017.
- [38] A. Mehranian, M. A. Belzunze, C. J. McGinnity et al., “Multi-modal synergistic pet and mr reconstruction using mutually weighted quadratic priors,” *Magnetic Resonance in Medicine*, 2018, in press.
- [39] J. Bland, M. Belzunze, S. Ellis, C. McGinnity, A. Hammers, and A. Reader, “Spatially-compact MR-Guided kernel EM for PET image reconstruction,” *IEEE Transactions on Radiation and Plasma Medical Sciences*, vol. 2, no. 5, pp. 470–482, 2018.
- [40] K. Thielemans, C. Tsoumpas, S. Mustafovic et al., “STIR: software for tomographic image reconstruction release 2,” *Physics in Medicine and Biology*, vol. 57, no. 4, pp. 867–883, 2012.
- [41] C. Calcagno, E. Vucic, V. Mani, G. Goldschlager, and Z. A. Fayad, “Reproducibility of black blood dynamic contrast-enhanced magnetic resonance imaging in aortic plaques of atherosclerotic rabbits,” *Journal of Magnetic Resonance Imaging*, vol. 32, no. 1, pp. 191–198, 2010.
- [42] N. A. Karakatsanis, R. Abgral, G. Boeykens et al., “18F-FDG: 18F-NaF PET/MR multi-parametric imaging with kinetics-based bone segmentation for enhanced dual-tracer PET quantification,” in *Proceedings of IEEE NSS/MIC/RTSD*, pp. 1–5, 2016.
- [43] A. Salavati, S. Houshmand, T. Werner, and A. Alavi, “Impact of methodological factors on assessment of atherosclerotic plaques using ¹⁸F-FDG and ¹⁸F-NaF PET/CT,” *Journal of Nuclear Medicine*, vol. 55, no. 1, p. 1321, 2014.
- [44] X. Li, D. Heber, W. Wadsak, M. Mitterhauser, and M. Hacker, “Combined 18F-FDG PET/CT and 18F-NaF PET/CT imaging in assessing vascular inflammation and osteogenesis in calcified atherosclerotic lesions,” *Journal of Nuclear Medicine*, vol. 57, no. 2, p. 68, 2016.
- [45] N. Karakatsanis, M. Trivieri, M. Dweck et al., “Simultaneous assessment of carotid plaque inflammation and micro-calcification with dual-tracer 18F-FDG: 18F-NaF PET-MR imaging: a clinical feasibility study,” *Journal of Nuclear Medicine*, vol. 58, no. 1, p. 446, 2017.
- [46] C. C. Watson, D. Newport, and M. E. Casey, *A Single Scatter Simulation Technique for Scatter Correction in 3D PET*, Springer, Berlin, Germany, 1996.
- [47] C. Tsoumpas, P. Aguiar, K. Nikita, D. Ros, and K. Thielemans, “Evaluation of the single scatter simulation algorithm implemented in the STIR library,” in *Proceedings of IEEE NSS/MIC/RTSD*, pp. 3361–3365, Rome, Italy, October 2004.

- [48] I. Polycarpou, K. Thielemans, R. Manjeshwar, P. Aguiar, P. K. Marsden, and C. Tsoumpas, "Comparative evaluation of scatter correction in 3D PET using different scatter-level approximations," *Annals of Nuclear Medicine*, vol. 25, no. 9, pp. 643–649, 2011.
- [49] M. W. Jacobson and K. Thielemans, "Optimizability of loglikelihoods for the estimation of detector efficiencies and singles rates in PET," in *Proceedings of IEEE NSS/MIC/RTSD*, pp. 4580–4586, Dresden, Germany, October 2008.
- [50] D. Hogg, K. Thielemans, T. Spinks, and N. Spyrou, "Maximum-likelihood estimation of normalisation factors for PET," in *Proceedings of IEEE NSS/MIC*, pp. 2065–2069, San Diego, CA, October 2001.
- [51] P. A. Yushkevich, J. Piven, H. C. Hazlett et al., "User-guided 3D active contour segmentation of anatomical structures: significantly improved efficiency and reliability," *Neuroimage*, vol. 31, no. 3, pp. 1116–1128, 2006.

Research Article

Sensitivity of Multiphase Pseudocontinuous Arterial Spin Labelling (MP pCASL) Magnetic Resonance Imaging for Measuring Brain and Tumour Blood Flow in Mice

Jessica Buck ¹, James R. Larkin ¹, Manon A. Simard ¹, Alexandre A. Khrapitchev ¹,
Michael A. Chappell ² and Nicola R. Sibson ¹

¹Cancer Research UK and Medical Research Council Oxford Institute for Radiation Oncology, Department of Oncology, University of Oxford, OX3 7LE, Oxford, UK

²Institute of Biomedical Engineering, University of Oxford, Old Road Campus Research Building, Oxford OX3 7DQ, Oxford, UK

Correspondence should be addressed to Nicola R. Sibson; nicola.sibson@oncology.ox.ac.uk

Received 14 June 2018; Revised 28 August 2018; Accepted 26 September 2018; Published 7 November 2018

Guest Editor: Charalampos Tsoumpas

Copyright © 2018 Jessica Buck et al. This is an open access article distributed under the Creative Commons Attribution License, which permits unrestricted use, distribution, and reproduction in any medium, provided the original work is properly cited.

Brain and tumour blood flow can be measured noninvasively using arterial spin labelling (ASL) magnetic resonance imaging (MRI), but reliable quantification in mouse models remains difficult. Pseudocontinuous ASL (pCASL) is recommended as the clinical standard for ASL and can be improved using multiphase labelling (MP pCASL). The aim of this study was to optimise and validate MP pCASL MRI for cerebral blood flow (CBF) measurement in mice and to assess its sensitivity to tumour perfusion. Following optimization of the MP pCASL sequence, CBF data were compared with gold-standard autoradiography, showing close agreement. Subsequently, MP pCASL data were acquired at weekly intervals in models of primary and secondary brain tumours, and tumour microvessel density was determined histologically. MP pCASL measurements in a secondary brain tumour model revealed a significant reduction in blood flow at day 35 after induction, despite a higher density of blood vessels. Tumour core regions also showed reduced blood flow compared with the tumour rim. Similarly, significant reductions in CBF were found in a model of glioma 28 days after tumour induction, together with an increased density of blood vessels. These findings indicate that MP pCASL MRI provides accurate and robust measurements of cerebral blood flow in naïve mice and is sensitive to changes in tumour perfusion.

1. Introduction

Reliable and accurate quantification of cerebral blood flow (CBF) by noninvasive methods, such as magnetic resonance imaging (MRI), is of critical importance in many neuropathologies. The measurement of tumour blood flow, for example, is key to both treatment planning and predicting response. Tumour perfusion is widely used as an indicator of tumour microenvironment, stage, and progression, and greatly influences treatment. Clinical studies have shown that tumour perfusion and, consequently, oxygenation are highly correlated with clinical outcome [1–3]. Critically, the increased use of antiangiogenic drugs and vascular normalising therapies in conjunction with radiotherapy to treat tumours has resulted in a need for improved quantitative, noninvasive

imaging measurements of vascular parameters to monitor treatment response.

The MRI method arterial spin labelling (ASL) is often used to image cerebral blood flow (CBF), as it requires no exogenous contrast agent and is easily implemented on clinical scanners. Moreover, this method can provide absolute quantitative measures of blood flow, which are not readily obtained by other modalities. Pseudocontinuous ASL (pCASL), in particular, has been recommended as the methodology of choice for clinical ASL [4], but no such recommendations currently exist for mice. Importantly, many potential therapeutic strategies for brain tumours are initially tested in mouse models. Consequently, there is a need for accurate methods of measuring preclinical brain and tumour blood flow, reflecting those used in the clinic, to enable assessment of likely therapeutic efficacy.

Despite initial reports developing ASL in rodents [5, 6], most implementations have focussed on clinical ASL. Many challenges exist in the adaptation of pCASL MRI for pre-clinical use, including higher blood flow velocities in the feeding arteries, smaller brain size, susceptibility artefacts from neighbouring air spaces, and B_0 inhomogeneities in high-field preclinical systems. Implementations of ASL in mice have historically produced CBF values that are semi-quantitative [7–9], single slice [10], or vary with the sequence [11–13] and body position [14] used. Moreover, the mean brain CBF values obtained are often unphysiologically high (>200 mL/100 g/min) [11, 15–17] and show little concordance with gold-standard autoradiography measurements (*ca.* 100 mL/100 g/min) in the normal mouse brain [18–22]. These values may be influenced by the use of anaesthetics, which at high concentrations can increase CBF dramatically [23, 24]. Whilst some preclinical studies have validated their ASL measurements using autoradiography [25–27] or microspheres [28], pCASL has not yet been validated in the mouse brain. A previous implementation of pCASL to measure CBF in mice not only showed clear advantages but also showed a loss of inversion efficiency stemming from phase offsets in the label-control acquisitions [12].

The use of multiphase pCASL (MP pCASL) has been shown to reduce these errors in both humans [29] and rats [27], but this sequence has not yet been applied in mice. We have recently implemented a multiphase pCASL method for use in the rat brain, which shows high reliability, reproducibility, and accuracy for CBF measurements [27]. However, given the even smaller size of the mouse brain, implementing this sequence in mice remains challenging. Movement artefacts from respiration affect the signal at the base of the brain in particular, and air spaces surrounding the brain produce distortions. Since most preclinical models of primary brain tumours and brain metastasis are established in mice rather than rats, developing this method further for robust and reliable application in mice is essential.

Thus, the primary aim of this study was to optimise and validate MP pCASL MRI for measuring CBF in naïve mice. Subsequently, we assessed the sensitivity of the optimised MP pCASL sequence to changes in blood flow in early stage tumours, using mouse models of secondary brain cancer (metastasis) and primary glioma.

2. Materials and Methods

2.1. Animals. Female BALB/c mice (Charles River, UK), 7–10 weeks old, were used in all naïve and metastasis model experiments. Female SCID mice (Charles River, UK), 7–10 weeks old, were used in all primary brain tumour model experiments. All animal experiments were approved by the UK Home Office (Animals (Scientific Procedures) Act 1986) and conducted in accordance with the University of Oxford Policy on the Use of Animals in Scientific Research and the ARRIVE guidelines [30]. Animals were housed in individually ventilated cages under a 12-h light/12-h dark cycle with food and water *ad libitum*. All animals were housed in cages of 4–6 animals.

2.2. Carotid Blood Flow Measurements. Mice ($n = 4$) were anaesthetised with 3% isoflurane in O_2 . Temperature was monitored and maintained at $37.0 \pm 0.5^\circ\text{C}$ throughout with a feedback heating system. Respiration was monitored and maintained between 30 and 80 breaths per minute. An electrocardiogram was also acquired. Using a Vevo 3100 ultrasound (Visualsonics, Amsterdam, Netherlands) and a mouse cardiology probe (MX550D), a respiration-gated 3D ultrasound image was acquired across the whole neck. The left carotid artery was located, and 10 Power Doppler blood flow clips of 30 s duration were acquired per mouse at respiration rates across the range of 30–80 breaths per minute, achieved by varying the concentration of isoflurane between 3 and 1%. Carotid blood flow values from the Power Doppler trace were extracted using an open-source plot digitiser [31], and values representing the systolic and diastolic flow velocities were used in pCASL simulations to determine labelling efficiency.

2.3. Labelling Efficiency Simulations. Bloch simulations were carried out to simulate labelling efficiency over a range of different gradient strengths, radiofrequency (RF) powers, labelling plane thicknesses, and blood flow velocities, as described by Okell [32]. We conducted Bloch simulations whilst varying G_{max} and G_{mean} ($G_{\text{mean}} = 0.05 \times G_{\text{max}}$ in our MP pCASL sequence) gradient strengths, equivalent to converted labelling plane thicknesses of 1–10 mm in 0.5 mm steps. Blood flow velocities of between 1 and 20 cm/s with steps of 1 cm/s were modelled with $T_{1\text{blood}} = 2.1$ s, $T_{2\text{blood}} = 0.033$ s (based on *ex vivo* rat blood measurements at 9.4 T) [27], and RF pulse amplitudes of 1–10 μT with steps of 0.5 μT for a train of 600 μs Hanning-shaped pulses, beginning every 1.2 ms. Simulations of the theoretical maximum saturation for different label durations were also carried out, and data are available in the Supplementary Information.

2.4. MP pCASL Optimisation. MP pCASL experiments were performed on a separate cohort of mice ($n = 4$) using a 9.4 T MRI spectrometer (Agilent Technologies Inc., Santa Clara, USA) with a 26 mm volume transmit-receive birdcage RF coil (Rapid Biomedical GmbH, Rimpar, Germany). Mice were anaesthetised with 3% isoflurane in 30% O_2 : 70% N_2 and positioned in a custom-built cradle in the volume coil. Mouse temperature was monitored and maintained at $37.0 \pm 0.5^\circ\text{C}$ with a rectal probe and feedback heating system. Respiration was monitored using a pressure balloon, and breathing rate was maintained at approximately 60 breaths per minute by adjusting isoflurane concentration; stable breathing was typically maintained with an isoflurane concentration of 1.2–1.5%. The respiration trace was recorded and used to inform respiratory triggering.

Zero- and first-order shimming was conducted manually using a PRESS sequence on a voxel encompassing the brain. The EPI readout was acquired with the following parameters: 2-shot spin-echo encoding, relaxation time (TR) = 4.0 s, echo time (TE) = 18.32 ms, spectral width (SW) = 250 kHz, field of view (FOV) = 20×20 mm, matrix size = 64×64 , slice thickness = 1 mm, and number of slices = 8, with the anterior

slice positioned just posterior to the olfactory sulcus. Respiratory triggering (with an associated variable post-trigger delay) was also employed to reduce signal fluctuation at the base of the brain caused by respiratory motion.

The MP pCASL parameters were optimised for use in mice. The MP pCASL labelling was implemented with a labelling train consisting of a set of slice-selective RF/gradient pulse pairs followed by a slice-refocusing gradient pulse; RF pulse duration 600 μ s, Hanning shape with effective flip angle (FA) = 40°, and slice-refocusing gradient pulse duration 600 μ s. The phase of these RF pulses was arrayed from 0° to 315° with incremental steps of 45°: 0°, 45°, 90°, 135°, 180°, 225°, 270°, and 315°. The labelling plane was oriented at -10° relative to the axial plane in order to be perpendicular to the carotid and vertebral arteries (Figure 1). The labelling pulse train was followed by a gradient crusher to remove residual transverse magnetisation, a postlabel delay (PLD) to enable labelled blood water spins to travel to the brain, and the EPI readout. Using these parameters and the variable respiration trigger, the duration of the scan varied from 3 minutes 12 seconds to a maximum of approximately 5 minutes. Labelling train duration was varied between 0.4 and 5.0 s (TR increased accordingly from 4–7.6 s) and PLD between 10 and 1000 ms, to optimise the MP pCASL signal.

2.5. Validation of MP pCASL by Autoradiography. For comparison of MP pCASL data with gold-standard autoradiography CBF measurements, naïve mice ($n = 4$) were anaesthetised using the same setup and isoflurane concentrations as for MRI described above. MP pCASL was performed on each animal on the day before autoradiography, owing to restrictions concerning the use of radioisotopes in certain rooms. Care was taken to ensure breathing rate and isoflurane concentration, and duration of anaesthesia prior to measurements was as similar as possible between the ASL and autoradiography sessions. For the MP pCASL MRI, a labelling pulse duration of 0.9 s and a postlabel delay of 0.4 s seconds was used with the parameters described above.

Autoradiography was performed using the method described by Maeda et al. [19]. Mice were injected intraperitoneally with 0.15 μ Ci of 4-iodo-*N*-methyl-[¹⁴C] antipyrine (Hartmann Analytic, Germany, specific activity 55 mCi/mmol), and 2 minutes later, they were injected intraperitoneally with an overdose of pentobarbitone then immersed in isopentane on dry ice until frozen. The frozen brain was extracted, and 20 μ m sections were collected at 200 μ m intervals and dried at 60°C for 10 min. These sections were exposed to film for 24 hours alongside calibrated radioactive standards, and films were scanned (Carestream Kodak BioMax MR Film; standards: 0–35 μ Ci/g, ARC; Expression 10000XL transmittance scanner, Epson, UK). Scanned films were background subtracted and calibrated against the standards. Absolute CBF was then calculated using the equation as described by Sakurada et al. [33]. Blood sampled from the frozen heart at end-point was used to calculate the final arterial tracer concentration using autoradiography. For calculation of regional CBF values, the

autoradiography images were perspective transformed, aligned to the MR images, and down-sampled to the same resolution as the MP pCASL images (64 \times 64 pixels). Subsequently, regional masks were created.

2.6. MP pCASL Data Analysis. ASL data analysis and perfusion quantification were performed using a custom version of the BASIL toolbox from the FMRIB Software Library (<http://www.fmrib.ox.ac.uk/fsl/BASIL>). The raw multiphase data were initially fitted to a modified Fermi function [27] ($\alpha = 70$, $\beta = 19$) to produce a raw phase map. The phase values were then smoothed and clustered using supervoxel clustering [34] to produce regions of interest (ROIs) for each supervoxel phase cluster. The raw multiphase data were combined with the supervoxel ROIs to produce high SNR means of the optimal phase for each supervoxel. The high SNR supervoxel data were then fitted to the Fermi function again to produce a high-precision phase map, which could be used to calculate the final CBF map.

Perfusion quantitation was performed according to the kinetic model of Buxton et al. [35] and calibration with Oxford_asl [36]. Reference scans acquired without labelling were used for absolute quantitation of CBF. Detailed postprocessing methods, including supervoxel clustering, are described by Larkin et al. [27].

2.7. Mouse Models of Brain Metastasis and Primary Brain Tumours. Sensitivity of the MP pCASL sequence to changes in tumour blood flow over time was first assessed in a brain metastasis model. Female BALB/c mice were anaesthetised with 3% isoflurane in 30% O₂: 70% N₂O, and focally microinjected using a finely drawn glass microcapillary (*ca.* 75 μ m tip diameter) with 5000 4T1-GFP, metastatic murine mammary carcinoma cells in 0.5 μ L sterile saline into the left striatum (+0.5 mm anterior, +2 mm lateral, 2.5 mm depth relative to bregma). Mice underwent MRI at day 7 ($n = 3$), 14 ($n = 5$), 21 ($n = 6$), 28 ($n = 8$), or 35 ($n = 6$) after tumour induction; mice were randomly assigned to each time point group.

To further assess the sensitivity of the MP pCASL method, a primary brain tumour model was also used. Female SCID mice were anaesthetised and injected in the left striatum, as above, with 5000 U87 human glioma cells. Mice underwent MRI at day 14 ($n = 10$) or 28 ($n = 6$), after tumour induction.

In addition to MP pCASL acquisitions, T_1 and T_2 maps, angiography, and T_1 and T_2 weighted anatomical scans were acquired for each mouse. Time-of-flight angiography was acquired with TR = 30 ms, TE = 1.78 ms, FA = 30°, matrix size = 128 \times 128 \times 128, and FOV = 20 \times 20 \times 30 mm. A T_1 -weighted spin-echo multislice anatomical scan was acquired with TR = 0.55 s, TE = 20 ms, number of averages = 2, and matrix size = 256 \times 256. A T_2 -weighted fast spin-echo multislice anatomical scan was acquired with TR = 3.5 s, echo spacing = 15 ms, effective TE = 60 ms, echo train length = 4, and matrix size = 256 \times 256; using the same slice plan and FOV as the MP pCASL. A contrast-enhanced scan was obtained 5 minutes following intravenous injection of 30 μ L

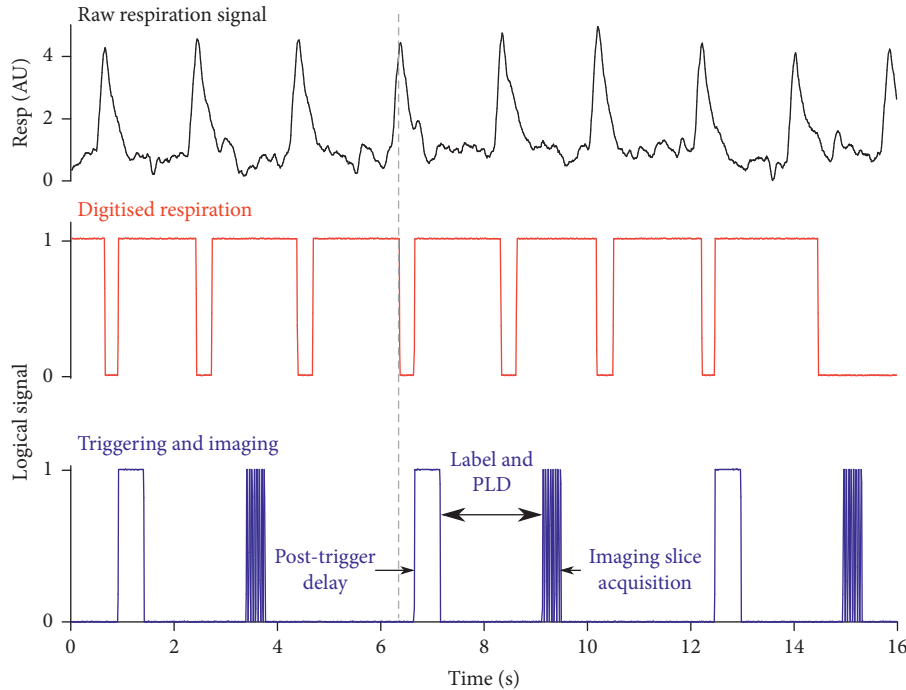


FIGURE 1: Optimisation of EPI readout using respiratory triggering to acquire the imaging readout during the plateau phase of respiration, reducing signal fluctuation at the base of the brain. Black trace = raw respiration trace; red trace = digitised respiration trace which acts as the trigger signal; and blue trace = readout of the post-trigger delay period, followed by the imaging slice acquisition. A variable encoding the post-trigger delay was implemented in the sequence to allow adjustment for changing respiration rates.

(15 μmol , approximately 0.75 mmol/kg based on a 20 g mouse) Gadodiamide (Omniscan, GE Healthcare) using the T_1 -weighted scan parameters described above.

Following imaging, mice underwent transcardial perfusion-fixation with 0.9% heparinised saline followed by 20 mL periodate-lysine-paraformaldehyde solution containing 0.025% glutaraldehyde, and the brains were collected for histology.

2.8. Immunohistochemistry. Sections were stained for the blood vessel marker CD31 (AF3628, R&D systems, Abingdon, UK) according to the method described by Andreou et al. [37]. Microvessel density (vessel area fraction) was quantified for the core and rim regions of the entire tumour, and also for the contralateral striatum, as the percentage of area covered using the “Positive Pixel Count 2004-08-11” algorithm in Imagescope (Leica Biosystems). The parameters used for perfusion-fixed tumour model 10 μm sections were moderately stained pixel intensity between 202 and 185 and strongly stained pixel intensity lower than 10. The parameters used for postfixed 20 μm autoradiography sections were moderately stained pixel intensity between 180 and 171, and strongly stained pixel intensity lower than 53.

2.9. Statistics. All data are reported as group mean \pm group standard deviation. Differences between groups were determined using two-tailed paired t -tests or one-way ANOVA (regional and histology analysis), or two-way repeated

measures (paired) ANOVA (time-course analysis) followed post hoc by the Bonferroni multiple test correction. An f -test was used to assess heterogeneity between groups.

3. Results

3.1. MP pCASL Sequence Optimisation. Blood velocity in the carotid artery was measured to inform Bloch simulations of pCASL. The mean blood velocity in the carotid artery was found to be 124 ± 17 mm/sec, and the maximum blood velocity was found to be 275 ± 58 mm/sec. Mean blood velocity was consistent between animals, but varied with the respiration rate in 3 of 4 animals (linear regression, slope = 0.3–1.4). Maximum blood velocity varied between animals (range = 214–556 mm/sec), and also varied with the respiration rate in 3 of 4 animals (linear regression, slope = 2.0–7.6). Using these values to inform the range of blood velocities in the Bloch simulations, a 2 mm label thickness was chosen as it provided sufficient theoretical inversion (labelling) efficiency (78.5%) at the RF pulse amplitude used in our system (5 μT) and average blood velocity of 124 mm/s, and lies within the linear portion of the feeding arteries in the neck.

Respiratory triggering, whereby the EPI readout was acquired during the plateau phase of respiration, was found to reduce signal fluctuation at the base of the brain (Supplementary Figure 1). The respiratory triggering also significantly increased the signal-to-noise ratio (SNR) of the MP pCASL data (15.1 ± 5.9) compared with the untriggered sequence (6.5 ± 1.5 , $p < 0.05$; Supplementary Figure 2). Finally, a variable post-trigger delay was encoded in the

sequence to allow adjustment for changing respiration rates in subsequent scans (Figure 1).

Following angiography, a labelling plane positioned at -10° relative to the axial plane was found to be perpendicular to the carotid and vertebral arteries. Label placement just posterior to the medulla oblongata enabled consistent labelling plane placement between animals using a distinct anatomical landmark, and is posterior to the vertebral flexure of the carotid arteries (Figure 2(a)).

All labelling pulse train durations tested yielded CBF values close to the physiological range expected from the literature (Figure 2(b)), and no significant differences in calculated CBF values were found between the different durations. Similarly, phase maps were stable across labelling durations. Thus, as a compromise between ensuring sufficient labelling (SNR simulations described in Supplementary information) and keeping scan time as short as possible, a label duration of 0.9 s was chosen.

To allow measurement of bolus arrival time in brain voxels, 12 PLDs from 10 to 1000 ms were acquired, each with 8 phases of labelling RF pulses. Arrival maps showed that the bolus arrived at over 95% of voxels in the most anterior slice and at 99% of voxels in the most posterior slice within 0.4 s (Figure 3(c)). Thus, 0.4 s was chosen as the optimal PLD to reduce signal loss from relaxation.

3.1.1. MP pCASL Validation. Use of the optimised MP pCASL sequence in naïve mice yielded measured CBF values of 96 ± 18 mL/100 g/min on average across the brain (Figure 4(a)), 103 ± 23 mL/100 g/min in the cortex, 90 ± 24 mL/100 g/min in the striatum, and 77 ± 21 mL/100 g/min in the corpus callosum. Using the gold-standard autoradiography method, we measured CBF to be 101 ± 32 mL/100 g/min across the whole brain, a difference of $<6\%$ when compared with MP pCASL results across the same region (Figure 4(a)). Average CBF values using autoradiography were 102 ± 32 mL/100 g/min in the cortex, 95 ± 25 mL/100 g/min in the striatum, and 87 ± 28 mL/100 g/min in the corpus callosum. No significant differences were found between MP pCASL and autoradiography CBF measurements (Figure 4(b)). Blood vessel density was calculated from histological sections stained for CD31 in these animals, yielding values of $3.0 \pm 0.6\%$, $2.2 \pm 0.8\%$, and $0.8 \pm 0.3\%$ for the cortex, striatum, and corpus callosum, respectively (Supplementary Figure 3). Although both CBF and vessel density appeared to decrease across the three regions studied (cortex > striatum > corpus callosum), no significant correlation between vessel density and CBF was found.

3.1.2. Mouse Model of Brain Metastasis. Application of the MP pCASL sequence in mice with intracerebral metastases showed a significant, 16%, decrease in CBF in the tumour-bearing striatum (84 ± 16 mL/100 g/min) compared with the contralateral (normal) striatum (99 ± 24 mL/100 g/min) at day 35 (ANOVA $p < 0.05$; post hoc Bonferroni test $p < 0.05$). The mean absolute reduction in CBF in the tumour-bearing striatum was 15.3 mL/100 g/min. No

differences were found between hemispheres at other time points. All tumours were confirmed histologically, and the mean tumour diameter measured by histology at day 35 was 2.14 ± 0.53 mm.

In a subset of animals from days 21–35 ($n = 7$), the striatum exhibited gadolinium enhancement throughout the area of metastatic foci and, in these animals, no difference in CBF was evident between the tumour (86 ± 26 mL/100 g/min) and contralateral striatum (92 ± 24 mL/100 g/min; Figures 5(a)–5(c)). Analysis of microvessel density within the metastatic foci showed an increased vessel area fraction ($7.7 \pm 2.2\%$; Figure 5(d)) in the enhancing tumour compared with normal tissue in the contralateral striatum ($0.9 \pm 0.4\%$, $p < 0.0005$; Figures 5(e)–5(f)).

However, in a further, distinct subset of animals from days 28 and 35 ($n = 6$), a gadolinium-enhancing tumour rim was evident surrounding a nonenhancing tumour core. Analysis of these animals showed a significant reduction in blood flow in the core of the tumour region (69 ± 14 mL/100 g/min) compared with the rim (83 ± 10 mL/100 g/min, $p < 0.05$; Figures 6(a)–6(c)). No difference was found between the enhancing rim of the tumour and normal tissue in the contralateral striatum (82 ± 13 mL/100 g/min; Figure 6(c)). The mean absolute reduction in CBF in the tumour core compared with that in the tumour rim was 13.4 mL/100 g/min. The tumour voxels (including core and rim) showed significantly greater heterogeneity, as demonstrated by higher intra-ROI voxel variance, than the contralateral striatum (F-test, $p < 0.001$). Analysis of microvessel density within the metastatic foci showed a greatly increased vessel area fraction ($13.5 \pm 2.5\%$) in the nonenhancing tumour core compared with the tumour rim ($6.6 \pm 2.5\%$, $p < 0.0001$; Figures 6(d)–6(f)), which in turn showed greater vessel area fraction than the normal tissue in the contralateral striatum ($1.2 \pm 0.7\%$, $p < 0.0001$; Figure 6(f)). Correlation analysis between microvessel density and CBF measured by MP pCASL MRI revealed a trend towards negative correlation in both tumour core and rim, but this did not reach significance (Supplementary Figure 4).

3.1.3. Mouse Model of Glioma. Application of the MP pCASL sequence in mice injected intracerebrally with U87 glioma cells showed a significant, 19%, reduction in CBF in the tumour-bearing striatum (61 ± 12 mL/100 g/min) compared with the contralateral striatum at day 28 (74 ± 10 mL/100 g/min, $p < 0.05$; Figures 7(a)–7(c)). The mean absolute reduction in CBF in the tumour-bearing striatum was 13.3 mL/100 g/min. Only two tumours showed gadolinium enhancement, and no tumours showed nonenhancing core regions. As for the metastasis model, analysis of microvessel density within the day 28 tumours showed an increased vessel area fraction ($10.7 \pm 2.9\%$; Figure 7(d)) in the tumour compared with the normal tissue in the contralateral striatum ($3.6 \pm 0.5\%$, $p < 0.05$; Figures 7(e)–7(f)). All tumours were confirmed histologically, and the mean tumour diameter measured by histology at day 28 was 1.20 ± 0.52 mm.

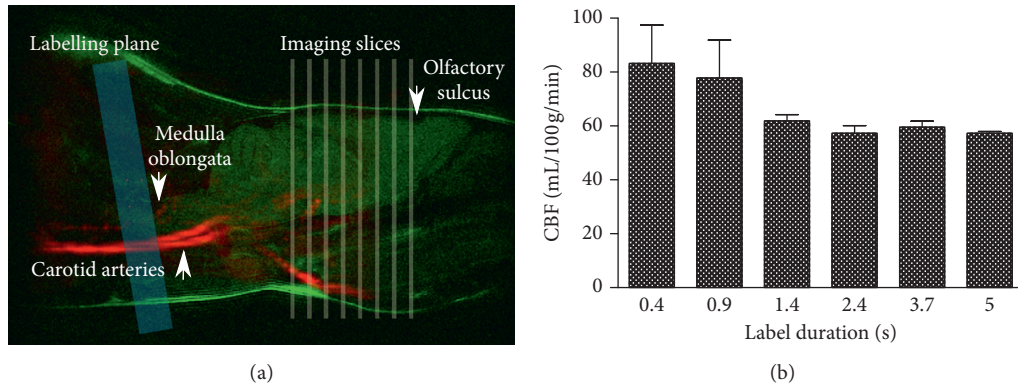


FIGURE 2: Optimisation of MP pCASL bolus duration. (a) A-10° labelling plane (blue) relative to the axial imaging plane (yellow) was optimal, as this was perpendicular to the carotid and vertebral arteries visible by angiography (red). Label plane placement posterior to the medulla oblongata, visible on a sagittal T_2 weighted anatomical image (green), enabled consistent label plane location between animals, while not interfering with imaging slices (yellow). (b) No significant differences were found in calculated CBF across the range of label duration times tested ($n = 3$).

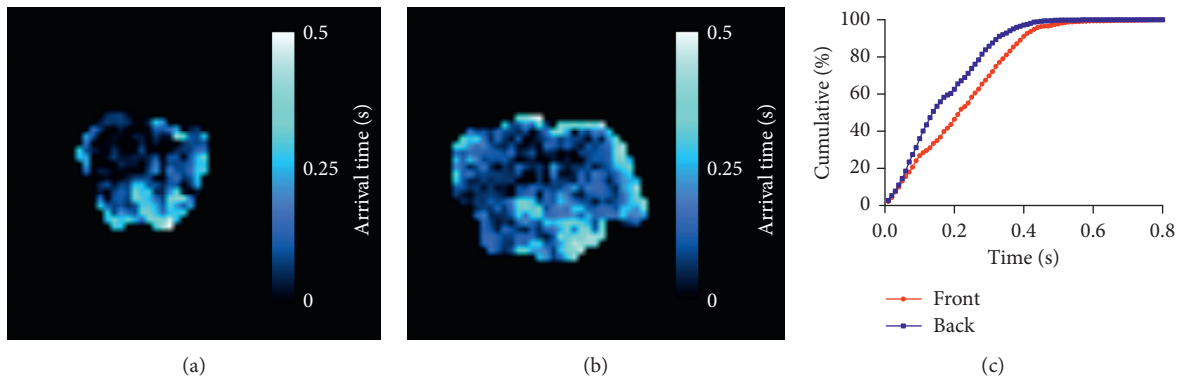


FIGURE 3: Optimisation of postlabel delay (a–b). Multi-PLD scans were acquired to measure arterial transit time at the front and back of the brain. Example maps of bolus arrival time in (a) anterior and (b) posterior slices. (c) Arrival maps showed bolus arrival in over 95% of voxels in the anterior slice and 99% of voxels in the posterior slice within 0.4 s ($n = 4$).

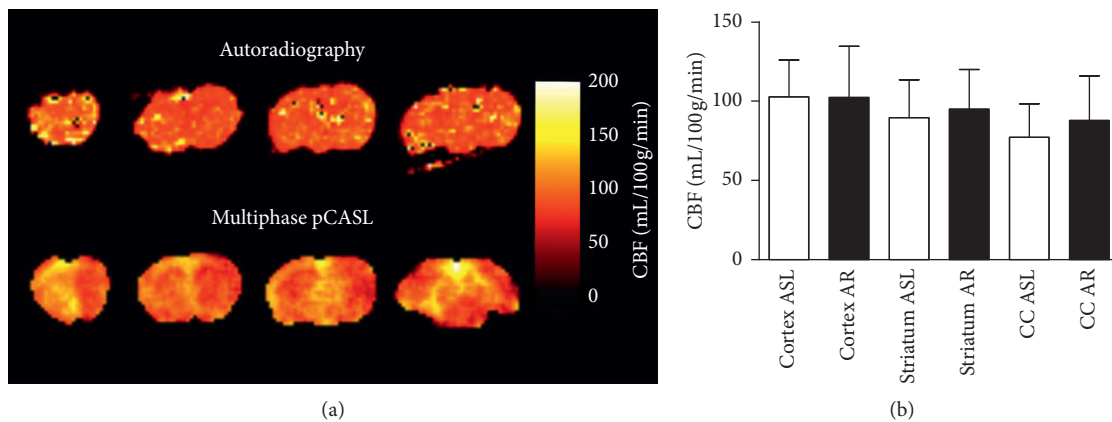


FIGURE 4: Cerebral blood flow maps and regional values. (a) Representative CBF maps produced using gold-standard autoradiography (top row), and the optimised MP pCASL sequence (bottom row). (b) Regional CBF values as measured by MP pCASL and autoradiography (AR). Average CBF values were 96 ± 18 mL/100 g/min across the whole brain using MP pCASL, and 101 ± 32 mL/100 g/min using autoradiography. No significant differences were found between MP pCASL and autoradiography CBF measurements either for whole brain, or by region. CC—corpus callosum.

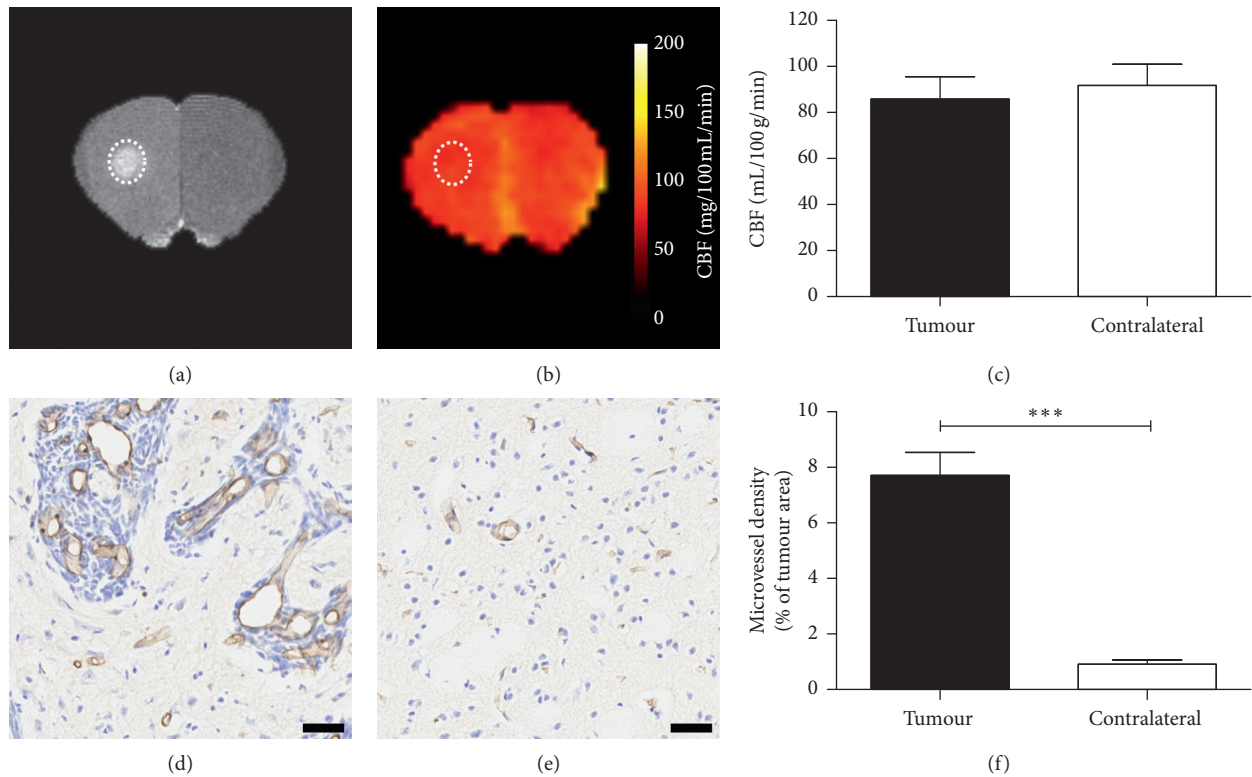


FIGURE 5: Application of the MP pCASL sequence in mice with intracerebral 4T1-GFP metastatic tumours showing gadolinium enhancement. (a) T_1 -weighted image showing enhancement (dotted outline) of metastatic foci. (b) CBF maps with the same ROI indicated. (c) Graph showing CBF values in tumour and contralateral regions; no significant decrease in perfusion is evident (d-e). Histological comparison of microvessel area fraction in tumour (d), and contralateral (e) regions. Scale bars = $20\ \mu\text{m}$. (f) Graph showing quantitation of microvessel area fraction in tumour and contralateral striatum regions; a significant increase in microvessel area fraction is evident in tumour compared with normal tissue in the contralateral striatum ($n = 7$). *** $p < 0.01$.

4. Discussion

Pseudocontinuous ASL is the recommended MRI sequence for clinical measurements of cerebral blood flow, and multiphase ASL sequences have many advantages in compensating for off-resonance effects that alter labelling efficiency, thus improving the quality and reliability of CBF maps produced. Despite these advantages, no studies have been published implementing multiphase pCASL in mice. We have now demonstrated that our optimised MP pCASL sequence provides reliable and accurate measures of CBF in naïve mice *in vivo* and is sensitive to changes in tumour blood flow.

In this study, our aim was to produce MP pCASL measurements that can be used to obtain CBF maps in mice that replicate blood flow values obtained using the gold-standard approach of autoradiography. Our results showed good concordance with autoradiography and were in accord with previous autoradiography findings [19], including those comparing ASL with autoradiography [22, 27]. As anticipated, the use of multiphase pCASL reduced the errors seen in the previous implementation of label-control pCASL in mice, owing to loss of inversion efficiency [12]. As an alternative to the MP pCASL approach described here, phase correction can also be applied using prescans [38]. However, this method requires processing during scan time rather

than post hoc. For this reason, the MP pCASL approach offers an easier implementation and potentially more time efficient approach for the measurement of CBF.

The inclusion of a respiration trigger in the sequence reduced signal fluctuation at the base of the brain and improved image quality. However, this technique does result in a variable TR between phase acquisitions. As the TR becomes longer than the minimum with triggering, it is expected that there will be no effect on the next acquisition. Extended TR values of up to 20 s have been tested with this sequence and have shown no effect on data quality (data not shown). The use of respiratory triggering also relies on a reasonably stable respiratory cycle, which was reliably achieved at ~ 60 breaths per minute with 1.2–1.5% isoflurane concentrations for up to two hours.

Our data show less regional variation in CBF than other autoradiography studies in mice, which may, at least in part, reflect differences in mouse strain and anaesthetic regime used [19, 21, 39]. Gaseous anaesthesia, in particular, is known to have region specific effects on CBF, and in rats the caudate/putamen shows a much greater ($\sim 70\%$) increase in CBF than in the cortex ($\sim 20\%$) under isoflurane-anaesthetised conditions compared with awake animals [23]. Consequently, regional differences in CBF under isoflurane anaesthesia are greatly reduced [23], and it is likely that this underlies the reduced regional variation in

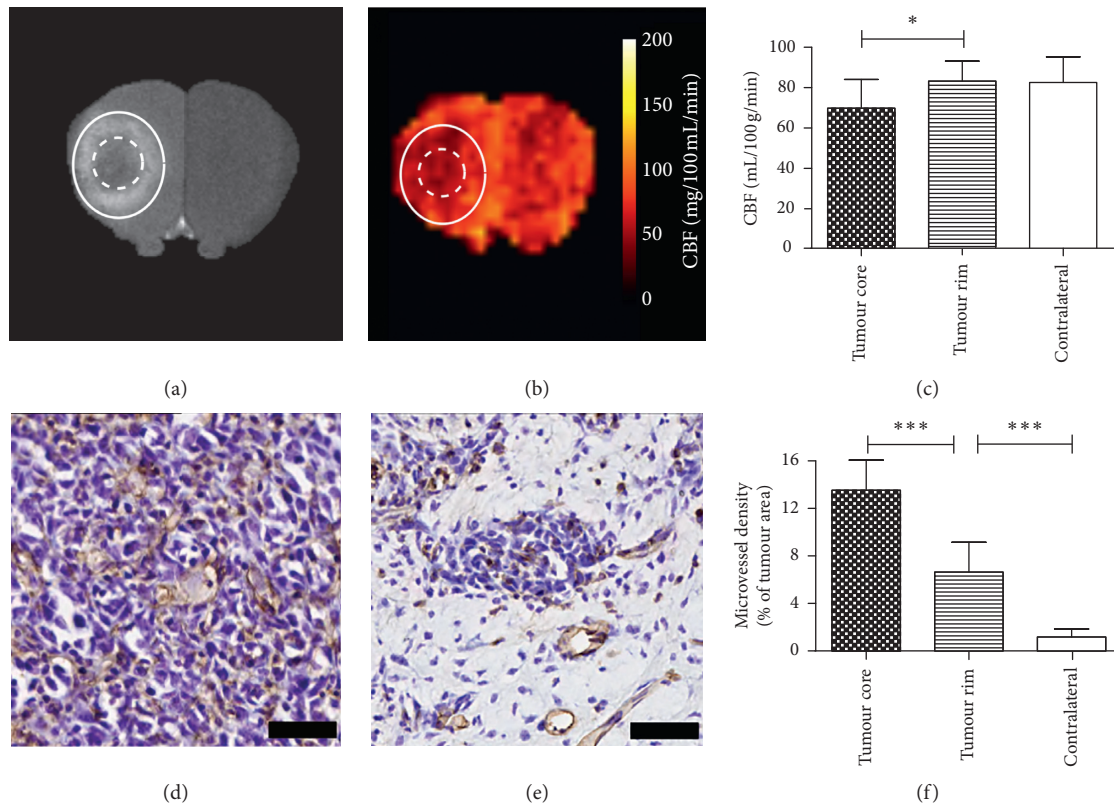


FIGURE 6: Application of the MP pCASL sequence in mice with intracerebral 4T1-GFP metastatic tumours showing a gadolinium enhancing rim and a nonenhancing core region. (a) T_1 -weighted image showing core (nongadolinium-enhancing central regions; dotted outline) and rim (gadolinium-enhancing regions; solid outline) of metastatic foci. (b) CBF maps with the same ROIs indicated. (c) Graph showing CBF values in core, rim, and contralateral regions; a significant decrease ($n = 6$) in perfusion is evident between the core and rim regions of tumours (d-e). Histological comparison of microvessel area fraction in core (d) and rim (e) regions. Scale bars = $20 \mu\text{m}$. (f) Graph showing quantitation of microvessel area fraction in core, rim, and contralateral striatum regions; a significant increase in vessel area fraction is evident in core regions compared with both the rim regions ($n = 6$) and normal tissue in the contralateral striatum. * $p < 0.05$; *** $p < 0.0001$.

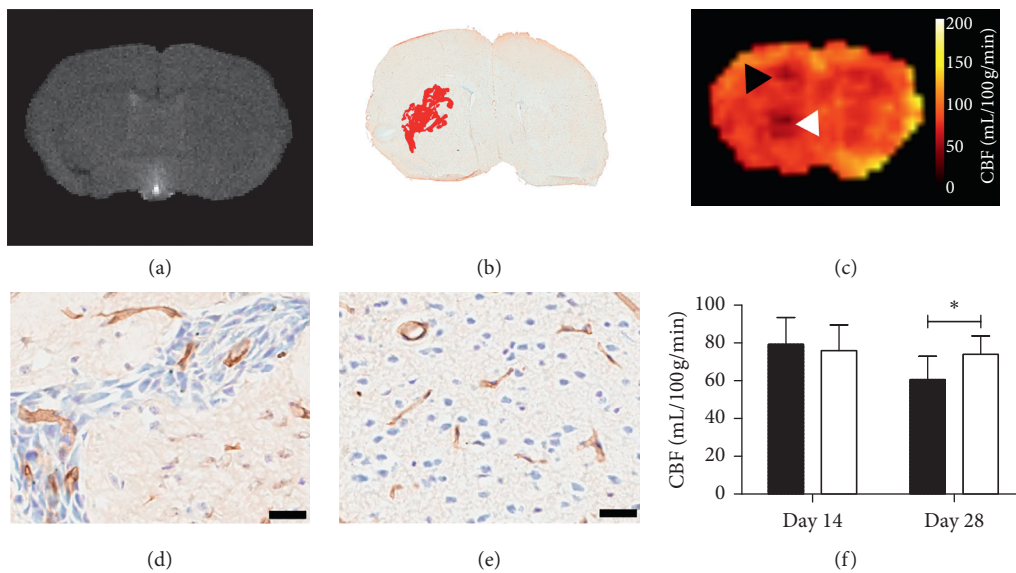


FIGURE 7: Application of the MP pCASL sequence in mice with intracerebral U87 glioma at the day 28 time point. (a) T_1 -weighted image showing no evidence of gadolinium enhancement in the tumour injected (left) hemisphere. (b) Immunohistochemical image showing an overlay of tumour area (red) combined from tissue sections spanning $500 \mu\text{m}$ corresponding to the MRI slice in (a). (c) CBF maps showing reduction in local CBF (arrowheads) (d-e). Immunohistochemical image showing CD31 staining of vessels (brown) in tumour-injected striatum (d) and contralateral striatum (e). (f) Graph showing CBF values in the tumour-bearing (black) and contralateral (white) striatum. CBF is reduced in the tumour-bearing compared with the contralateral striatum at day 28 time point ($p = 0.02$). Scale bars = $20 \mu\text{m}$.

CBF observed in the current study. The reduced regional variation was observed in both MP pCASL and autoradiography data, supporting the above conclusion. To reduce the effects of isoflurane on our CBF measurements, we used the lowest possible concentration of isoflurane in order to achieve a stable breathing rate of ~60 breaths per minute.

The MP pCASL technique was found to be sensitive to changes in tumour perfusion in mouse models of both brain metastasis and glioma at later time points. The technique was also sensitive to perfusion heterogeneity within metastatic tumours, showing significantly reduced (but not absent) perfusion in the nonenhancing tumour core compared with normal tissue in the contralateral striatum and increased heterogeneity in perfusion compared with the contralateral striatum. As autoradiography has only been used to validate CBF measurements in the naïve brain, it is possible that differences in tumour arterial transit time or tissue relaxation time may affect the CBF quantification from MP pCASL data in these tumour-bearing animals. However, these results are in line with other preclinical primary brain tumour perfusion studies, which showed reduced perfusion in the tumour core [7, 40–42]. The reduction in tumour blood flow observed in the current study was considerably smaller than other (primary) tumour perfusion studies. The majority of previous studies have investigated large tumours (>5 mm diameter in mice) [7, 9, 40, 42], which often have a large necrotic core with few blood vessels [7, 43] resulting in a substantial perfusion deficit. In contrast, in both the metastasis and glioma models used here, the tumour foci were considerably smaller (1–2 mm diameter) and more diffusely growing. Moreover, histological analysis demonstrated that the core regions, rather than being necrotic and devoid of vessels, in fact contained large numbers of blood vessels. Such tumours would be ideal candidates, clinically, for treatment with vascular modifying agents, and the ability to quantitatively measure changes in blood flow in such small tumours could be of considerable use in preclinical testing.

Tumours have a number of distinct vascular phenotypes, each of which may confer changes in blood flow. One such phenotype, which is present in our model, is that of a highly branched network of nonfunctional angiogenic vessels. In this case, despite an increase in the density of vessels, a decrease in CBF may be observed in this region, owing their highly branched and dysfunctional nature. Another vascular phenotype often seen in solid tumours is the rapid growth of the tumour faster than the vasculature can keep up, resulting in a tumour core with low vascularity, and hence a decreased CBF. Both of these phenotypes are characterised by a decrease in CBF, despite the differences in tumour vascularity.

Gadolinium contrast enhancement on MRI reports on both vessel permeability and blood flow, and a lack of gadolinium enhancement in tumour core regions is typically taken to reflect tissue necrosis and complete absence of vessels. In contrast, blood vessel density measurements provide no information on whether vessels are perfused, but only whether they are present. However, in both models used in the current study, although core tumour areas showed significant reductions in blood flow in areas devoid

of gadolinium enhancement, histological assessment revealed a significant increase in microvessel density and only very small areas of necrosis. Together, these findings suggest that these core vessels are either structurally abnormal or have abnormal flow patterns, as is common in angiogenic tumour vessels [44–46], and that MP pCASL measurements may complement histology and contrast-enhanced MRI to provide useful insights into vessel patency and tumour blood flow.

Interestingly, the rim of the metastatic tumour area also showed an increase in microvessel density histologically, but in this region, CBF measured by MP pCASL MRI was normal. Similarly, in those tumours showing enhancement throughout the tumour core, microvessel density was increased, but no change in CBF was evident. These findings suggest that MP pCASL MRI identifies heterogeneity in tumour blood flow that could not be predicted from histological assessment of vascularity alone. Thus, by identifying areas of reduced (but not absent) flow, MP pCASL MRI may enable identification of brain tumours in which vascular normalising therapy or antiangiogenic therapy could be beneficial prior to, or in conjunction with, radiotherapy.

5. Conclusions

Multiphase pCASL MRI has been successfully implemented and validated for imaging cerebral blood flow in naïve mice and has been shown to overcome the limitations inherent in standard nonmultiphase ASL methods. The data show high reproducibility in CBF measurements between animals and concordance with gold-standard autoradiography measurements. Further, this imaging approach is sensitive to changes in perfusion in mouse models of both primary and secondary brain tumours, even in very small tumours, and provides insight into tissue blood flow dynamics that complements vessel density measurements and contrast-enhanced MRI. This method could be of high value for noninvasive measurement of brain tumour blood flow prior to and following therapy, increasing the potential for clinical translation.

Data Availability

The data used to support the findings of this study are available from the corresponding author upon request. The supervoxel clustering and perfusion quantification methods are available at <http://www.quantiphyse.org>.

Disclosure

Dr Chappell reports personal fees from FMRI Software Library, outside the submitted work. In addition, Dr Chappell, Dr Larkin, and Ms Simard have a patent “Methods and Systems of Multiphase Arterial Spin Labelling (USPTO 62/577,994)” pending.

Conflicts of Interest

The authors declare that they have no conflicts of interest.

Acknowledgments

The authors thank James Meakin and Tom Okell for assistance with the pCASL sequence, Bloch simulations, and data processing; Martin Craig for assistance with the supervoxel analysis; Kevin Ray, Sean Smart, and Paul Kinchesh for assistance with the MRI. This work was supported by Cancer Research UK (grant number C5255/A15935); the CRUK/EPSRC Cancer Imaging Centre in Oxford (grant number C5255/A16466); and the Engineering and Physical Sciences Research Council (grant number EP/P012361/1). JB is supported by Charlie Perkins, Chevening, and Green Templeton College Scholarships.

Supplementary Materials

Supplementary Figure 1 (video): example MP pCASL images with (A) and without (B) respiratory triggering. Respiratory triggering reduces signal fluctuation at the base of the brain. Supplementary Figure 2: signal-to-noise ratio (SNR) of the MP pCASL sequence with and without respiratory triggering ($n = 4$, $*p < 0.05$). Supplementary Figure 3: microvessel density of brain regions in naïve animals used for autoradiography ($n = 4$). $*p < 0.05$; $**p < 0.01$ Supplementary Figure 4: plot showing correlations between CBF and microvessel density in a subset of animals ($n = 6$) with a gadolinium enhancing rim and nonenhancing core structure. Linear regression lines for each dataset are plotted, showing a trend towards an inverse correlation between CBF and microvessel density for core and rim regions. Supplementary Figure 5: change in theoretical signal saturation over a range of label durations. (*Supplementary Materials*)

References

- [1] F. Collietz, B. Gallez, and B. F. Jordan, "Assessing tumor oxygenation for predicting outcome in radiation oncology: a review of studies correlating tumor hypoxic status and outcome in the preclinical and clinical settings," *Frontiers in Oncology*, vol. 7, p. 10, 2017.
- [2] P. Vaupel and A. Mayer, "Hypoxia in cancer: significance and impact on clinical outcome," *Cancer and Metastasis Reviews*, vol. 26, no. 2, pp. 225–239, 2007.
- [3] R. W. C. Pang and R. T. P. Poon, "Clinical implications of angiogenesis in cancers," *Vascular Health and Risk Management*, vol. 2, no. 2, pp. 97–108, 2006.
- [4] D. C. Alsop, J. A. Detre, X. Golay et al., "Recommended implementation of arterial spin-labeled perfusion MRI for clinical applications: a consensus of the ISMRM perfusion study group and the European consortium for ASL in dementia," *Magnetic Resonance in Medicine*, vol. 73, no. 1, pp. 102–116, 2015.
- [5] D. S. Williams, J. A. Detre, J. S. Leigh, and A. P. Koretsky, "Magnetic resonance imaging of perfusion using spin inversion of arterial water," *Proceedings of the National Academy of Sciences*, vol. 89, no. 1, pp. 212–216, 1992.
- [6] J. A. Detre, J. S. Leigh, D. S. Williams, and A. P. Koretsky, "Perfusion imaging," *Magnetic Resonance in Medicine*, vol. 23, no. 1, pp. 37–45, 1992.
- [7] Y. Sun, N. O. Schmidt, K. Schmidt et al., "Perfusion MRI of U87 brain tumors in a mouse model," *Magnetic Resonance in Medicine*, vol. 51, no. 5, pp. 893–899, 2004.
- [8] A. Vallatos, L. Gilmour, A. J. Chalmers, and W. M. Holmes, "Multiple bolus arterial spin labeling for high signal-to-noise rodent brain perfusion imaging," *Magnetic Resonance in Medicine*, vol. 79, no. 2, pp. 1020–1030, 2018.
- [9] P. Coutinho de Souza et al., "Inhibition of pediatric glioblastoma tumor growth by the anti-cancer agent OKN-007 in orthotopic mouse xenografts," *PLOS ONE*, vol. 10, no. 8, Article ID e0134276, 2015.
- [10] B. Zheng, P. T. H. Lee, and X. Golay, "High-sensitivity cerebral perfusion mapping in mice by kbGRASE-FAIR at 9.4 T," *NMR in Biomedicine*, vol. 23, no. 9, pp. 1061–1070, 2010.
- [11] F. Kober, G. Duhamel, and P. J. Cozzone, "Experimental comparison of four FAIR arterial spin labeling techniques for quantification of mouse cerebral blood flow at 4.7 T," *NMR in Biomedicine*, vol. 21, no. 8, pp. 781–792, 2008.
- [12] G. Duhamel, V. Callot, M. Tachrount, D. C. Alsop, and P. J. Cozzone, "Pseudo-continuous arterial spin labeling at very high magnetic field (11.75 T) for high-resolution mouse brain perfusion imaging," *Magnetic Resonance in Medicine*, vol. 67, no. 5, pp. 1225–1236, 2012.
- [13] L. Hirschler, L. P. Munting, A. Khmelinskii et al., "Transit time mapping in the mouse brain using time-encoded pCASL," *NMR in Biomedicine*, vol. 31, no. 2, p. e3855, 2018.
- [14] L. M. Foley, T. K. Hitchens, P. M. Kochanek, J. A. Melick, E. K. Jackson, and C. Ho, "Murine orthostatic response during prolonged vertical studies: effect on cerebral blood flow measured by arterial spin-labeled MRI," *Magnetic Resonance in Medicine*, vol. 54, no. 4, pp. 798–806, 2005.
- [15] J. Xu, Q. Qin, D. Wu et al., "Steady pulsed imaging and labeling scheme for noninvasive perfusion imaging," *Magnetic Resonance in Medicine*, vol. 75, no. 1, pp. 238–248, 2016.
- [16] Y. Gao, C. L. Goodnough, B. O. Erokwu et al., "Arterial spin labeling-fast imaging with steady-state free precession (ASL-FISP): a rapid and quantitative perfusion technique for high-field MRI," *NMR in Biomedicine*, vol. 27, no. 8, pp. 996–1004, 2014.
- [17] B. P. Chugh, J. Bishop, Y.-Q. Zhou, J. Wu, R. M. Henkelman, and J. G. Sled, "Robust method for 3D arterial spin labeling in mice," *Magnetic Resonance in Medicine*, vol. 68, no. 1, pp. 98–106, 2012.
- [18] D. C. Engel, G. Mies, N. A. Terpolilli et al., "Changes of cerebral blood flow during the secondary expansion of a cortical contusion assessed by 14C-iodoantipyrine autoradiography in mice using a non-invasive protocol," *Journal of Neurotrauma*, vol. 25, no. 7, pp. 739–753, 2008.
- [19] K. Maeda, G. Mies, L. Oláh, and K.-A. Hossmann, "Quantitative measurement of local cerebral blood flow in the anesthetized mouse using intraperitoneal [14C]iodoantipyrine injection and final arterial heart blood sampling," *Journal of Cerebral Blood Flow and Metabolism*, vol. 20, no. 1, pp. 10–14, 2000.
- [20] W. Jiang, W. Gu, K.-A. Hossmann, G. Mies, and P. Wester, "Establishing a photothrombotic 'ring' stroke model in adult mice with late spontaneous reperfusion: quantitative measurements of cerebral blood flow and cerebral protein synthesis," *Journal of Cerebral Blood Flow and Metabolism*, vol. 26, no. 7, pp. 927–936, 2006.
- [21] T. M. Jay, G. Lucignani, A. M. Crane, J. Jehle, and L. Sokoloff, "Measurement of local cerebral blood flow with [14C]iodoantipyrine in the mouse," *Journal of Cerebral Blood Flow and Metabolism*, vol. 8, no. 1, pp. 121–129, 1988.
- [22] C. Leithner, K. Gertz, H. Schröck et al., "A flow sensitive alternating inversion recovery (FAIR)-MRI protocol to measure hemispheric cerebral blood flow in a mouse stroke

- model,” *Experimental Neurology*, vol. 210, no. 1, pp. 118–127, 2008.
- [23] K. Sicard, Q. Shen, M. E. Brevard et al., “Regional cerebral blood flow and BOLD responses in conscious and anesthetized rats under basal and hypercapnic conditions: implications for functional MRI studies,” *Journal of Cerebral Blood Flow and Metabolism*, vol. 23, no. 4, pp. 472–481, 2003.
- [24] C.-X. Li, S. Patel, D. J. J. Wang, and X. Zhang, “Effect of high dose isoflurane on cerebral blood flow in macaque monkeys,” *Magnetic Resonance Imaging*, vol. 32, no. 7, pp. 956–960, 2014.
- [25] T. A. Baskerville, C. McCabe, C. J. Weir, I. M. Macrae, and W. M. Holmes, “Noninvasive MRI measurement of CBF: evaluating an arterial spin labelling sequence with ^{99m}Tc -HMPAO CBF autoradiography in a rat stroke model,” *Journal of Cerebral Blood Flow and Metabolism*, vol. 32, no. 6, pp. 973–977, 2012.
- [26] J. R. Ewing, Y. Cao, R. A. Knight, and J. D. Fenstermacher, “Arterial spin labeling: validity testing and comparison studies,” *Journal of Magnetic Resonance Imaging*, vol. 22, no. 6, pp. 737–740, 2005.
- [27] J. R. Larkin, M. A. Simard, A. A. Khrapitchev et al., “Quantitative blood flow measurement in rat brain with multiphase arterial spin labelling magnetic resonance imaging,” *Journal of Cerebral Blood Flow and Metabolism*, article 0271678X1875621, 2018, In press.
- [28] N. S. Artz, A. L. Wentland, E. A. Sadowski et al., “Comparing kidney perfusion using noncontrast arterial spin labeling MRI and microsphere methods in an interventional swine model,” *Investigative Radiology*, vol. 46, no. 2, pp. 124–131, 2011.
- [29] Y. Jung, E. C. Wong, and T. T. Liu, “Multiphase pseudo-continuous arterial spin labeling (MP-PCASL) for robust quantification of cerebral blood flow,” *Magnetic Resonance in Medicine*, vol. 64, no. 3, pp. 799–810, 2010.
- [30] C. Kilkenny, W. J. Browne, I. C. Cuthill, M. Emerson, and D. G. Altman, “Improving bioscience Research reporting: the ARRIVE guidelines for reporting animal Research,” *PLoS Biology*, vol. 8, no. 6, Article ID e1000412, 2010.
- [31] A. Rohatgi, *WebPlotDigitizer*, 2017, <http://arohatgi.info/webplotdigitizer/app/>.
- [32] T. W. Okell, “Assessment of collateral blood flow in the brain using magnetic resonance imaging,” Doctor of Philosophy Thesis, University of Oxford, Oxford, England, 2011.
- [33] O. Sakurada, C. Kennedy, J. Jehle, J. D. Brown, G. L. Carbin, and L. Sokoloff, “Measurement of local cerebral blood flow with iodo [^{14}C] antipyrine,” *American Journal of Physiology - Heart and Circulatory Physiology*, vol. 234, no. 1, pp. H59–H66, 1978.
- [34] B. Irving, “maskSLIC: regional superpixel generation with application to local pathology characterisation in medical images,” CoRR, 2016, <https://arxiv.org/pdf/1606.09518.pdf>, 2016.
- [35] R. B. Buxton, L. R. Frank, E. C. Wong, B. Siewert, S. Warach, and R. R. Edelman, “A general kinetic model for quantitative perfusion imaging with arterial spin labeling,” *Magnetic Resonance in Medicine*, vol. 40, no. 3, pp. 383–396, 1998.
- [36] M. A. Chappell, A. R. Groves, B. Whitcher, and M. W. Woolrich, “Variational bayesian inference for a non-linear forward model,” *IEEE Transactions on Signal Processing*, vol. 57, no. 1, pp. 223–236, 2009.
- [37] K. E. Andreou, M. S. Soto, D. Allen et al., “Anti-inflammatory microglia/macrophages as a potential therapeutic target in brain metastasis,” *Frontiers in Oncology*, vol. 7, 2017.
- [38] L. Hirschler, C. S. Debacker, J. Voiron et al., “Interpulse phase corrections for unbalanced pseudo-continuous arterial spin labeling at high magnetic field,” *Magnetic Resonance in Medicine*, vol. 79, no. 3, pp. 1314–1324, 2018.
- [39] T. Frietsch, M. H. Maurer, J. Vogel, M. Gassmann, W. Kuschinsky, and K. F. Waschke, “Reduced cerebral blood flow but elevated cerebral glucose metabolic rate in erythropoietin overexpressing transgenic mice with excessive erythrocytosis,” *Journal of Cerebral Blood Flow and Metabolism*, vol. 27, no. 3, pp. 469–476, 2007.
- [40] A. C. Silva, S.-G. Kim, and M. Garwood, “Imaging blood flow in brain tumors using arterial spin labeling,” *Magnetic Resonance in Medicine*, vol. 44, no. 2, pp. 169–173, 2000.
- [41] M. A. Weber, S. Zoubaa, M. Schlieter et al., “Diagnostic performance of spectroscopic and perfusion MRI for distinction of brain tumors,” *Neurology*, vol. 66, no. 12, pp. 1899–1906, 2006.
- [42] X. Hong, L. Liu, M. Wang et al., “Quantitative multiparametric MRI assessment of glioma response to radiotherapy in a rat model,” *Neuro-Oncology*, vol. 16, no. 6, pp. 856–867, 2014.
- [43] R. Schor-Bardach, D. C. Alsop, I. Pedrosa et al., “Does arterial spin-labeling MR imaging-measured tumor perfusion correlate with renal cell cancer response to antiangiogenic therapy in a mouse model?,” *Radiology*, vol. 251, no. 3, pp. 731–742, 2009.
- [44] J. A. Nagy, S. H. Chang, A. M. Dvorak, and H. F. Dvorak, “Why are tumour blood vessels abnormal and why is it important to know?,” *British Journal of Cancer*, vol. 100, no. 6, pp. 865–869, 2009.
- [45] S. Morikawa, P. Baluk, T. Kaidoh et al., “Abnormalities in pericytes on blood vessels and endothelial sprouts in tumors,” *American Journal of Pathology*, vol. 160, no. 3, pp. 985–1000, 2002.
- [46] P. Vajkoczy and M. D. Menger, “Vascular microenvironment in gliomas,” *Journal of Neuro-Oncology*, vol. 50, no. 1–2, pp. 99–108, 2000.

Research Article

Image-Guided Neutron Capture Therapy Using the Gd-DO3A-BTA Complex as a New Combinatorial Treatment Approach

Ki-Hye Jung ¹, Ji-Ae Park ¹, Jung Young Kim ¹, Mi Hyun Kim,¹ Seyoung Oh,¹ Hee-Kyung Kim,² Eun-Ji Choi,³ Han-Jun Kim,³ Sun Hee Do ³, Kyo Chul Lee,¹ Kyeong Min Kim ¹, Yong Jin Lee ¹ and Yongmin Chang ^{4,5}

¹Division of Applied RI, Korea Institute of Radiological and Medical Science, Seoul 139-706, Republic of Korea

²BK21 Plus KNU Biomedical Convergence Program, School of Medicine, Kyungpook National University, Daegu 700-721, Republic of Korea

³College of Veterinary Medicine, Konkuk University, Seoul 05029, Republic of Korea

⁴Department of Molecular Medicine, School of Medicine, Kyungpook National University, Daegu 700-721, Republic of Korea

⁵Department of Radiology, Kyungpook National University Hospital, Daegu 700-721, Republic of Korea

Correspondence should be addressed to Yong Jin Lee; yjlee@kirams.re.kr and Yongmin Chang; ychang@knu.ac.kr

Received 4 June 2018; Revised 17 August 2018; Accepted 30 September 2018; Published 1 November 2018

Guest Editor: Charalampos Tsoumpas

Copyright © 2018 Ki-Hye Jung et al. This is an open access article distributed under the Creative Commons Attribution License, which permits unrestricted use, distribution, and reproduction in any medium, provided the original work is properly cited.

Gadolinium-neutron capture therapy (Gd-NCT) is based on the nuclear capture reaction that occurs when ^{157}Gd is irradiated with low energy thermal neutrons to primarily produce gamma photons. Herein, we investigated the effect of neutron capture therapy (NCT) using a small molecular gadolinium complex, Gd-DO3A-benzothiazole (Gd-DO3A-BTA), which could be a good candidate for use as an NCT drug due to its ability to enter the intracellular nuclei of tumor cells. Furthermore, MRI images of Gd-DO3A-BTA showed a clear signal enhancement in the tumor, and the images also played a key role in planning NCT by providing accurate information on the *in vivo* uptake time and duration of Gd-DO3A-BTA. We injected Gd-DO3A-BTA into MDA-MB-231 breast tumor-bearing mice and irradiated the tumors with cyclotron neutrons at the maximum accumulation time (postinjection 6 h); then, we observed the size of the growing tumor for 60 days. Gd-DO3A-BTA showed good therapeutic effects of chemo-Gd-NCT for the *in vivo* tumor models. Simultaneously, the Gd-DO3A-BTA groups ([Gd-DO3A-BTA(+), NCT(+)]) showed a significant reduction in tumor size ($p < 0.05$), and the inhibitory effect on tumor growth was exhibited in the following order: [Gd-DO3A-BTA(+), NCT(+)] > [Gd-DO3A-BTA(+), NCT(-)] > [Gd-DO3A-BTA(-), NCT(+)] > [Gd-DO3A-BTA(-), NCT(-)]. On day 60, the [Gd-DO3A-BTA(+), NCT(+)] and [Gd-DO3A-BTA(-), NCT(-)] groups exhibited an approximately 4.5-fold difference in tumor size. Immunohistochemistry studies demonstrated that new combinational therapy with chemo-Gd-NCT could treat breast cancer by both the inhibition of tumor cell proliferation and induction of apoptosis-related proteins, with *in vivo* tumor monitoring by MRI.

1. Introduction

Neutron capture therapy (NCT) is a well-known approach to cancer treatment based on the accumulation of neutron capture agents at the tumor site [1], followed by irradiation with thermal neutrons. NCT is a very effective technique for cancer treatment because the thermal neutrons with low energy do not cause damage to normal cells that lack the

neutron capture compounds. This technique thus provides a solution to the major problem of radiation therapy, which is the radiation-induced damage to normal tissue. Therefore, the strategy for the accumulation of NCT compounds specifically within the tumor is critical to avoid damage to normal tissues [2–5].

Gadolinium (^{157}Gd)-based NCT (Gd-NCT) has generated recent interest as a cancer treatment due to the

following merits. (i) The ^{157}Gd atom captures neutrons ($^{157}\text{Gd} + n_{\text{th}} (0.025 \text{ eV}) \rightarrow [^{158}\text{Gd}] \rightarrow ^{158}\text{Gd} + \gamma + 7.94 \text{ MeV}$) across a very large cross section ($\sigma_{\text{th}} = 240,000 \text{ b}$). (ii) The kinetic energy of Gd-NCT, with a mixture of low- and high-energy ionizing particles, is more uniformly distributed throughout tumor tissues, and can be used to solve the shortcomings of heterogeneous *in vivo* dose distribution. (iii) ^{157}Gd complexes are widely developed as magnetic resonance imaging (MRI) contrast agents by chelation chemistry and have been routinely used in clinical applications including Gadovist® (gadobutrol), Dotarem® (gadoterate meglumine) and Omniscan® (gadodiamide) [6]. Gadolinium MRI contrast agents could thus be first considered as NCT agents, but it is difficult to specifically target tumor cells *in vivo*. These agents do not accumulate well in tumor tissue during neutron irradiation after an intravenous injection for therapy, as shown in Table 1. The data show high uptake of the contrast agents into tumor cells at 5 mins, but they exhibit very low uptake at 2 hrs. To obtain success with ^{157}Gd -NCT, ^{157}Gd must be transferred into tumor cells at high concentrations during neutron irradiation. In a previous study, a 50–200 $\mu\text{g } ^{157}\text{Gd/g}$ tumor was reported as an effective cancer treatment.

For the ^{157}Gd neutron capture reaction, the majority of the energy is released as long-range gamma radiation, while, 0.63% of the time, this emission occurs as Auger and conversion electrons. Auger electrons generated from Gd-NCT have strong *in vivo* cytotoxicity by high linear energy transfer (LET), which can induce DNA double-strand breaks (DSB) and restrain the proliferation of tumor cells. Thus, increase in the therapeutic effects is observed when Gd atoms are highly internalized into tumor cells [18, 19].

As therapeutic candidates, various benzothiazoles deserve special attention, as they are known to possess diverse biological properties such as anti-inflammatory, antimicrobial, and anticancer effects. Some of the compounds containing the benzothiazole system are in clinical usage for the treatment of various diseases/disorders [20]. In our previous study, the complexes have not only displayed tumor specificity but also enhanced intracellular MR images of the cytosol and nuclei of a series of tumor cells. The anti-proliferative activity of Gd-DO3A-BTA (Chart 1), which contains a chelating moiety (DO3A) and a chemoagent region (BTA), was demonstrated by determining the *in vitro* growth inhibition values (GI_{50} and TGI) and monitoring tumor volume regression *in vivo*. In particular, Gd-DO3A-BTA has been reported to specifically accumulate intracellularly in tumors arising from MDA-MB-231 breast cancer cells [9, 21]. On the basis of this result, we make attempts to treat *in vivo* tumor tissue by neutron beam irradiation with a medical cyclotron, preserving the high tumor uptake of ^{157}Gd complexes.

2. Results

2.1. *In Vivo* MR Imaging. Figure 1(a) shows the *in vivo* T1-weighted MR images of mice that were injected with Gd-DO3A-BTA (0.1 mmol Gd/kg) via the tail vein. T1-weighted MR images were used because the T1 shortening effect is more dominant at the relatively low Gd concentrations used

(~0.1 mmol Gd/kg). The MR image reveals clear tumor enhancement, which increased for 6 h before gradually decreasing (Figure 1(b)). This result is consistent with the biodistribution data reported in our previous study [9], demonstrating that we can effectively define the starting point of NCT with *in vivo* MR imaging.

2.2. Gd-NCT Inhibited Tumor Growth with Gd-DO3A-BTA.

A small animal study was performed in which mice were irradiated with a neutron beam at 6 h p.i. to determine the optimal time at which the highest uptake of Gd-DO3A-BTA into the tumor tissue occurred. All other tissues, except the tumor tissues, were covered with a plastic box of Teflon to protect them from irregular showering with neutron beams. Figure 2(a) shows the time-course of change in tumor volume after irradiation with neutron beam for 60 days. The Gd-DO3A-BTA-injected and neutron-irradiated mice group ([Gd-DO3A-BTA(+), NCT(+)]) showed a significant decrease in tumor size than the nontreated groups ([Gd-DO3A-BTA(+), NCT(-)], [Gd-DO3A-BTA(-), NCT(+)], and [Gd-DO3A-BTA(-), NCT(-)]). Four groups began to show significant changes in tumor volume on day 15. In particular, the difference between [Gd-DO3A-BTA(+), NCT(+)] and nontreated groups on days 42, 50, and 60 was significant ($p < 0.05$). The tumor growth suppression was observed in the following order: [Gd-DO3A-BTA(+), NCT(+)] > [Gd-DO3A-BTA(+), NCT(-)] > [Gd-DO3A-BTA(-), NCT(+)] > [Gd-DO3A-BTA(-), NCT(-)]. On day 60, [Gd-DO3A-BTA(+), NCT(+)] and [Gd-DO3A-BTA(-), NCT(-)] groups showed an approximately 4.5-fold difference in tumor size. The mean tumor volume (relative tumor volume) of the [Gd-DO3A-BTA(+), NCT(+)] group was 11.99 ± 5.05 , which was much smaller than that in the other groups ($p < 0.05$) on day 60. Due to the tumor suppressive effects of BTA, the antitumor activity of Gd-DO3A-BTA alone (no neutron beam irradiation) was higher than that of neutron irradiation alone. Consistent with earlier reports [10, 22, 23], the neutron irradiation [Gd-DO3A-BTA(-), NCT(+)] alone group also showed some inhibition of tumor growth than the group that did not receive either treatment [Gd-DO3A-BTA(-), NCT(-)]. After irradiation by neutron beams, changes in the body weight of the mice were measured as well as tumor volume. As shown in Figure 2(b), no significant weight loss was observed, suggesting the safety of Gd-DO3A-BTA for NCT. The suppression of tumor growth could be clearly seen from the MR images and morphological findings shown in Figure 3.

2.3. Gd-NCT Inhibited Tumor Cell Proliferation and Induced Tumor Cell Apoptosis with Gd-DO3A-BTA.

The *in vivo* antitumor activity of Gd-DO3A-BTA in NCT was further verified with histological evaluation and immunohistochemistry, as shown in Figure 4. H&E staining of tumor sections showed proliferating tumor cells and necrotic regions. There were no apparent differences in growth patterns and areas of necrosis between groups. To assess the effect of Gd-NCT on tumor suppression and apoptosis, immunohistochemistry for Ki-67, cleaved caspase 3, and caspase 8, as well as TUNEL staining, was performed. The expression of

TABLE 1: Various types of gadolinium agents for NCT.

	Form	Injection route	Injection amount (Gd)	Tumor accumulation Gd/g tumor	Highest uptake time (ICP time)	Reference
Low molecules	Gd-DTPA	i.t.	1200 $\mu\text{g}/\text{mouse}$	451 $\mu\text{g}/\text{g}$ 5.3 $\mu\text{g}/\text{g}$	5 min 24 h	[7]
	Gd-DTPA	i.v.	0.1 mmol/kg	70.39 \pm 8.75 $\mu\text{g}/\text{g}$ 30.22 \pm 4.91 $\mu\text{g}/\text{g}$	5 min 2 h	[8]
	Gd-BOPTA	i.v.	0.1 mmol/kg	100.33 \pm 7.91 $\mu\text{g}/\text{g}$ 40.93 \pm 1.83 $\mu\text{g}/\text{g}$	5 min 2 h	[8]
	Gd-DO3A-BTA	i.v.	0.1 mmol/kg	221 $\mu\text{g}/\text{g}$	6 h	[9]
Nanoparticles	Liposome	i.v.	N/D	40.277 \pm 2.512 $\mu\text{g}/\text{g}$	2 h	[10]
	Liposome	i.v.	20 mg/kg	158.8 \pm 115.6 $\mu\text{g}/\text{g}$	12 h	[11, 12]
	Lipid emulsions	i.p.	6 mg/hamster	107 $\mu\text{g}/\text{g}$	48 h	[13]
	Micelles	i.v.	0.02 mmol/kg	3.9% ID/g ^a	10 h	[14]
	Lipid NPs	i.v.	6 mg/hamster	100.7 $\mu\text{g}/\text{g}$	12 h	[15]
	Chitosan NPs	i.t.	2.4 mg/mouse ^b	1766 \pm 96 $\mu\text{g}/\text{tumor tissue}^c$	8 h	[16, 17]
	Chitosan NPs	i.t.	1200 $\mu\text{g}/\text{mouse}$	897.1 $\mu\text{g}/\text{g}$	24 h	[7]

N/D: not determined; i.t.: intratumoral; i.v.: intravenous; i.p.: intraperitoneal. ^aID/g: percentages of the total injected dose per organ weight. ^bAdministered twice by i.t. injection 24 h and 8 h before the assay. ^cThe Gd content in melanoma tissue in mice.

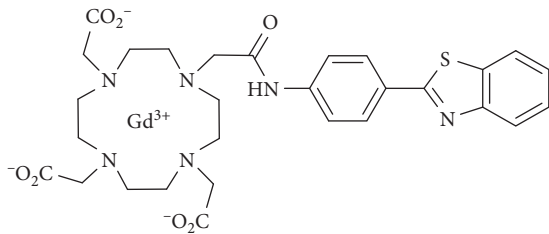


CHART 1: Structure of Gd-DO3A-BTA.

the proliferation marker Ki-67 was significantly decreased in the [Gd-DO3A-BTA(+), NCT(+)] group compared to that of the [Gd-DO3A-BTA(-), NCT(-)] group. All irradiated groups including [Gd-DO3A-BTA(+), NCT(+)] and [Gd-DO3A-BTA(-), NCT(+)] showed a decrease in Ki-67 expression, indicating that the neutron beam irradiation has tumor suppressive effects. In addition, the [Gd-DO3A-BTA(+), NCT(-)] group also showed decreased Ki-67 expression, implying the antitumor activity of BTA without neutron beam irradiation. Caspase 8 acts as an initiator of apoptosis and is involved in the extrinsic pathway, whereas caspase 3 acts as an effector of apoptosis [24]. The expression of cleaved caspase 3 and 8 did not show significant differences between groups. However, the expressions of both cleaved caspase 3 and 8 were slightly increased in the irradiated groups [Gd-DO3A-BTA(+), NCT(+)] and [Gd-DO3A-BTA(-), NCT(+)] compared to that in the nonirradiated [Gd-DO3A-BTA(+), NCT(-)] and [Gd-DO3A-BTA(-), NCT(-)] groups. Moreover, the evaluation of apoptotic cell death by TUNEL staining revealed that the percentage of cells undergoing apoptosis was greater in all treated groups, including the [Gd-DO3A-BTA(+), NCT(+)] group. These results correlate with the finding that the [Gd-DO3A-BTA(+), NCT(+)] group had the smallest tumor volumes, suggesting that the reduced Ki-67 activity and increased apoptotic cell death

after BTA injection and neutron beam irradiation induced tumor growth suppression.

3. Discussion

For the success of Gd-NCT as a therapeutic modality for cancer, it is important to effectively deliver and sufficiently accumulate Gd into tumors. For an effective *in vivo* Gd-NCT, an optimal dose of 50–200 $\mu\text{g}\cdot\text{Gd}/\text{g}$ tumor tissue has been reported [11, 25]. As shown in Table 1, 0.1 mmol/kg of Gd-DO3A-BTA administered as an intravenous injection resulted in approximately 221 μg of Gd/g tumor tissue [9]. This uptake was approximately 1.4 times higher than that reported previously (158 $\mu\text{g}\cdot\text{Gd}/\text{g}$ tumor tissue) with an intravenous injection of Gd-DTPA-encapsulated liposomes [11, 12].

Various nano-based formulations have been developed to deliver sufficient amounts of Gd into tumor cells for Gd-NCT, and these include nanoparticles [15–17, 26–28], liposomes [10, 11, 12], emulsions [13, 29], and microcapsules [7, 30]. Most of these particles were designed to be approximately 100 nm in size to avoid high uptake by the reticuloendothelial system (RES). However, these particles have limited specific tumor targeting ability, since their delivery completely depends on the enhanced permeability and retention (EPR) effect around tumor sites [11, 14, 31]. Furthermore, these nanoparticles often show high *in vivo* instability by releasing Gd from the nano-based formulations due to the high solubility of Gd-DTPA in an aqueous solution [11, 13, 15]. Therefore, some nano-based formulations for Gd-NCT use a lipophilic complex such as Gd-DTPA/pLL or Gd-acetylacetonate (Gd-acac) to prevent the possible release of Gd [11, 29]. However, as shown in Table 1, these nano-based formulations can be injected only by intraperitoneal or intratumoral methods and cannot be administered intravenously.

Gd-DO3A-BTA, however, is readily administered intravenously. Furthermore, Gd-DO3A-BTA has a relatively

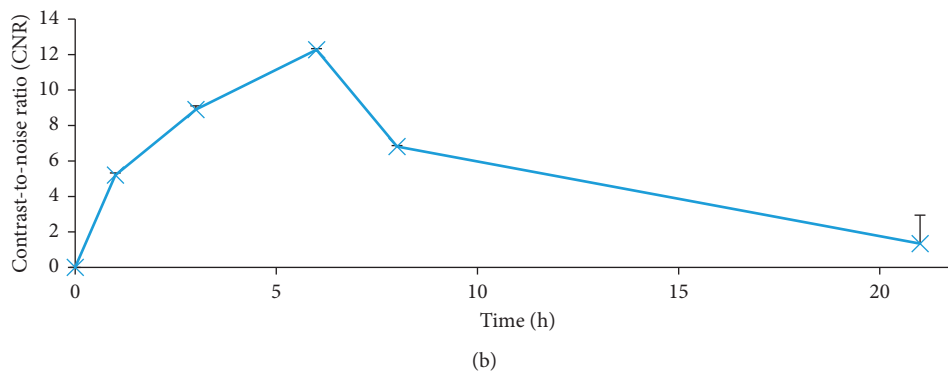
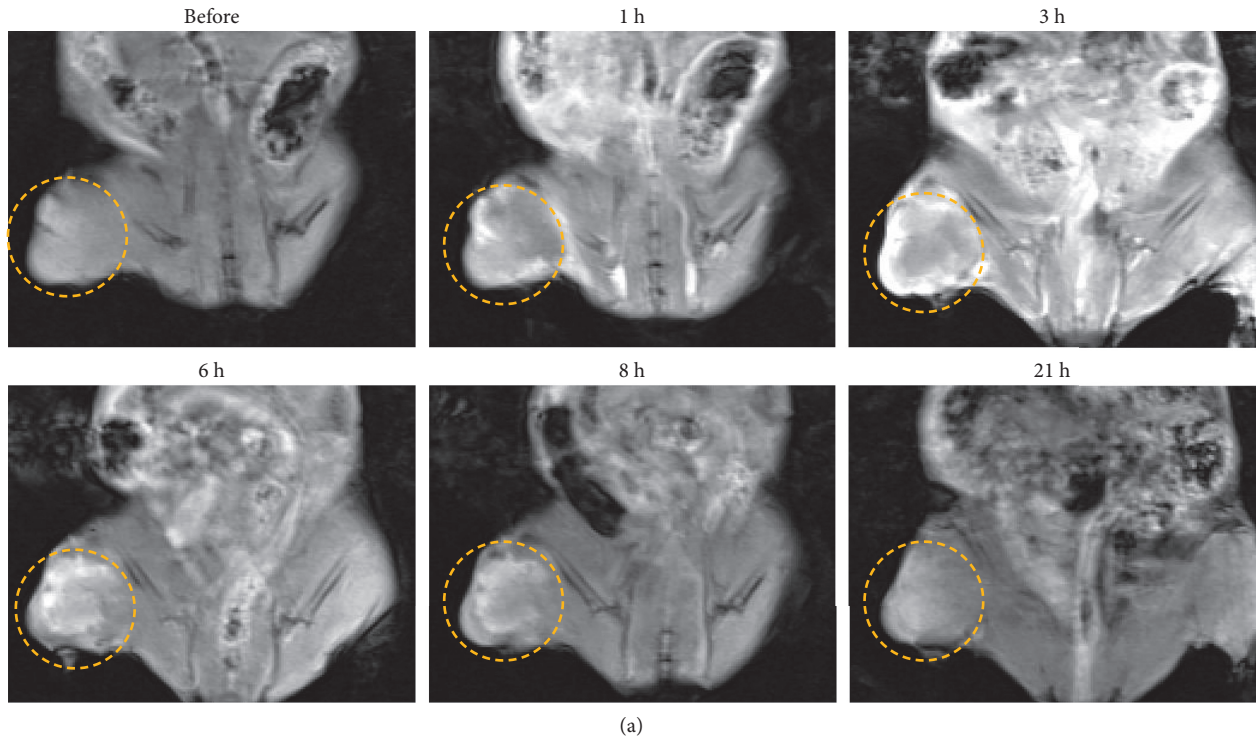


FIGURE 1: (a) *In vivo* MR images of nude mice with MDA-MB-231 tumors after intravenous injection of Gd-DO3A-BTA. Tumors are indicated with circles. (b) Contrast-to-noise ratio (CNR) as a function of time.

small molecular weight (M.W. 767) and high chemical stability, which makes it a better tumor-theranostic agent for MR image-guided NCT with a good therapeutic dosage for clinical use. However, for the success of Gd-NCT, Gd must be transferred into tumors at high concentrations during neutron irradiation. The MR imaging data demonstrated that Gd-DO3A-BTA preferentially accumulated in tumor tissue *in vivo*. Gd-DO3A-BTA delivers more Gd to tumor tissue than conventional Gd-based MRI contrast agents, which may result in a more efficient uptake by the tumor. The effective tumor ablation by Gd-DO3A-BTA could therefore be associated with the high accumulation of Gd in tumor tissue, which in turn captures sufficient thermal neutrons to kill the tumor. Although enriched ^{157}Gd compound would be preferable for Gd-NCT, in this experiment, we utilized the natural Gd compound. The natural abundance of ^{157}Gd is only 15.65%, while enriched compounds may contain up to 90% ^{157}Gd [20]. Therefore, in the

near future, it would be important to perform Gd-NCT experiment with enriched ^{157}Gd compounds to confirm the current results using the natural Gd compound. The tumors in mice that were irradiated and injected with Gd-DO3A-BTA were much smaller than those observed in other groups, demonstrating that the Gd-DO3A-BTA could significantly enhance the therapeutic effect of Gd-NCT. In addition, the tumor-therapeutic effects of Gd-DO3A-BTA in combination with NCT were confirmed by MR imaging and histological evaluation. Furthermore, the tumor suppressive effects were evident even after 60 days, suggesting that early treatment of the tumor with a Gd-DO3A-BTA injection, and NCT has the potential to suppress further tumor progression. However, the limitation of the current study should be mentioned. In this study, the neutron beam was generated by irradiating a proton beam upon a beryllium target using an MC-50 cyclotron, and the thermal neutron flux was low. Because the high flux of thermal neutrons is usually used for

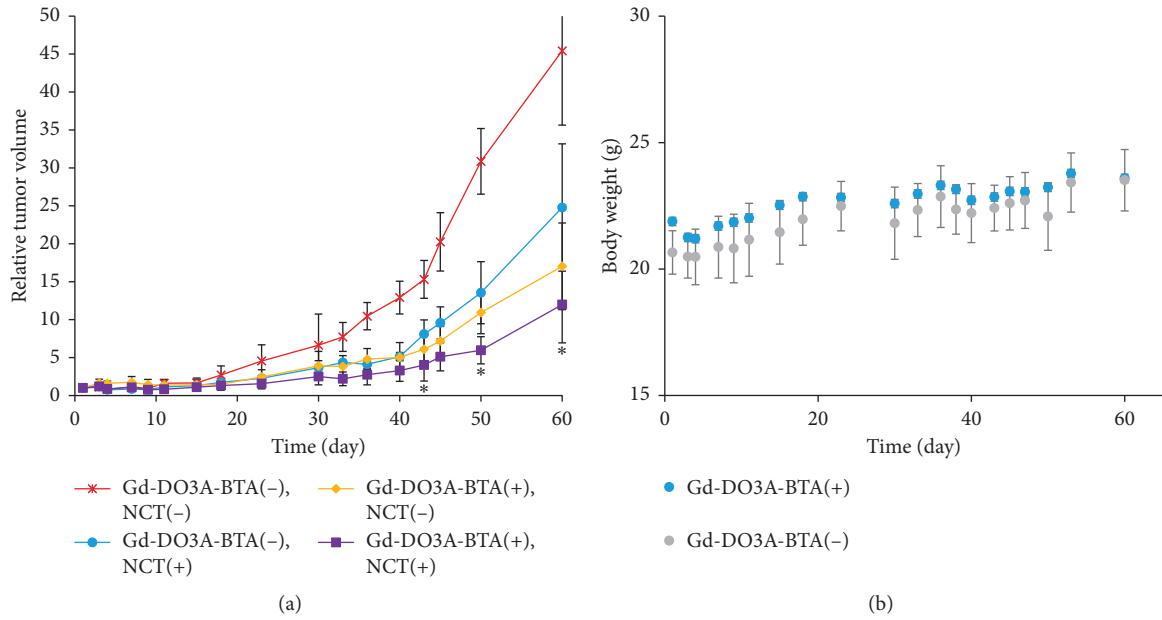


FIGURE 2: (a) Time-course changes in the relative tumor volume after neutron irradiation. Data are expressed as the mean \pm SD ($n = 5$), * $p < 0.05$ compared to other groups. (b) Relative changes in the body weight of the mice.

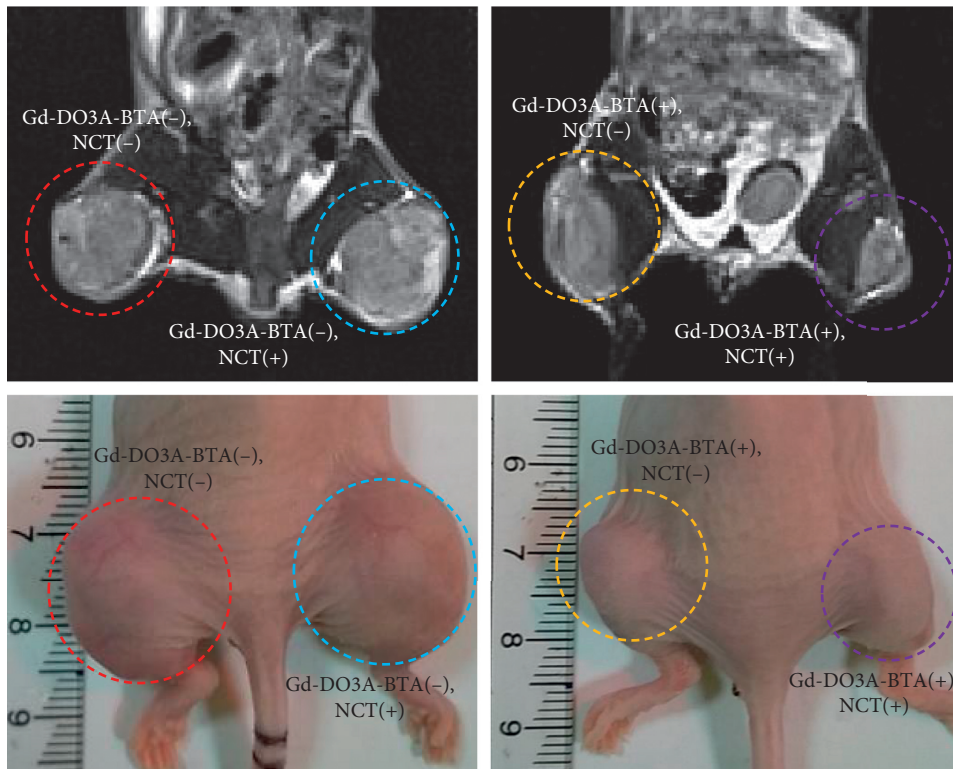
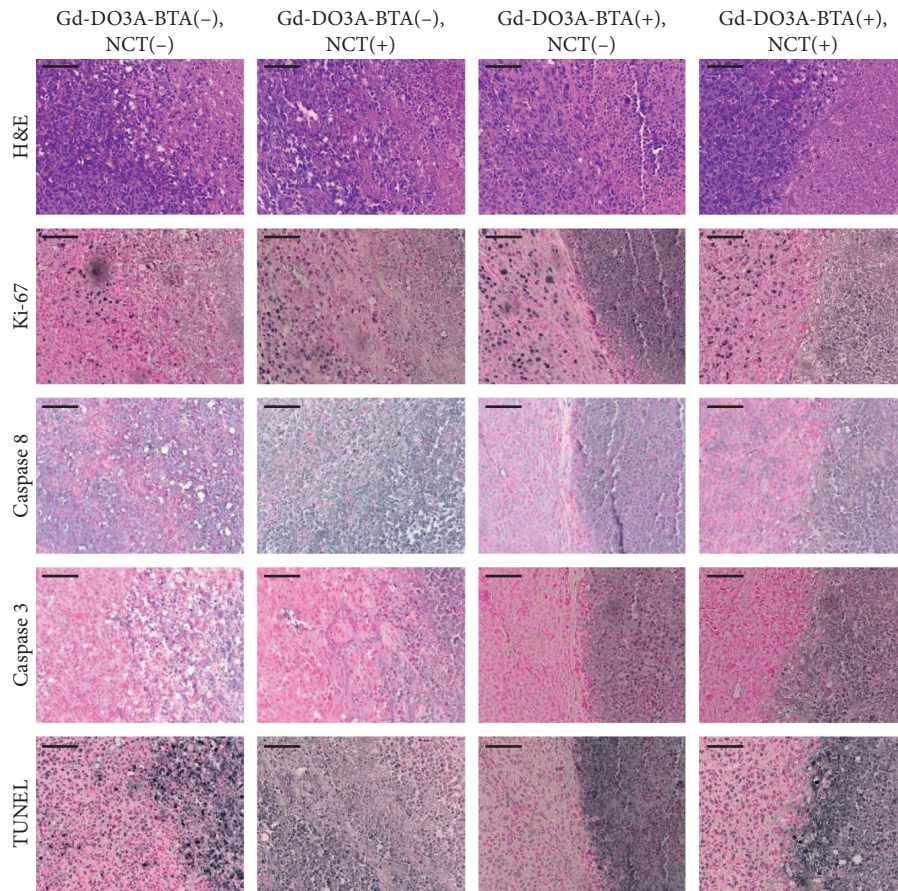


FIGURE 3: MRI (above) and morphological findings (below) of tumors at 60 days after Gd-NCT. [Gd-DO3A-BTA(+), NCT(+)], Gd-DO3A-BTA administered and neutron irradiated; [Gd-DO3A-BTA(+), NCT(-)], Gd-DO3A-BTA administered and non-neutron irradiated; [Gd-DO3A-BTA(-), NCT(+)], non-Gd administered and neutron irradiated; [Gd-DO3A-BTA(-), NCT(-)], non-Gd administered and non-neutron irradiated.



(a)

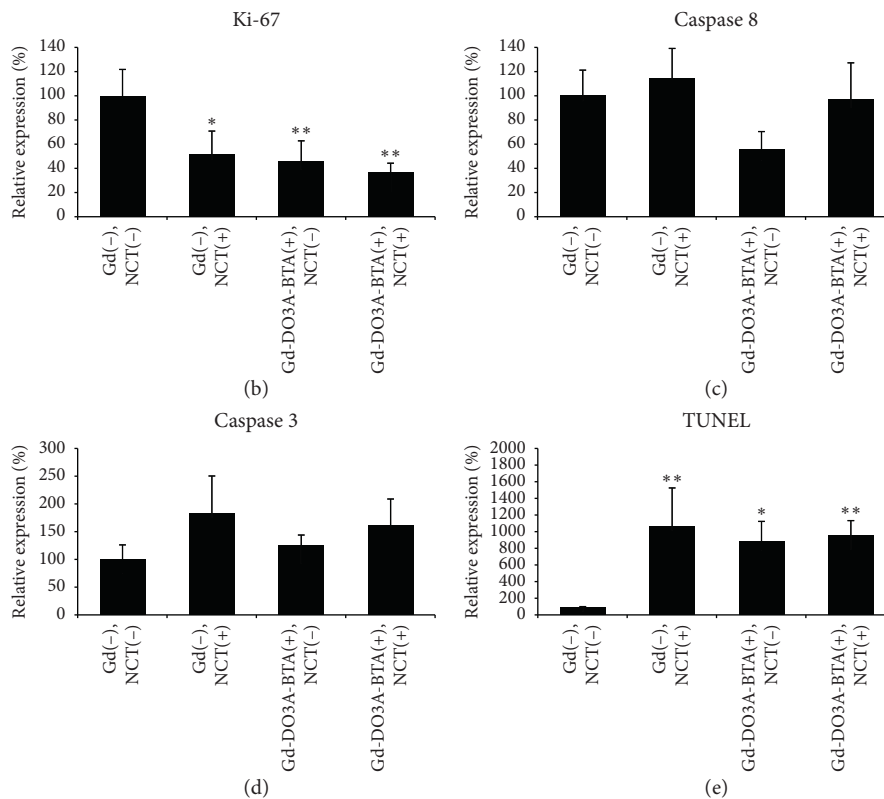


FIGURE 4: (a) Representative images of hematoxylin and eosin (H&E) staining and immunohistochemical staining of Ki-67, caspase 3, caspase 8, and TUNEL in tumor samples. Graphic plots show an increase in apoptotic cells as determined by (b) Ki-67, (c) caspase 8, (d) caspase 3, and (e) TUNEL staining in Gd-NCT. Scale bars on the images represent 100 μ m. * $p < 0.05$; ** $p < 0.01$ compared to [Gd-DO3A-BTA(-), NCT(-)].

NCT, it is necessary to perform NCT experiment with low energy neutron at high flux to be sure that the effect shown in the current study is due to NCT.

4. Conclusions

The present study presented the potential for Gd-NCT using low molecular weight Gd chelate as a new combinatorial chemo-NCT approach in cancer treatment. Despite the simple chemical structure of the metal complex, Gd-DO3A-BTA shows a high therapeutic effect when used in Gd-NCT against solid tumors. The high accumulation of Gd-DO3A-BTA in tumor tissues effectively damaged the tumor cells. Furthermore, as an MR contrast agent, Gd-DO3A-BTA can guide NCT and monitor tumor growth via MR imaging.

5. Materials and Methods

5.1. General. The Gd-DO3A-BTA (nonenriched Gd) was prepared as described previously [10, 21]. All animal experiments were conducted in compliance with the Guidelines for the Care and Use of Research Animals under protocols approved by the Korea Institute of Radiological and Medical Sciences (KIRAMS) Animal Studies Committee. The neutron beam irradiations including low content thermal neutrons were performed using an MC-50 cyclotron (Scanditronix, Sweden, 1985). When the neutron beam was generated by irradiating a proton beam ($20\ \mu\text{A}$, 35 MeV) upon a beryllium target of 15 mm thickness, the following results were previously reported: the thermal neutron (0.24% of total neutrons) flux was approximately $1.94 \times 10^4\ \text{n/cm}^2\text{-sec}$ and the cross section was 13.79 ± 0.45 barn (a). At that time, the absorbed dose of neutron beams was 9.36–8.69 cGy/min (including the gamma ray of 1.42–1.57 cGy/min) at the depth of 15–30 mm with the field size of $26 \times 26\ \text{cm}^2$ (b). The irradiation time of neutron beams in our studies was typically performed as the standard point of approximately 1 Gy/12 min [32, 33].

5.2. Tumor Model. The human breast adenocarcinoma cancer cell line MDA-MB-231 (ATCC CRM-HTB-26) was purchased from the American Type Culture Collection (ATCC). MDA-MB-231 is a highly aggressive, invasive, and poorly differentiated triple-negative breast cancer (TNBC; estrogen receptor (ER), progesterone receptor (PR), and HER2 (human epidermal growth factor receptor 2)) cell line. The cells were maintained in RPMI-1640 containing 10% fetal bovine serum (FBS) and 1% antibiotics and were grown in a humidified incubator at 37°C and 5% CO_2 . MDA-MB-231 tumor cells ($1 \times 10^8\ \text{cells}\cdot\text{mL}^{-1}$) suspended in RPMI-1640 medium without FBS, and antibiotics were injected into the subcutaneous tissue (sc) of female BALB/c nude mice (aged 6 weeks, 18–25 g of body weight) in both legs. One week after tumor cell implantation, the mice were divided into two groups ($n = 5/\text{group}$). To compare the effect of chemotherapy and NCT on solid tumor, the mice were administered (A) none or (B) Gd-DO3A-BTA (0.1 mmol/kg) intravenously through the tail vein. Only the right-sided tumors were irradiated by neutrons.

5.3. In Vivo MR Imaging. The mice were anesthetized with 1.5% isoflurane in oxygen. Tumor measurements were made before and after injection of 0.1 mmol-Gd/kg via the tail vein. MR images were taken with a 3 T MR unit (Magnetom Tim Trio, Siemens Medical solution, Erlangen, Germany) using an animal coil. The T1-weighted fast spin-echo imaging was performed under the following conditions: repetition time = 9.9 ms; echo time = 3.2 ms; 10 mm field of view; 256×256 matrix size; 1 mm slice thickness; and average = 3.

The contrast to noise ratio (CNR) was defined as the difference in signal-to-noise ratio (SNR) between adjacent anatomic structures.

$$\text{CNR} = \text{SNR}_{\text{post}} - \text{SNR}_{\text{pre}}. \quad (1)$$

5.4. In Vivo Gd-NCT. Gd-DO3A-BTA was administered intravenously as a bolus (0.1 mmol/kg) into the tail vein of female mice with MDA-MB-231 tumors. After 6 h, the mice were locally irradiated on one side with a 0.3 Gy neutron beam, while the other side was shielded using Teflon as shown. Figure 5 shows the overall experimental scheme for Gd-NCT. The tumor size was measured before and after irradiation, and the volume (V) was calculated using the following equation:

$$V = \frac{a \times b^2}{2}, \quad (2)$$

where a and b are the major and minor axes of the tumor measured by a caliper.

5.5. Tissue Preparation and Histological Evaluation. The animals were sacrificed after 60 days, and tumor tissues were obtained. The samples were fixed in 10% neutral buffered formalin, processed, and embedded in paraffin, according to standard procedures. The sections were then stained with hematoxylin and eosin (H&E) using an automated processor (Tissue-Tek, PrismaE2, Sakura, Japan). The images were acquired using a digital scanner (Panoramic MIDI, 3D HISTECH Ltd, Hungary).

5.6. Immunohistochemical Analysis. The tumor samples were serially sectioned ($4\ \mu\text{m}$ sections), deparaffinized, and rehydrated. The sections were incubated in 0.3% hydrogen peroxide to quench the endogenous peroxidase after antigen retrieval by heating in 10 mM citrate buffer (pH 6.0). The immunohistochemistry was performed according to the avidin-biotinylated-HRP complex (ABC) method using the Vectastain Elite ABC kit (Vector Laboratories, Burlingame, CA, USA). The primary antibodies used were Ki-67 and caspase 8 (both 1:100, Abcam, Cambridge, MA, USA) and caspase 3 (1:100, Santa Cruz, Santa Cruz, CA, USA). Apoptosis was assessed by terminal deoxynucleotidyl transferase-mediated dUTP nick-end labeling (TUNEL; Roche Diagnostics, Indianapolis, IN, USA) according to the manufacturer's instructions. All immunohistochemistry reactions and TUNEL staining were visualized by Vector SG (Vector Laboratories) and counterstained with fast nuclear

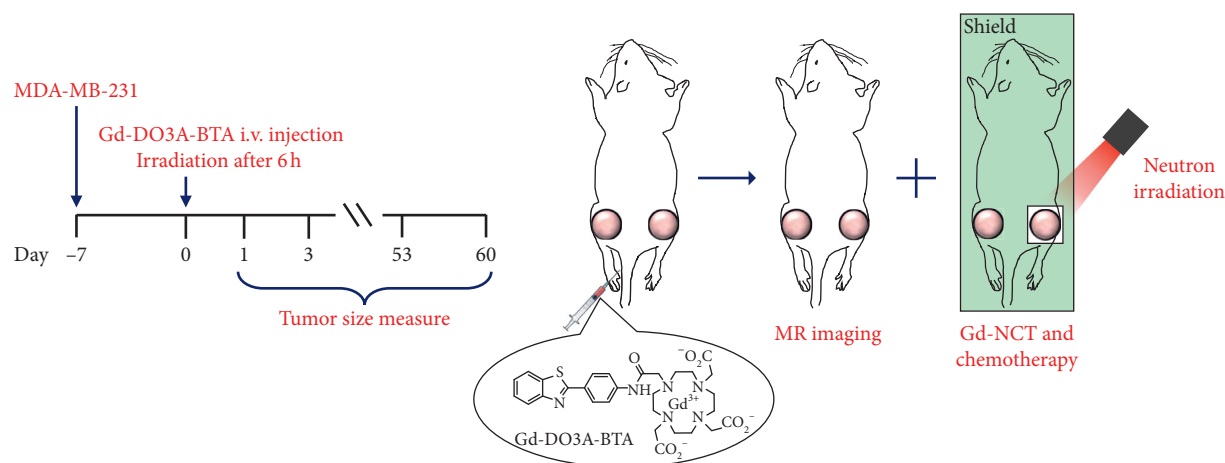


FIGURE 5: Schematic illustration of *in vivo* Gd-NCT. Except for the right tumor region irradiated by neutrons, the whole body was shielded by Teflon.

solutions (Vector Laboratories). Staining was quantified using ImageJ image analysis software (NIH, Bethesda, MD, USA).

5.7. Statistical Analysis. Data in the manuscript are expressed as the mean and standard deviation (SD), and the significance of the results was analyzed by Student's *t*-test. $p < 0.05$ was considered statistically significant.

Data Availability

The data used to support the findings of this study are included within the article.

Conflicts of Interest

The authors declare that they have no conflicts of interest.

Acknowledgments

This study was supported by a grant from the Korea Institute of Radiological and Medical Sciences (KIRAMS) funded by the Ministry of Science, ICT and Future Planning, Republic of Korea. (no. 50532–2018). This work was also supported by the Basic Research Laboratory (BRL) Program (2013R1A4A1069507) and by the Basic Science Research Program (2017R1A2B3003214) through the National Research Foundation funded by the Ministry of Science, ICT and Future Planning.

References

- [1] R. M. Brugger and J. A. Shih, "Evaluation of gadolinium-157 as a neutron capture therapy agent," *Strahlentherapie und Onkologie*, vol. 165, no. 2-3, pp. 153–156, 1989.
- [2] C. Salt, A. J. Lennox, M. Takagaki, J. A. Maguire, and N. S. Hosmane, "Boron and gadolinium neutron capture therapy," *Russian Chemical Bulletin*, vol. 53, no. 9, pp. 1871–1888, 2004.
- [3] P. Mi, H. Yanagie, N. Dewi et al., "Block copolymer-boron cluster conjugate for effective boron neutron capture therapy of solid tumors," *Journal of Controlled Release*, vol. 254, pp. 1–9, 2017.
- [4] R. F. Barth, M. G. H. Vicente, O. K. Harling et al., "Current status of boron neutron capture therapy of high grade gliomas and recurrent head and neck cancer," *Radiation Oncology*, vol. 7, no. 1, pp. 146–167, 2012.
- [5] R. F. Barth, Z. Zhang, and T. Liu, "A realistic appraisal of boron neutron capture therapy as a cancer treatment modality," *Cancer Communications*, vol. 38, no. 1, pp. 1–7, 2018.
- [6] Z. Zhou and Z.-R. Lu, "Gadolinium-based contrast agents for magnetic resonance cancer imaging," *Wiley Interdisciplinary Reviews: Nanomedicine and Nanobiotechnology*, vol. 5, no. 1, pp. 1–18, 2013.
- [7] H. Tokumitsu, H. Ichikawa, and Y. Fukumori, "Chitosan-gadopentetic acid complex nanoparticles for gadolinium neutron-capture therapy of cancer: preparation by novel emulsion-droplet coalescence technique and characterization," *Pharmaceutical Research*, vol. 16, no. 12, pp. 1830–1835, 1999.
- [8] T. Zhang, A. Matsumura, T. Yamamoto, F. Yoshida, and T. Nose, "Comparison of gadobenate dimeglumine and gadopentetate Dimeglumine: a study of MR imaging and inductively coupled plasma atomic emission spectroscopy in rat brain tumors," *American Journal of Neuroradiology*, vol. 23, no. 1, pp. 15–18, 2002.
- [9] H. K. Kim, M. K. Kang, K. H. Jung et al., "Gadolinium complex of DO3A-benzothiazole aniline (BTA) conjugate as a theranostic agent," *Journal of Medicinal Chemistry*, vol. 56, no. 20, pp. 8104–8111, 2013.
- [10] N. Dewi, H. Yanagie, H. Zhu et al., "Tumor growth suppression by gadolinium-neutron capture therapy using gadolinium-entrapped liposome as gadolinium delivery agent," *Biomedicine and Pharmacotherapy*, vol. 67, no. 6, pp. 451–457, 2013.
- [11] U. M. Le and Z. Cui, "Long-circulating gadolinium-encapsulated liposomes for potential application in tumor neutron capture therapy," *International Journal of Pharmaceutics*, vol. 312, no. 1-2, pp. 105–112, 2006.
- [12] U. M. Le and Z. Cui, "Biodistribution and tumor-accumulation of gadolinium (Gd) encapsulated in long-circulating liposomes in tumor-bearing mice for potential neutron capture therapy," *International Journal of Pharmaceutics*, vol. 320, no. 1-2, pp. 96–103, 2006.

- [13] M. M. Iyamoto, K. H. Irano, H. I. Chikawa, Y. F. Ukumori, and Y. A. Kine, "Biodistribution of gadolinium incorporated in lipid emulsions intraperitoneally administered for neutron-capture therapy with tumor-bearing hamsters," *Biological and Pharmaceutical Bulletin*, vol. 22, no. 12, pp. 1331–1340, 1999.
- [14] P. Mi, N. Dewi, H. Yanagie et al., "Hybrid calcium phosphate-polymeric micelles incorporating gadolinium chelates for imaging-guided gadolinium neutron capture tumor therapy," *ACS Nano*, vol. 9, no. 6, pp. 5913–5921, 2015.
- [15] N. Dewi, P. Mi, H. Yanagie, and Y. Sakurai, "In vivo evaluation of neutron capture therapy effectivity using calcium phosphate-based nanoparticles as Gd-DTPA delivery agent," *Journal of Cancer Research and Clinical Oncology*, vol. 142, no. 4, pp. 767–775, 2016.
- [16] H. Ichikawa, T. Uneme, T. Andoh, Y. Arita, and T. Fujimoto, "Gadolinium-loaded chitosan nanoparticles for neutron-capture therapy: influence of micrometric properties of the nanoparticles on tumor-killing effect," *Applied Radiation and Isotopes*, vol. 88, pp. 109–113, 2014.
- [17] H. Tokumitsu, J. Hiratsuka, Y. Sakurai, T. Kobayashi, H. Ichikawa, and Y. Fukumori, "Gadolinium neutron-capture therapy using novel gadopentetic acid-chitosan complex nanoparticles: in vivo growth suppression of experimental melanoma solid tumor," *Cancer Letters*, vol. 150, no. 2, pp. 177–182, 2000.
- [18] A. Narmani, B. Farhood, H. Haghi-aminjan, and T. Mortezaadeh, "Gadolinium nanoparticles as diagnostic and therapeutic agents: their delivery systems in magnetic resonance imaging and neutron capture therapy," *Journal of Drug Delivery Science and Technology*, vol. 44, pp. 457–466, 2018.
- [19] G. de Stasio, P. Casalbore, R. Pallini et al., "Gadolinium in human glioblastoma cells for gadolinium neutron capture therapy," *Cancer research*, vol. 61, no. 10, pp. 4272–4277, 2001.
- [20] A. Kamal, M. A. H. Syed, and S. M. Mohammed, "Therapeutic potential of benzothiazoles: a patent review (2010–2014)," *Expert Opinion on Therapeutic Patents*, vol. 25, no. 3, pp. 335–349, 2015.
- [21] K. H. Jung, S. H. Kang, M. K. Kang et al., "Synthesis and structure-activity relationships of gadolinium complexes of DO3A-benzothiazole conjugates as potential theranostic agents," *European Journal of Inorganic Chemistry*, vol. 2015, no. 4, pp. 599–604, 2015.
- [22] P. C. Burge, F. Stephen Vogel, S. B. Green, and T. A. Strike, "Glioblastoma multiforme and anaplastic astrocytoma pathologic criteria and prognostic implications," *Cancer*, vol. 56, no. 5, pp. 1106–1111, 1985.
- [23] J. M. Bruner, "Neuropathology of malignant gliomas," *Seminars in Oncology*, vol. 21, no. 2, pp. 126–138, 1994.
- [24] B. A. Edadah and A. I. Faden, "Caspase pathways, neuronal apoptosis, and CNS injury," *Journal of Neurotrauma*, vol. 17, no. 10, pp. 811–829, 2000.
- [25] J. Shih and R. Brugger, "Gadolinium as a neutron capture therapy agent," *Medical Physics*, vol. 19, no. 3, pp. 733–744, 1992.
- [26] T. Watanabe, H. Ichikawa, and Y. Fukumori, "Tumor accumulation of gadolinium in lipid-nanoparticles intravenously injected for neutron-capture therapy of cancer," *European Journal of Pharmaceutics and Biopharmaceutics*, vol. 54, no. 2, pp. 119–124, 2002.
- [27] F. Shikata, H. Tokumitsu, H. Ichikawa, and Y. Fukumori, "In vitro cellular accumulation of gadolinium incorporated into chitosan nanoparticles designed for neutron-capture therapy of cancer," *European Journal of Pharmaceutics and Biopharmaceutics*, vol. 53, no. 1, pp. 57–63, 2002.
- [28] D. Alberti, N. Protti, M. Franck et al., "Theranostic nanoparticles loaded with imaging probes and rubrocurcumin for combined cancer therapy by folate receptor targeting," *ChemMedChem*, vol. 12, no. 7, pp. 502–509, 2017.
- [29] A. M. Dierling, B. R. Sloat, and Z. Cui, "Gadolinium incorporated reconstituted chylomicron emulsion for potential application in tumor neutron capture therapy," *European Journal of Pharmaceutics and Biopharmaceutics*, vol. 62, no. 3, pp. 275–281, 2006.
- [30] K. J. Ono, H. I. Chikawa, K. F. Ujioka, Y. F. Ukumori, and Y. A. Kine, "Preparation of lecithin microcapsules by a dilution method using the wurster process for intraarterial administration in gadolinium neutron capture therapy," *Chemical and Pharmaceutical Bulletin*, vol. 47, no. 1, pp. 54–63, 1999.
- [31] M. R. Longmire, M. Ogawa, P. L. Choyke, and H. Kobayashi, "Biologically optimized nanosized molecules and particles: more than just size," *Bioconjugate Chemistry*, vol. 22, no. 6, pp. 993–1000, 2011.
- [32] S. Park and N. H. Jang, "Estimation and calibration of thermal neutron flux for neutron activation analysis," *Bulletin of the Korean Chemical Society*, vol. 27, no. 12, pp. 2061–2063, 2006.
- [33] K.-Y. Eom, H.-G. Wu, H. J. Park et al., "Evaluation of biological characteristics of neutron beam generated from MC50 cyclotron," *Journal of the Korean Society for Therapeutic Radiology and Oncology*, vol. 24, no. 4, pp. 280–284, 2006.

Research Article

Multimodal PET/MRI Imaging Results Enable Monitoring the Side Effects of Radiation Therapy

Noémi Kovács,¹ Krisztián Szigeti ,² Nikolett Hegedűs ,² Ildikó Horváth,²
Dániel S Veres ,² Michael Bachmann,³ Ralf Bergmann,³ and Domokos Máthé ^{1,2}

¹CROmed Translational Research Centers, H-1047 Budapest, Hungary

²Department of Biophysics and Radiation Biology, Semmelweis University, H-1094 Budapest, Hungary

³Helmholtz-Zentrum Dresden-Rossendorf, Institute of Radiopharmaceutical Cancer Research, 01328 Dresden, Germany

Correspondence should be addressed to Krisztián Szigeti; szigeti.krisztian@med.semmelweis-univ.hu

Received 24 May 2018; Revised 12 September 2018; Accepted 10 October 2018; Published 1 November 2018

Guest Editor: Pablo Aguiar

Copyright © 2018 Noémi Kovács et al. This is an open access article distributed under the Creative Commons Attribution License, which permits unrestricted use, distribution, and reproduction in any medium, provided the original work is properly cited.

Radiotherapy is one of the most frequently applied treatments in oncology. Tissue-absorbed ionizing radiation damages not only targeted cells but the surrounding cells too. The consequent long-term induced oxidative stress, irreversible tissue damage, or second malignancies draw attention to the urgent need of a follow-up medical method by which personalized treatment could be attained and the actually dose-limiting organ could be monitored in the clinical practice. We worked out a special hemisphere irradiation technique for mice which mimics the radiation exposure during radiotherapy. We followed up the changes of possible brain imaging biomarkers of side effects, such as cerebral blood flow, vascular endothelial function, and cellular metabolic processes for 60 days. BALB/c mice were divided into two groups ($n = 6$ per group) based on the irradiation doses (5 and 20 Gy). After the irradiation procedure arterial spin labeling (ASL), diffusion-weighted imaging (DWI) in magnetic resonance modality and [¹⁸F]fluoro-deoxy-D-glucose positron emission tomography (FDG-PET) scans of the brain were obtained at several time points (3, 7, 30, and 60 days after the irradiation). Significant physiological changes were registered in the brain of animals following the irradiation by both applied doses. Elevated standard uptake values were detected all over the brain by FDG-PET studies 2 months after the irradiation. The apparent diffusion coefficients from DWI scans significantly decreased one month after the irradiation procedure, while ASL studies did not show any significant perfusion changes in the brain. Altogether, our sensitive multimodal imaging protocol seems to be an appropriate method for follow-up of the health status after radiation therapy. The presented approach makes possible parallel screening of healthy tissues and the effectiveness of tumor therapy without any additional radiation exposure.

1. Introduction

Radiotherapy is one of the most widely spread anticancer treatments in the field of clinical oncology. The paradigm of radiotherapy declares the therapeutic effect is based on indirect and direct DNA damages [1, 2]. Although every cell has well-developed repair mechanisms for DNA impairments, the less-differentiated cancerous cells have diminished ability to repair their broken DNA double-strand based on their uncontrolled and fast reproduction. This unique physiological property serves as the base of radiation therapy where the accumulated absorbed dose determines

the severity of the evolving damages (slowed down reproduction, necrosis, or cell death) [1].

Shortly after the exposure, enhanced reactive chemical species concentration can be observed. But, the level of these species continues to arise for several days and months [3]. These oxidative changes affect not only the targeted but also the nontargeted cell population and their progenies as well via intercellular communication pathways [1, 4–9]. They often cause from mild to severe inflammation, irritation, fatigue, xerostomia, oral and gastrointestinal mucositis, radiation dermatitis, and cystitis depending on the irradiated region [10]. The persistence of these stressful effects has

significant consequences. Among others, they are responsible for long-term health risks of irradiation such as cardiovascular disease, vascular cell damage, neuropathy, and nerve demyelination as well [1–13]. The second malignancies following radiotherapy are also presumably based on oxidative DNA damages of tumor suppressor genes (p53 and Rb) [14, 15].

One of the most frequently occurring severe late side effects of radiation therapy is myelopathy. Radiation myelopathy (RM) is an irreversible impairment of the brain and spinal cord that has received much attention in the last years [16, 17]. In the case of neuro-oncological irradiation treatments, the healthy brain and spinal cord are critical dose-limiting organs during therapy [1, 17–20].

In clinical oncology, use of medical imaging technologies and the introduction of personalized treatment could refine the whole RT protocol. Thus, it offers a chance to minimize radiation-related side effects. The innovation of medical devices, imaging agents, standardized protocols, and imaging analysis allows to noninvasively capture quantitative and qualitative information about intratumoral heterogeneity. This further helps to personalize radiotherapy for each patient. Thus, the application of imaging radiomics in the wider field of oncology involving toxicity, pathology, imaging, blood biomarkers, demographics, genomics, and proteomics related studies could increase the number of quality years of patients' life. Imaging radiomics for personalized cancer therapy promotes cost effectiveness in the long term too [21]. The quality of life and effectiveness in cost is an important aspect of brain radiation treatments, too.

Due to the fact that widespread use of radiotherapy in the clinical routine currently comes without any standardized and routine monitoring protocol for acute side effects, there is high medical need for an early, sensitive, and harmless *in vivo* diagnostic imaging method to follow up radiotherapy and continuously monitor the status of patients. This is especially true in the case of patients with primary or secondary brain malignancies. Radiotherapy to the brain can lead to the rise of radiation myelopathy both by focused or whole-brain irradiation techniques. Our approach was to develop and to test multimodal image analysis techniques, which are able to investigate the emerging metabolic, perfusion, and diffusion-related changes in the body after the irradiation of neural tissues. To this end, we chose widely accessible imaging methods in magnetic resonance imaging (MRI) and in [¹⁸F] fluoro-deoxy-D-glucose (FDG) positron emission tomography (PET). FDG-PET and MRI are clinically easily accessible modalities that are usually applied in the work-up of almost all cancer patients especially in cancer patients with brain involvement. We applied a mouse model of partial brain irradiation. Our purposes included detection of neural correlates. Radiation-induced effects reach not only the immediate environment of the tumor but seemingly distant parts and regions of the brain too. To investigate this phenomenon, we applied the image analysis technique of correlations between brain regions. This way, effects of irradiation to, e.g., one hemisphere could be detected in the other seemingly unaffected hemisphere too. We applied two

single absorbed dose levels of 5 Gy and 20 Gy to investigate the standalone effect of single doses applied in the clinical practice of multidose fractionated radiotherapy. These two radiation doses were selected to account for the low-dose clinical fraction value and the high-dose clinical fraction value.

2. Methods

2.1. Animals. All applicable international, national, and institutional guidelines for the care and use of animals were followed, and in particular, all animal experiments were carried out according to the guidelines of German Regulations for Animal Welfare and have been approved by the Landesdirektion Dresden. The experimental procedure conforms in particular to the European Convention for the Protection of Vertebrate Animals Used for Experimental and Other Scientific Purposes (ETS No. 123). 12 BALB/c female mice were divided into two groups ($n = 6$) differing in irradiation doses (5 and 20 Gy). Animals were fed *ad libitum* and maintained under controlled temperature, humidity, and light conditions.

2.2. Irradiation. The irradiation was made under ketamine/medetomidine anesthesia. The schedule of our study regarding irradiation and imaging protocols is illustrated on Figure 1.

Instead of whole-brain irradiation, the left hemisphere irradiation was chosen. For reproducible positioning, a custom-made mouse holder and lead collimator were used. The holder consisted of a plastic box with lead covering on the top and ear and teeth sticks for fixing the position of the mice. The irradiated area (0.7×1 cm hole in the lead shielding) was defined based on an MRI scan. To avoid the high eye-dose, the eyes were shielded as well. Irradiation was done by an Xyclon X-ray tube (MGC-41 Maxishot, calibrated at 200 kV and 20 mA) with an ambient filter (combination of 3 mm beryllium, 3 mm aluminium, and 0.5 mm copper). Two different irradiation schemes were tested in our experiments, which differed only in the duration of the irradiation, thus in dose of 5 Gy and 20 Gy.

2.3. Imaging. Imaging was made under desflurane anesthesia at 5 different time points—before irradiation (“*pre*”), 3 days (“*p3d*”), 7 days (“*p7d*”), 30 days (“*p30d*”), and 60 days (“*p60d*”) after irradiation.

FDG-PET imaging was performed on a nanoScan PET-CT small-animal imaging system (Mediso Ltd., Budapest, Hungary) with a special custom-made animal bed capable of scanning two mice simultaneously. The mice were fastened for 14 hours prior to scanning. 60 minutes before the brain scans, the animals were generally anesthetised with desflurane (9% desflurane in 30% oxygen/air), and 30 min before the scan, 5.05 ± 3.04 MBq [¹⁸F]FDG was administered intravenously in the tail vein. The imaging parameters were normal mode with packet timestamping and 50% axial overlap. The reconstruction used the Monte Carlo-based OSEM technique with 4 iterations, 3 subsets, a 400–600 keV

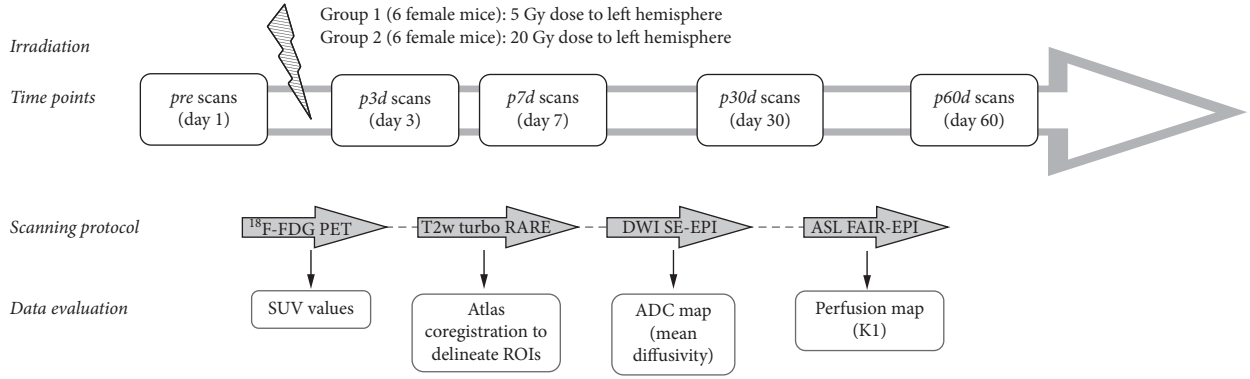


FIGURE 1: The schedule of irradiation and image data processing.

energy window, 1:5 coincidence window, and attenuation correction.

MRI scans were performed on a 7 T small animal MRI system (BioSpec 70/30, Bruker, Germany) equipped with active shielded 200 mT/m gradients and a head surface coil only for receiving. The scanning protocol started with a fat-suppressed and respiratory-triggered T2-weighted turbo rapid acquisition with refocused echoes (TurboRARE) sequence as an anatomical background at the same position as the following scans. The imaging parameters were 16 axial slices, slice thickness of 0.8 mm, gap of 0.2 mm, in-plane resolution of 0.15 mm, TR/TE 4315/45 ms, 4 averages, RARE factor of 8.

Diffusion-weighted imaging (DWI) based on an echo-planar imaging (EPI-SE) sequence had the same geometrical parameters as the anatomical scan except in this case the in-plane resolution was 0.234 mm and TR/TE 3000/31 ms. Diffusion-weighting parameters were chosen to be Δ/δ 14/7 ms and b -values (0, 100, 200, 400, 600, 800, and 1000 s/mm^2) in three orthogonal directions.

For the perfusion measurements, the arterial spin labeling (ASL) technique using the flow alternating inversion recovery (FAIR) method was performed with adiabatic hyperbolic secant inversion pulse and echo-planar imaging acquisition (EPI-SE, TR/TE 9000/14.67 ms, 5 averages). This single-shot, multiphase ASL measurement was acquired on a single slice (slice thickness of 0.8 mm, in-plane resolution of 0.18×0.225 mm) containing both thalamus and hippocampus, repeated 22 times (minimal inversion recovery time (TIR), 26 ms and 200 ms increment between the successive inversion times).

2.4. Postprocessing. The first step of our postprocessing was the manually atlas-based (mouse brain atlas from Brookhaven National Laboratory [22]) registration of each scan using VivoQuant software (inviCRO, USA). The further evaluation of MRI scans to create parametric maps was performed by a self-written code in MATLAB (The Mathworks Inc., USA). Thus, parametric maps could be investigated in the hypothalamus, thalamus, hippocampus, neocortex, amygdala, and striatum separately (Figure 2). Cerebellum was excluded from the evaluation based on the imperfect shimming and EPI distortion on the MRI scans.

In case of $[^{18}\text{F}]$ FDG-PET scans, activity concentration (A_{conc}) was calculated in ROIs and the standard uptake value (SUV in g/mm^3) as a measure of $[^{18}\text{F}]$ FDG uptake was determined as follows:

$$\text{SUV} = \frac{A_{\text{conc}}}{(A_{\text{inj}}/\text{BW})}, \quad (1)$$

where A_{inj} is the decay-corrected injected activity and BW is the body weight of the mouse. Based on the diffusion-weighted scans, the apparent diffusion coefficient (ADC) map was calculated with a voxel-wise monoexponential curve fitting in all three diffusion weighting directions. Not to incorporate direction-dependence, the mean ADC value was determined as the mean of the three apparent diffusion coefficients corresponding to the different orthogonal diffusion-weighting directions.

In the ASL, a scan evaluation one-tissue compartment model was used to describe the transport kinetics of water molecules accounting for the limited membrane permeability of the blood-brain barrier (BBB) [23]. The calculated K_1 map (equivalent with the uptake rate) practically equals to the blood flow if the BBB is considered perfectly permeable for water:

$$K_1 = V_d * R_{1,a} \frac{R_{1,s} - R_{1,ns}}{R_{1,ns}}, \quad (2)$$

where volume of distribution of water in tissue (V_d) is considered to be known in our model $V_d = 0.95$ mLH₂O/mL [24]. $R_{1,i}$ is the reciprocal of longitudinal relaxation rates, respectively, to the arterial water (a), selective scan (s), and nonselective scan (ns). The last two were determined voxel-wise by least square fitting of

$$S_{s,ns} = c + \left| S_0 \left(\frac{1 - 2eT_1}{R_{1s,ns}} \right) \right|, \quad (3)$$

where S is the MRI signal of the selective or nonselective FAIR scan, c is a bias, S_0 corresponds to the proton density, and $T_{1,a}$ is the relaxation rate of arterial water—in our model, $T_{1,a} = 2s$ [25].

2.5. Data Analysis. For statistical analysis, the mean MRI signals and calculated SUV, ADC, and K_1 values were

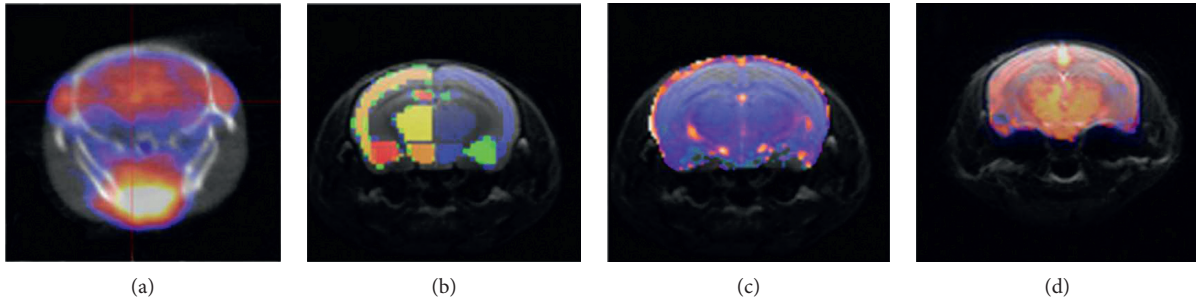


FIGURE 2: [^{18}F]FDG-PET-CT coregistered to MRI images (a). Atlas coregistered T2w turboRARE (b). ADC map coregistered to T2w turboRARE (c). Perfusion map coregistered to T2w turboRARE (d) (all images are from individual studies).

exported from every ROI. The analysis was performed for all 3 modalities. At first, difference between the left and right whole (the mean of different regions' ROI values was calculated) hemispheres was determined and related to the left hemisphere for each rat at each time point. Thereafter, correlation (using Pearson correlation coefficients) between hemispheres among brain regions was determined regardless the time points. The time trend was analyzed on the whole brain using a linear mixed effect model (random slope and intercept model with quadratic time effect using restricted maximum likelihood calculation) and with controlling for dose (Stata/IC 15.0, StataCorp LLC, Texas, USA).

3. Results

3.1. FDG-PET. FDG-PET studies were able to register the metabolic changes within the brain of animals. Figure 3 illustrates the mean SUV values of brain regions at five different time points using 5 Gy (A) and 20 Gy (B). Strong correlation (except the cerebellum and amygdala) was found between contralateral brain regions in either dose groups as shown in Figures 3(c) and 3(d). The relative SUV difference between the hemispheres was only 0.1%; thus the sum of the SUVs was acceptable. The time trend analysis of the whole brain did not show any statistical evidence for difference in the effect of 5 Gy and 20 Gy ($p < 0.05$) but revealed significant ($p < 0.05$) quadratic effect (Figure 3(e)).

Shortly after the irradiation, no relevant [^{18}F]FDG uptake changes (in term of mean SUV) could be seen in the investigated brain areas, but two months later, relevant increased SUVs were registered in the whole brain.

3.2. DWI. Figure 4 illustrates the mean ADC values of brain regions at five different time points using 5 Gy (A) and 20 Gy (B). Strong correlation was found between contralateral brain regions in either dose groups as shown in Figures 4(c) and 4(d). The relative ADC value difference between the hemispheres was only 1.2%; thus ADC values were summed. The time trend analysis of the whole brain did not show any statistical evidence for difference in the effect of 5 Gy and 20 Gy ($p < 0.05$) but revealed a significant ($p < 0.05$) quadratic effect (Figure 4(e)).

As the fitted trend line shows no ADC value, changes were detected at the first week. One month after the

irradiation, relevant ADC value decreasing was registered in all brain regions, whose values did not alter until the end of the measurement (Figure 4(e)).

3.3. ASL. Figure 5 illustrates the mean K_1 values of brain regions at five different time points using 5 Gy (A) and 20 Gy (B). Moderate correlation was found between contralateral brain regions in either dose groups as shown in Figures 5(c) and 5(d). The relative K_1 value difference between the hemispheres was 0.8%; thus the ASL values were summed. The time trend analysis of the whole brain did not show any statistical evidence for difference in the effect of 5 Gy and 20 Gy ($p > 0.1$). There was no significant trend in time ($p > 0.1$).

4. Discussion

We have investigated the short- and long-term risks and side effects of radiation therapy to the brain. In this study, a custom-made small animal irradiation system using two different doses mimicked the effects of high- and low-dose single RT fractions in clinical practice. The applied multimodal imaging method has monitored important physiological parameters (cerebral blood flow, vascular endothelial function, and cellular metabolic processes) for 60 days.

The 5 Gy and 20 Gy single-fraction radiation doses are equivalents of the single dose of the lowest and the highest human doses during a fractionated RT [26].

[^{18}F]FDG-PET scans made possible to follow up brain glucose use of animals after the irradiation [27]. The [^{18}F]FDG uptake and the calculated SUV strictly correlate with local glucose metabolism, reflecting different constituents of brain glucose uptake: glial metabolism, neuronal and synaptic activity, and local immune processes [28]. As such, [^{18}F]FDG could be used to monitor eventual microglial or other inflammatory conditions in the brain postirradiation therapy too.

Diffusion-weighted MRI has been used for the monitoring of physiological changes (oedema, inflammation, fibrosis, and necrosis) within the brain tissue and for the quantification of MRI signal loss using ADC. ADC as a clinically validated measurand in the field of oncology is able to differentiate between the RT-induced tissue changes. Malignant tumor disease is often described with lower ADC

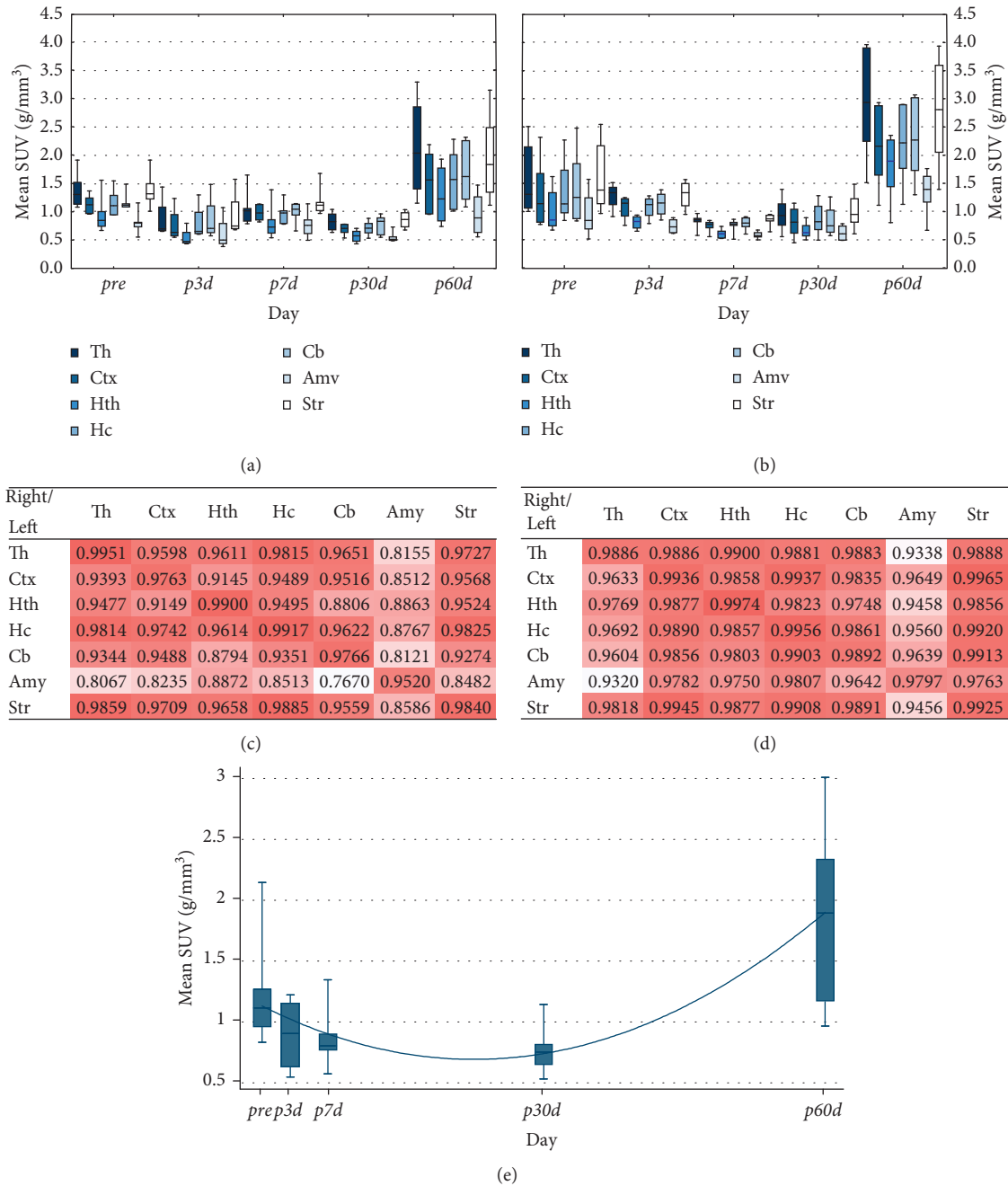


FIGURE 3: The effect of irradiation on brain $[^{18}\text{F}]$ FDG uptake values. The mean SUVs of the left (irradiated) brain regions (Th: thalamus; Ctx: cortex; Hth: hypothalamus; Hc: hippocampus; Cb: cerebellum; Amy: amygdala; Str: striatum) are shown at five different time points by 5 Gy (a) and 20 Gy (b) dose groups. The boxplots show median with quartiles, minimum, and maximum. Correlation maps of $[^{18}\text{F}]$ FDG uptake values of the left versus right brain areas (regardless of the time points) by 5 Gy (c) and 20 Gy (d) dose groups are shown. The heat maps visualize the Pearson correlation of irradiation effects between each investigated brain region. The time trend analysis of the whole brain is shown in (e).

values while oedema and inflammation are manifested in higher ADC values [29, 30]. Besides these changes, decreased ADC values were reported after RT in case of noncancerous tissues by Takayama et al. [31].

In our study, a trend of decrease in ADC of both the irradiated and the correlating hemispherical brain structures could be observed starting a month after radiation therapy and it was maintained up to the end of the 60 day observation period. Our results of ADC values are close to

these and other previous findings [32–34]. The effect of RT is assumed to be related to the damage of vascular endothelial cells, which influences the swelling of the concerned cells and decreases the extracellular space in case of inflammation.

The arterial spin labeling technique, as a proposed alternative of PET scan, has the potential for detection and quantitative follow-up the cerebral blood flow changes without any contrast material [24]. Following RT, there is

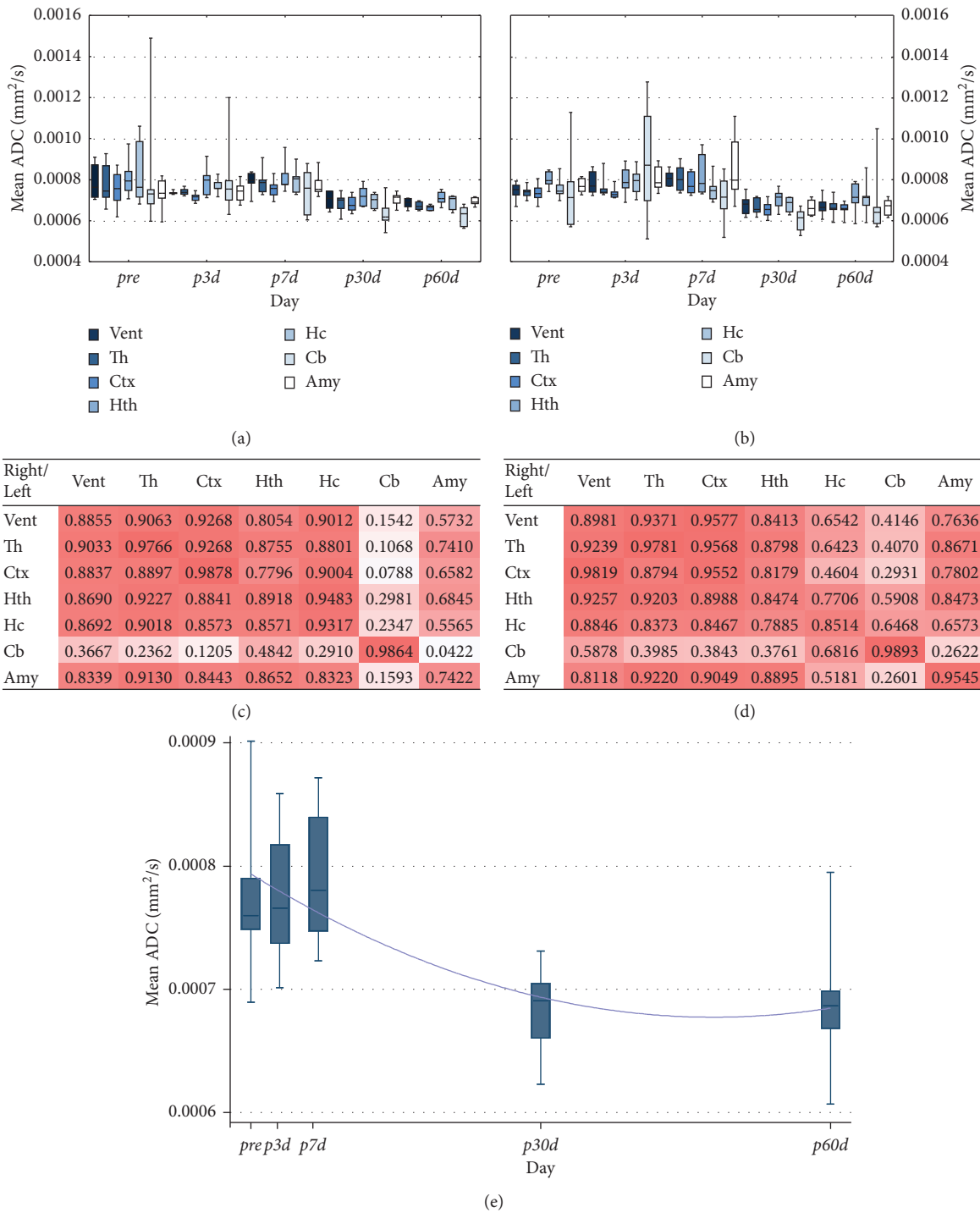


FIGURE 4: The effect of irradiation on the brain ADC values. The mean ADC values of the left (irradiated) brain regions (Vent: ventricles; Th: thalamus; Ctx: cortex; Hth: hypothalamus; Hc: hippocampus; Cb: cerebellum; Amy: amygdala) are shown at five different time points by 5 Gy (a) and 20 Gy (b) dose groups. The boxplots show median with quartiles, minimum, and maximum. The correlation maps of the ADC values of the left versus right brain areas (regardless of the time points) by 5 Gy (c) and 20 Gy (d) dose groups are shown. The heat maps visualize the Pearson correlation of irradiation effects between each investigated brain region. The time trend analysis of the whole brain ADC changes is shown in (e).

a “latent period” when no significant perfusion and vascular changes could be registered. However, the length of this period is absolutely depending on the applied doses which vary from a few months to a few years. 20 Gy dose whose

effect on rat brain equivalent with the tissue response to a mean total dose of human-fractionated brain RT—applied by Reinhold et al. caused significant transient neurotransmitter enhancement, increased CBF, and decreased

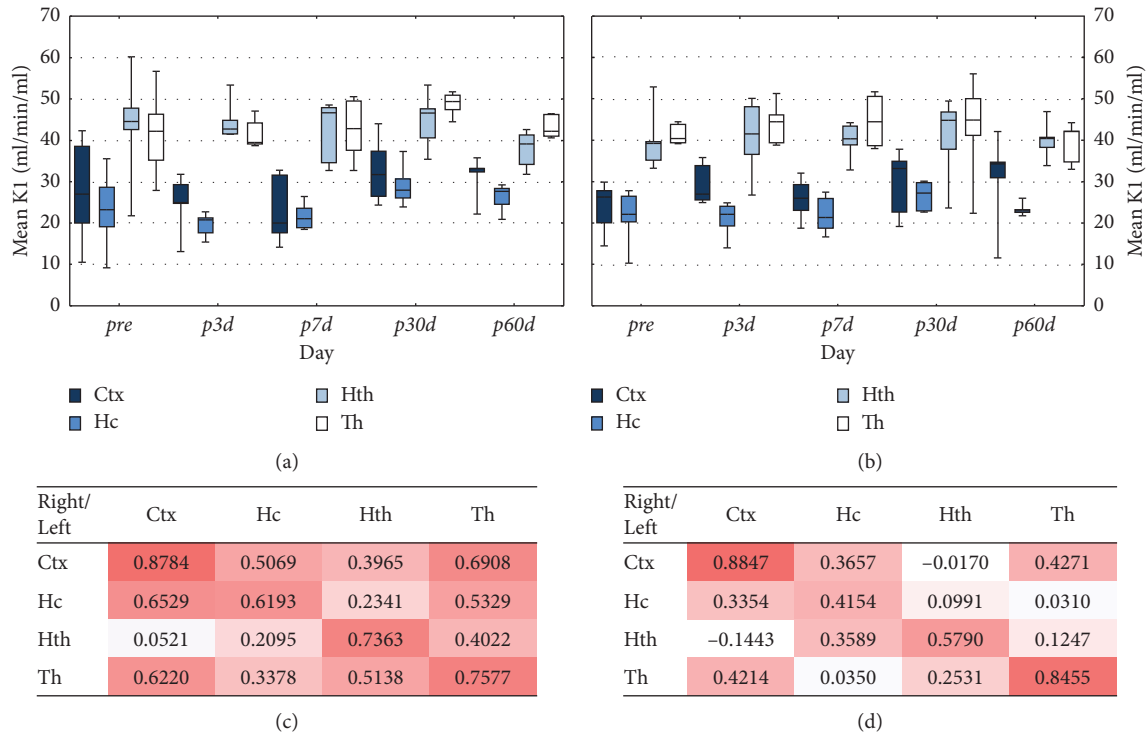


FIGURE 5: The effect of irradiation on the brain K_1 values. The mean K_1 values of the left (irradiated) brain regions (Ctx: cortex; Hc: hippocampus; Hth: hypothalamus; Th: thalamus) are shown at five different time points by 5 Gy (a) and 20 Gy (b) dose groups. The boxplots show median with quartiles, minimum, and maximum. The correlation maps of the K_1 values of the left versus right brain areas (regardless of the time points) by 5 Gy are presented in (c) and for 20 Gy dose groups in (d). The heat maps visualize the Pearson correlation of irradiation effects between each investigated brain region.

extravascular space in rats 3 months after the RT [35]. In our 2 month long experiments, the animals did not show any perfusion changes in either dose groups (5/20 Gy dose groups). Based on the high intersubject variability, the inherently low signal-to-noise ratio (SNR) of this technique and the potential presence of “latency period” after irradiation showing up in perfusion changes more animals, and a longer follow-up period would have been necessary to observe eventual trends in perfusion changes in the brain with MRI.

No hemisphere-related changes were observed in the case of 5/20 Gy dose groups using either FDG-PET and DWI MRI. However, statistical trend analysis could detect the methods’ applicability for monitoring course of the side effects. Interestingly, the results of correlation analysis of regions show a high correlation between the hemispheres. This may indicate long-distance bystander side effects of radiotherapy in the CNS. The detectability and effects of irradiation between the 5–20 Gy dose range were not different which draws the attention to an existing side effect profile of even low-dose fractionated radiotherapy.

5. Conclusions

We successfully developed a new multimodal imaging protocol which is able to monitor the irradiation-related side effects and follow up the health status of the animals for several weeks. The most relevant imaging biomarkers in the

field of neuroscience were able to responsibly indicate the forming side effects of RT. Elevated brain glucose consumption and decreased diffusion with nearly constant cerebral blood flow were the first detectable signs of the altered local circulation and transportation, the changed metabolic activity, and the induced inflammation by reactive oxygen species (ROS) production.

Based on the high translational power of this quantitative MRI/PET technique and the availability of these modalities in clinics, it is assumed that our scientific results could support and refine the radiation therapy via the monitoring of side effects and follow up the health status of patients. In addition, this imaging protocol can support the realization of personalized therapy in medical practice.

Hereby, a new multimodal imaging protocol is presented which the authors consider an appropriate monitoring method to follow both effects of irradiation of the tumor and side effects of radiation therapy.

Data Availability

The data used to support the findings of this study are available from the corresponding author upon request.

Conflicts of Interest

The authors declare that they have no conflicts of interest.

Authors' Contributions

NK and KSz contributed equally. RB and DM are joint senior authors.

Acknowledgments

The research leading to these results has received funding from the European Union's Framework Programme 7 under grant agreement no. 305311 (INSERT). KSz was supported by Bolyai Janos Research Scholarship of the Hungarian Academy of Sciences. We thank Regina Herrlich and Sebastian Meister for the technical support in the animal MRI and FDG-PET experiments.

References

- [1] E. I. Azzam, S. M. de Toledo, and J. B. Little, "Oxidative metabolism, gap junctions and the ionizing radiation-induced bystander effect," *Oncogene*, vol. 22, no. 45, pp. 7050–7057, 2003.
- [2] E. J. Hall and A. Giaccia, *Radiobiology for the Radiologist*, Lippincott Williams & Wilkins, Philadelphia, PA, USA, 6th edition, 2006.
- [3] A. Petkau, "Role of superoxide dismutase in modification of radiation injury," *British Journal of Cancer. Supplement*, vol. 8, pp. 87–95, 1987.
- [4] D. R. Spitz, E. I. Azzam, J. J. Li, and D. Gius, "Metabolic oxidation/reduction reactions and cellular responses to ionizing radiation: a unifying concept in stress response biology," *Cancer and Metastasis Reviews*, vol. 23, no. 3, pp. 311–322, 2004.
- [5] T. B. Kryston, A. B. Georgiev, P. Pissis, and A. G. Georgakilas, "Role of oxidative stress and DNA damage in human carcinogenesis," *Mutation Research/Fundamental and Molecular Mechanisms of Mutagenesis*, vol. 711, no. 1-2, pp. 193–201, 2011.
- [6] J. Tamminga and O. Kovalchuk, "Role of DNA damage and epigenetic DNA methylation changes in radiation-induced genomic instability and bystander effects in germline in vivo," *Current Molecular Pharmacology*, vol. 4, no. 2, pp. 115–125, 2011.
- [7] T. K. Hei, H. Zhou, Y. Chai, B. Ponnaiya, and V. N. Ivanov, "Radiation induced non-targeted response: mechanism and potential clinical implications," *Current Molecular Pharmacology*, vol. 4, no. 2, pp. 96–105, 2011.
- [8] C. B. Seymour and C. Mothersill, "Radiation-induced bystander effects-implications for cancer," *Nature Reviews Cancer*, vol. 4, no. 2, pp. 158–164, 2004.
- [9] K. M. Prise and J. M. O'Sullivan, "Radiation-induced bystander signalling in cancer therapy," *Nature Reviews Cancer*, vol. 9, no. 5, pp. 351–360, 2009.
- [10] E. J. Hall and A. J. Giaccia, *Radiobiology for the Radiologist*, Lippincott Williams & Wilkins, Vol. 8, Lippincott Williams & Wilkins, Philadelphia, PA, USA, 6th edition, 2018.
- [11] F. A. Cucinotta and L. J. Chappell, "Non-targeted effects and the dose response for heavy ion tumor induction," *Mutation Research/Fundamental and Molecular Mechanisms of Mutagenesis*, vol. 687, no. 1-2, pp. 49–53, 2010.
- [12] M. Tubiana, "Can we reduce the incidence of second primary malignancies occurring after radiotherapy? a critical review," *Radiotherapy and Oncology*, vol. 91, no. 1, pp. 4–15, 2009.
- [13] National Research Council, "Committee to assess health risks from exposure to low levels of ionizing radiation," in *Health Risks from Exposure to Low Levels of Ionizing Radiation: Beir VII Phase II*, National Academic Press, Washington, DC, USA, 2006.
- [14] J. H. Hendry, "Genomic instability: potential contributions to tumour and normal tissue response, and second tumours, after radiotherapy," *Radiotherapy and Oncology*, vol. 59, no. 2, pp. 117–126, 2001.
- [15] A. I. Robles, S. P. Linke, and C. C. Harris, "The p53 network in lung carcinogenesis," *Oncogene*, vol. 21, no. 45, pp. 6898–6907, 2002.
- [16] M. W. Chao, A. Wirth, G. Ryan, M. MacManus, and K. Liew, "Radiation myelopathy following transplantation and radiotherapy for non-Hodgkin's lymphoma," *International Journal of Radiation Oncology*Biophysics*, vol. 41, no. 5, pp. 1057–1061, 1998.
- [17] E. Maranzano, R. Bellavita, P. Floridi et al., "Radiation-induced myelopathy in long-term surviving metastatic spinal cord compression patients after hypofractionated radiotherapy: a clinical and magnetic resonance imaging analysis," *Radiotherapy and Oncology*, vol. 60, no. 3, pp. 281–288, 2001.
- [18] S. Okada and R. Okeda, "Pathology of radiation myelopathy," *Neuropathology*, vol. 21, no. 4, pp. 247–265, 2001.
- [19] F. Sarica, K. Ozgur, M. Cekinmez, A. Nur, and T. Kadir, "Delayed radiation myelopathy: differential diagnosis with positron emission tomography/computed tomography examination," *Asian Journal of Neurosurgery*, vol. 7, no. 4, p. 206, 2012.
- [20] S. J. Kempf, O. Azimzadeh, M. J. Atkinson, and S. Tapio, "Long-term effects of ionising radiation on the brain: cause for concern?," *Radiation and Environmental Biophysics*, vol. 52, no. 1, pp. 5–16, 2013.
- [21] P. Lambin, E. Rios-Velazquez, R. Leijenaar et al., "Radiomics: extracting more information from medical images using advanced feature analysis," *European Journal of Cancer*, vol. 48, no. 4, pp. 441–446, 2012.
- [22] Brookhaven National Laboratory; BNL, <http://brainatlas.mbi.ufl.edu/>.
- [23] A. Boš, R. Bergmann, K. Strobel, F. Hofheinz, J. Steinbach, and J. van den Hoff, "Cerebral blood flow quantification in the rat: a direct comparison of arterial spin labeling MRI with radioactive microsphere PET," *EJNMMI Research*, vol. 2, no. 1, p. 47, 2012.
- [24] C. Leithner, S. Müller, M. Fuchtemeier, U. Lindauer, U. Dirnagl, and G. Rojl, "Determination of the brain-blood partition coefficient for water in mice using MRI," *Journal of Cerebral Blood Flow and Metabolism*, vol. 30, no. 11, pp. 1821–1824, 2010.
- [25] M. C. Dobre, K. Uğurbil, and M. Marjanska, "Determination of blood longitudinal relaxation time (T1) at high magnetic field strengths," *Magnetic Resonance Imaging*, vol. 25, no. 5, pp. 733–735, 2007.
- [26] A. Pollack and M. Ahmed, *Hypofractionation: Scientific Concepts and Clinical Experiences*, LumiText Publishing, Ellicott City, MD, USA, 2011.
- [27] T. E. Peterson and H. C. Manning, "Molecular imaging: 18F-FDG PET and a whole lot more," *Journal of Nuclear Medicine Technology*, vol. 37, no. 3, pp. 151–161, 2009.
- [28] V. Berti, L. Mosconi, and A. Pupi, "Brain: normal variations and benign findings in fluorodeoxyglucose-PET/computed tomography imaging," *PET clinics*, vol. 9, no. 2, pp. 129–140, 2014.

- [29] T. L. Chenevert, C. R. Meyer, B. A. Moffat et al., "Diffusion MRI: a new strategy for assessment of cancer therapeutic efficacy," *Molecular Imaging*, vol. 1, no. 4, 2002.
- [30] B. D. Ross, B. A. Moffat, T. S. Lawrence et al., "Evaluation of cancer therapy using diffusion magnetic resonance imaging¹," *Molecular Cancer Therapeutics*, vol. 2, no. 6, pp. 581–587, 2003.
- [31] Y. Takayama, R. Kishimoto, S. Hanaoka et al., "ADC value and diffusion tensor imaging of prostate cancer: changes in carbon-ion radiotherapy," *Journal of Magnetic Resonance Imaging*, vol. 27, no. 6, pp. 1331–1335, 2008.
- [32] P. Kozlowski, S. D. Chang, E. D. Jones, K. W. Berean, H. Chen, and S. L. Goldenberg, "Combined diffusion-weighted and dynamic contrast-enhanced MRI for prostate cancer diagnosis—correlation with biopsy and histopathology," *Journal of Magnetic Resonance Imaging*, vol. 24, no. 1, pp. 108–113, 2006.
- [33] V. Kumar, N. R. Jagannathan, R. Kumar et al., "Correlation between metabolite ratios and ADC values of prostate in men with increased PSA level," *Magnetic Resonance Imaging*, vol. 24, no. 5, pp. 541–548, 2006.
- [34] A. Tanimoto, J. Nakashima, H. Kohno, H. Shinmoto, and S. Kuribayashi, "Prostate cancer screening: the clinical value of diffusion-weighted imaging and dynamic MR imaging in combination with T2-weighted imaging," *Journal of Magnetic Resonance Imaging*, vol. 25, pp. 146–152, 2007.
- [35] H. S. Reinhold and J. W. Hopewell, "Late changes in the architecture of blood vessels of the rat brain after irradiation," *British Journal of Radiology*, vol. 53, no. 631, pp. 693–696, 1980.

Research Article

Quantification of Nanoparticle Enhancement in Polarized Breast Tumor Macrophage Deposits by Spatial Analysis of MRI and Histological Iron Contrast Using Computer Vision

Avigdor Leftin ¹ and Jason A. Koutcher^{1,2,3}

¹Department of Medical Physics, Memorial Sloan Kettering Cancer Center, New York, NY, USA

²Department of Medicine, Memorial Sloan Kettering Cancer Center, New York, NY, USA

³Molecular Pharmacology Program, Memorial Sloan Kettering Cancer Center, New York, NY, USA

Correspondence should be addressed to Avigdor Leftin; leftina@mskcc.org

Received 7 June 2018; Accepted 13 August 2018; Published 30 October 2018

Academic Editor: Filippo Galli

Copyright © 2018 Avigdor Leftin and Jason A. Koutcher. This is an open access article distributed under the Creative Commons Attribution License, which permits unrestricted use, distribution, and reproduction in any medium, provided the original work is properly cited.

Magnetic resonance imaging applications utilizing nanoparticle agents for polarized macrophage detection are conventionally analyzed according to iron-dependent parameters averaged over large regions of interest (ROI). However, contributions from macrophage iron deposits are usually obscured in these analyses due to their lower spatial frequency and smaller population size compared with the bulk of the tumor tissue. We hypothesized that, by addressing MRI and histological pixel contrast heterogeneity using computer vision image analysis approaches rather than statistical ROI distribution averages, we could enhance our ability to characterize deposits of polarized tumor-associated macrophages (TAMs). We tested this approach using *in vivo* iron MRI (FeMRI) and histological detection of macrophage iron in control and ultrasmall superparamagnetic iron oxide (USPIO) enhanced mouse models of breast cancer. Automated spatial profiling of the number and size of iron-containing macrophage deposits according to localized high-iron FeMRI or Prussian blue pixel clustering performed better than using distribution averages to evaluate the effects of contrast agent injections. This analysis was extended to characterize subpixel contributions to the localized FeMRI measurements with histology that confirmed the association of endogenous and nanoparticle-enhanced iron deposits with macrophages in vascular regions and further allowed us to define the polarization status of the macrophage iron deposits detected by MRI. These imaging studies demonstrate that characterization of TAMs in breast cancer models can be improved by focusing on spatial distributions of iron deposits rather than ROI averages and indicate that nanoparticle uptake is dependent on the polarization status of the macrophage populations. These findings have broad implications for nanoparticle-enhanced biomedical imaging especially in cancer.

1. Introduction

Widespread efforts have succeeded in integrating nanoparticles in virtually all areas of medical imaging. The appeal of these formulations derives from their ability to be tailored to specific applications ranging from neuroscience to oncology by chemical manipulation of nanoparticle composition rendering them visible to multiple imaging modalities such as MRI, PET, and optical imaging systems [1]. Moreover, the ability to functionalize these particles using delivery systems such as polymers or lipids and bioaffinity tags such as antibodies further enhances our ability to probe,

monitor, and control ubiquitous biological processes spanning drug delivery and cell tracking [2].

Nanoparticles formulated from iron are ubiquitous contrast agents for MRI. One common agent used consists of ultrasmall superparamagnetic iron oxide (USPIO) nanoparticles solubilized with dextran polymer to facilitate suspension and delivery in aqueous solution [3, 4]. Cancer research is a premier application of these USPIO nanoparticles, and they have been used to investigate virtually every cancer type. They provide information about both vascular and immune cell properties of the tumor that are key determinants of the pharmacodynamic behavior of

drugs and the cellular immune response to therapies [5–7].

Quantification of tissue uptake of iron nanoparticles and deposition in macrophages is conventionally performed using region of interest (ROI) analysis of MRI images [8]. Pixel contrast levels, relaxation times, rates, or the susceptibility phase [9–12] are measured over tissue cross-sectional areas and analyzed according to pixel distribution statistics. Changes in iron concentration following USPIO injection can be further quantified from these pixel distributions according to parametric relations between these observables and known iron standards, iron-labeled cells, or biopsy iron measurement to provide quantitative estimates on nanoparticle delivery, cellular uptake, and concentration [13–16]. So-called iron MRI (FeMRI) approaches can estimate iron nanoparticle uptake by the measurement of parametric distribution statistics. However, it has long been an accepted caveat of the quantitative interpretation of most cellular MRI applications that ROI-based distribution analysis is biased by contributions from the abundant low-iron areas of the tissue, i.e., those not containing the iron deposit or contrast agent, which limits the specificity of the MRI pixel distribution analysis for iron accumulation in rare cellular targets such as macrophages in tumors.

Macrophages are important imaging targets in cancer because they can function in both inflammatory and wound-healing roles that influence tumor growth and therapeutic response [17–19]. Nanoparticle injection and uptake is dependent upon and can influence this polarization status of the targeted cellular populations as these cells exhibit plasticity in these functional roles that in turn is coupled to their innate role in iron metabolism [20, 21]. While MRI studies do not directly report on polarization, immunofluorescence imaging can be used to evaluate changes in TAM iron deposit polarization and provide subpixel information about the dependence of the USPIO contrast agent uptake on TAM polarization [22–24]. However, nanoparticle delivery to the tumor rarely exceeds a few percent of the injected dose [25], and therefore, only a small fraction of macrophages present in the tumor will be engaged by the nanoparticles and give rise to localized detectable iron contrast. Therefore, similar to cellular iron MRI, whole ROI analysis of histological polarization state measurements is more representative of the nanoparticle-free macrophage populations rather than subpopulations containing iron. Therefore, scoring macrophage polarization with immunofluorescence using whole ROI distribution analysis also will generally not be representative of the relatively rare iron-handling populations targeted by the nanoparticle injections. Thus, alternative unbiased analysis approaches that better quantify the local distributions of these iron-containing cells and their phenotypes are required to evaluate the polarization status of the macrophage targets and to provide cellular level corroboration of FeMRI applications.

In the current study, we advance a computer vision approach to localize polarized macrophages according to iron status in order to improve their quantification in USPIO-enhanced cellular imaging by MRI and histology. We have previously shown that, by addressing the spatial

heterogeneity of iron-dependent image contrast, we could enhance the quantification of these macrophage deposits without contrast agents using MRI and histology because the type of iron stored in the macrophages generates stronger MRI contrast enhancement compared with venous or hemorrhagic blood [26–30] and Prussian blue only labels macrophage with solid iron deposits corresponding to those of the highest iron concentration. These endogenous stores conferred sufficient cellular sensitivity and specificity to detect macrophage iron deposits in multiple cancer models including prostate cancer and breast cancer, in both primary and distant disseminated metastatic locations of the lung and brain, as well as systemically in organs which naturally or pathologically accumulate macrophage iron such as the liver and spleen [29, 30]. In the current study, we continue our translational development of this approach by combining it with the USPIO contrast agent injection to evaluate iron deposition in polarized breast tumor macrophages.

2. Results

To demonstrate the difference between the ROI average distribution measurements and the localized measurements of cellular iron deposition with and without dextran-USPIO injection, we initiated orthotopic MMTV-PyMT murine mammary tumors and injected USPIO (0.5 mmol/kg) or saline intravenously once tumor volumes reached approximately 1 cm^3 . Mapping iron-dependent contrast 24 hrs after injection at 7T showed that both the nanoparticle-free (Figure 1(a), -USPIO) and contrast-enhanced tumors (Figure 1(b), +USPIO) evidenced heterogeneous distributions of pixel iron levels, with both cohorts exhibiting numerous high-iron pixel regions, i.e., clusters indicative of iron deposits, at the periphery of the tumor, and iron oxide-injections increased the numbers of these clusters.

Analysis of the iron MRI maps was then performed to quantify these pixel distributions. Parametric pixel distributions expressed as number of pixel clusters (Figure 1(c)) and cluster size measured in mm^2 (Figure 1(d)) were reconstructed as a function of iron concentration with high and low ranges defined with respect to the median iron level of the distribution range. Frequency (number of pixel clusters) and size distribution maxima fell well within the low-iron contrast range in both control and USPIO-injected tumors and appeared to shift nominally towards higher concentrations with USPIO injection. In the high iron range of the frequency distribution, clear increases of pixel clusters occurred with the USPIO uptake, while the size of these high-iron clusters appeared to remain constant in the control and nanoparticle-treated groups suggesting that iron injection changed only the number of the deposits but not their size. Statistical analysis of the ROI-based parametric iron distributions was then performed to quantify the observations. First, median values were calculated from ROI analysis over whole tumor cross sections as is conventionally performed. Median iron levels of the parametric pixel distributions from the ROI showed small but significant increases in frequency (Figure 1(e); $p < 0.05$) and size (Figure 1(f); $p < 0.05$) with USPIO enhancement. In

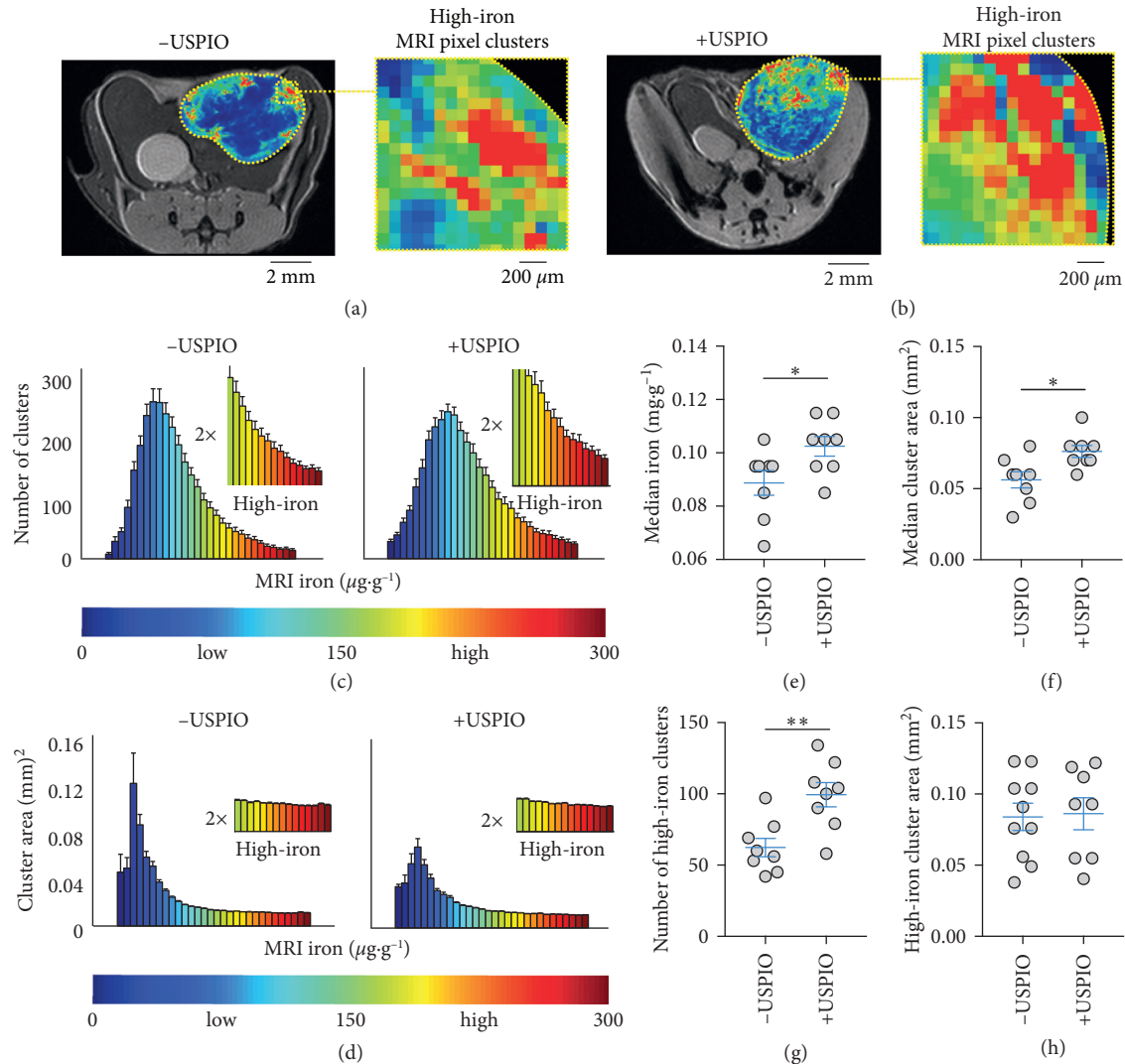


FIGURE 1: Spatial quantification of endogenous and nanoparticle-enhanced iron deposits with MRI *in vivo*. T₂-weighted MRI and iron concentration overlay images of (a) control (-USPIO) and (b) iron nanoparticle-injected (+USPIO) tumors. Expansion shows high-iron pixel contrast in clustered areas. (c) Number (#) of clusters and (d) area of the pixel clusters in control (-USPIO) and nanoparticle-injected (+USPIO) tumors as a function of iron concentration. Distributions are from whole cross-sectional regions of interest (ROI) areas of tumors measuring approximately 1 cm³ (mean ± SEM shown, $n = 8$ tumors/group). MRI iron concentration range at bottom corresponds to values in iron images above. Control (-USPIO) and nanoparticle-injected (+USPIO) (e) median iron concentrations and (f) pixel cluster sizes. (g) Number (#) of high-iron pixel clusters and (h) size of the high-iron clusters from localized computer vision analysis (mean ± SEM shown, $n = 8$ tumors/group, n.s. $p > 0.05$, * $p < 0.05$, *** $p < 0.001$, two-tailed unpaired Student's t -test). Scale bars are shown for all images.

order to more specifically quantify local accumulation of iron deposits indicated by the high-iron range stratification, the frequency of high-iron clusters in the maps was counted, and the areas were measured. This revealed significant increases of the high-iron pixel clusters with iron nanoparticle injection (Figure 1(g); $p < 0.001$) and provided an additional measurement of the size of these regions of iron accumulation with and without contrast agents (Figure 1(h); $p > 0.05$). This demonstrates an improvement over the ROI quantification in terms of the significant increases in iron deposit accumulation detected and confirms the observation that the number of high-iron clusters increase but the size remains relatively unchanged with USPIO injection.

To confirm the cellular identity of the iron⁺ species and characterize the microenvironment of the iron deposits, Prussian blue iron histochemistry (Figure 2(a)) and immunofluorescence for F4/80⁺ (Figure 2(b)) macrophages and CD31⁺ vasculature (Figure 2(c)) was performed. Iron staining of the MMTV-PyMT tumor sections evidenced iron⁺ cellular species in stromal regions almost exclusively at peripheral tumor margins. These localized cellular iron sources clustered as multicellular deposits in both the control and USPIO-treated tumors. Macrophage immunofluorescence of these tissue cross sections further confirmed that the iron⁺ cells identified in the Prussian blue histology were colocalized with F4/80⁺ macrophages. These iron⁺ F4/80⁺ macrophages were

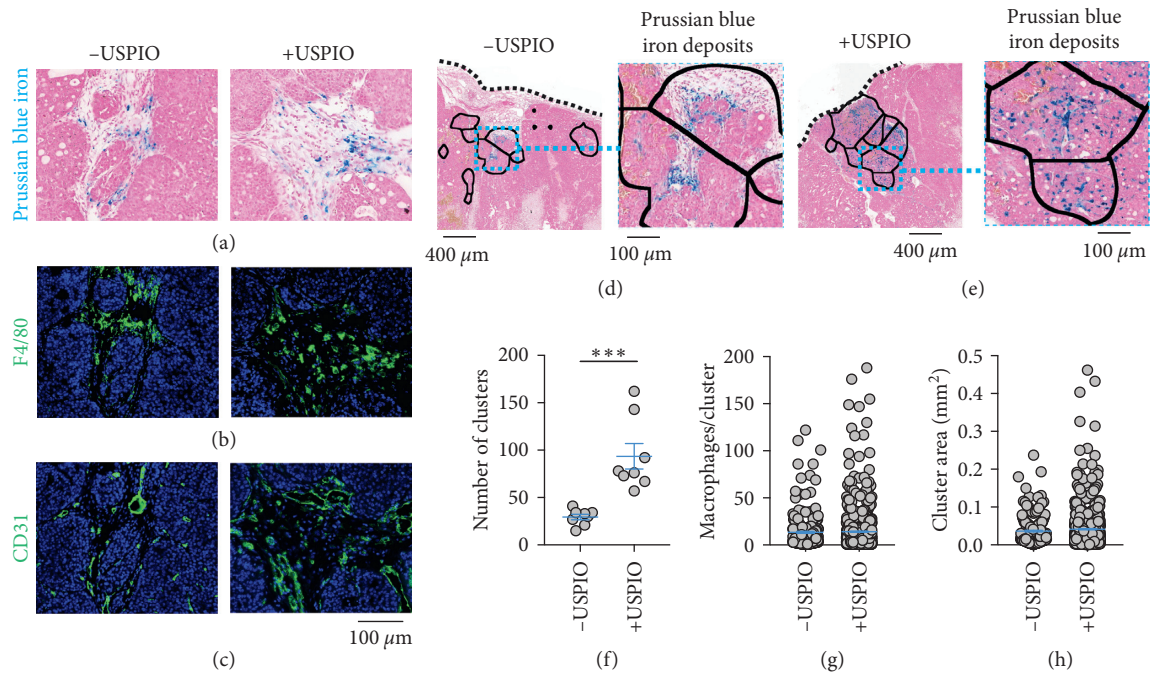


FIGURE 2: Spatial quantification of endogenous and contrast-enhanced macrophage deposits by iron histology. Paraffin-embedded sections from control (-USPIO) and iron nanoparticle-injected (+USPIO) tumors. (a) Prussian blue iron staining, (b) F4/80 macrophage immunofluorescence, and (c) CD31 vascular immunofluorescence were performed in the same sections to demonstrate the colocalization of iron deposits with infiltrating macrophages in vascular areas of the tumor microenvironment. Histological fields from (d) control and (e) iron nanoparticle-injected mice showing deposits of Prussian blue iron⁺ macrophages localized in infiltrative border regions in discrete clusters. Black borders are regions of interest drawn automatically around deposits of cells according to iron status. Expansion shows iron⁺ macrophages in the deposit regions. (f) Number of iron deposits (clusters) per tumor cross section in control (-USPIO) and nanoparticle-injected (+USPIO) mice (mean \pm SEM shown, $n = 8$ tumors/group, *** $p < 0.001$, two-tailed unpaired Student's t -test). (g) Number of iron⁺ macrophages per deposit, and (h) size of each of the deposits measured over the whole Paraffin-embedded tumor cross sections stained by Prussian blue (mean \pm SEM shown, -USPIO $n = 235$ total clusters/group, +USPIO $n = 748$ total clusters/group, n.s. $p > 0.05$). Scale bar is shown for all images.

invariably found in close proximity to CD31⁺ vasculature in both control and USPIO-injected cohorts suggesting that the accumulation of metabolic or nanoparticle-derived iron is dependent upon their spatial distribution beside tumor vasculature.

The spatial characteristics of the histologically detected macrophage iron deposits were then analyzed in a manner similar to the FeMRI pixel cluster analysis. The endogenous (Figure 2(d)) and USPIO-enhanced deposits (Figure 2(e)) found in the localized regions were automatically identified and the number of the clusters (Figure 2(f)), the number of iron⁺ macrophages per deposit (Figure 2(g)), and the areas of the clusters (Figure 2(h)) were measured exhaustively from whole tumor axial cross sections. The number of deposits containing iron⁺ macrophages increased significantly with USPIO injection ($p < 0.001$), and deposit areas in the control and injected groups were found to be equivalent, approximately a few MRI square-pixels ($p > 0.05$). These regions also equivalently contained an average of approximately 14 iron⁺ macrophages per control or USPIO-enhanced deposit ($p > 0.05$) supporting the cellular sensitivity of the FeMRI measurement and specificity of the pixel cluster analysis for these cellular species.

To determine the polarization status of general macrophage populations in the tumors and their changes with injection of USPIO, immunofluorescence staining of the tumor cross sections was conducted for pan-macrophage (CD68), inflammatory (M1-like AIF1 (allograft inflammatory factor 1)), and wound-healing surface marker phenotypes (M2-like CD206 (mannose receptor)), besides Prussian blue iron histology as the primary observable (Figures 3(a)–3(e)). Absolute counts of CD68⁺ macrophages conducted over whole tissue cross-sectional areas were performed to score CD68 infiltrates (Figure 3(f); $p > 0.05$). AIF1⁺ and CD206⁺ polarization markers were similarly quantified to evaluate phenotypic shifts. Exhaustive counts performed over the control tumor cross sections and calculation of frequency of these populations with respect to total numbers of these macrophages (M1 or M2/(M1+M2)) (Figure 3(g)) showed that USPIO injection did not lead to significant changes in absolute counts of macrophages ($p > 0.05$). Phenotypic populations in the control mice were significantly biased towards M2-like polarization with 42% M1-like AIF1⁺ and 58% of macrophages CD206⁺ ($p < 0.05$). This analysis of TAM

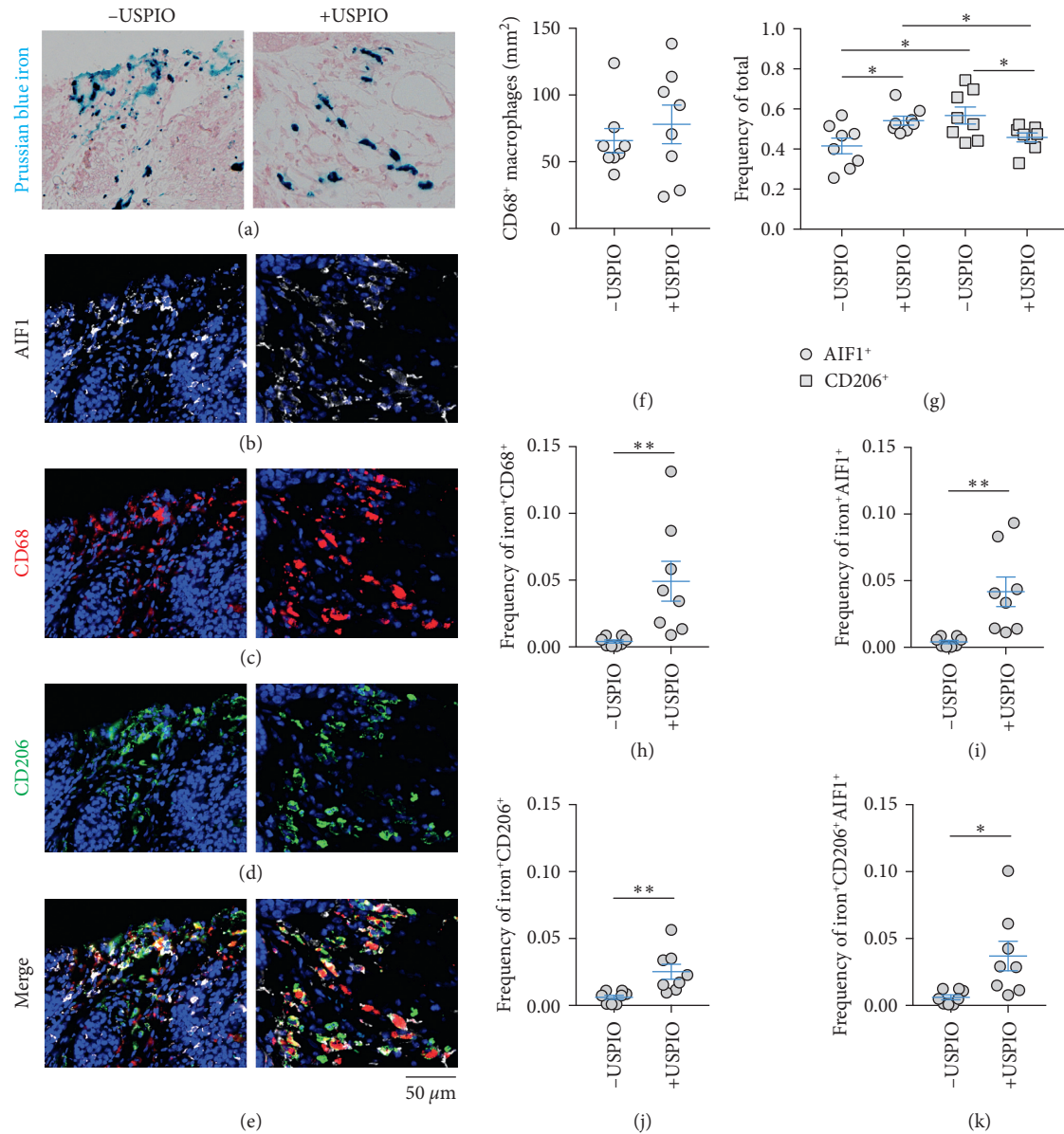


FIGURE 3: Characterization of endogenous and contrast-enhanced macrophage iron deposit polarization. Fields of paraffin-embedded tumor cross sections from control (left, -USPIO) and iron nanoparticle-injected (right, +USPIO) mice showing deposits of (a) Prussian blue iron⁺ macrophages and colocalized (b) AIF1, (c) CD68, (d) CD206, and (e) merged immunofluorescent markers. (f) Absolute count of CD68⁺ macrophages per mm² tumor cross section and (g) frequency of total M1-like (AIF1) and M2-like (CD206) macrophages determined by whole tumor cross section ROI analysis of immunofluorescent images in control (-USPIO) and nanoparticle-injected (+USPIO) cohorts (mean ± SEM shown, *n* = 8 tumors/group, **p* < 0.05, two-tailed Student's *t*-test). Frequency of total iron⁺ macrophage calculated as (h) iron⁺CD68⁺/CD68⁺, (i) iron⁺AIF1⁺/AIF1⁺, (j) iron⁺CD206⁺/CD206⁺, and (k) iron⁺CD206⁺AIF1⁺/CD206⁺AIF1⁺ cells (mean ± SEM shown, *n* = 8 tumors/group, **p* < 0.05, ***p* < 0.01, two-tailed Student's *t*-test). Scale bar is shown for all images.

polarization was also performed in the USPIO-injected animals and showed that M1 and M2 status was significantly different with 54% AIF1⁺ and 46% CD206⁺ TAMs present (*p* < 0.05) indicating that USPIO injection caused a significant increase in M1-like cells and reduction of M2-like cells (*p* < 0.05). This demonstrates that TAM polarization and not number of macrophages in the tissue changed as a function of iron nanoparticle injection in these measurements.

We then measured the frequency of specifically iron⁺-polarized TAMs with respect to their respective general population (iron⁺M1⁺ or iron⁺M2⁺/M1⁺ or M2⁺), performed counts of iron⁺CD68⁺ cells as a function of total CD68, and also counted the frequency of the iron⁺AIF1⁺CD206⁺ population expressing both general macrophage polarization markers selected in this study (Figures 3(h)–3(k)). The numbers of iron⁺ cells were less frequent than the general populations assessed above. In control tumors, 0.41% were

iron⁺, 0.40% of AIF1⁺ were iron⁺, 0.61% of CD206⁺ TAMs were iron⁺, and 0.60% were iron⁺AIF1⁺CD206⁺ cells. Injection of USPIO led to significant increases in all these macrophage subsets with 4.9% iron⁺CD68⁺ cells ($p < 0.01$), 4.1% iron⁺AIF1⁺ ($p < 0.01$), 2.5% iron⁺CD206⁺ ($p < 0.01$), and 3.7% iron⁺AIF1⁺CD206⁺ cells observed after USPIO injection ($p < 0.05$). This indicates that SPIO injection increases iron in all polarized macrophage subsets but also indicates that inflammatory subsets take up relatively, but not significantly ($p > 0.05$), more iron than M2-like populations.

3. Discussion

The main purpose of the current work was to evaluate a computer vision method for detection and quantification of USPIO-enhanced macrophages by MRI and extend this analysis to histological images in order to characterize sub-MRI pixel phenotypes of the cells. By targeting the spatial heterogeneity in iron-based pixel contrast arising from endogenous or iron contrast agent-enhanced cellular iron deposits, this approach improved statistical quantification of macrophages over conventional ROI-average distribution analysis, and provided measured constraints on the size and frequency of the polarized macrophage deposits.

The MRI analysis approach presented here improves on current conventional ROI-based approaches by parsing the spatial distributions of iron image contrast. This was accomplished by constructing parametric iron MRI maps and then quantifying the number and size of pixel cluster areas as a function of stratified iron concentration range. This indicated that most of the area of tumor pixels in both control and nanoparticle-injected groups were predominantly of low iron contrast, reflecting a cellular distribution characteristic of the location of low-iron cancer cells and stroma in the tumor. The ROI distribution analysis only revealed minor shifts towards high iron concentrations with USPIO injection, while counting of the localized iron clusters increased the statistical differences between the control and USPIO-injected groups. A similar approach was used to evaluate the size of macrophage iron deposits in the histological analysis with and without contrast agents. This revealed areas of iron-laden macrophage colonies that were on the order of the size and frequency of the high-iron MRI clusters. This side-by-side spatial analysis confirmed the cellular sensitivity and specificity of the MRI and histological methods for detecting localized macrophage deposits according to the iron status, and provided per unit area cellularity estimates of the iron-laden macrophages detected *in vivo* by MRI.

To complement the iron histology analysis, we also performed immunofluorescent imaging focusing on the microenvironment and polarization characteristics of both general macrophage populations and specifically the iron⁺ macrophage subpopulations. The polarization of macrophages is a multifactorial process that depends on the tissue and microenvironment in which they are found as well as complex signaling between tissue resident and infiltrating immune cells with the macrophages [31, 32].

As such, myriad intracellular and surface protein markers have been developed that allow one to specify their position along the continuum of accessible polarization states [33]. Iron itself is a central metabolic factor in macrophage function and is associated with many polarization states [21]. To determine the association of iron deposits with the tumor microenvironment and polarization, we adopted a panel of general tissue and macrophage biomarkers which showed the iron⁺ macrophages were predominantly found in vascularized CD31⁺ regions of the stroma where they likely serve iron-handling functions in heme homeostasis [34–36]. Overall, these iron⁺ macrophages were found as a subpopulation of the total macrophages detected in the whole cross sections of stained tissues. Characterization of these general populations indicated that frequency of CD68⁺ macrophage infiltrates remained approximately unchanged with USPIO injection and further confirmed previous studies indicating that phenotypic inflammatory M1-like macrophage markers are increased and protumor M2-like phenotypes decreased with USPIO injection.

In our spatial analysis, we further characterized effects of USPIO on polarized endogenous and nanoparticle-enhanced iron⁺ macrophage deposits. We observed that USPIO injections increase iron in pan-macrophage CD68⁺ populations as expected and also found relative differences in frequency of iron-laden populations following USPIO injection in polarized subsets. Here, although inflammatory (AIF1⁺), wound-healing (CD206⁺), and double-positive macrophage populations (AIF1⁺CD206⁺) all increased frequency with USPIO injection, inflammatory macrophage populations experienced the largest relative increases presumably due to their predominant role in iron scavenging during the acute inflammatory response caused by the iron nanoparticles [22–24]. Therefore, spatial histological segmentation approaches based on iron status combined with macrophage polarization measurements in these regions allow for the further characterization of subpixel phenotypes of the iron-laden macrophage giving rise to the contrast measured by MRI. This provides further insight into the biological function of the macrophages detected and reveals differences in their iron handling roles in the tumor microenvironment.

4. Conclusions

While the spatial image analysis approach described here is based on identification of the macrophage according to the iron status, similar machine-based analyses are envisioned to be conducted utilizing other parametric MRI contrasts and other multimodality imaging contrasts. Further, in the current work, the approach is specific for the macrophage due to their high innate capacity for iron uptake; however, integrating other endogenous and contrast-agent enhanced parameters with these analysis tools can also potentially provide spatial information about different cellular populations in diverse tissues settings. We anticipate that the current findings will motivate the use of computer-assisted image analysis routines and accelerate the translation of these methods towards the clinic to aid in our imaging investigations of complex cellular microenvironments and physiological processes in diseases such as cancer.

5. Methods

5.1. Animal Procedures. All animal work was approved and performed according to the guidelines of the Animal Care and Use Committee of MSKCC. Mice were anesthetized with 1–3% isoflurane in O₂ gas, and respiration was monitored during all imaging sessions. Female 6-week-old FVB/N mice underwent orthotopic injection into the lower mammary fat pad of 1×10^6 syngeneic TS1 MMTV-PyMT tumor cells grown under standard tissue culture conditions and suspended in 100 μ L 50% Matrigel (BD Bioscience). Mice bearing orthotopic TS1 MMTV-PyMT tumors (approximately 1 cm³) were injected with either 0.5 mmol/kg dextran coated superparamagnetic 5 nm iron oxide nanoparticle contrast agent (Ocean NanoTech) or saline and were imaged 24 hr after injection.

5.2. MRI. ¹H MRI was conducted on a 7T/30 cm horizontal bore Biospec MRI system (Bruker BioSpin Corporation) with a custom-built 30 mm inner-diameter transmit-receive quadrature coil. A 2D multigradient echo (MGE) relaxation pulse sequence with fat suppression was used with the following parameters: 16 evenly spaced 3 ms TEs, TR 1.2 s, matrix 256 \times 256 in the plane data matrix with 25–49 slices, an in-plane spatial resolution of 0.1 mm \times 0.1 mm with a slice thickness of 0.5 mm, and RF flip angle of 90°. Each phase encode acquisition was gated on the animal's respiratory cycle. The first image of the gradient-echo series was used as reference images shown in the figures.

Aqueous solutions of Fe³⁺(NO₃)₃ (Fisher Scientific) were used as reference iron concentrations over the 0.0–0.3 mg iron(III) g⁻¹ range at 7T [29]. The T_2^* values for these solutions were determined by pixel-wise mono-exponential fitting of the MGE images using Matlab (Mathworks) and/or Fiji [37]. A linear relation between the relaxation rate $R_2^* = 1/T_2^*$ and known iron concentration was found and was subsequently used to generate parametric iron MRI maps. Iron MRI maps were stratified by high concentration (total range, 0.0–0.3 mg·g⁻¹; high, 0.15–0.3 mg·g⁻¹). Spatial characteristics of the high-iron pixels were then quantified by performing cluster analysis over whole tissue MRI cross sections with the Fiji Analyze Cluster tool.

5.3. Histology. Whole tissue cross sections were sliced from the axial midpoint regions of PBS-perfused tumors following MRI studies, fixed in 4% PFA for 24 hours at 4°C, and then washed with H₂O and resuspended in 70% ethanol (Fisher Scientific). Tissues were paraffin embedded, cut into 5 μ m sections, and placed on glass slides for immunohistochemistry.

The Prussian blue histochemical detection of iron(III) was performed by manually deparaffinizing in xylene and rehydration in series of alcohol dilutions (100%, 95%, and 70%) and tap water. Slides were then placed in a working solution of equal parts of 10% potassium ferricyanide (Fisher Scientific) and 10% hydrochloric acid (Fisher Scientific) prepared in distilled water and stained for 30 minutes. Slides were rinsed in distilled water, counterstained with nuclear-fast red, and cover slipped with Permount (Fisher Scientific).

The immunofluorescent detection of F4/80, CD31, CD68, AIF1, and CD206 was performed using a Discovery XT processor (Ventana Medical Systems). The tissue sections were deparaffinized with EZPrep buffer (Ventana Medical Systems), antigen retrieval was performed with the CC1 buffer (Ventana Medical Systems), and sections were blocked for 30 minutes with Background Buster solution (Innovex) followed by avidin/biotin blocking for 8 minutes. F4/80 (Abcam, cat# ab6640, 5 μ g/ml), CD31 (Dianova, cat# DIA-310 1 μ g/ml), CD68 (Boster, cat# PA1518, 5 μ g/ml), AIF1(Wako, cat# 019-19741, 0.5 μ g/ml), and CD206 (Abcam, cat# ab64693, 1 μ g/ml) were applied, and sections were incubated for 5 hours, followed by 60 minutes incubation with biotinylated goat anti-rabbit antibodies (Vector Labs, cat# PK6101) at 1 : 200 dilution. The detection was performed with Streptavidin-HRP D (part of the DABMap kit, Ventana Medical Systems), followed by incubation with Tyramide Alexa Fluor A488 (Invitrogen, cat# T20922), Tyramide Alexa Fluor 568 (Invitrogen, cat# T20948), or Tyramide Alexa 647 (Invitrogen, cat# B40958), respectively, prepared according to manufacturer's instructions with predetermined dilutions. After staining, slides were counterstained with DAPI (Sigma-Aldrich, cat# D9542, 5 μ g/ml) for 10 min and coverslipped with Mowiol. Histological sections were digitized with a Mirax Scan system and read with Panoramic Viewer (3DHISTECH, Budapest, Hungary). Images were first visually inspected, and then the whole images were exported and processed in Fiji. Iron deposits were quantified as described by Leftin et al. [29]. Briefly, iron deposit maps were generated by resizing the histological images by using pixel averaging and bilinear interpolation to down-sample the image size (1 : 100) to the resolution of the MRI experiment. The resulting masks of regions containing iron⁺ macrophages were discretized by watershed gradient processing, and spatial characteristics of the clusters were determined using the Fiji Analyze Cluster tool. The number of iron⁺ macrophages per cluster was then determined by using the cluster maps to define regions of interest for cell counts in the full-resolution histological images. Polarization state was determined by either exhaustive whole cross section counting of AIF1 or CD206 immunostained macrophages or localized analysis that was restricted to colocalized iron⁺ macrophages contained in the iron deposit regions.

5.4. Statistics. Two-tailed Student's *t*-tests were performed with significance determined as $p < 0.05$. All statistical calculations indicated in the text were performed with the GraphPad Prism 7 Software.

Data Availability

All supporting data are found in the manuscript.

Conflicts of Interest

The authors declare that they have no conflicts of interest.

Acknowledgments

We thank the Molecular Cytology Core Facility at the Memorial Sloan Kettering Cancer Center for histological processing services. This study was funded by National Institutes of Health PO1 (CA115675) and P30 (CA008748), Department of Defense (BC161705), and the National Cancer Institute Kirschstein National Research Service Award Individual Postdoctoral Fellowship (1F32CA206277).

References

- [1] R. Weissleder and M. Nahrendorf, "Advancing biomedical imaging," *Proceedings of the National Academy of Sciences*, vol. 112, no. 47, pp. 14424–14428, 2015.
- [2] J. R. McCarthy and R. Weissleder, "Multifunctional magnetic nanoparticles for targeted imaging and therapy," *Advanced Drug Delivery Reviews*, vol. 60, no. 11, pp. 1241–1251, 2008.
- [3] H. E. Daldrup-Link, "Ten things you might not know about iron oxide nanoparticles," *Radiology*, vol. 284, no. 3, pp. 616–629, 2017.
- [4] G. B. Toth, C. G. Varallyay, and A. Horvath, "Current and potential imaging applications of ferumoxytol for magnetic resonance imaging," *Kidney International*, vol. 92, no. 1, pp. 47–66, 2017.
- [5] J. Condeelis and R. Weissleder, "In vivo imaging in cancer," *Cold Spring Harbor Perspectives in Biology*, vol. 2, no. 12, article a003848, 2010.
- [6] M. A. Miller, S. Arlauckas, and R. Weissleder, "Prediction of anti-cancer nanotherapy efficacy by imaging," *Nanotheranostics*, vol. 1, no. 3, pp. 296–312, 2017.
- [7] R. Weissleder, M. C. Schwaiger, S. S. Gambhir, H. Hricak et al., "Imaging approaches to optimize molecular therapies," *Science Translational Medicine*, vol. 8, no. 355, article 355ps16, 2016.
- [8] W. Liu and J. A. Frank, "Detection and quantification of magnetically labeled cells by cellular MRI," *European Journal of Radiology*, vol. 70, no. 2, pp. 258–264, 2009.
- [9] R. Kuhlper, H. Dahnke, L. Matuszewski et al., " R_2 and R_2^* mapping for sensing cell-bound superparamagnetic nanoparticles: in vitro and murine in vivo testing," *Radiology*, vol. 245, no. 2, pp. 449–457, 2007.
- [10] J. Zhang, H. L. Ring, K. R. Hurley et al., "Quantification and biodistribution of iron oxide nanoparticles in the primary clearance organs of mice using T1 contrast for heating," *Magnetic Resonance in Medicine*, vol. 78, no. 2, pp. 702–712, 2017.
- [11] R. P. Moonen, P. van der Tol, S. J. C. G. Hectors, L. W. E. Starmans, K. Nicolay, and G. J. Strijkers, "Spin-lock MR enhances the detection sensitivity of superparamagnetic iron oxide particles," *Magnetic Resonance in Medicine*, vol. 74, no. 6, pp. 1740–1749, 2015.
- [12] S. Liu, S. Buch, Y. Chen et al., "Susceptibility-weighted imaging: current status and future directions," *NMR Biomed*, vol. 30, no. 4, p. e3552, 2017.
- [13] R. Fischer and P. R. Harmatz, "Non-invasive assessment of tissue iron overload," *Hematology*, vol. 2009, no. 1, pp. 215–221, 2009.
- [14] M. W. Garbowski, J.-P. Carpenter, G. Smith et al., "Biopsy-based calibration of $T2^*$ magnetic resonance for estimation of liver iron concentration and comparison with R2 Ferriscan," *Journal of Cardiovascular Magnetic Resonance*, vol. 16, no. 1, pp. 1–40, 2014.
- [15] A. Neuwelt, N. Sidhu, C.-A. A. Hu, G. Mlady, S. C. Eberhardt, and L. O. Sillerud, "Iron-based superparamagnetic nanoparticle contrast agents for MRI of infection and inflammation," *American Journal of Roentgenology*, vol. 204, no. 3, pp. w302–w313, 2014.
- [16] E. M. Shapiro, S. Skrtic, K. Sharer, J. M. Hill, C. E. Dunbar, and A. P. Koretsky, "MRI detection of single particles for cellular imaging," *Proceedings of the National Academy of Sciences*, vol. 101, no. 30, pp. 10901–10906, 2004.
- [17] S. Jaiswal, M. P. Chao, R. Majeti, I. L. Weissman et al., "Macrophages as mediators of tumor immunosurveillance," *Trends in Immunology*, vol. 31, no. 6, pp. 212–219, 2010.
- [18] R. Noy and J. W. Pollard, "Tumor-associated macrophages: from mechanisms to therapy," *Immunity*, vol. 17, pp. 49–61, 2014.
- [19] B. Ruffell and L. M. Coussens, "Macrophages and therapeutic resistance in cancer," *Cancer Cell*, vol. 27, no. 4, pp. 462–472, 2015.
- [20] G. Corna, L. Campana, E. Pignatti et al., "Polarization dictates iron handling by inflammatory and alternatively activated macrophages," *Haematologica*, vol. 95, no. 11, pp. 1814–1822, 2010.
- [21] S. Recalcati, M. Locati, E. Gammella, P. Invernizzi, G. Cairo et al., "Iron levels in polarized macrophages: regulation of immunity and autoimmunity," *Autoimmunity Reviews*, vol. 11, no. 12, pp. 883–889, 2012.
- [22] M. Costa da Silva, M. O. Breckwoldt, F. Vinchi et al., "Iron induces anti-tumor activity in tumor-associated macrophages," *Frontiers in Immunology*, vol. 8, p. 1479, 2017.
- [23] A. Laskar, J. Eilertsen, W. Li, X.-M. Yuan et al., "SPION primes THP1 derived M2 macrophages towards M1-like macrophages," *Biochemical and Biophysical Research Communications*, vol. 441, no. 4, pp. 737–742, 2013.
- [24] S. Zanganeh, G. Hutter, R. Spitler et al., "Iron oxide nanoparticles inhibit tumour growth by inducing pro-inflammatory macrophage polarization in tumour tissues," *Nature Nanotechnology*, vol. 11, no. 11, pp. 986–994, 2016.
- [25] A. J. Tavares, W. Poon, Y.-N. Zhang et al., "Effect of removing Kupffer cells on nanoparticle tumor delivery," *Proceedings of the National Academy of Sciences*, vol. 114, no. 51, pp. E10871–E10880, 2017.
- [26] R. A. Brooks, J. Vymazal, C. D. Baumgarner, V. Tran, J. W. M. Bulte et al., "Comparison of T2 relaxation in blood, brain, and ferritin," *Journal of Magnetic Resonance Imaging*, vol. 5, no. 4, pp. 446–450, 1995.
- [27] K. R. Thulborn, A. G. Sorensen, N. W. Kowall et al., "The role of ferritin and hemosiderin in the MR appearance of cerebral hemorrhage: a histopathologic biochemical study in rats," *American Journal of Roentgenology*, vol. 154, no. 5, pp. 1053–1059, 1990.
- [28] X. Zhou, R. L. Magin, J. C. Alameda, H. A. Reynolds, and P. C. Lauterbur, "Three-dimensional NMR microscopy of rat spleen and liver," *Magnetic Resonance in Medicine*, vol. 30, no. 1, pp. 92–97, 1993.
- [29] A. Leftin, N. Ben-Chetrit, F. Klemm, J. A. Joyce, and J. A. Koutcher, "Iron imaging reveals tumor and metastasis macrophage hemosiderin deposits in breast cancer," *PLoS One*, vol. 12, no. 9, Article ID e0184765, 2017.
- [30] A. Leftin, H. Zhao, M. Turkecul, E. de Stanchina, K. Manova, and J. A. Koutcher, "Iron deposition is associated with differential macrophage infiltration and therapeutic response to iron chelation in prostate cancer," *Scientific Reports*, vol. 7, no. 1, p. 11632, 2017.

- [31] S. Gordon, A. Plueddemann, and F. M. Estrada, "Macrophage heterogeneity in tissues: phenotypic diversity and functions," *Immunological Reviews*, vol. 262, no. 1, pp. 36–55, 2014.
- [32] E. Van Overmeire, D. Laoui, J. Keirsse, J. A. Van Ginderachter, and A. Sarukhan, "Mechanisms driving macrophage diversity and specialization in distinct tumor microenvironments and parallelisms with other tissues," *Frontiers in Immunology*, vol. 5, p. 127, 2014.
- [33] A. Sica and A. Mantovani, "Macrophage plasticity and polarization: *in vivo* veritas," *Journal of Clinical Investigation*, vol. 122, no. 3, pp. 787–795, 2012.
- [34] C. E. Lewis and J. W. Pollard, "Distinct role of macrophages in different tumor microenvironments," *Cancer Research*, vol. 15, pp. 605–612, 2006.
- [35] J. W. Pollard, "Tumor-educated macrophages promote tumor progression and metastasis," *Nature Reviews Cancer*, vol. 4, no. 1, pp. 71–78, 2004.
- [36] E. Gammella, P. Buratti, G. Cairo, and S. Recalcati, "Macrophages: central regulators of iron balance," *Metallomics*, vol. 6, no. 8, pp. 1336–1345, 2014.
- [37] J. Schindelin, I. Arganda-Carreras, E. Frise et al., "Fiji: an open-source platform for biological-image analysis," *Nature Methods*, vol. 28, no. 7, pp. 676–682, 2012.

Review Article

How to Modulate Tumor Hypoxia for Preclinical In Vivo Imaging Research

Sven De Bruycker ¹, **Christel Vangestel**,^{1,2} **Steven Staelens**,¹ **Tim Van den Wyngaert**,^{1,2} and **Sigrid Stroobants** ^{1,2}

¹Molecular Imaging Center Antwerp (MICA), University of Antwerp, Universiteitsplein 1, 2610 Wilrijk, Antwerp, Belgium

²Department of Nuclear Medicine, Antwerp University Hospital (UZA), Wilrijkstraat 10, 2650 Edegem, Antwerp, Belgium

Correspondence should be addressed to Sigrid Stroobants; sigrid.stroobants@uza.be

Received 9 May 2018; Revised 24 July 2018; Accepted 13 August 2018; Published 18 October 2018

Academic Editor: Pablo Aguiar

Copyright © 2018 Sven De Bruycker et al. This is an open access article distributed under the Creative Commons Attribution License, which permits unrestricted use, distribution, and reproduction in any medium, provided the original work is properly cited.

Tumor hypoxia is related with tumor aggressiveness, chemo- and radiotherapy resistance, and thus a poor clinical outcome. Therefore, over the past decades, every effort has been made to develop strategies to battle the negative prognostic influence of tumor hypoxia. For appropriate patient selection and follow-up, noninvasive imaging biomarkers such as positron emission tomography (PET) radiolabeled ligands are unprecedentedly needed. Importantly, before being able to implement these new therapies and potential biomarkers into the clinical setting, preclinical in vivo validation in adequate animal models is indispensable. In this review, we provide an overview of the different attempts that have been made to create differential hypoxic in vivo cancer models with a particular focus on their applicability in PET imaging studies.

1. Background

Hypoxia, which frequently occurs in solid tumors, is related with an aggressive phenotype, chemo- and radiotherapy resistance, and thus a poor clinical outcome. To a considerable extent, hypoxia-inducible factor-1 (HIF-1), the major transcriptional regulator of the cellular response to hypoxia (Figure 1), is responsible for these observed phenomena. Encouragingly, tremendous progress with strategies to overcome the unfavorable effects of hypoxia has been made, paving the way for new personalized medicine opportunities. However, as not all patients will benefit from this new, promising radiosensitizing treatment schedules, molecular biomarkers are of utmost importance for adequate patient selection. Imaging biomarkers, such as positron emission tomography (PET) radiolabeled compounds, allow non-invasive and longitudinal assessment of molecular and functional characteristics of a tumor, thereby coping with inter- and intratumoral heterogeneity. Therefore, over the past decades, imaging biomarkers have tremendously increased in significance.

From this perspective, adequate animal models may accelerate translation of new therapies and personalized approaches, and also potential new molecular imaging biomarkers, into routine clinical practice. In hypoxia research in particular, it is often crucial to be able to distinguish between a positive and negative model for tumor hypoxia, i.e., tumors that are poorly and well oxygenated, respectively. Obviously, these models should also accurately reflect human disease. From this point of view, cell-line derived xenograft models may be inferior to genetically engineered models, orthotopic models, or patient-derived xenografts [1]. However, based on historic knowledge obtained in subcutaneous xenograft models, the fact that tumors are externally visible and easily measurable and the relatively straightforward experimental procedures that are required for their creation and follow-up, subcutaneous models are still frequently used in preclinical cancer studies, including hypoxia research.

A prerequisite to be able to differentiate between a positive and negative model for tumor hypoxia is the availability of methods to quantify tumor oxygenation. To

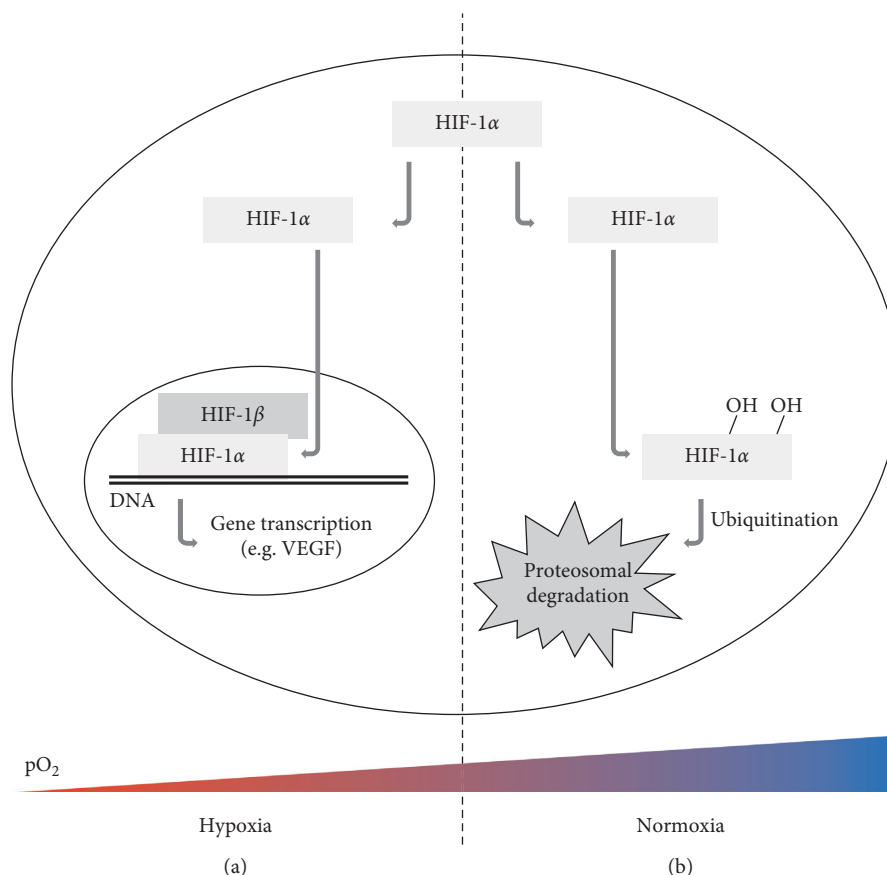


FIGURE 1: The HIF-1 pathway. (a) Under hypoxic conditions, HIF-1 α stabilizes, and its transcriptional activity is regulated by heterodimerization with the constitutively expressed HIF-1 β and binding to the hypoxia-response elements in the promoters of genes that regulate a variety of biological processes. These include genes involved in tumor survival, progression, and proliferation, such as VEGF. (b) Under normoxic conditions, the HIF-1 α subunit is rapidly degraded by the proteasome after hydroxylation and ubiquitination.

date, a variety of techniques has been used to measure tumor hypoxia, as recently reviewed by Fleming et al. [2]: oxygen (O₂) electrodes such as OxyLite; electron paramagnetic resonance (EPR); histological assessment with extrinsic biomarkers, mainly pimonidazole, and intrinsic biomarkers such as carbonic anhydrase IX (CAIX); blood O₂ level-dependent (BOLD) magnetic resonance imaging (MRI); and single photon emission tomography (SPECT) or PET with for instance hypoxia-targeting 2-nitroimidazole-based radiotracers [2, 3]. However, correlations between the different measuring techniques are often absent [4, 5] as they all provide information on different locations within the tumor, e.g., intracellular hypoxia, interstitial hypoxia, or blood oxygenation [2]. Moreover, some techniques such as OxyLite inevitably damage the tumor tissue. Therefore, the question remains if one of these techniques can be considered as the reference standard for measuring tumor hypoxia.

Over the past decades, several 2-nitroimidazole derivatives have been developed for hypoxia PET imaging (Figure 2). [¹⁸F]fluoromisonidazole ([¹⁸F]FMISO), considered as the prototype tracer, is a lipophilic compound that is highly metabolized in the liver and cleared via hepatobiliary and gastrointestinal pathways. The more hydrophilic

next-generation 2-nitroimidazole derivatives, such as [¹⁸F]flortanidazole ([¹⁸F]HX4), have better pharmacokinetic properties, resulting in chiefly renal excretion of the intact compound and only limited (<20%) hepatobiliary clearance. This gives rise to improved hypoxia-to-normoxia tissue ratios and thus images with higher contrast in comparison to [¹⁸F]FMISO [2,6–9].

Molecular imaging techniques, such as PET with 2-nitroimidazole-based probes (Figure 2), may offer considerable advantages over the other techniques because of their noninvasive nature, accuracy and reliability, and the opportunity to measure hypoxia directly, both spatially and temporally [2, 10]. From the preclinical point of view, PET imaging has the added advantages that its use is directly translatable to the clinic and that the same set of animals can be followed over time, thereby reducing the required number of animals for a single experiment and allowing individual therapy response assessments. Since animals function as their own controls over time, their intrinsic intra-animal analysis increases statistical power [1].

Furthermore, PET imaging allows absolute quantification of hypoxia. Ideally, this is achieved by performing dynamic acquisitions and kinetic modelling [11]. Accordingly, longer anesthesia regimens will be required, and

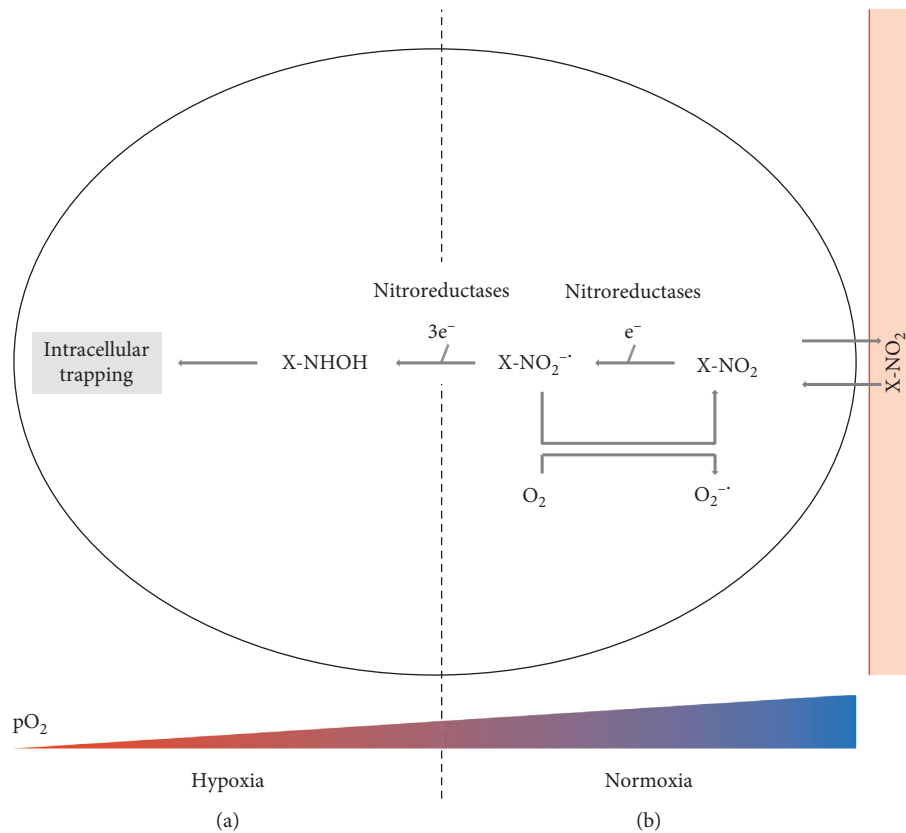


FIGURE 2: The binding mechanism of 2-nitroimidazole tracers here represented as X-NO₂. (a) Under hypoxic conditions, tracer diffuses into the cell, where the NO₂ group undergoes a series of reductions and some of the intermediate products that are formed during these reactions will bind to macromolecules within the cell. (b) Under normoxic conditions, the first reduction is reversed, giving rise to the original compound which can unhindered exit the cell. Importantly, for removal of 2-nitroimidazole background signal, an uptake time of minimal 3 hours is needed [3].

especially for hypoxia imaging, this may induce (re)oxy- genation (cf Section 2.3.1). Evidently, dynamic imaging also decreases the experimental throughput [12] which might prove cumbersome in large groups of animals ideally being scanned in identical hypoxia settings. Therefore, most studies use semiquantitative parameters derived from static images, such as standardized uptake values (SUV) or tumor-to-background ratios (TBR). Importantly, as it has been shown that these static parameters are time-dependent [3, 13, 14], it should always be taken into account that these semiquantitative approaches inherently lead to higher degrees of inaccuracy. To a certain extent, this can be overcome by respecting and maintaining an invariable tracer uptake time of at least 3 hours within an experimental set-up [3, 13]. However, for the more hydrophilic next-generation hypoxia tracers such as [¹⁸F]HX4, which are dependent on renal clearance, interanimal variability will remain substantial, due to intrinsic differences in kidney function [3]. In line with this, in therapy response evaluation studies, in which animals undergo multiple PET scans (i.e., pre- and post-therapy), drug-induced alterations of renal excretion may influence tracer clearance [3]. Unfortunately, no established standardized quantification methodologies have been developed for hypoxia PET imaging yet, particularly in the preclinical setting. Therefore, the difficulties discussed

above need to be confronted when analyzing hypoxia PET images.

In this review, we provide an overview of the different experimental approaches and study designs that may be applicable for manipulating the tumor oxygenation state for in vivo hypoxia research (Figure 3) with a particular focus on preclinical hypoxia PET imaging, considering the inherent difficulties of this imaging technique. For each modulation approach, we will indicate its respective opportunities and pitfalls, and share our own experiences and the difficulties we run up against in our own attempts to create a differential hypoxia murine cancer or tumor model.

2. Generating Differential Hypoxia in Tumor Models

2.1. Tumor Physiological Parameters

2.1.1. Inherent Variation without Manipulations. The ability to detect differential hypoxia in a single xenograft model without underlying external manipulation is the ultimate paradigm for in vivo cancer hypoxia research. However, where inoculation of some cancer cell lines inherently leads to tumors with different degrees of tumor hypoxia regardless of the tumor volume [15], this is not the case for other cell

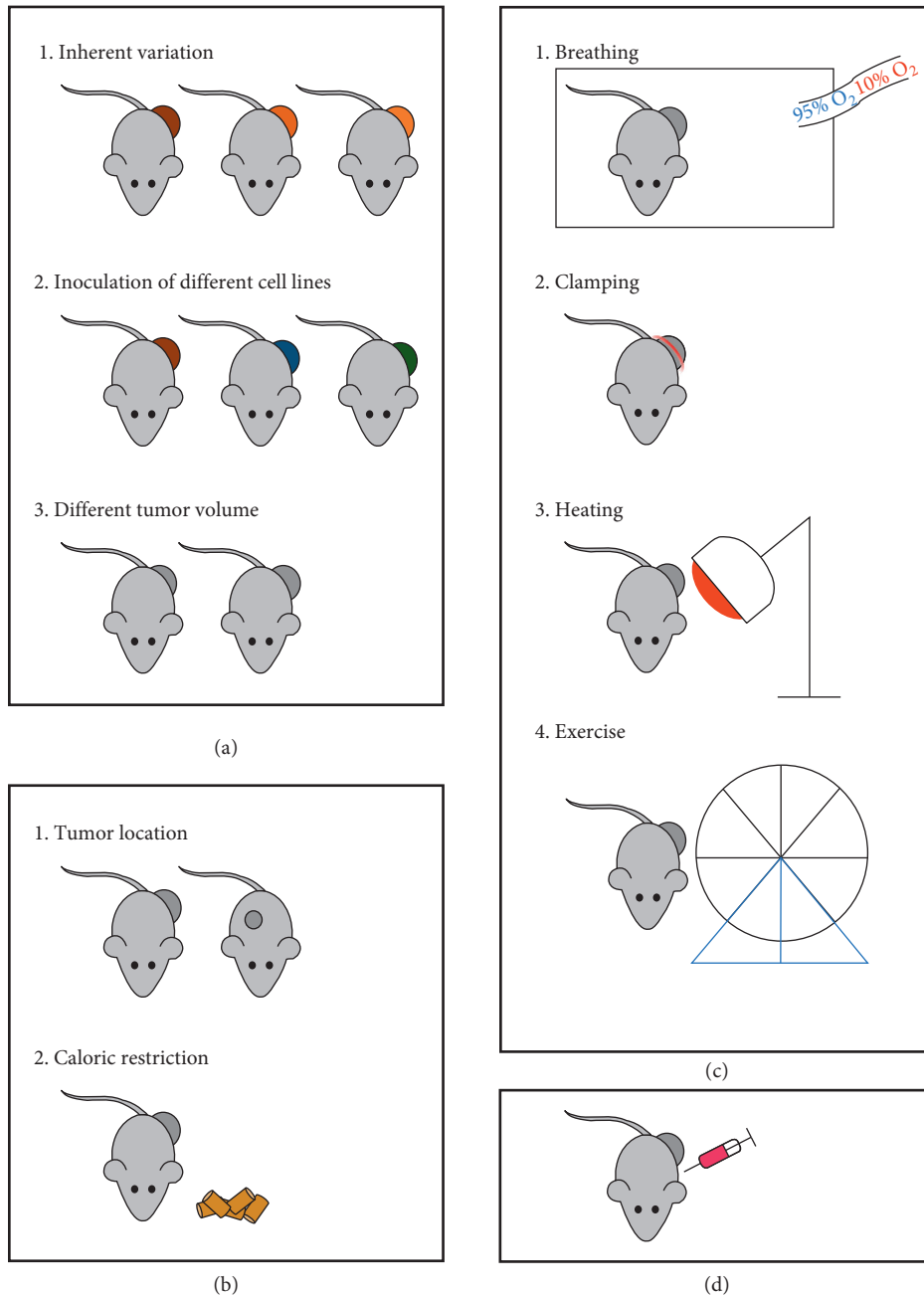


FIGURE 3: In vivo hypoxia modulation. Overview of the different experimental techniques and study designs that may be applicable for manipulating the tumor oxygenation state for hypoxia research. (a) Tumor physiological parameters. (b) Animal physiological parameters. (c) External interventions. (d) Pharmacological interventions.

lines. For instance, heterogeneous [¹⁸F]-2-nitroimidazol-pentafluoropropyl acetamide ([¹⁸F]EF5) uptake was observed in A549 non-small cell lung cancer (NSCLC) xenografts, but not in RKO and HT29 colon carcinoma xenograft models [16].

In some xenograft models, the observed intertumoral variation in tumor oxygenation allowed to show the properties of hypoxia PET as a predictive biomarker. For instance, considerable intertumoral variation in oxygenation has been observed in 9L glioma tumors, which enabled the

detection of significant correlations between [¹⁸F]EF5 uptake and response to single-dose radiotherapy [17]. In line with these results, Beck et al. performed [¹⁸F]fluoroazomycin arabinoside ([¹⁸F]FAZA) imaging on 67 EMT6 breast tumor-bearing mice and used the median tumor-to-background ratio to discriminate between hypoxic and normoxic tumors. Based on this distinction, significantly faster tumor growth of the hypoxic tumors as compared to their normoxic counterparts was observed. Moreover, it was

possible to show that administration of the radiosensitizer tirapazamine prior to radiotherapy was beneficial in hypoxic, but not in normoxic, tumors. Importantly, in this study, tumor volumes were uniformly distributed across both groups [18]. Similarly, it was found that baseline [^{18}F]FAZA TBR, which ranged from 1.17 to 5.83, was higher in radioresistant than in radiosensitive esophageal carcinoma xenograft tumors [19]. Finally, [^{18}F]FAZA TBR predicted that rhabdomyosarcoma and glioma tumors were sensitized to the effects of radiotherapy by nimorazole [20] and identified colorectal xenograft tumors that benefited from addition of the hypoxic prodrug evofosfamide to standard chemoradiotherapy regimens [21].

Despite these promising results which have been successful in validating the predictive character of hypoxia PET, this approach is not without pitfalls. For instance, in most cases, rather large cohorts of animals may be required to detect differential hypoxia, which is not preferable from an ethical point of view. Also, the relationship between tumor volume and oxygenation as such can also be an interfering factor and will therefore be discussed in a separate section (2.1.3) within this review. The most important concern may however be the lack of a clear cutoff value to discriminate between “hypoxic” and “normoxic” (i.e., “less hypoxic”) tumors in these studies. Indeed, the chosen thresholds that have been reported seem rather arbitrary [4,16,18–20,22], which renders the comparison of different studies difficult. Also, interpretation of intermediate values, i.e., values fluctuating around the threshold, may be complicated. Moreover, as these studies are predominantly semiquantitative and both SUV and TBR are extremely dependent on the pharmacokinetic properties of the used 2-nitroimidazole tracer and the PET imaging protocol [3, 14, 23], the comparison of studies with different tracers may be impossible in any case.

2.1.2. Inoculation of Different Cell Lines. The unique characteristics of different cancer cell lines give rise to different tumor phenotypes with typical features that will conceivably lead to differential tumor hypoxia. Using pimonidazole immunostaining and [^{18}F]FMISO, [^{18}F]-2-nitroimidazol-trifluoropropyl acetamide ([^{18}F]EF3) and [^{18}F]EF5 PET, differential tumor hypoxia could be observed in animal models of osteosarcoma [24], fibrosarcoma [7], glioma [25–27], head and neck cancer [28–31], lung cancer [15], melanoma [32], and prostate cancer [15, 33, 34] that were all derived from different cell lines, and in a panel of colorectal cancer (CRC) patient-derived xenograft tumors [21]. Similarly, the different stages of castration responsiveness in the Shionogi prostate cancer tumor model could be differentiated using [^{18}F]EF5 PET [35].

The investigation of different cell lines may be very relevant from a clinical point of view, as it may accurately reflect the high degree of intra- and intertumor heterogeneity observed in and between cancer patients. However, for fundamental research purposes, this approach may result in very complex analyses. When for instance therapy response is compared between different models, the different oxygenation status of the tumors may be only one of many

factors that influence therapy outcome. Indeed, the diverse genetic and phenotypic profiles arising from the different cell lines will also contribute to therapy responsiveness independently from the degree of hypoxia.

To undo the potential complexity of comparing experimental results obtained in tumors arising from different cell lines, knockdown or knockout cell lines can be used. In these cells, the expression of only one or some genes is either reduced or prevented, respectively. This allows the investigation of the functional roles of particular genes. The most obvious gene to be eliminated in regard to tumor hypoxia is HIF-1 (Figure 1). Using this approach, an inhibition in tumor growth was observed in subcutaneous HIF-1 knockout HCT116, but not RKO CRC xenograft models. Interestingly, the amount of hypoxia as determined with pimonidazole was not affected [36]. In subcutaneous lung and gastric xenograft tumors on the other hand, HIF-1 α knockdown stimulated tumor growth [37–39]. In the case of gastric cancer, knockdown additionally resulted in aggressive peritoneal dissemination via upregulation of matrix metalloproteinase-1 and in increased sensitivity to 5-FU chemotherapy through increased susceptibility to apoptosis and downregulation of drug efflux transporters [37–39]. In subcutaneous xenografts derived from HIF-1 α deficient embryonic stem cells, HIF-1 α deficiency resulted in accelerated tumor growth, decreased perfusion, and increases in tumor hypoxia as observed by pimonidazole staining [40, 41]. Genetic ablation of vascular endothelial growth factor (VEGF), a proangiogenic signal protein that is one of the downstream targets of HIF-1 (Figure 1), has been shown to give rise to increases in pimonidazole staining and thus tumor hypoxia on top of reductions in vascularity and tumor volume in a variety of tumors [36, 41–43]. Interestingly, genetic disruption of both HIF-1 and VEGF further inhibited CRC xenograft tumor growth as compared to VEGF disruption alone, but no additive effect on the hypoxic tumor compartments could be observed [36].

It should however be noted that the observed alterations in tumor vasculature rather than the degree of hypoxia itself may have influenced pimonidazole uptake (cf Section 2.4). Logically, this potential complication factor may also hold in PET imaging studies. The observed effects may also depend on the inoculation site. For instance, subcutaneous inoculation of HIF-1 α -deficient and VEGF-deficient transformed astrocytes resulted in reduced vessel density and tumor growth. Intracranial inoculation on the other hand led to accelerated growth of HIF-1 α -deficient tumor growth, whereas VEGF-deficient astrocytomas still exhibited a growth disadvantage. This suggests that the differences in the microenvironment and the vascular structure between the two inoculation sites determine the behavior and aggressiveness of the tumor [44]. The influence of the inoculation site on tumor hypoxia will be discussed more extensively in Section 2.2.1.

To wind up with, in orthotopic MDA-MB-231 breast cancer xenograft models, exposure of cells to hypoxic culturing conditions prior to inoculation not only accelerated tumor growth, but also contributed to multidrug resistance,

most importantly via increased HIF-1 α levels. Indeed, the hypoxia-driven induction of a differential protein expression makes this technique very interesting for imaging purposes. However, differences between tumors derived from hypoxic and normoxic cells tend to diminish with increases in tumor volume, starting from 100 mm³ onwards [45]. Moreover, the effects of in vitro exposure of cells to hypoxic conditions prior to inoculation may be tissue-dependent or cell line-dependent. Indeed, in recent studies, it was shown that xenografts from lung cancer cells cultured under hypoxic conditions show decelerated tumor growth but enhanced cell survival, whereas the same strategy resulted in accelerated subcutaneous tumor growth in a CRC model [46, 47]. In our own quest to create a differential hypoxic xenograft model, we investigated the effect of hypoxia-pretreatment of Colo205 cells 72 hours prior to inoculation. Fourteen days after inoculation, we observed a nonsignificant Colo205 tumor growth inhibition of 56% of the tumors arising from hypoxia-pretreated cells, but [¹⁸F]FMISO uptake was not affected by the hypoxia-pretreatment (Figure 4). This may not be surprising since tumor volume may also affect hypoxia tracer uptake, as discussed in Section 2.1.3. Therefore, seeing the unpredictable effect on tumor proliferation, we do not believe that exposure of cells to hypoxic conditions prior to inoculation is a reliable method for in vivo tumor hypoxia modulation.

2.1.3. Tumor Volume. In rat rhabdomyosarcoma tumors, it was observed that the hypoxic volume assessed with both pimonidazole staining and [¹⁸F]FMISO autoradiography increased with increases in tumor volume [48]. In murine sarcoma models on the other hand, inverse correlations between autoradiographically determined [¹⁸F]fluoroerythronitroimidazole ([¹⁸F]FETNIM) and tumor volume were found [49], whereas in other models, [¹⁸F]FETNIM, [¹⁸F]FMISO, or [¹⁸F]FAZA uptake did not correlate with tumor volume [50–52]. These conflicting observations may be due to the presence of tumor necrosis [49–51], since, 2-nitroimidazole PET tracers will be not retained by necrotic cancer cells. As necrosis may be more wide-spread in larger tumors [16], whether or not areas of necrosis are included within the determined volume of interest (VOI) can potentially lead to underestimation or slight overestimation of the amount of tumor hypoxia, respectively, dependent on the quantification method. These important observations should be considered particularly when exclusively focusing on tumor volume.

The use of autoradiographs allows an easy and accurate quantification of the amount of tumor necrosis, although only in ex vivo tissue samples. Corrections for the influence of necrosis on in vivo hypoxia are more complicated. For instance, in a CH3 mammary carcinoma model, [¹⁸F]FMISO TBR did not correlate with tumor volume, despite the existing correlation between tumor volume and pO₂ electrode measurements [5]. Again, this apparent discrepancy between these two measuring techniques has been attributed to the presence of tumor necrosis [54]. Indeed, the automatic thresholding technique which was used in this study to

delineate tumors on PET images [5] may exclude macroscopically necrotic areas without tracer uptake. The polarographic method on the other hand cannot distinguish between viable and necrotic tumor fractions. Interestingly however, by applying necrosis correction in murine rhabdomyosarcoma tumors, it was observed that polarographically-determined pO₂ values did not really change as tumors grew larger and did not correlate with the degree of necrosis, unless when tumors reached a weight of more than 2 grams [55].

Depending on the tumor delineation method (manual or automatic) on static PET images, areas of macroscopic necrosis will or will be not included within the VOI. Importantly, in studies that investigated the relationship between tumor volume and hypoxia PET tracer uptake [16,23,26,27,31,33,56–58], it is not always clear if areas of necrosis were included within the VOI, which renders the interpretation and comparability difficult. Moreover, the resolution of preclinical PET may in any case be too low to discriminate areas of microscopic necrosis. The use of parametric images based on different tracer uptake patterns over time between normoxic, hypoxic, and necrotic regions also looked promising to overcome these shortcomings [11], but the need for dynamic imaging may preclude general use in rodent models for tumor hypoxia.

To what extent tumor volume influences the degree of hypoxia remains an intriguing question. Therefore, we do not recommend the use of different volumes as a model for tumor hypoxia for preclinical PET investigations. If opting for this methodology regardless, the exclusion of macroscopic areas of necrosis during hypoxia PET tracer quantification is advisable.

Taken together, to be able to make a more well-defined distinction between “hypoxic” and “normoxic” tumors, and to broaden the intertumoral oxygenation range, experimental manipulation may be required. In what follows we will discuss the different procedures that have been adopted for this purpose.

2.2. Animal Physiological Parameters

2.2.1. Tumor Location. In a study by Graves et al., the uptake of the glucose analogue 2-deoxy-2-[¹⁸F]fluoro-D-glucose ([¹⁸F]FDG), [¹⁸F]FAZA, and pimonidazole was compared between genetically induced lung tumors in situ, subcutaneous, and orthotopic A549 xenograft models. [¹⁸F]FDG uptake was comparable between all models, whereas [¹⁸F]FAZA and pimonidazole were only trapped in subcutaneous tumors, but not in lesions growing within the lung. Those observations were confirmed by administering the hypoxic prodrug PR-104 to all models, as therapy response was only observed in subcutaneous tumors [59]. Taken together, these data show that the presence of hypoxia in lung cancer may depend on the inoculation site and thus the present microenvironment. It has been hypothesized that this may be either a result of the tumor vasculature being more functional in orthotopic than in subcutaneous tumors, or the accessibility of O₂ via the alveoli in orthotopic

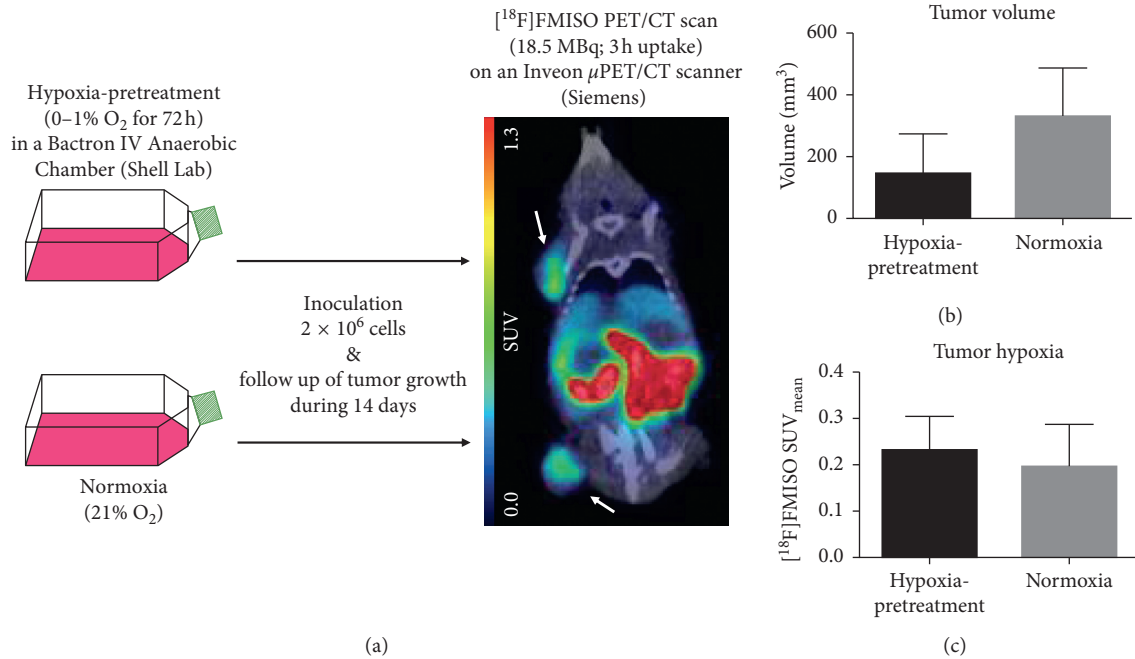


FIGURE 4: Hypoxia-pretreatment experiment, approved by the Antwerp University Ethical Committee (2012-69). All applicable institutional and European guidelines for animal care and use were followed. (a) Colo205 cells (Perkin Elmer) were exposed to hypoxia (0-1% O₂) for 72 h in a Bactron IV Anaerobic Chamber (Shell Lab) or to normoxia (21% O₂) in a common incubator. CD-1 nude mice (Charles River, $n = 5$) were inoculated with 2×10^6 “hypoxic” cells in the shoulder and with 2×10^6 “normoxic” cells in the hind leg. Fourteen days later, animals underwent a [18F]FMISO PET/CT scan as previously described [53]. Images were analyzed as previously described [53]. One representative mouse is shown. Arrows indicate tumors. As [18F]FMISO clearance mainly occurs via the hepatobiliary pathway and the gastrointestinal tract [8], tracer uptake can be observed in liver and intestines. (b) “Hypoxic” tumors were numerically, but not significantly, smaller than “normoxic” tumors ($144 \pm 129 \text{ mm}^3$ vs $328 \pm 158 \text{ mm}^3$ [mean \pm SEM], respectively; $p = 0.19$). (c) [18F]FMISO SUV did not differ between “hypoxic” and “normoxic” tumors (0.228 ± 0.074 vs 0.195 ± 0.090 , respectively; $p = 0.71$).

but not in subcutaneous tumors, thereby suggesting that this inoculation site-specific differential hypoxia is seen exclusively in lung cancer [60]. Nevertheless, our research group recently observed significantly lower tumor hypoxia, as assessed with CAIX immunohistochemistry, in an orthotopic CRC xenograft model as compared to subcutaneous tumors [61].

As already mentioned earlier in Section 2.1.2, the growth and differentiation of HIF-1 α -deficient and VEGF-deficient astrocytomas is also dependent on the inoculation site and its corresponding microenvironment [44]; however, the degree of hypoxia was not quantified in the cited study. Similarly, it has been observed that orthotopically and subcutaneously grown gliomas derived from the same cell line exhibit different gene expression profiles [62]. Thus, it is clear that the inoculation site influences tumor characteristics. Again, a major drawback of such technique is the different growth rate of subcutaneously and orthotopically growing tumors. Moreover, the different growth patterns [59] will inevitably lead to different tumor volumes. Both factors may complicate the interpretation of data on tumor hypoxia (cf Section 2.1.3).

2.2.2. Caloric Restriction. The Warburg effect, i.e., the upregulation of glycolysis in cancer cells regardless of the partial O₂ pressure, accounts for tumors’ high dependency

on the supply of nutrients, especially glucose. Therefore, caloric restriction (CR), which is the reduction in energy uptake without malnutrition as compared to ad libitum feeding, has been considered as a promising synergistic treatment option. CR can be achieved via different ways: via intermittent fasting, via short-term fasting, or via chronic daily energy restriction whereby animals are only fed a certain percentage of normal intake [63]. As tumor hypoxia is inextricably bound with the Warburg effect, CR may provide another obvious way to experimentally influence tumor oxygenation. Indeed, in A549 lung cancer xenograft models, it was shown with EF5 immunostaining that daily food restriction caused significant decreases in tumor hypoxia, on top of significant inhibition of tumor growth. In line with this, HIF-1 α expression, VEGF expression, and microvessel density (MVD) were all reduced [64]. Similar observations were made in rat, mouse, and human brain tumor models, where decreases in HIF-1 α , VEGF, and MVD could be observed [65, 66]. In line with this, it was shown in orthotopic allograft breast cancer models that CR and radiotherapy worked synergistically [67]. Within the context of tumor hypoxia, VEGF inhibition by CR was suggested to account for its observed radiosensitizing capacities, as this may result in vascular normalization and thus increases in the O₂ tension [63].

Taken together, these data are promising for the use of CR to create a differential hypoxic tumor model. However, it has been reported that some cell lines may be resistant for

CR [68]. Moreover, some considerations should be taken into account when using CR in combination with PET imaging. First, CR lowers blood glucose and body weight [63–67] and these disturbances should be taken into account during PET image quantification. Second, the dietary status may determine the intratumoral tracer distribution pattern. In A549 xenograft models, [^{18}F]FDG accumulated predominantly in the hypoxic cancer cells of fasted animals, whereas in fed animals, radiotracer accumulated in the noncancerous stroma [69]. Third, CR also influences tumor volume [64–67], which potentially could alter tumor hypoxia as discussed in Section 2.1.3.

2.3. External Interventions

2.3.1. Breathing. Mortensen et al. separated a hypoxic and a normoxic mammary carcinoma group based on the median [^{18}F]FAZA TBR, although in this study, intertumoral oxygenation heterogeneity was increased by exposing some of the animals to carbogen breathing prior to [^{18}F]FAZA scanning and radiotherapy [4]. The exposure of tumor-bearing animals acutely or chronically to a gas mixture containing a reduced O_2 concentration (e.g., 5–10% O_2) or, exactly the opposite, to an increased O_2 concentration (most commonly carbogen, i.e., 95% O_2), whether or not under hyperbaric pressure conditions, is indeed the most applied technique to modulate tumor oxygenation *in vivo*. In this way, O_2 diffusion distances decrease or increase, respectively, thereby deteriorating or improving the degree of chronic hypoxia within the tumor. In the study of Mortensen et al., significantly different tumor control probabilities were observed in both tumor groups. Interestingly, when the carbogen-breathing animals were excluded from the analysis, significance of the radiotherapy efficacy was lost. The authors therefore correctly suggested that in general, intertumoral variability in tumor hypoxia within one model may be too low without any external manipulations [4].

In a variety of cancer xenograft models, the breathing technique has proven to be very useful to detect different degrees of hypoxia with numerous hypoxia PET tracers, including [^{18}F]FMISO [5, 6, 14, 29, 50, 53, 70–72], [^{18}F]EF3 [6, 7, 73], [^{18}F]FETNIM [50], [^{18}F]FAZA [4, 14, 22, 71, 74, 75], [^{18}F]fluoroetanidazole ([^{18}F]FETA) [76], and [^{18}F]HX4 [8, 14, 77]. An important issue of this breathing technique is that tracer metabolism and trace uptake of background regions may also be affected [14], which may hamper image quantification using background normalization. It has been observed that carbogen or hypoxic gas breathing significantly altered [^{18}F]FMISO uptake in fat tissue [50] and [^{18}F]FETNIM and [^{18}F]FAZA uptake in muscle [14, 50, 71]. Similar observations were made by Cairns et al., who found drops in pO_2 in normal muscle tissue when animals breathed 5–7% O_2 and rises in pO_2 when ambient air was reintroduced [78]. Taken together, exposure to an altered breathing atmosphere obviously alters hypoxia tracer uptake of noncancerous tissue too. Therefore, it may not be appropriate to calculate TBRs, without thorough understanding of the magnitude and

dynamics of these changes. By contrast, it has also been argued that calculating TBRs is a way to anticipate the possible confounding effects on background tracer uptake [75].

Carbogen breathing is often combined with the administration of nicotinamide, a vitamin B3 derivate that induces vasodilation and thus improves tumor perfusion. In this way, not only chronic but also acute hypoxia can be counterbalanced [79]. Indeed, regional short-lived changes in blood flow could possibly influence tracer circulation and cause considerable day-to-day variations in hypoxia tracer uptake. Nevertheless, given the relatively low temporal resolution of (micro)PET (i.e., 10 seconds dynamic frames) and the long uptake period required for 2-nitroimidazole-based tracers, acute hypoxia may not be detectable with PET [80]. Moreover, in different models, it was shown that the combination of carbogen and nicotinamide gave rise to similar or even less pronounced decreases in the hypoxic fraction compared to carbogen alone [81, 82]. These two facts question the additional value of nicotinamide. In spite of this, it has been observed that depending on the amount of carbon dioxide in the gas mixture, breathing of a high- O_2 gas mixture may cause vasoconstriction [83], thereby deteriorating tumor oxygenation state and also tracer delivery. In this particular case, administering nicotinamide may compensate for that [75, 81, 84], but it should be noted that changes in tumor vascularity are not necessarily accompanied by a reduced accessibility of radionuclide tracers to tumor tissue [85, 86]. The eventual positive or negative influence of breathing an altered atmosphere on the oxygenation state and on tumor progression appears to be tissue-dependent and cell line-dependent [46, 83, 87–89].

The effectiveness of breathing models has also been shown in numerous experiments in which hypoxia-evoked therapy resistance was investigated. The most straightforward, yet clinically less relevant approach is the investigation of the influence of breathing an altered O_2 atmosphere on the effect of a single therapy dose. For instance, in fibrosarcoma, colon carcinoma, and hepatoma models, tumor growth decreased significantly when a single dose of 5-fluorouracil (5-FU) was administered during short-term carbogen breathing [90–93]. In line with these results, our study demonstrated a reduced 5-FU chemotherapy effect in colorectal carcinoma xenografts exposed to short-term hypoxic breathing conditions during administration of a single dose of 5-FU, as predicted on a baseline [^{18}F]FMISO scan [53]. In yet another study, rhabdomyosarcoma-bearing rats and lung tumor-bearing mice were exposed to modified O_2 concentrations 4 hours per day during 5 consecutive days. Using this approach, the investigators were able to show that treatment efficacy of the hypoxic prodrug TH-302 was dependent on tumor oxygenation: daily short-term exposure of the xenograft models to carbogen abolished the effect of TH-302, whereas 7% O_2 breathing increased the therapeutic potential [77]. Accordingly, the hypoxic prodrug CEN-209 was induced more effectively in subcutaneous HCT116 tumors of mice exposed to a hypoxic atmosphere, whereas hyperbaric O_2 breathing suppressed CEN-209 activation when the drug was administered after irradiation [94]. The

use of breathing an altered atmosphere for improving radiotherapy response is also being studied extensively. For instance, accelerated radiotherapy with carbogen and nicotinamide (ARCON) enhanced therapeutic response in a variety of tumor models, including mammary adenocarcinoma and sarcoma models [88, 95, 96].

Nevertheless, the breathing approach may become technically challenging for longitudinal therapy schedules. In particular, it has been shown in murine and rat tumors that the effect of breathing an adapted atmosphere can be reversed immediately when the intervention stops [82, 97, 98], is time-dependent [84], and may even be lost after prolonged exposure times [22, 99]. Things may even become more complex when considering that anesthesia potentially influences the experimental outcome. Indeed, to avoid motion-related artefacts during preclinical in vivo imaging, the use of anesthetics is inevitable, and these anesthetics or their carrier gasses (in case of volatile drugs) can have a substantial influence on tumor oxygenation. For instance, drops in pO_2 in tumor and muscle tissue of ketamine/xylazine-anesthetized animals when compared to isoflurane-anesthetized mice have been observed [100]. In CT26 colorectal carcinoma-bearing mice, [^{18}F]FAZA PET uptake was increased in both tumor and muscle tissue in ketamine/xylazine-anesthetized animals as compared to isoflurane-anesthetized animals. Yet these changes were less pronounced in muscle, resulting in higher [^{18}F]FAZA TBR in ketamine/xylazine-anesthetized animals [101]. In a murine adenocarcinoma model on the other hand, no difference in [^{18}F]FMISO TBR between the two anesthesia regimens was found, despite the observation of higher tumoral uptake in ketamine/xylazine-anesthetized animals compared to their isoflurane counterparts [102]. Surprisingly however, in both imaging studies, it was shown that [^{18}F]FAZA and [^{18}F]FMISO TBR, respectively, did not differ between animals breathing room air or animals breathing O_2 during isoflurane anesthesia [101, 102].

2.3.2. Clamping. The O_2 state of tumors can be temporarily reduced by physically occluding the blood supply to the tumor. This clamping technique gives rise to severe hypoxia. In general, animals are subcutaneously inoculated in the hind leg. When tumors have reached the desired volume, animals are anesthetized whereupon the proximal part of the leg is clamped with a rubber band or a metal clamp for a limited time period. In this way, transient acute tumor hypoxia is mimicked. For instance, it was observed that clamping induces expression of HIF-1 α [103]. Deteriorated radiotherapy response after clamping has also been observed [104]. Similarly, this clamping technique has been successfully applied in an orthotopic liver tumor model, where severe hypoxia could be induced via hepatic artery ligation [105].

On top of being painful and stressful [106], clamping has some other major limitations. First, by occluding the blood supply to the tumor, the delivery of therapy or radiotracer will also be extremely hampered [104]. It was hypothesized that this could be prevented by administering [^{18}F]FMISO

prior to initiation of the clamping procedure. Indeed, in two different glioblastoma models, this approach resulted in significantly increased tracer and pimonidazole uptake. On the opposite, it was emphasized that clamping after PET tracer administration may just cause trapping of unbound radiotracer in the tumor [107]. A second drawback of the clamping technique is that ischemia can occur instead of hypoxia, leading to irreversible damage and cell death. Third, the occluded artery may clot during the clamping, hampering reperfusion [105].

2.3.3. Temperature Modification. As excellently reviewed by Song et al. [108], ample evidence in a variety of xenograft models shows that tumor oxygenation improves during and after heating at 39 to 42°C. This observation is probably the result of a combination of an increase in tumor blood perfusion and a decrease in the O_2 consumption rate. Moreover, mild hyperthermia oxygenates both chronic and acute hypoxic cells, and this effect may last for up to 48 hours after heating [108]. A second proposed mechanism of action of hyperthermia is that it may kill hypoxic cells directly [109, 110]. In order to avoid this so-called hyperthermic cytotoxicity, which is beneficial from the therapeutic point of view, but may complicate therapy response evaluation experiments focusing on tumor hypoxia, the applicable temperature range is rather narrow.

Practically, the tumor-bearing leg of restrained or anesthetized animals is immersed into heated water. In a subcutaneous CRC model, this resulted in an immediate decrease in the hypoxic fraction, assessed with the extrinsic hypoxia markers pimonidazole and EF5, but the effect disappeared 24 hours after heating [111]. In a mammary carcinoma model, HIF-1 α increased immediately after 1 hour of hyperthermia treatment and was restored 48 hours later. VEGF however was elevated up to 48 hours after treatment, which on its turn was responsible for the induction of angiogenesis, increased tumor perfusion, and consequent decreases in tumor hypoxia [112].

Another way to achieve hyperthermia is whole-body heating. By placing mice in a heated environmental chamber, body temperature and thus tumor temperature can be raised, leading to improved tumor perfusion [113]. After 6 hours of whole-body heating, pimonidazole staining showed an initial decrease in hypoxia in a CRC xenograft model, possibly by an increase in vascular volume, but slightly increased again after heating [113].

Although it was suggested that temporal increases in HIF-1 α may lead to tumor reoxygenation and may therefore be beneficial in particular cases [112], the role of HIF-1 in therapy resistance is irrefutable and its upregulation via heating may most likely be detrimental. Second, raising the temperature of deep-seated orthotopic tumors may be technically challenging or even impossible using external heating. Whole-body heating may overcome this short-coming but can cause systemic stress. Third, it has been argued that anesthetics, which are indispensable in imaging research, may limit the thermoregulatory response as they cause vasoconstriction and thus may hamper the

efficacy of hyperthermia [113]. Fourth, seeing its transient nature, long-term use of hyperthermia may be complicated. Thus, tumor heating may not be a straightforward approach for the creation of a differential hypoxic tumor model.

2.3.4. Exercise. In two studies by Jones et al., the effects of long-term voluntary wheel running on tumor perfusion, hypoxia, and angiogenesis were investigated in two different orthotopic cancer models. In both models, significantly higher hypoxia, epitomized by an increase in HIF-1 α expression, and also improved tumoral blood perfusion were observed in the exercise group as compared to the sedentary group. As speculated by the authors, exercise may cause an increase in O₂ delivery towards muscle and heart tissue, thereby redirecting the O₂ supply from tumors to these metabolically active tissues. This in turn will activate the HIF-1 cascade in the tumor in order to preserve the local homeostasis, which possibly leads towards angiogenesis [114, 115]. Similarly, increased orthotopic breast tumor perfusion without affecting tumor oxygenation has been observed after forced daily treadmill running [116]. In order to investigate the influence of this altered microenvironment on chemotherapy efficacy, the group of Jones et al. conducted another study in two different murine orthotopic breast cancer models using the same study protocol. As opposed to the authors' previous data, tumor hypoxia, now assessed with EF5 immunohistochemistry, was significantly lower in the exercise groups as compared to controls. MVD and vessel maturity were significantly higher in the exercised animals, which led to increases in tumor perfusion as observed before [117]. Importantly, these results were in line with other preclinical data obtained in a rat orthotopic prostate cancer model [118].

Voluntary wheel running as used in the mouse studies described above [114, 115, 117], may be an animal-friendly, stressless way to influence tumor oxygenation. Moreover, as it is sufficient to provide running wheels in the animals' cages, this method is relatively cheap and uncomplicated since it does not require sophisticated technical equipment. Another major advantage is that low intensity exercise does not influence tumor growth [114, 115, 117]. Nevertheless, results may seem contradictory. In the studies where increases in HIF-1 were observed, hypoxia as such was not quantified [114, 115]. Importantly, the upregulation of HIF-1 α can also be the result of other mechanisms than a hypoxic microenvironment. The observed changes in perfusion [114, 115] on the other hand are most probably acute phenomena, whereas the hypoxia marker EF5 [117] primarily stains chronic hypoxia. Also, the site of inoculation should always be taken into consideration. As already discussed in Section 2.2.1, the subcutaneous space and its adjacent tissues are poorly perfused, which may explain at least partially why subcutaneously implanted tumors experience acute hypoxia during exercise [119]. More cell lines and more models should be studied in order to fully explore the high potential of exercise to create a differential hypoxic tumor model.

2.3.5. Other Approaches. Other, less-studied external interventions to decrease tumor hypoxia include electrical stimulation [120] and the addition of Matrigel during tumor inoculations [121]. By studying the effect of electrical stimulation of the sciatic nerve in intramuscularly implanted liver and rhabdomyosarcoma tumors, significant increases in tumor pO₂ and tumor blood flow were observed in both models, accompanied by decreases in the O₂ consumption rate [120]. However, seeing its invasiveness and technical complexity, this technique may be less applicable, especially in longitudinal therapy response evaluation studies. In line with this, the use of Matrigel is also not supported, as no differences in hypoxia could be observed between tumors originating from FaDu cells in medium with or without Matrigel, respectively [121].

2.4. Pharmacological Interventions. Last decades, the search for radiosensitizers and hypoxia-targeting therapies has led to the development of a variety of promising pharmacological interventions to overcome tumor hypoxia. For an excellent recent review of this matter, we refer to Horsman and Overgaard [110]. Some examples of these therapeutics with potential usefulness for the creation of differential hypoxia are described below.

In order to increase O₂ delivery to tumors, administration of erythropoietin (EPO), a substance naturally produced by the body, seems evident. For instance, in glioblastoma and carboplatin-treated NSCLC xenograft tumors, EPO administration resulted in significantly lower hypoxia as assessed polarographically or with HIF-1 α immunofluorescence, respectively [122, 123]. However, EPO also improved muscle oxygenation [122], which potentially complicates hypoxia tracer TBR calculations (cf Section 2.3.1). Since EPO also acts as a stimulatory growth factor, it may have detrimental tumor effects via processes that are not hypoxia-related [110].

A more promising drug may be metformin, a relatively safe antidiabetic with a favorable pharmacokinetic profile. It could be argued that the administration of metformin to laboratory animals may mimic the clinical situation to a certain extent, as the drug is widely prescribed to diabetes patients. However, it should be emphasized that in most preclinical experiments, the drug is administered to non-diabetic mice, often using doses exceeding those considered safe in humans which may impair direct translation. Among different anticancer effects attributed to this drug, metformin is supposed to improve tumor oxygenation via its inhibitory effect on complex I of the mitochondrial electron transport chain [124]. Zannella et al. showed in HCT116 CRC models that administration of a single dose of metformin indeed decreased tumor hypoxia and consequently improved radiotherapy response using [¹⁸F]FAZA PET [125], results that we were able to confirm in a comparable set-up using [¹⁸F]HX4 PET in A549 NSCLC xenografts [126]. These observations are supported by similar observations obtained in xenograft models of prostate cancer and lung carcinoma using another inhibitor of the

mitochondrial complex I, BAY 87-2243; [^{18}F]FAZA uptake was significantly reduced after administration of this novel drug [86]. In FaDu xenografts, no effect of a single dose of metformin on EF5 staining was observed, but treatment for seven consecutive days caused a nonsignificant decrease in tumor hypoxia [127]. Despite these observations, the way in which metformin influences radiation response is not fully understood and may not be fully attributable to hypoxia-related phenomena [128]. Moreover, in highly hypoxic pediatric sarcoma models, it was shown that metformin had no additive value to chemotherapy response, as opposed to tumors with a better oxygenation state [129].

Another way to influence tumor oxygenation is the use of vascular-targeting agents. A well-studied example of such drugs is hydralazine, a vasodilator that relaxes arterial smooth muscle. At high doses, hydralazine decreases tumor perfusion through the “steal” phenomenon and thus increases tumor hypoxia [79]. For instance, uptake of the hypoxia tracer PrognostixTM ([$^{99\text{m}}\text{Tc}$]HL91) was increased after hydralazine administration in NSCLC and CRC xenograft models when compared to controls [130, 131]. Similarly, drops in pO_2 were observed after hydralazine administration in CRC models [132]. However, the use of hydralazine to create a hypoxic model for investigating the cytotoxicity of the hypoxic prodrug AQ4N produced conflicting results [133, 134]. It was therefore suggested that in some tumor models, the effect of hydralazine may be too limited and too short-lived [134]. Other vascular-targeting agents include vascular disrupting agents [110], such as the novel combretastatin analogue OXi-4503, a tubulin-binding agent that selectively targets endothelial cells and damages existing tumor vessels [135, 136]. However, administration of such vascular-targeting drugs may lead to severe reductions in blood flow and thus ischemic cell death. This may in turn lead to difficulties in interpreting longitudinal PET imaging results as radiotracer delivery may be severely hampered. Another category includes the angiogenesis inhibiting agents [110]. It is generally believed that administration of angiogenesis inhibitors in a correct dose leads to vascular normalization and consequent decreases in tumor hypoxia [137], as shown with [^{18}F]FMISO PET in two patient-derived pancreas xenograft models after dovitinib treatment [138]. However, also increases in [^{18}F]FMISO after antiangiogenesis treatment have been reported [139]. Moreover, for all vascular targeting agents, timing of administration in combination with other therapies, mainly radiotherapy, is still controversial. It is supposed that vascular disrupting agents should be administered shortly after irradiation in order to be additive [110], which makes them unsuitable for the creation of differential hypoxic models.

Yet another drug-based approach is the use of agents that specifically target hypoxic cells. A first class includes O_2 mimetics such as nimorazole. In Denmark, this drug is incorporated in routine radiotherapy treatment of head and neck cancer [119]. A second class includes hypoxic prodrugs such as TH-302 [110]. For instance, it was shown that TH-302 significantly decreased the hypoxic fraction, as assessed with [^{18}F]HX4 PET, in rhabdomyosarcoma and NSCLC xenograft tumors. However, administration of TH-302 for

five consecutive days also resulted in a significant growth delay as compared to control tumors [77], which limits its potential as an exclusive hypoxia modulator.

Despite the promising potential of some of the therapies discussed above as a radiosensitizer, pharmacological intervention may not be the optimal choice for the creation of a differential hypoxic model. Indeed, drugs may disturb the physiological state of the tumor or alter the clearance properties of the tracer [3] and may moreover give rise to complex drug interactions when performing therapy response evaluation studies.

3. Conclusions

In an ideal world, one would be able to detect inherently differential hypoxia within a single cohort of tumor-bearing laboratory animals. However, external manipulations may be indispensable, especially for the investigation and validation of novel hypoxia-targeting therapies. In this article, we reviewed a substantial number of promising techniques with the potential to alter tumor oxygenation in a preclinical *in vivo* setting. Obviously, none of these models will accurately mimic the complexity of human disease. Indeed, each individual discussed technique entails specific practical or ethical drawbacks and is subject to the influence of the other parameters. For instance, when creating a differential hypoxia model using the breathing approach, one should also take into consideration that the studied cell line, the range of tumor volumes, the food type, and fasting periods, body temperature, or anesthesia during imaging studies may all have a substantial influence on the degree of tumor hypoxia, or hypoxia PET tracer uptake, independently from the administered breathing gasses. Therefore, in theory, all of these factors should be monitored very strictly in order to prevent experimental disturbances. Tumor hypoxia is such a transient, complex, and very sensitive process, as a result of which it is extremely susceptible to a lot of internal and external influencing factors.

Indeed, the smallest disturbance in one of the discussed variables mentioned above may individually or in combination lead to unpredictable, unexpected, unreliable, or unreplicable experimental outcomes. Nevertheless, application in a clinical setting is not free of influence from external factors. In this respect, the use of mouse models offers important advantages over clinical research, such as the ease of biopsy specimen collection, the nondependence on laborious patient recruitment and not running the risk of failing to reach target goals, and the curtailment of patient heterogeneity, among others.

Mouse models have actually proven their usefulness, as, for instance, [^{18}F]FMISO has successfully been implemented in patients after extensive preclinical *in vivo* validation. Validation of other hypoxia tracers is however still evolving. In this regard, this review provides a comprehensive overview and a better understanding of the applicable *in vivo* hypoxia modulation methods, but it also reveals that experimental modulation of tumor oxygenation remains a challenge. All of the reviewed methods may serve for

specific experimental designs or hypotheses and in this way, they undoubtedly all contribute to the ongoing search for new biomarkers and cures for cancer.

Conflicts of Interest

The authors declare that there are no conflicts of interest regarding the publication of this paper.

Acknowledgments

This work was funded by the University of Antwerp, Belgium, through a PhD grant for SDB, an associate professor position for TVdW, and a full professor position for StS and SiS, and by the Antwerp University Hospital, Belgium, through a postdoctoral position for CV and a departmental position for TVdW and SiS. CV and SiS are also supported by the Innovative Medicines Initiative (IMI) Joint Undertaking (<http://www.imi.europa.eu>) under grant agreement no. 115151, resources of which are composed of financial contribution from the European Union's Seventh Framework Program (FP7/2007-2013) and in-kind contributions from members of the European Federation of Pharmaceutical Industries and Associations (EFPIA).

References

- [1] M. de Jong, J. Essers, and W. M. Van Weerden, "Imaging preclinical tumour models: improving translational power," *Nature Reviews Cancer*, vol. 14, no. 7, pp. 481–493, 2014.
- [2] I. N. Fleming, R. Manavaki, P. J. Blower et al., "Imaging tumour hypoxia with positron emission tomography," *British Journal of Cancer*, vol. 112, no. 2, pp. 238–250, 2014.
- [3] L. J. Wack, D. Mönnich, W. Van Elmpt et al., "Comparison of [¹⁸F]-FMISO, [¹⁸F]-FAZA and [¹⁸F]-HX4 for PET imaging of hypoxia – a simulation study," *Acta Oncologica*, vol. 54, no. 9, pp. 1370–1377, 2015.
- [4] L. S. Mortensen, M. Busk, M. Nordmark et al., "Assessing radiation response using hypoxia PET imaging and oxygen sensitive electrodes: a preclinical study," *Radiotherapy and Oncology*, vol. 99, no. 3, pp. 418–423, 2011.
- [5] L. Bentzen, S. Keiding, M. R. Horsman et al., "Assessment of hypoxia in experimental mice tumours by [¹⁸F]fluoromisonidazole PET and pO₂ electrode measurements," *Acta Oncologica*, vol. 41, no. 3, pp. 304–312, 2002.
- [6] P. Mahy, M. De Bast, T. De Groot et al., "Comparative pharmacokinetics, biodistribution, metabolism and hypoxia-dependent uptake of [¹⁸F]-EF3 and [¹⁸F]-MISO in rodent tumor models," *Radiotherapy and Oncology*, vol. 89, no. 3, pp. 353–360, 2008.
- [7] P. Mahy, M. De Bast, P. H. Leveque et al., "Preclinical validation of the hypoxia tracer 2-(2-nitroimidazol-1-yl)-N-(3,3,3-[¹⁸F]trifluoropropyl)acetamide, [¹⁸F]EF3," *European Journal of Nuclear Medicine and Molecular Imaging*, vol. 31, no. 9, pp. 1–10, 2004.
- [8] L. J. Dubois, N. G. Lieuwes, M. H. M. Janssen et al., "Pre-clinical evaluation and validation of [¹⁸F]HX4, a promising hypoxia marker for PET imaging," *Proceedings of the National Academy of Sciences*, vol. 108, no. 35, pp. 14620–14625, 2011.
- [9] M. Doss, J. J. Zhang, M.-J. Bélanger et al., "Biodistribution and radiation dosimetry of the hypoxia marker ¹⁸F-HX4 in monkeys and humans determined by using whole-body PET/CT," *Nuclear Medicine Communications*, vol. 31, pp. 1016–1024, 2010.
- [10] M. R. Horsman, L. S. Mortensen, J. B. Petersen et al., "Imaging hypoxia to improve radiotherapy outcome," *Nature Reviews Clinical Oncology*, vol. 9, no. 12, pp. 674–687, 2012.
- [11] D. Thorwarth, S. M. Eschmann, F. Paulsen, and M. Alber, "A kinetic model for dynamic [¹⁸F]-Fmiso PET data to analyse tumour hypoxia," *Physics in Medicine and Biology*, vol. 50, no. 10, pp. 2209–2224, 2005.
- [12] W. A. Weber and F. Kiessling, "Imaging in oncology research," in *Small Animal Imaging*, F. Kiessling, B. J. Pichler, and P. Hauff, Eds., pp. 793–820, Springer International Publishing, Cham, Switzerland, 2nd edition, 2017.
- [13] S. Carlin, H. Zhang, M. Reese et al., "A comparison of the imaging characteristics and microregional distribution of 4 hypoxia PET tracers," *Journal of Nuclear Medicine*, vol. 55, no. 3, pp. 515–521, 2014.
- [14] S. G. J. A. Peeters, C. M. L. Zegers, N. G. Lieuwes et al., "A comparative study of the hypoxia PET tracers [¹⁸F]HX4, [¹⁸F]FAZA, and [¹⁸F]FMISO in a preclinical tumor model," *International Journal of Radiation Oncology Biology Physics*, vol. 91, no. 2, pp. 351–359, 2015.
- [15] M. T. Wyss, M. Honer, P. A. Schubiger, and S. M. Ametamey, "NanoPET imaging of [¹⁸F]fluoromisonidazole uptake in experimental mouse tumours," *European Journal of Nuclear Medicine and Molecular Imaging*, vol. 33, no. 3, pp. 311–318, 2005.
- [16] R. Ali, S. Apte, M. Vilalta et al., "¹⁸F-EF5 PET is predictive of response to fractionated radiotherapy in preclinical tumor models," *PLoS One*, vol. 10, no. 10, Article ID e0139425, 2015.
- [17] C. J. Koch, A. L. Shuman, W. T. Jenkins et al., "The radiation response of cells from 9L gliosarcoma tumours is correlated with [F18]-EF5 uptake," *International Journal of Radiation Biology*, vol. 85, no. 12, pp. 1137–1147, 2010.
- [18] R. Beck, B. Roper, J. M. Carlsen et al., "Pretreatment ¹⁸F-FAZA PET predicts success of hypoxia-directed radiochemotherapy using tirapazamine," *Journal of Nuclear Medicine*, vol. 48, no. 6, pp. 973–980, 2007.
- [19] E. Melsens, E. De Vlieghere, B. Descamps et al., "Hypoxia imaging with ¹⁸F-FAZA PET/CT predicts radiotherapy response in esophageal adenocarcinoma xenografts," *Radiotherapy and Oncology*, vol. 13, no. 1, p. 39, 2018.
- [20] L.-B.-A. Tran, A. Bol, D. Labar et al., "Predictive value of ¹⁸F-FAZA PET imaging for guiding the association of radiotherapy with nimorazole: a preclinical study," *Radiotherapy and Oncology*, vol. 114, no. 2, pp. 189–194, 2015.
- [21] J. Haynes, T. D. McKee, A. Haller et al., "Administration of hypoxia-activated prodrug evofosfamide after conventional adjuvant therapy enhances therapeutic outcome and targets cancer-initiating cells in preclinical models of colorectal cancer," *Clinical Cancer Research*, vol. 24, no. 9, pp. 2116–2127, 2018.
- [22] L.-B.-A. Tran, A. Bol, D. Labar et al., "Hypoxia imaging with the nitroimidazole ¹⁸F-FAZA PET tracer: a comparison with OxyLite, EPR oximetry and ¹⁹F-MRI relaxometry," *Radiotherapy and Oncology*, vol. 105, no. 1, pp. 29–35, 2012.
- [23] L. Dubois, W. Landuyt, L. Cloetens et al., "[¹⁸F]EF3 is not superior to [¹⁸F]FMISO for PET-based hypoxia evaluation as measured in a rat rhabdomyosarcoma tumour model," *European Journal of Nuclear Medicine and Molecular Imaging*, vol. 36, no. 2, pp. 209–218, 2008.
- [24] C. Campanile, M. J. E. Arlt, S. D. Kramer et al., "Characterization of different osteosarcoma phenotypes by PET

- imaging in preclinical animal models,” *Journal of Nuclear Medicine*, vol. 54, no. 8, pp. 1362–1368, 2013.
- [25] A. Corroyer-Dulmont, E. A. Pérès, E. Petit et al., “Non-invasive assessment of hypoxia with 3-[¹⁸F]-fluoro-1-(2-nitro-1-imidazolyl)-2-propanol ([¹⁸F]-FMISO): a PET study in two experimental models of human glioma,” *Biological Chemistry*, vol. 394, no. 4, pp. 529–539, 2013.
- [26] S. Valable, E. Petit, S. Roussel et al., “Complementary information from magnetic resonance imaging and ¹⁸F-fluoromisonidazole positron emission tomography in the assessment of the response to an antiangiogenic treatment in a rat brain tumor model,” *Nuclear Medicine and Biology*, vol. 38, pp. 781–793, 2011.
- [27] A. M. Stokes, C. P. Hart, and C. C. Quarles, “Hypoxia imaging with PET correlates with antitumor activity of the hypoxia-activated prodrug evofosfamide (TH-302) in rodent glioma models,” *Tomography*, vol. 2, no. 3, pp. 229–237, 2016.
- [28] E. G. C. Troost, J. Bussink, J. H. A. M. Kaanders et al., “Comparison of different methods of CAIX quantification in relation to hypoxia in three human head and neck tumor lines,” *Radiotherapy and Oncology*, vol. 76, no. 2, pp. 194–199, 2005.
- [29] E. G. C. Troost, P. Laverman, M. E. P. Philippens et al., “Correlation of [¹⁸F]FMISO autoradiography and pimonidazole immunohistochemistry in human head and neck carcinoma xenografts,” *European Journal of Nuclear Medicine and Molecular Imaging*, vol. 35, no. 10, pp. 1803–1811, 2008.
- [30] J. Wobb, S. A. Krueger, J. L. Kane et al., “The effects of pulsed radiation therapy on tumor oxygenation in 2 murine models of head and neck squamous cell carcinoma,” *International Journal of Radiation Oncology Biology Physics*, vol. 92, no. 4, pp. 820–828, 2015.
- [31] A. Silvoniemi, J. Silén, S. Forsback et al., “Evaluation of repeated [¹⁸F]EF5 PET/CT scans and tumor growth rate in experimental head and neck carcinomas,” *EJNMMI Research*, vol. 4, no. 1, p. 393, 2014.
- [32] J.-V. Gaustad, T. G. Simonsen, L. M. K. Andersen, and E. K. Rofstad, “Vascular abnormalities and development of hypoxia in microscopic melanoma xenografts,” *Journal of Translational Medicine*, vol. 15, no. 1, p. 241, 2017.
- [33] P. Mena-Romano, C. Chang, C. Glowa et al., “Measurement of hypoxia-related parameters in three sublines of a rat prostate carcinoma using dynamic ¹⁸F-FMISO-PET-CT and quantitative histology,” *American Journal of Nuclear Medicine and Molecular Imaging*, vol. 5, pp. 348–362, 2015.
- [34] J. A. O’Donoghue, P. Zanzonico, A. Pugachev et al., “Assessment of regional tumor hypoxia using ¹⁸F-fluoromisonidazole and ⁶⁴Cu(II)-diacetyl-bis(N4-methylthiosemicarbazone) positron emission tomography: comparative study featuring microPET imaging, pO₂ probe measurement, autoradiography, and fluorescent microscopy in the R3327-AT and FaDu rat tumor models,” *International Journal of Radiation Oncology Biology Physics*, vol. 61, no. 5, pp. 1493–1502, 2005.
- [35] D. T. T. Yapp, J. Woo, A. Kartono et al., “Non-invasive evaluation of tumour hypoxia in the Shionogi tumour model for prostate cancer with ¹⁸F-EF5 and positron emission tomography,” *BJU International*, vol. 99, no. 5, pp. 1154–1160, 2007.
- [36] D. T. Dang, F. Chen, L. B. Gardner et al., “Hypoxia-inducible factor-1 promotes nonhypoxia-mediated proliferation in colon cancer cells and xenografts,” *Cancer Research*, vol. 66, no. 3, pp. 1684–1936, 2006.
- [37] W. Li, Y.-Q. Chen, Y.-B. Shen et al., “HIF-1 α knockdown by miRNA decreases survivin expression and inhibits A549 cell growth in vitro and in vivo,” *International Journal of Molecular Medicine*, vol. 32, no. 2, pp. 271–280, 2013.
- [38] J. Nakamura, Y. Kitajima, K. Kai et al., “HIF-1 α is an unfavorable determinant of relapse in gastric cancer patients who underwent curative surgery followed by adjuvant 5-FU chemotherapy,” *International Journal of Cancer*, vol. 127, no. 5, pp. 1158–1171, 2009.
- [39] M. Hiraki, Y. Kitajima, K. Kai et al., “Knockdown of hypoxia-inducible factor-1 α accelerates peritoneal dissemination via the upregulation of MMP-1 expression in gastric cancer cell lines,” *Experimental and Therapeutic Medicine*, vol. 4, no. 3, pp. 355–362, 2012.
- [40] P. Carmeliet, Y. Dor, J.-M. Herbert et al., “Role of HIF-1 α in hypoxia-mediated apoptosis, cell proliferation and tumour angiogenesis,” *Nature*, vol. 394, no. 6692, pp. 485–490, 1998.
- [41] Y. Tsuzuki, D. Fukumura, B. Oosthuysen et al., “Vascular endothelial growth factor (VEGF) modulation by targeting hypoxia-inducible factor-1 α \rightarrow hypoxia response element \rightarrow VEGF cascade differentially regulates vascular response and growth rate in tumors,” *Cancer Research*, vol. 60, pp. 6248–6252, 2000.
- [42] T. Takeda, H. Okuyama, Y. Nishizawa et al., “Hypoxia inducible factor-1 α is necessary for invasive phenotype in *Vegf*-deleted islet cell tumors,” *Scientific Reports*, vol. 2, no. 1, p. 494, 2012.
- [43] M. Inoue, J. H. Hager, N. Ferrara et al., “VEGF-A has a critical, nonredundant role in angiogenic switching and pancreatic beta cell carcinogenesis,” *Cancer Cell*, vol. 1, no. 2, pp. 193–202, 2002.
- [44] B. Blouw, H. Song, T. Tihan et al., “The hypoxic response of tumors is dependent on their microenvironment,” *Cancer Cell*, vol. 4, no. 2, pp. 133–146, 2003.
- [45] L. Milane, Z. Duan, and M. Amiji, “Role of hypoxia and glycolysis in the development of multi-drug resistance in human tumor cells and the establishment of an orthotopic multi-drug resistant tumor model in nude mice using hypoxic pre-conditioning,” *Cancer Cell International*, vol. 11, no. 1, p. 3, 2011.
- [46] L. Yu and C. A. Hales, “Long-term exposure to hypoxia inhibits tumor progression of lung cancer in rats and mice,” *BMC Cancer*, vol. 11, no. 1, p. 331, 2011.
- [47] L. Zhang and R. P. Hill, “Hypoxia enhances metastatic efficiency in HT1080 fibrosarcoma cells by increasing cell survival in lungs, not cell adhesion and invasion,” *Cancer Research*, vol. 67, no. 16, pp. 7789–7797, 2007.
- [48] L. Dubois, W. Landuyt, K. Haustermans et al., “Evaluation of hypoxia in an experimental rat tumour model by [¹⁸F]fluoromisonidazole PET and immunohistochemistry,” *British Journal of Cancer*, vol. 91, no. 11, pp. 1947–1954, 2004.
- [49] J.-K. Chung, Y. S. Chang, Y. J. Lee et al., “The effect of tumor size on F-18-labeled fluorodeoxyglucose and fluoroerythronitroimidazole uptake in a murine sarcoma model,” *Annals of Nuclear Medicine*, vol. 13, no. 5, pp. 303–308, 1999.
- [50] T. Grönroos, L. Bentzen, P. Marjamäki et al., “Comparison of the biodistribution of two hypoxia markers [¹⁸F]FETNIM and [¹⁸F]FMISO in an experimental mammary carcinoma,” *European Journal of Nuclear Medicine and Molecular Imaging*, vol. 31, no. 4, pp. 513–520, 2004.
- [51] H. J. Tochon-Danguy, J. I. Sachinidis, F. Chan et al., “Imaging and quantitation of the hypoxic cell fraction of viable tumor in an animal model of intracerebral high grade glioma using

- [18F]fluoromisonidazole (FMISO),” *Nuclear Medicine and Biology*, vol. 29, no. 2, pp. 191–197, 2002.
- [52] B. Solomon, D. Binns, P. Roselt et al., “Modulation of intratumoral hypoxia by the epidermal growth factor receptor inhibitor gefitinib detected using small animal PET imaging,” *Molecular Cancer Therapeutics*, vol. 4, no. 9, pp. 1417–1422, 2005.
- [53] S. De Bruycker, C. Vangestel, T. Van Den Wyngaert et al., “Baseline [¹⁸F]FMISO μPET as a predictive biomarker for response to HIF-1α inhibition combined with 5-FU chemotherapy in a human colorectal cancer xenograft model,” *Molecular Imaging and Biology*, vol. 18, no. 4, pp. 606–616, 2016.
- [54] A. A. Khalil, M. R. Horsman, and J. Overgaard, “The importance of determining necrotic fraction when studying the effect of tumour volume on tissue oxygenation,” *Acta Oncologica*, vol. 34, no. 3, pp. 297–300, 1995.
- [55] K. De Jaeger, F. M. Merlo, M.-C. Kavanagh et al., “Heterogeneity of tumor oxygenation: relationship to tumor necrosis, tumor size, and metastasis,” *International Journal of Radiation Oncology Biology Physics*, vol. 42, no. 4, pp. 717–721, 1998.
- [56] P. Zanzonico, J. O’Donoghue, J. D. Chapman et al., “Iodine-124-labeled iodo-azomycin-galactoside imaging of tumor hypoxia in mice with serial microPET scanning,” *European Journal of Nuclear Medicine and Molecular Imaging*, vol. 31, no. 1, pp. 117–128, 2003.
- [57] D. Zhao, A. Constantinescu, E. W. Hahn, and R. P. Mason, “Tumor oxygen dynamics with respect to growth and respiratory challenge: investigation of the Dunning prostate R3327-HI tumor,” *Radiation Research*, vol. 156, no. 5, pp. 510–520, 2001.
- [58] J.-I. Saitoh, H. Sakurai, Y. Suzuki et al., “Correlations between in vivo tumor weight, oxygen pressure, ³¹P NMR spectroscopy, hypoxic microenvironment marking by β-D-iodinated azomycin galactopyranoside (β-D-IAZGP), and radiation sensitivity,” *International Journal of Radiation Oncology Biology Physics*, vol. 54, no. 3, pp. 903–909, 2002.
- [59] E. E. Graves, M. Vilalta, I. K. Cecic et al., “Hypoxia in models of lung cancer: implications for targeted therapeutics,” *Clinical Cancer Research*, vol. 16, no. 19, pp. 4843–4852, 2010.
- [60] A. Maity and C. Koumenis, “Location, location, location - makes all the difference for hypoxia in lung tumors,” *Clinical Cancer Research*, vol. 16, no. 19, pp. 4685–4687, 2010.
- [61] S. Rapic, C. Vangestel, J. Verhaeghe et al., “Characterization of an orthotopic colorectal cancer mouse model and its feasibility for accurate quantification in positron emission tomography,” *Molecular Imaging and Biology*, vol. 19, no. 5, pp. 762–771, 2017.
- [62] K. Camphausen, B. Purow, M. Sproull et al., “Orthotopic growth of human glioma cells quantitatively and qualitatively influences radiation-induced changes in gene expression,” *Cancer Research*, vol. 65, no. 22, pp. 10389–10393, 2005.
- [63] R. J. Klement and C. E. Champ, “Calories, carbohydrates, and cancer therapy with radiation: exploiting the five R’s through dietary manipulation,” *Cancer and Metastasis Reviews*, vol. 33, no. 1, pp. 217–229, 2014.
- [64] B.-Q. Lin, Z.-Y. Zeng, S.-S. Yang, and C.-W. Zhuang, “Dietary restriction suppresses tumor growth, reduces angiogenesis, and improves tumor microenvironment in human non-small-cell lung cancer xenografts,” *Lung Cancer*, vol. 79, no. 2, pp. 111–117, 2013.
- [65] M. A. Mahlke, L. A. Cortez, M. A. Ortiz et al., “The anti-tumor effects of calorie restriction are correlated with reduced oxidative stress in ENU-induced gliomas,” *Pathobiology of Aging & Age-related Diseases*, vol. 1, no. 1, p. 7189, 2011.
- [66] P. Mukherjee, “Antiangiogenic and proapoptotic effects of dietary restriction on experimental mouse and human brain tumors,” *Clinical Cancer Research*, vol. 10, no. 16, pp. 5622–5629, 2004.
- [67] A. Saleh, B. Simone, J. Palazzo et al., “Caloric restriction augments radiation efficacy in breast cancer,” *Cell Cycle*, vol. 12, no. 12, pp. 1955–1963, 2014.
- [68] N. Y. Kalaany and D. M. Sabatini, “Tumours with PI3K activation are resistant to dietary restriction,” *Nature*, vol. 458, no. 7239, pp. 725–731, 2009.
- [69] G. Zhang, J. Li, X. Wang et al., “The reverse Warburg effect and ¹⁸F-FDG uptake in non-small cell lung cancer A549 in mice: a pilot study,” *Journal of Nuclear Medicine*, vol. 56, no. 4, pp. 607–612, 2015.
- [70] L. Bentzen, S. Keiding, M. R. Horsman et al., “Feasibility of detecting hypoxia in experimental mouse tumours with ¹⁸F-fluorinated tracers and positron emission tomography: a study evaluating [¹⁸F]fluoromisonidazole and [¹⁸F]fluoro-2-deoxy-D-glucose,” *Acta Oncologica*, vol. 39, no. 5, pp. 629–637, 2000.
- [71] G. Reischl, D. S. Dorow, C. Cullinane et al., “Imaging of tumor hypoxia with [¹²⁴I]IAZA in comparison with [¹⁸F]FMISO and [¹⁸F]FAZA - first small animal PET results,” *Journal of Pharmacy & Pharmaceutical Sciences*, vol. 10, pp. 203–211, 2007.
- [72] K.-I. Matsumoto, L. Szajek, M. Krishna et al., “The influence of tumor oxygenation on hypoxia imaging in murine squamous cell carcinoma using [⁶⁴Cu]Cu-ATSM or [¹⁸F]fluoromisonidazole positron emission tomography,” *International Journal of Oncology*, vol. 30, pp. 873–881, 2007.
- [73] P. Mahy, M. De Bast, J. Gillart et al., “Detection of tumour hypoxia: comparison between EF5 adducts and [¹⁸F]EF3 uptake on an individual mouse tumour basis,” *European Journal of Nuclear Medicine and Molecular Imaging*, vol. 33, no. 5, pp. 553–556, 2006.
- [74] F. C. Maier, M. Kneilling, G. Reischl et al., “Significant impact of different oxygen breathing conditions on non-invasive in vivo tumor-hypoxia imaging using [¹⁸F]-fluoroazomycin-arabino-furanoside ([¹⁸F]FAZA),” *Radiation Oncology*, vol. 6, no. 1, p. 165, 2011.
- [75] M. Piert, H.-J. Machulla, M. Picchio et al., “Hypoxia-specific tumor imaging with ¹⁸F-fluoroazomycin arabinoside,” *Journal of Nuclear Medicine*, vol. 46, pp. 106–113, 2005.
- [76] H. Barthel, H. Wilson, D. R. Collingridge et al., “In vivo evaluation of [¹⁸F]fluoroetanidazole as a new marker for imaging tumour hypoxia with positron emission tomography,” *British Journal of Cancer*, vol. 90, no. 11, pp. 2232–2242, 2004.
- [77] S. G. J. A. Peeters, C. M. L. Zegers, R. Biemans et al., “TH-302 in combination with radiotherapy enhances the therapeutic outcome and is associated with pretreatment [¹⁸F]HX4 hypoxia PET imaging,” *Clinical Cancer Research*, vol. 21, no. 13, pp. 2984–2992, 2015.
- [78] R. A. Cairns, T. Kalliomaki, and R. P. Hill, “Acute (cyclic) hypoxia enhances spontaneous metastasis of KHT murine tumors,” *Cancer Research*, vol. 61, pp. 8903–8908, 2001.
- [79] P. Sonveaux, “Provascular strategy: targeting functional adaptations of mature blood vessels in tumors to selectively influence the tumor vascular reactivity and improve cancer treatment,” *Radiotherapy and Oncology*, vol. 86, no. 3, pp. 300–313, 2008.

- [80] M. Busk, M. R. Horsman, P. E. G. Kristjansen et al., "Aerobic glycolysis in cancers: implications for the usability of oxygen-responsive genes and fluorodeoxyglucose-PET as markers of tissue hypoxia," *International Journal of Cancer*, vol. 122, no. 12, pp. 2726–2734, 2008.
- [81] J. Bussink, J. H. Kaanders, P. F. Rijken et al., "Vascular architecture and microenvironmental parameters in human squamous cell carcinoma xenografts: effects of carbogen and nicotinamide," *Radiotherapy and Oncology*, vol. 50, no. 2, pp. 173–184, 1999.
- [82] S. P. Robinson, F. A. Howe, M. Stubbs, and J. R. Griffiths, "Effects of nicotinamide and carbogen on tumour oxygenation, blood flow, energetics and blood glucose levels," *British Journal of Cancer*, vol. 82, pp. 2007–2014, 2000.
- [83] T. J. Dunn, R. D. Braun, W. E. Rhemus et al., "The effects of hyperoxic and hypercarbic gases on tumour blood flow," *British Journal of Cancer*, vol. 80, no. 1-2, pp. 117–126, 1999.
- [84] S. A. Hill, D. R. Collingridge, B. Vojnovic, and D. J. Chaplin, "Tumour radiosensitization by high-oxygen-content gases: influence of the carbon dioxide content of the inspired gas on pO₂, microcirculatory function and radiosensitivity," *International Journal of Radiation Oncology Biology Physics*, vol. 40, no. 4, pp. 943–951, 1998.
- [85] B. Thézé, N. Bernards, A. Beynel et al., "Monitoring therapeutic efficacy of sunitinib using [¹⁸F]FDG and [¹⁸F]FMISO PET in an immunocompetent model of luminal B (HER2-positive)-type mammary carcinoma," *BMC Cancer*, vol. 15, no. 1, p. 534, 2015.
- [86] E. Chang, H. Liu, K. Unterschemmann et al., "¹⁸F-FAZA PET imaging response tracks the reoxygenation of tumors in mice upon treatment with the mitochondrial complex I inhibitor BAY 87-2243," *Clinical Cancer Research*, vol. 21, no. 2, pp. 335–346, 2015.
- [87] N. Khan, H. Li, H. Hou et al., "Tissue pO₂ of orthotopic 9L and C6 gliomas and tumor-specific response to radiotherapy and hyperoxygenation," *International Journal of Radiation Oncology Biology Physics*, vol. 73, no. 3, pp. 878–885, 2009.
- [88] G. Stüben, M. Stuschke, K. Knühmann et al., "The effect of combined nicotinamide and carbogen treatments in human tumour xenografts: oxygenation and tumour control studies," *Radiotherapy and Oncology*, vol. 48, no. 2, pp. 143–148, 1998.
- [89] H. W. M. Van Laarhoven, J. Bussink, J. Lok et al., "Effects of nicotinamide and carbogen in different murine colon carcinomas: immunohistochemical analysis of vascular architecture and microenvironmental parameters," *International Journal of Radiation Oncology Biology Physics*, vol. 60, no. 1, pp. 310–321, 2004.
- [90] P. M. McSheehy, S. P. Robinson, A. S. Ojugo et al., "Carbogen breathing increases 5-fluorouracil uptake and cytotoxicity in hypoxic murine RIF-1 tumors: a magnetic resonance study in vivo," *Cancer Research*, vol. 58, pp. 1185–1194, 1998.
- [91] P. M. J. McSheehy, R. E. Port, L. M. Rodrigues et al., "Investigations in vivo of the effects of carbogen breathing on 5-fluorouracil pharmacokinetics and physiology of solid rodent tumours," *Cancer Chemotherapy and Pharmacology*, vol. 55, no. 2, pp. 117–128, 2004.
- [92] H. W. M. Van Laarhoven, G. Gambarota, J. Lok et al., "Carbogen breathing differentially enhances blood plasma volume and 5-fluorouracil uptake in two murine colon tumor models with a distinct vascular structure," *Neoplasia*, vol. 8, no. 6, pp. 477–487, 2006.
- [93] Y. J. L. Kamm, G. J. Peters, W. E. Hull et al., "Correlation between 5-fluorouracil metabolism and treatment response in two variants of C26 murine colon carcinoma," *British Journal of Cancer*, vol. 89, no. 4, pp. 754–762, 2003.
- [94] J. Wang, A. Foehrenbacher, J. Su et al., "The 2-nitroimidazole EF5 is a biomarker for oxidoreductases that activate the bioreductive prodrug CEN-209 under hypoxia," *Clinical Cancer Research*, vol. 18, no. 6, pp. 1684–1695, 2012.
- [95] A. Rojas, V. K. Hirst, A. S. Calvert, and H. Johns, "Carbogen and nicotinamide as radiosensitizers in a murine mammary carcinoma using conventional and accelerated radiotherapy," *International Journal of Radiation Oncology Biology Physics*, vol. 34, no. 2, pp. 357–365, 1996.
- [96] M. R. Horsman and J. Overgaard, "Preclinical studies on how to deal with patient intolerance to nicotinamide and carbogen," *Radiotherapy and Oncology*, vol. 70, no. 3, pp. 301–309, 2004.
- [97] O. Thews and P. Vaupel, "Zeitliche Veränderungen der Tumoroxygenierung und -durchblutung während normo- und hyperbarer inspiratorischer Hyperoxie," *Strahlentherapie und Onkologie*, vol. 192, no. 3, pp. 174–181, 2015.
- [98] K.-I. Matsumoto, M. Bernardo, S. Subramanian et al., "MR assessment of changes of tumor in response to hyperbaric oxygen treatment," *Magnetic Resonance in Medicine*, vol. 56, no. 2, pp. 240–246, 2006.
- [99] J. H. Kaanders, J. Bussink, and A. J. Van Der Kogel, "ARCON: a novel biology-based approach in radiotherapy," *The Lancet Oncology*, vol. 3, no. 12, pp. 728–737, 2002.
- [100] C. Baudalet and B. Gallez, "Effect of anesthesia on the signal intensity in tumors using BOLD-MRI: comparison with flow measurements by laser Doppler flowmetry and oxygen measurements by luminescence-based probes," *Magnetic Resonance Imaging*, vol. 22, no. 7, pp. 905–912, 2004.
- [101] M. Mahling, K. Fuchs, W. M. Thaiss et al., "A comparative pO₂ probe and [¹⁸F]-fluoro-azomycinarabino-furanoside ([¹⁸F]FAZA) PET study reveals anesthesia-induced impairment of oxygenation and perfusion in tumor and muscle," *PLoS One*, vol. 10, no. 4, Article ID e0124665, 2015.
- [102] V. Kersemans, B. Cornelissen, R. Hueting et al., "Hypoxia imaging using PET and SPECT: the effects of anesthetic and carrier gas on [⁶⁴Cu]-ATSM, [^{99m}Tc]-HL91 and [¹⁸F]-FMISO tumor hypoxia accumulation," *PLoS One*, vol. 6, no. 11, Article ID e25911, 2011.
- [103] A. Ferrario, K. F. Tiehl Von, N. Rucker et al., "Antiangiogenic treatment enhances photodynamic therapy responsiveness in a mouse mammary carcinoma," *Cancer Research*, vol. 60, pp. 4066–4069, 2000.
- [104] K. Kubota, M. Tada, S. Yamada et al., "Comparison of the distribution of fluorine-18 fluoromisonidazole, deoxyglucose and methionine in tumour tissue," *European Journal of Nuclear Medicine and Molecular Imaging*, vol. 26, no. 7, pp. 750–757, 1999.
- [105] P. Brader, C. C. Riedl, Y. Woo et al., "Imaging of hypoxia-driven gene expression in an orthotopic liver tumor model," *Molecular Cancer Therapeutics*, vol. 6, no. 11, pp. 2900–2908, 2007.
- [106] S. Rockwell, J. E. Moulder, and D. F. Martin, "Effectiveness and biological effects of techniques used to induce hypoxia in solid tumors," *Radiotherapy and Oncology*, vol. 5, no. 4, pp. 311–319, 1986.
- [107] E. G. C. Troost, P. Laverman, J. H. A. M. Kaanders et al., "Imaging hypoxia after oxygenation-modification: comparing [¹⁸F]FMISO autoradiography with pimonidazole

- immunohistochemistry in human xenograft tumors,” *Radiation Therapy and Oncology*, vol. 80, no. 2, pp. 157–164, 2006.
- [108] C. W. Song, H. Park, and R. J. Griffin, “Improvement of tumor oxygenation by mild hyperthermia,” *Radiation Research*, vol. 155, no. 4, pp. 515–528, 2001.
- [109] M. R. Horsman and J. Overgaard, “Hyperthermia: a potent enhancer of radiotherapy,” *Clinical Oncology*, vol. 19, no. 6, pp. 418–426, 2007.
- [110] M. R. Horsman and J. Overgaard, “The impact of hypoxia and its modification of the outcome of radiotherapy,” *Journal of Radiation Research*, vol. 57, no. S1, pp. i90–i98, 2016.
- [111] X. Sun, X.-F. Li, J. Russell et al., “Changes in tumor hypoxia induced by mild temperature hyperthermia as assessed by dual-tracer immunohistochemistry,” *Radiation Therapy and Oncology*, vol. 88, no. 2, pp. 269–276, 2008.
- [112] E. J. Moon, P. Sonveaux, P. E. Porporato et al., “NADPH oxidase-mediated reactive oxygen species production activates hypoxia-inducible factor-1 (HIF-1) via the ERK pathway after hyperthermia treatment,” *Proceedings of the National Academy of Sciences*, vol. 107, no. 47, pp. 20477–20482, 2010.
- [113] A. Sen, M. L. Capitano, J. A. Spornyak et al., “Mild elevation of body temperature reduces tumor interstitial fluid pressure and hypoxia and enhances efficacy of radiotherapy in murine tumor models,” *Cancer Research*, vol. 71, no. 11, pp. 3872–3880, 2011.
- [114] L. W. Jones, B. L. Viglianti, J. A. Tashjian et al., “Effect of aerobic exercise on tumor physiology in an animal model of human breast cancer,” *Journal of Applied Physiology*, vol. 108, no. 2, pp. 343–348, 2010.
- [115] L. W. Jones, J. Antonelli, E. M. Masko et al., “Exercise modulation of the host-tumor interaction in an orthotopic model of murine prostate cancer,” *Journal of Applied Physiology*, vol. 113, no. 2, pp. 263–272, 2012.
- [116] J. M. Wiggins, L. Rice, S. Lepler et al., “The impact of daily exercise on tumor perfusion,” in *Proceedings of the 110th Annual Meeting of the American Association for Cancer Research (AACR)*, Abstract nr 5913, AACR, Philadelphia, PA, USA, April 2017.
- [117] A. S. Betof, C. D. Lascola, D. Weitzel et al., “Modulation of murine breast tumor vascularity, hypoxia and chemotherapeutic response by exercise,” *Journal of the National Cancer Institute*, vol. 107, no. 5, article djv040, 2015.
- [118] D. J. McCullough, J. N. Stabley, D. W. Siemann, and B. J. Behnke, “Modulation of blood flow, hypoxia, and vascular function in orthotopic prostate tumors during exercise,” *Journal of the National Cancer Institute*, vol. 106, no. 4, article dju036, 2014.
- [119] D. W. Siemann and M. R. Horsman, “Modulation of the tumor vasculature and oxygenation to improve therapy,” *Pharmacology & Therapeutics*, vol. 153, pp. 107–124, 2015.
- [120] B. F. Jordan, P. Sonveaux, O. Feron et al., “Nitric oxide-mediated increase in tumor blood flow and oxygenation of tumors implanted in muscles stimulated by electric pulses,” *International Journal of Radiation Oncology Biology Physics*, vol. 55, no. 4, pp. 1066–1073, 2003.
- [121] F. P. Fliedner, A. E. Hansen, J. T. Jørgensen, and A. Kjær, “The use of matrigel has no influence on tumor development or PET imaging in FaDu human head and neck cancer xenografts,” *BMC Medical Imaging*, vol. 16, no. 1, p. 5, 2016.
- [122] S. Scigliano, S. Pinel, S. Poussier et al., “Measurement of hypoxia using invasive oxygen-sensitive electrode, pimonidazole binding and ^{18}F -FDG uptake in anaemic or erythropoietin-treated mice bearing human glioma xenografts,” *International Journal of Oncology*, vol. 32, pp. 69–77, 2008.
- [123] D. Doleschel, A. Rix, S. Arns et al., “Erythropoietin improves the accumulation and therapeutic effects of carboplatin by enhancing tumor vascularization and perfusion,” *Theranostics*, vol. 5, no. 8, pp. 905–918, 2015.
- [124] W. W. Wheaton, S. E. Weinberg, R. B. Hamanaka et al., “Metformin inhibits mitochondrial complex I of cancer cells to reduce tumorigenesis,” *eLife*, vol. 3, article e02242, 2014.
- [125] V. E. Zannella, A. Dal Pra, H. Muaddi et al., “Reprogramming metabolism with metformin improves tumor oxygenation and radiotherapy response,” *Clinical Cancer Research*, vol. 19, no. 24, pp. 6741–6750, 2013.
- [126] S. De Bruycker, C. Vangestel, T. Van Den Wyngaert et al., “ ^{18}F -flortanidazole hypoxia PET holds promise as a prognostic and predictive imaging biomarker in a lung cancer xenograft model treated with metformin and radiotherapy,” *Journal of Nuclear Medicine*, 2018, In press.
- [127] T. M. Ashton, E. Fokas, L. A. Kunz-Schughart et al., “The anti-malarial atovaquone increases radiosensitivity by alleviating tumour hypoxia,” *Nature Communications*, vol. 7, p. 12308, 2016.
- [128] M. Koritzinsky, “Metformin: a novel biological modifier of tumor response to radiation therapy,” *International Journal of Radiation Oncology Biology Physics*, vol. 93, no. 2, pp. 454–464, 2015.
- [129] C. Garofalo, M. Capristo, M. C. Manara et al., “Metformin as an adjuvant drug against pediatric sarcomas: hypoxia limits therapeutic effects of the drug,” *PLoS One*, vol. 8, no. 12, Article ID e83832, 2013.
- [130] B.-F. Lee, N.-T. Chiu, C.-C. Hsia, and L.-H. Shen, “Accumulation of Tc-99m HL91 in tumor hypoxia: in vitro cell culture and in vivo tumor model,” *Kaohsiung Journal of Medical Sciences*, vol. 24, no. 9, pp. 461–472, 2008.
- [131] S. Kinuya, K. Yokoyama, X.-F. Li et al., “Hypoxia-induced alteration of tracer accumulation in cultured cancer cells and xenografts in mice: implications for pre-therapeutic prediction of treatment outcomes with $^{99\text{m}}\text{Tc}$ -sestamibi, ^{201}Tl chloride and $^{99\text{m}}\text{Tc}$ -HL91,” *European Journal of Nuclear Medicine and Molecular Imaging*, vol. 29, no. 8, pp. 1006–1011, 2002.
- [132] G. Mees, R. Dierckx, C. Vangestel et al., “Pharmacologic activation of tumor hypoxia: a means to increase tumor 2-deoxy-2- ^{18}F fluoro-D-glucose uptake?,” *Molecular Imaging*, vol. 12, no. 1, pp. 49–58, 2013.
- [133] L. H. Patterson and S. R. McKeown, “AQ4N: a new approach to hypoxia-activated cancer chemotherapy,” *British Journal of Cancer*, vol. 83, no. 12, pp. 1589–1593, 2000.
- [134] E. Manley and D. J. Waxman, “Impact of tumor blood flow modulation on tumor sensitivity to the bioreductive drug banoxantrone,” *Journal of Pharmacology and Experimental Therapeutics*, vol. 344, no. 2, pp. 368–377, 2013.
- [135] A. B. Iversen, M. Busk, and M. R. Horsman, “Induction of hypoxia by vascular disrupting agents and the significance for their combination with radiation therapy,” *Acta Oncologica*, vol. 52, no. 7, pp. 1320–1326, 2013.
- [136] T. R. Wittenborn and M. R. Horsman, “Targeting tumour hypoxia to improve outcome of stereotactic radiotherapy,” *Acta Oncologica*, vol. 54, no. 9, pp. 1385–1392, 2015.
- [137] R. K. Jain, “Normalization of tumor vasculature: an emerging concept in antiangiogenic therapy,” *Science*, vol. 307, no. 5706, pp. 58–62, 2005.
- [138] E. Hernández-Agudo, T. Mondejar, M. L. Soto-Montenegro et al., “Monitoring vascular normalization induced by

- antiangiogenic treatment with ^{18}F -fluoromisonidazole-PET,” *Molecular Oncology*, vol. 10, no. 5, pp. 704–718, 2016.
- [139] M. Murakami, S. Zhao, Y. Zhao et al., “Evaluation of changes in the tumor microenvironment after sorafenib therapy by sequential histology and ^{18}F -fluoromisonidazole hypoxia imaging in renal cell carcinoma,” *International Journal of Oncology*, vol. 41, no. 5, pp. 1593–1600, 2012.

Research Article

MT1-MMP as a PET Imaging Biomarker for Pancreas Cancer Management

Miguel Ángel Morcillo,¹ Ángel García de Lucas,¹ Marta Oteo,¹ Eduardo Romero,¹ Natalia Magro,¹ Marta Ibáñez,¹ Alfonso Martínez,¹ Guillermo Garaulet,² Alicia G. Arroyo,³ Pedro Pablo López-Casas,⁴ Manuel Hidalgo,⁴ Francisca Mulero ,² and Jorge Martínez-Torrecuadrada ⁵

¹Biomedical Applications of Radioisotopes and Pharmacokinetics, Research Centre for Energy, Environment and Technology (CIEMAT), Madrid, Spain

²Molecular Imaging Unit, Spanish National Cancer Research Centre (CNIO), Madrid, Spain

³Matrix Metalloproteinases in Angiogenesis and Inflammation Lab, Centro de Investigaciones Biológicas (CIB-CSIC), Madrid, Spain

⁴Gastrointestinal Cancer Clinical Research Unit, CNIO, Madrid, Spain

⁵Crystallography and Protein Engineering Unit, CNIO, Madrid, Spain

Correspondence should be addressed to Francisca Mulero; fmulero@cnio.es and Jorge Martínez-Torrecuadrada; jlmartinez@cnio.es

Received 7 June 2018; Accepted 25 July 2018; Published 26 August 2018

Academic Editor: Pablo Aguiar

Copyright © 2018 Miguel Ángel Morcillo et al. This is an open access article distributed under the Creative Commons Attribution License, which permits unrestricted use, distribution, and reproduction in any medium, provided the original work is properly cited.

Pancreatic ductal adenocarcinoma (PDAC) continues to be one of the deadliest cancers for which optimal diagnostic tools are still greatly needed. Identification of PDAC-specific molecular markers would be extremely useful to improve disease diagnosis and follow-up. MT1-MMP has long been involved in pancreatic cancer, especially in tumour invasion and metastasis. In this study, we aim to ascertain the suitability of MT1-MMP as a biomarker for positron emission tomography (PET) imaging. Two probes were assessed and compared for this purpose, an MT1-MMP-specific binding peptide (MT1-AF7p) and a specific antibody (LEM2/15), labelled, respectively, with ⁶⁸Ga and with ⁸⁹Zr. PET imaging with both probes was conducted in patient-derived xenograft (PDX), subcutaneous and orthotopic, PDAC mouse models, and in a cancer cell line (CAPAN-2)-derived xenograft (CDX) model. Both radiolabelled tracers were successful in identifying, by means of PET imaging techniques, tumour tissues expressing MT1-MMP although they did so at different uptake levels. The ⁸⁹Zr-DFO-LEM2/15 probe showed greater specific activity compared to the ⁶⁸Ga-labelled peptide. The mean value of tumour uptake for the ⁸⁹Zr-DFO-LEM2/15 probe ($5.67 \pm 1.11\%ID/g$, $n = 28$) was 25–30 times higher than that of the ⁶⁸Ga-DOTA-AF7p ones. Tumour/blood ratios (1.13 ± 0.51 and 1.44 ± 0.43 at 5 and 7 days of ⁸⁹Zr-DFO-LEM2/15 after injection) were higher than those estimated for ⁶⁸Ga-DOTA-AF7p probes (of approximately tumour/blood ratio = 0.5 at 90 min after injection). Our findings strongly point out that (i) the *in vivo* detection of MT1-MMP by PET imaging is a promising strategy for PDAC diagnosis and (ii) labelled LEM2/15 antibody is a better candidate than MT1-AF7p for PDAC detection.

1. Introduction

Pancreatic adenocarcinoma (PDAC) remains one of the most common and deadly cancers, in great need of optimal diagnostic tools [1]. Abdominal ultrasound is currently the

method of choice for an initial examination when pancreatic cancer is suspected, followed by endoscopic ultrasound, contrast-enhanced multidetector computed tomography, or magnetic resonance imaging combined with magnetic resonance cholangiopancreatography for further evaluation

once a pancreatic mass is detected [2]. Since these imaging techniques provide only morphological information on the tumour, they are therefore of limited value. Positron emission tomography (PET) could be a valuable alternative imaging technology; however, the metabolic marker most commonly used, 18-fluorodeoxyglucose (^{18}F -FDG), lacks sufficient specificity to allow for an accurate diagnosis of PDAC. In addition, the desmoplastic reaction associated with PDAC may cause the malignancy to show up as a hypometabolic lesion under this imaging technique [3]. Additional limitations of ^{18}F -FDG include false-positive inflammatory processes and false-negative carcinoma in patients afflicted with diabetes, hyperglycemia, and islet cell tumours. Identification of PDAC-specific molecular markers would then be very useful for improving diagnosis, for identifying those patients more likely to respond to certain treatments, and for monitoring therapy progress, which will in turn significantly enhance current survival rates. Because pancreatic cancer is a heterogeneous process of a complex nature, it has not been possible to date to validate any tumour marker as a noninvasive diagnostics tool for this pathology.

Matrix metalloproteinases (MMPs) are a family of zinc-dependent endopeptidases associated with tumour progression and metastasis since they are involved in the degradation of the basement membrane and extracellular matrix (ECM) components. In particular, membrane-tethered MT1-MMP overexpresses in many tumours and associates with tumour growth, invasion, metastasis, and poor prognosis [4, 5]. In PDAC, the observed collagen-mediated upregulation of MT1-MMP in the desmoplastic regions of the tumours promotes both tumour progression and gemcitabine resistance in a PDAC xenograft mouse model [6]. Given that MT1-MMP plays a major role in tumour invasion and metastasis, several pharmaceutical developments have already been carried out using small molecule MT1-MMP inhibitors targeting the active site [7]. This first generation of MMP inhibitors has, however, so far failed to deliver the expected results when assayed in cancer clinical trials due to low net efficacy behaviour and arisen adverse off-target effects since these inhibitors can simultaneously interact with multiple MMPs and other related enzymes harbouring structurally conserved catalytic clefts [8]. This has led to the current exploration of new inhibition strategies based on highly specific antibodies targeting MT1-MMP exosites and allosteric interactions, rather than the catalytic site region, as promising therapeutic alternatives to control MT1-MMP activity [9–12]. Antibody LEM2/15, raised against the exposed surface loop V-B of MT1-MMP [13], has exhibited highly potent and selective inhibition of the metalloproteinase. Protein crystallography studies have accurately detailed the underlying molecular mechanism of inhibition [14], thus supporting the notion that antibody LEM2/15 might be a suitable lead for the development of novel and improved therapeutics.

MT1-MMP would therefore represent a candidate biomarker to facilitate noninvasive PDAC detection, imaging, and the assessment of therapeutic response using specific probes. Several previous studies using MT1-MMP-specific antibodies or peptides have already established the importance of MT1-MMP as an imaging agent in numerous cancer

models. Among these, the nonsubstrate peptide termed MT1-AF7p (sequence HWKHLHNTKTFL) that specifically binds to MT-loop of MT1-MMP is worth mentioning. When tagged with a near-infrared fluorescent (NIRF) dye Cy5.5 this peptide provided clear visualization by optical imaging of MT1-MMP-expressing breast tumours in a xenograft mouse model [15]. MT1-AF7p peptide was also used as a radioiodinated peptidic probe for SPECT/CT imaging in a fibrosarcoma mouse model [16] and as a $^{99\text{m}}\text{Tc}$ -labelled imaging agent for breast cancer diagnosis [17], thus highlighting the potential of using MT1-AF7p for MT1-MMP-targeted tumour detection. This antibody labelling approach has also been explored as probes for the monitoring of MT1-MMP. A $^{99\text{m}}\text{Tc}$ -labelled anti-MT1-MMP IgG [18] and an ^{111}In -labelled miniaturized antibody have been generated for SPECT imaging of fibrosarcoma mouse models where a high accumulation of probes in MT1-MMP-positive areas was observed.

Bearing in mind that PET imaging is far more sensitive and accurate than other imaging techniques in clinic and that it also holds a great promise in the visualization of biology activities, we have developed in this study some MT1-MMP-specific PET probes for pancreatic cancer detection. When designing these types of PET probes, careful consideration should be given beforehand to the values of the half-life of the biomolecule and of the physical life of the positron-emitting radionuclide that are to be linked. Thus, PET radionuclides with longer half-lives, such as ^{89}Zr (78.4 hours), are ideally suited for conjugation with intact antibodies (which remain in the blood for long) while smaller peptides (which have shorter clearance times) must be labelled with PET isotopes featuring short or intermediate half-lives such as ^{68}Ga . We have recently developed an ^{89}Zr -labelled LEM15/2-based probe for the effective monitoring of MT1-MMP by PET in preclinical GBM mouse models [19]. Here, we have tested and assessed this probe in pancreatic cancer mouse models, together with a ^{68}Ga -labelled MT1-AF7p peptide. We have compared performance of both probes.

2. Materials and Methods

2.1. Radiolabelling

2.1.1. Labelling of LEM2/15 Antibody with ^{89}Zr . LEM2/15 hybridoma cells were cultured as described [13], and the monoclonal antibodies (mAb) were purified from the hybridoma supernatant following standard methods using protein A-based chromatography. The bifunctional chelator DFO-NCS (Macrocyclics, Dallas, TX) was conjugated to LEM2/15, and subsequent ^{89}Zr radiolabelling was performed by adaptation of published protocols [20, 21]. ^{89}Zr ($T_{1/2} = 78.4\text{ h}$, $\beta^+ = 22.6\%$; $\sim 2.7\text{ GBq/ml}$ supplied in 1 M oxalic acid) was obtained from BV Cyclotron VU (Amsterdam, the Netherlands).

For conjugation, 2 mg of LEM2/15 in 1 mL solution at pH 9.0, adjusted with 0.1 M Na_2CO_3 (max. 100 μL), were mixed with DFO-NCS (dissolved in DMSO at a concentration 3.5 mM) at a molar ratio of 1 : 5. The reaction was

incubated for 40 min at 37°C. Nonconjugated chelator was removed by G25-Sephadex size-exclusion chromatography using a PD-10 column (GE Healthcare Life Sciences) and 5 mg/ml gentisic acid in 0.25 M sodium acetate trihydrate (pH 5.4–5.6) as eluent. For the radiolabelling procedure, the required volume of ^{89}Zr -oxalic acid solution corresponding to 37–74 MBq was adjusted to a total volume of 200 μL using 1 M oxalic acid, and 90 μL of 2 M Na_2CO_3 were added and incubated for 3 min at room temperature. 1 mL of 0.5 M HEPES and 710 μL of DFO-LEM2/15 (1 mg/mL) were subsequently added and incubated at room temperature for 90 min on a rotating shaker. pH was checked to be at 7.0–7.5. Finally, the reaction mixture was loaded onto a previously equilibrated PD-10 column and eluted with phosphate-buffered saline (PBS) into fractions of 250 μL . After purification, the collected fractions were measured in a dose calibrator (IBC, Veenstra Instruments). Radiochemical purity of the radiolabelled antibody was performed by instant thin-layer chromatography (ITLC) on ITLC strips (model 150–771, Biodex) using 0.02 M citrate buffer (pH 5.0): acetonitrile (9:1) as eluent followed by exposure to phosphor imaging screen-K (Bio-Rad); images were acquired with a Personal Molecular Imager FX system (Bio-Rad).

The stability of ^{89}Zr -DFO-LEM2/15 was investigated by incubation in human serum and plasma for 7 days at 4°C and 37°C. The radiochemical purity was determined by ITLC as discussed above.

2.1.2. Labelling of DOTA-AF7p Peptides with ^{68}Ga . The peptides DOTA-HWKHLHNTKTFL (denoted as DOTA-AF7p-1) and HWK(DOTA)HLHNTKTFL (denoted as DOTA-AF7p-2) were purchased from Bachem AG (Bubendorf, Switzerland). The molecular mass of both peptides, estimated by MALDI-MS, was 1948.25 and 1948.38 g/mol, respectively; the purity (estimated by HPLC) was 95.0% and 97.7%, respectively, as indicated by the seller.

Radiolabelling of DOTA-AF7p-1 and DOTA-AF7p-2 with ^{68}Ga was performed using fractionated elution. The ^{68}Ga solution was eluted from a $^{68}\text{Ge}/^{68}\text{Ga}$ -generator, based on nano-SnO₂ and developed at CIEMAT [22], with 7 mL of 1 M HCl prepared from 30% HCl (JT Baker). Seven vials containing 1 mL eluate each were collected and measured in a dose calibrator. One millilitre of the vial with the highest amount of radioactivity (which contained approximately 85% of total elutable ^{68}Ga) was transferred to a reaction vial containing 210 mg (± 5 mg) of HEPES (Sigma-Aldrich) dissolved in 0.5 mL deionized water to adjust the pH in the solution at 3–3.5; next, 2–15 nmol of DOTA-peptide dissolved in deionized water (0.1 nmol/ μL) was added to the radiolabelling reaction mixture. After very careful shaking, the complex formation was performed at $90 \pm 5^\circ\text{C}$ for 5 min using a microwave with monomodal radiation and then cooled to room temperature with nitrogen.

The labelled peptides were purified using a Sep-Pak Light C18 cartridge (Waters) conditioned and equilibrated previously with 4 mL of pure ethanol and 4 mL of deionized water. Thus, the reaction mixture was transferred onto

Sep-Pak where the ^{68}Ga -DOTA-AF7p and colloidal ^{68}Ga were retained, whereas free $^{68}\text{GaCl}_3$ passed through the cartridge [23]. Next, the cartridge was rinsed with 4 mL of deionized water, and the activity on the Sep-Pak cartridge was recovered with 0.5 mL ethanol 96% (v/v). Finally, ethanol was evaporated to dryness, and ^{68}Ga -DOTA-AF7p was dissolved in 0.9% saline solution.

Radiochemical yield was determined as % activity recovered in ethanol with respect to total activity used, after the radioactivity was decay-corrected to the start of procedure. An aliquot was taken to analyse the radiochemical purity (RQP) of the final product by radio-HPLC. The radio-HPLC method used a Jasco HPLC system equipped with a photodiode array UV-detector MD-4015 (Jasco), a radioactivity detector LB 507A (Berthold), and a reversed-phase Phenomenex Jupiter Proteo 90 Å column (4 μm , 250 \times 4.6 mm). The flow rate was 1 mL/min. The mobile phase was 95% solvent A (0.1% TFA in 5% acetonitrile) and 5% solvent B (0.1% TFA in 95% acetonitrile). The linear gradient started 2 min after sample injection with 95% solvent A and 5% solvent B to 0% solvent A and 100% solvent B at 12 min, maintained at 15 min and followed with 95% solvent A and 5% solvent B at 18 min.

2.2. Cell Culture. Human pancreas adenocarcinoma cell line Capan-2 was obtained from the American Type Culture Collection (ATCC HTB-80™) and cultured at 37°C in 5% CO₂ humidity according to standard mammalian tissue culture protocols in McCoy's 5A medium (Gibco) supplemented with 20% fetal bovine serum (FBS) (Gibco), 100 units/ml penicillin/100 $\mu\text{g}/\text{ml}$ streptomycin (Sigma), 2 mM L-glutamine (Gibco), and 10 mM Hepes buffer (Sigma).

2.3. Tumour-Bearing Mice (CAPAN-2 and Patient-Derived Xenografts). All animal experimental procedures were performed by the following protocols approved by the CNIO-ISCIII Ethics Committee for Research and Animal Welfare (CElyBA) and the CIEMAT Animal Ethical Committee; they were performed in strict adherence to the guidelines stated in the International Guiding Principles for Biomedical Research Involving Animals, established by the Council for International Organizations of Medical Sciences (CIOMS). All animal experimental procedures had also been approved by the Competent Authority of the Regional Government of Madrid (CAM), Spain (projects PROEX 104/16 and PROEX 094/15).

Three tumour models were used: (i) CAPAN-2 subcutaneous, (ii) subcutaneous patient-derived xenograft (PDX), and (iii) orthotopic PDX models.

For the cell line-derived model, 1×10^6 CAPAN-2 cells were injected subcutaneously into the flanks of female athymic nude-*Foxn1nu* (*nu/nu*) mice (Harlan Laboratories). Tumours were allowed to develop until palpable prior to PET imaging. Mice were sacrificed when the tumour mass reached a maximum size of 1500 mm³ or tumour ulceration was observed, or mice were symptomatic from their tumours which included signs of lethargy, poor grooming, weight loss, and hunching.

PDX models used in this work were established as described by Rubio-Viqueira et al. [24] and Hidalgo et al. [25] using four- to six-week-old female athymic nude-*Foxn1nu* (*nu/nu*) mice, purchased from Envigo (Barcelona, Spain). Animals were maintained at the Spanish National Cancer Research Centre (CNIO) Animal Facility (awarded with the AAALAC accreditation). Orthotopic tumours were monitored by ultrasonography, and those implanted into the flanks were allowed to grow to approximately 40 to 200 mm³ prior to perform PET imaging studies.

2.4. PET/CT Imaging. PET imaging was performed with a small-animal Argus PET-CT scanner (SEDECAL, Madrid, Spain). PET studies (energy window 250–700 KeV and 30 min static acquisition) and CT studies (voltage 45 kV, current 150 μ A, 8 shots, 360 projections, and standard resolution) were performed either at 90 min or at various time points after injection of ⁶⁸Ga-DOTA-AF7p or ⁸⁹Zr-DFO-LEM2/15, respectively, in mice anesthetized by inhalation of 2–2.5% isoflurane. PET image reconstruction was accomplished using a 2D-OSEM (ordered subset expectation maximization) algorithm (16 subsets and two iterations), with random and scatter correction. A calibration factor predetermined by scanning a cylindrical phantom containing a known activity of ⁶⁸Ga or ⁸⁹Zr was used to convert counts per pixel/sec to kBq/cm³. Manually drawn regions of interest (ROIs) selected from PET images using CT anatomical guidelines were used to determine the mean radiotracer accumulation in units of %ID/g tissue (decay corrected to the time of injection) by dividing the obtained average tracer concentration (kBq/cm³) in the region by the total ID (injected dose, expressed in kBq). Tumour-to-blood and tumour-to-background ratios were calculated from % ID/g values in ROIs for the whole tumour, heart (a measure of the blood pool), and brain (for background measurements). Images were analysed with the image analysis software ITK-SNAP [26] (<http://www.itksnap.org>).

2.5. Immunohistochemistry. Tumour-bearing mice were sacrificed after acquisition of the last PET image, and tumours were excised, fixed in 10% buffered formalin (Sigma), and embedded in paraffin. For MT1-MMP expression analysis, we performed immunohistochemical staining with anti-MT1-MMP LEM2/15 antibody at 1:400 dilution after antigen retrieval with low pH buffer in Autostainer platform (Dako) and counterstaining with hematoxylin. Slides were digitalized in the Mirax Scan (Carl Zeiss AG, Oberkochen, Germany), and pictures were registered with the Panoramic Viewer software (3DHitech Ltd., Ramsey, NJ, USA).

2.6. Statistics. Univariate methods such as the *t*-test and ANOVA were used to compare means of one variable across two or more groups. The significance of differences was tested at the 95% confidence level by Bonferroni's multiple comparisons test; a *P* value of 0.05 or less was considered significant. Data in graphs are presented as the

mean \pm SD. The Grubbs test was applied to detect eventual outliers in data sets with the online "Outlier Calculator" tool provided by GraphPad software (<http://www.graphpad.com/quickcalcs/Grubbs1.cfm>).

3. Results and Discussion

Initial studies on ⁸⁹Zr-labelled LEM2/15, an antihuman MT1-MMP mAb, as an immunoPET probe for glioblastoma in xenograft mice were previously reported by our group [19]. Now in this study, the use of ⁸⁹Zr-DFO-LEM2/15 was validated as an immunoPET probe in CAPAN-2 cell line as well as in patient-derived pancreatic ductal adenocarcinoma xenografts. The *in vivo* PET imaging of ⁸⁹Zr-DFO-LEM2/15 was additionally compared with that of ⁶⁸Ga-DOTA-AF7p, a peptide that binds to the MT-loop region of MT1-MMP [15].

3.1. Probe Radiosynthesis

3.1.1. ⁸⁹Zr-DFO-LEM2/15. Conjugation of LEM2/15 to desferrioxamine was achieved via an N-succinimidyl linkage in an mAb:deferoxamine ratio of approximately 1:2-3 as reported previously [19]. ⁸⁹Zr-DFO-LEM2/15 was successfully synthesized at a radiochemical yield of >85%. After PD-10 column purification, RQP was determined by ITLC to be above 95% (Figure 1(a)). The specific activity of final product was measured to be 9.675 \pm 2.445 MBq/nmol (*n* = 3).

The stability of the radiolabelled antibody was assessed with ITLC. Figure 1(b) illustrates that during the 7-day incubation period at 37°C, the ⁸⁹Zr-DFO-LEM2/15 in human serum and plasma decreased slightly from 94.9 \pm 6.5% and 97.1 \pm 3.9% at the beginning, respectively, to values of 91.9 \pm 8.8% and 85.0 \pm 3.9%, respectively. Similarly, the amount in human serum and plasma decreased from 98.7 \pm 1.5% and 96.7 \pm 4.0% at the beginning, respectively, to 95.4 \pm 6.2% and 94.9 \pm 8.2%, respectively, during the 7-day incubation period at 4°C. Therefore, the data indicated that probe displayed a high kinetic stability and was suitable for further *in vivo* studies.

3.1.2. ⁶⁸Ga-DOTA-AF7p. The radiochemical yield of both ⁶⁸Ga-labelled DOTA-peptides, DOTA-HWKHLHNTKTF (DOTA-AF7p-1) and HWK(DOTA)HLHNTKTF (DOTA-AF7p-2), was 30.1 \pm 17.9% (*n* = 29) indicating a high interexperiment variability in the radiolabelling procedures. No statistically significant differences between the two peptides were found. The radiochromatogram of the reaction mixture prior to passing through the Sep-Pak Light C18 cartridge showed two distinct peaks corresponding to free ⁶⁸Ga and ⁶⁸Ga-DOTA-AF7p-1 with retention times of 2.5 and 8.7 min, respectively. Figure 1(c) shows a representative chromatogram of peptide labelling with a low yield aiming at demonstrating that even in those cases, a final product can be successfully obtained. After purification, the radiochromatogram showed just one single peak corresponding to the radiolabelled probe (Figure 1(d)); RQP was greater than 95%. The radiochromatogram corresponding to

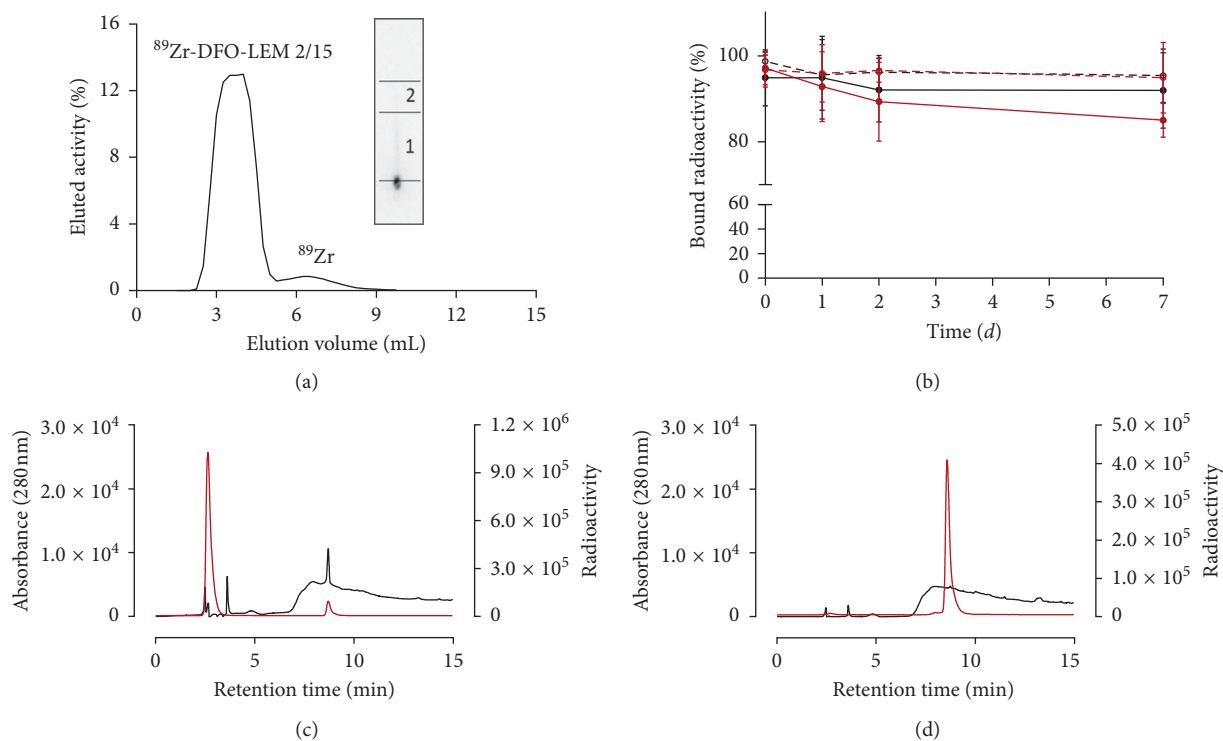


FIGURE 1: (a) Purification of ^{89}Zr -DFO-LEM2/15 in a PD-10 column; the antibody elutes between volume fractions 2.5 and 5.0 ml. Inset: ITLC image illustrating RQP of the ^{89}Zr -DFO-LEM2/15 peak. 1 corresponds to the radioimmunoconjugate and 2 to the free radionuclide. (b) Percentage of bound radioactivity to LEM2/15 after 7-day incubation of ^{89}Zr -DFO-LEM2/15 with human serum at 37°C (—●—) and 4°C (---○---) and human plasma at 37°C (—●—) and 4°C (---○---); data expressed as mean \pm SD. ($n = 4$). Representative HPLC chromatogram of ^{68}Ga -DOTA-AF7p-1 before (c) or after (d) Sep-Pak Light C18 cartridge purification. ^{68}Ga -DOTA-AF7p-1 is detected at 8.7 min by UV absorbance at 280 nm (—) and radioactivity detector (—).

^{68}Ga -DOTA-AF7p-2 is not presented because it was similar to that of ^{68}Ga -DOTA-AF7p-1. The specific activity of the final product once radiolabelling was completed was estimated to be 8.4 ± 6.0 MBq/nmol ($n = 29$).

3.2. ^{68}Ga -DOTA-Peptides PET Imaging

3.2.1. CAPAN-2-Tumour-Bearing Mice. Most of the current understanding of cancer and its hallmarks is based on the establishment of long-term *in vitro*-cultured tumour cell lines and their *in vivo* inoculation in mice. Ellenrieder et al. [27] reported high levels of MT1-MMP expression in most pancreatic cancer cell lines including CAPAN-2. To evaluate if both radiolabelled peptides could image MT1-MMP expression *in vivo* by PET, we administered 4 ± 3 MBq ($n = 25$) of ^{68}Ga -DOTA-AF7p-1 or ^{68}Ga -DOTA-AF7p-2 intravenously into mice bearing CAPAN-2 bilateral flank xenografts ($n = 9$), and we performed PET/CT imaging at distinct time points for a month. *In vivo* small-animal PET imaging showed accumulation of radiolabelled peptide in CAPAN-2 tumours, and we did not find differences in the tumour uptake visualization between the two radiolabelled peptides. Figure 2(a) shows a representative example.

The tumour uptake of ^{68}Ga -DOTA-AF7p-1 and ^{68}Ga -DOTA-AF7p-2 was found to be very similar, and there were no statistically significant differences between the two

radiolabelled peptides, 0.171 ± 0.095 ($n = 33$) and 0.216 ± 0.095 ($n = 17$) %ID/g for ^{68}Ga -DOTA-AF7p-1 and ^{68}Ga -DOTA-AF7p-2, respectively (Figure 2(c)). This is in good agreement with the results obtained by Kondo et al. [16], who developed a radiolabelled peptide probe by adding a Cys residue at the N-terminus of the peptide MT1-AF7p to allow facile radiolabelling of the thiol moiety by *N*-(*m*- $^{123/125}\text{I}$ iodophenyl) maleimide ($^{123/125}\text{I}$ IPM) for SPECT/CT imaging in HT1080-tumour-bearing mice (HT1080 is a human fibrosarcoma cell line known to highly express MT1-MMP); the radiolabelled probe was therefore similar to DOTA-AF7p but with IPM instead of DOTA. Kondo et al. [16] determined that the tumour accumulation at 60 and 120 min after injection was of 0.19 ± 0.06 and 0.10 ± 0.01 %ID/g, respectively. These findings, however, clash with the results reported by Min et al. [17] which used HYNIC as the bifunctional chelating agent (instead of DOTA or IPM) and tricine/TPPTS as coligands to prepare $^{99\text{mTc}}$ -(HYNIC-AF7p)(tricine)(TPPTS) for *in vivo* SPECT imaging of breast cancer. They found a highly tumour uptake of the probe (2.18 ± 0.11 %ID/g at 2 h post-injection) in MDA-MB-231-tumour-bearing mice. These differences in the uptake of the AF7p tracer can be due to many parameters playing a role in targeting such as the diverse density of MT1-MMP in the tissues, the affinity of peptide after labelling, the rate of tracer delivery, the vascular permeability of tumours, and the interstitial pressure among others [28].

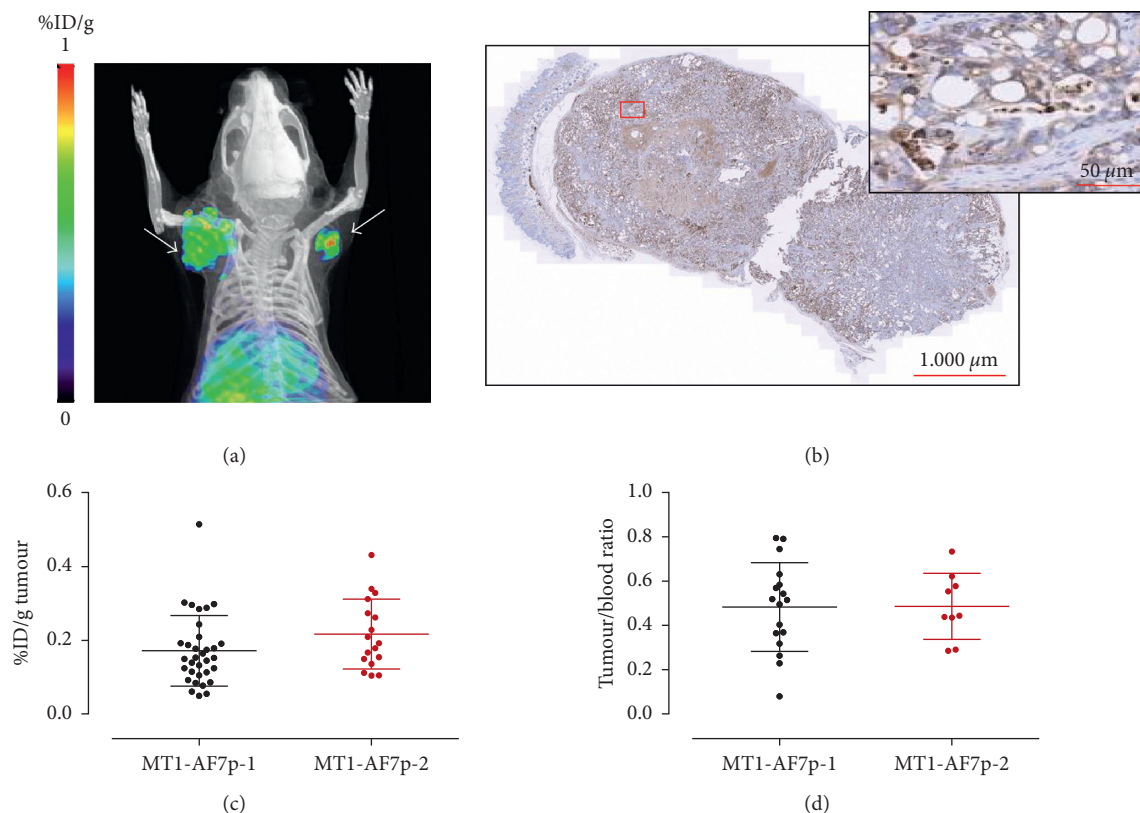


FIGURE 2: CAPAN-2-tumour-bearing mice injected with ^{68}Ga -DOTA-AF7p probes. (a) PET/CT image of representative mouse with subcutaneous CAPAN-2 xenograft (white arrows) that was injected with ^{68}Ga -DOTA-AF7p-1. Image was acquired 90 min after injection. (b) Immunohistochemistry of tumour tissue from xenografted mice. MT1-MMP was detected using LEM2/15 antibody. Scale bar: 1000 μm . Higher magnification of the boxed area is shown at the right corner. Scale bar: 50 μm . (c) Tumour uptake (expressed as %ID/g) of ^{68}Ga -DOTA-AF7p-1 and ^{68}Ga -DOTA-AF7p-2 probes as quantified by PET imaging. (d) Tumour-to-blood ratio derived from PET images for both radiolabelled probes.

As for the tumour-to-blood ratio, often used as a measure of image contrast, we did not observe any statistically significant differences between ^{68}Ga -DOTA-AF7p-1 and ^{68}Ga -DOTA-AF7p-2 (0.48 ± 0.20 and 0.49 ± 0.15 , resp.) at 90 min after injection (Figure 2(d)). This ratio was similar to that found by Kondo et al. [16] and lower than that determined by Min et al. [17].

All tumours contained tumour cells embedded in desmoplastic tumour stroma, a typical feature of pancreatic tissue. Immunohistochemical examination of tumour sections for MT1-MMP revealed expression of MT1-MMP in tumour cells but not in stromal cells (Figure 2(b)).

3.2.2. Heterotopic Patient-Derived Xenograft Model.

Patient-derived xenografts (PDXs) are typically generated by the subcutaneous implantation of fresh, surgically derived human tumour material into immunodeficient mice. PDXs retain stably molecular, genetic, and histopathological features of their originating tumours and therefore are currently the only model system able to incorporate directly the vast interpatient and intratumour heterogeneity inherent to human cancer [29]. With the aim to determine the applicability of PET imaging of PDAC tumours in a more

clinically relevant model with ^{68}Ga -DOTA-AF7p, we performed PET/CT imaging with this radiolabelled probe at four-time points during two weeks in patient-derived tumour-bearing mice ($n = 5$). As we did not find any statistically significant differences between the two radiolabelled peptides tested in CAPAN-2-bearing tumour mice, we decided to carry out our PET/CT studies after injecting 1.9 ± 1.8 MBq ($n = 17$) of ^{68}Ga -DOTA-AF7p-1. Figure 3(a) shows a representative PET/CT image taken 90 min after injection. After performing *in vivo* imaging, we also assessed the overexpression of MT1-MMP in patient-derived tumours by means of immunohistochemistry making use of the LEM2/15 antibody. Immunohistochemistry analyses revealed that MT1-MMP localized to the membranes of pancreatic ductal cells while no expression was detected in the stromal cells (Figure 3(b)).

Each mouse carried two patient-derived tumours implanted bilaterally subcutaneously. We used CT to evaluate volume growth; Jensen et al. had demonstrated that microCT was a more accurate than other methods (as external calliper) for the *in vivo* volumetric measurements of subcutaneous tumours in mice [30]. All mice developed subcutaneous tumours in both flanks, with a mean tumour volume that increased from 122 ± 89 mm³ to 208 ± 137 mm³ along the

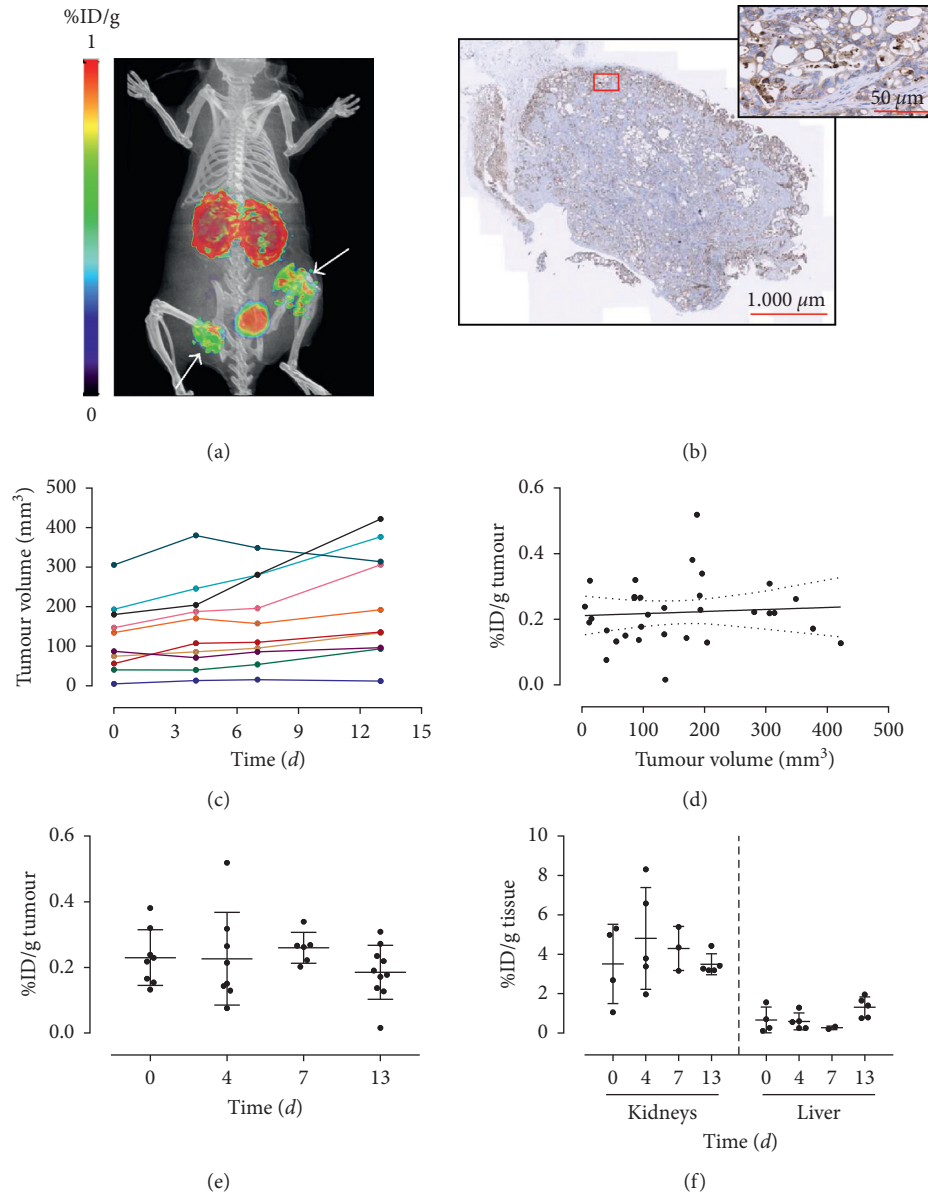


FIGURE 3: Heterotopic patient-derived xenografted mice injected with ^{68}Ga -DOTA-AF7p-1. (a) PET/CT image of representative heterotopic PDX mouse injected with ^{68}Ga -DOTA-AF7p-1 acquired 90 min after injection. Tumour locations are indicated by white arrows. (b) Immunohistochemistry of tumour tissue from PDX mice. MT1-MMP was detected using LEM2/15 antibody. Scale bar: 1000 μm . Higher magnification of the boxed area is shown at the right corner. Scale bar: 50 μm . (c) Tumour volume was measured by CT four times after onset of PET imaging study. Each tumour is represented by a different colour line on the graph. (d) Tumour uptake (quantified by PET imaging and expressed as %ID/g) as a function of tumour volume for all scanned mice, showing that there is no relationship between tumour size and ^{68}Ga -DOTA-AF7p-1 uptake. (e) Variation of tumour uptake of ^{68}Ga -DOTA-AF7p-1 along the PET imaging study. (f) Variation of kidneys and liver uptakes of ^{68}Ga -DOTA-AF7p-1 along the PET imaging study.

whole duration of the PET imaging study (Figure 3(c)). Although a variable tumour volume between repeated scans may *per se* cause variability in the tumour uptake of ^{68}Ga -DOTA-AF7p-1, our analysis revealed the absence of significant correlation between the tumour uptake and tumour size (Figure 3(d)). At the start of the PET study, the tumour displayed an uptake of $0.230 \pm 0.085\% \text{ID/g}$ ($n = 8$) and it remained at this level throughout the time course: 0.227 ± 0.142 ($n = 8$), 0.260 ± 0.047 ($n = 6$), and 0.185 ± 0.082 ($n = 10$) %ID/g tumour at 5, 8, and 14 days, respectively

(Figure 3(e)). The mean tumour uptake of ^{68}Ga -DOTA-AF7p-1 was of $0.221 \pm 0.096\% \text{ID/g}$ tumour ($n = 32$). This is in good agreement with the results reported by Kondo et al. [16] in their study of CAPAN-2-bearing tumour xenograft mice. The mean value of the tumour-to-blood ratio at 90 min ^{68}Ga -DOTA-AF7p-1 after injection in PDX (1.36 ± 0.98 , $n = 26$) was higher than that measured in CAPAN-2-bearing tumour mice (0.48 ± 0.20 , $n = 17$), demonstrating that for the PET visualization of the radiolabelled probe, the PDX model is better one than the CAPAN-2-derived model.

It should be noted that in addition to the tumour, kidneys and bladder also showed signals, indicating that the tracer is mainly excreted through the renal route (Figure 3(f)). The mean accumulation of the probe was significantly lower in liver than in kidneys (0.80 ± 0.60 , $n = 16$ versus 4.03 ± 1.73 , $n = 17$ resp.).

We are aware of, at least, one limitation in our research, that is the relatively low tumour accumulation level of both radiolabelled peptides, which was also occurred in the study of Kondo et al. [16]. A setup allowing for an increase of the ^{68}Ga -DOTA-AF7p uptake in pancreatic tumours would be required if we were to carry out further studies. A possible strategy could be to increase the affinity of the radiolabelled probe for MT1-MMP inserting a spacer linker that imposes a separation between the bifunctional chelating agent (DOTA) and the peptide, as it has already been suggested by several other authors [16, 31]. Our study is nevertheless the first report of the use of a radiolabelled peptide probe for the PET imaging of MT1-MMP in PDAC cell- and patient-derived xenograft mice.

3.3. ^{89}Zr -DFO-LEM2/15 PET Imaging

3.3.1. CAPAN-2-Tumour-Bearing Mice. We had already reported the quantitative assessment of MT1-MMP expression by means of immunoPET using a specific mAb (LEM 2/15), readily labelled with ^{89}Zr and employed in the *in vivo* preclinical imaging of glioblastoma MT1-MMP⁺ tumours [19]. ^{89}Zr -DFO-LEM 2/15 small-animal PET was conducted on mice harbouring xenografted tumours at opposite flanks with CAPAN-2 cells ($n = 4$) after injection of 0.55 ± 0.01 MBq ($n = 4$). Figure 4(a) presents some typical images of a CAPAN-2-tumour-bearing nude mouse at 1 and 7 days after injection, showing an excellent visualization of tumours. Levels of radioactivity in tumours, tumour-to-blood, and tumour-to-background ratios were estimated from PET images. In tumours, radioactivity did not vary significantly in a time-dependent manner, with the uptake being 5.93 ± 0.98 , 6.29 ± 0.64 , 5.35 ± 1.70 , and $5.09 \pm 0.52\%$ ID/g ($n = 7$) at 1, 3, 5, and 7 days after injection, respectively, in CAPAN-2 tumours (Figure 4(c)). The mean value of tumour uptake for the ^{89}Zr -DFO-LEM 2/15 probe ($5.67 \pm 1.11\%$ ID/g, $n = 28$) was 25–30 times higher than that for the ^{68}Ga -DOTA-AF7p ones. Sections of tumours immunostained for MT1-MMP confirmed the expression of this protein in the tumour cells but not in the stromal cells (Figure 4(b)) as we have remarked earlier on in this report (Figure 2(b)).

Tumour/blood ratios in CAPAN-2 tumours increased lightly with time (0.67 ± 0.08 , 0.93 ± 0.17 , 1.13 ± 0.51 , and 1.44 ± 0.43 at 1, 3, 5, and 7 d ^{89}Zr -DFO-LEM 2/15 after injection, resp.) (Figure 4(d)). These values also were higher than those estimated for ^{68}Ga -DOTA-AF7p probes (approximately tumour/blood ratio = 0.5 at 90 min after injection). These results indicate that the visualization and quantification of the tumour uptake by noninvasive PET imaging is better with ^{89}Zr -DFO-LEM 2/15 than it is with ^{68}Ga -DOTA-AF7p. The difference in signal between tumour and normal tissue in the context of nuclear medicine

imaging depends upon the tumour-localizing agent. Tumour-to-background ratios can be anything from 1:1 to >10:1 when using radiolabelled antibodies [32]. Thus, tumour/background ratios in CAPAN-2 tumours exhibited high values (5.85 ± 1.56 , 6.37 ± 0.57 , 5.14 ± 2.23 , and 5.53 ± 2.06 at 1, 3, 5, and 7 days after injection, resp.) (Figure 4(d)) confirming previous findings.

In addition to the tumour uptake, visible signal was observed in the liver due to the metabolization and the nonspecific clearance of the radiolabelled antibody, which is a characteristic feature of the distribution pattern of monoclonal antibodies (Figure 4(e)). Liver uptake of ^{89}Zr -DFO-LEM 2/15 at 1, 3, 5, and 7 days after injection was 8.84 ± 2.56 , 9.83 ± 2.59 , 9.46 ± 1.30 , and $7.08 \pm 3.30\%$ ID/g, respectively. Lastly, bone uptake was low and did not increase over time, in support of the notion of the *in vivo* stability of the radioimmunoconjugate (free Zr^{4+} salts can manifest tropism towards the bone); the ^{89}Zr -DFO-LEM 2/15 uptake was 2.75 ± 0.44 , 2.78 ± 0.61 , 2.77 ± 0.58 , and 2.46 ± 0.19 at 1, 3, 5, and 7 days after injection, respectively (Figure 4(e)).

^{89}Zr immunoPET continues to drive research and development in the field of the application of mAbs in PET molecular imaging [33] and has shown great potential in cancer imaging [34]. Although ^{89}Zr -immunoPET is a highly attractive technique to measure tumour-associated antigens as well as the *in vivo* distribution of mAbs, it has to be mentioned that it is restrained by a few limitations. First of all, the enhanced permeability and retention effect characteristic of the leaky nature of tumour vasculature and reduced lymphatic drainage [35] may result in nonreceptor-mediated uptake of radiolabelled antibodies producing, thus, false-positive results. Second, a low target expression may lead to false-negative results due to low imaging contrast derived from the long circulatory half-life of monoclonal antibodies [32]. Finally, as a longer-lived medical radioisotope, one of the principal concerns regarding the use of ^{89}Zr in the clinic is the substantial radiation dose that patients receive in comparison to shorter-lived nuclides. However, as long as the radiotracer clears the healthy tissue as expected, the prevailing viewpoint is that the increased diagnostic value is worth the additional dose [36]. Along these lines, the uptake in bones is a notable issue with ^{89}Zr PET imaging in preclinical mouse models. Biodistribution analyses commonly show up to 10% injected dose per gram activity in the bone [34], which is consistent with the results we have obtained in our research. Localization of radioactivity to the bone is disadvantageous since it implies that an increased radioactivity dose is delivered to the bone marrow. To overcome such limitations, our current work aims at extending these initial findings using engineered and miniaturized derivatives of the LEM2/15 antibody. The miniaturized antibodies could improve the tumour penetration ratio and therefore result in an improved tumour-targeted imaging [37]. Moreover, labelling with PET isotopes characterized by short or intermediate half-lives such as ^{68}Ga would optimize the pharmacokinetics and facilitate wide access to this technology since ^{68}Ga can be easily produced at most facilities using a $^{68}\text{Ge}/^{68}\text{Ga}$ generator system, thus avoiding the complexity of a cyclotron facility. They facilitate

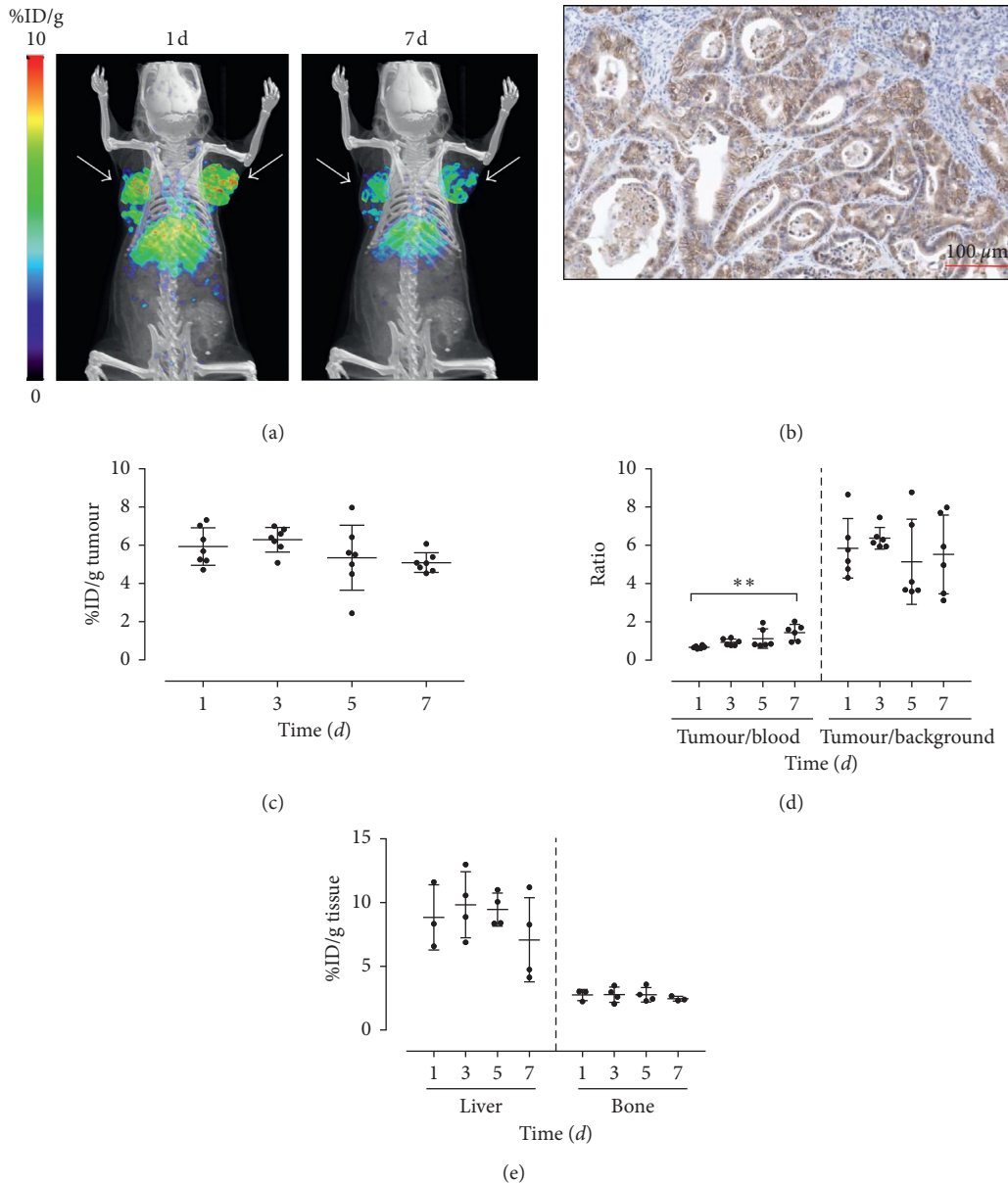


FIGURE 4: CAPAN-2-tumour-bearing mice injected with ^{89}Zr -DFO-LEM2/15. (a) Representative PET/CT images of a mouse with subcutaneous CAPAN-2 xenograft injected with ^{89}Zr -DFO-LEM2/15 acquired at 1 and 7 days after injection. Tumour locations are indicated by white arrows. (b) Immunohistochemistry of tumour tissue from xenografted mice. MT1-MMP was detected using LEM2/15 antibody. Scale bar: $100\ \mu\text{m}$. (c) Tumour uptake (expressed as %ID/g) of ^{89}Zr -DFO-LEM2/15 as quantified by PET imaging. (d) Tumour-to-blood and tumour-to-background ratios derived from PET images. (e) Liver and bone uptake of ^{89}Zr -DFO-LEM2/15 as quantified by PET imaging at different times after injection.

the implementation of a same-day imaging approach, much like the current practice for ^{18}F -FDG-PET, and their employment leads to a lower radiation exposure versus immunoPET with intact antibodies, making them appealing for routine use in the clinic [38]. This approach is very promising to assess target expression levels in individual patients so to identify patients that will likely benefit from targeted treatments.

3.3.2. Orthotopic Patient-Derived Xenograft Model. To evaluate the ability of ^{89}Zr -DFO-LEM2/15 to noninvasively

determine MT1-MMP protein levels in nude mice bearing orthotopic PDX tumours ($n = 5$) as described above, the radioimmunoconjugate was prepared and injected ($1.8 \pm 1.6\ \text{MBq}$, $n = 7$) to the subject mice once the presence of tumours was confirmed by ultrasonography, and serial PET imaging was performed at 1, 2, 4, and 7 days. ^{89}Zr -DFO-LEM2/15 was also injected in mice free of tumours ($n = 2$) used as a control group. The PET images presented in Figure 5(a) were taken at different time points after injection and are compared to control mice; they show that the tumours were clearly visualized in orthotopic PDX mice after injection of ^{89}Zr -labelled mAb LEM2/15. Tumour uptake

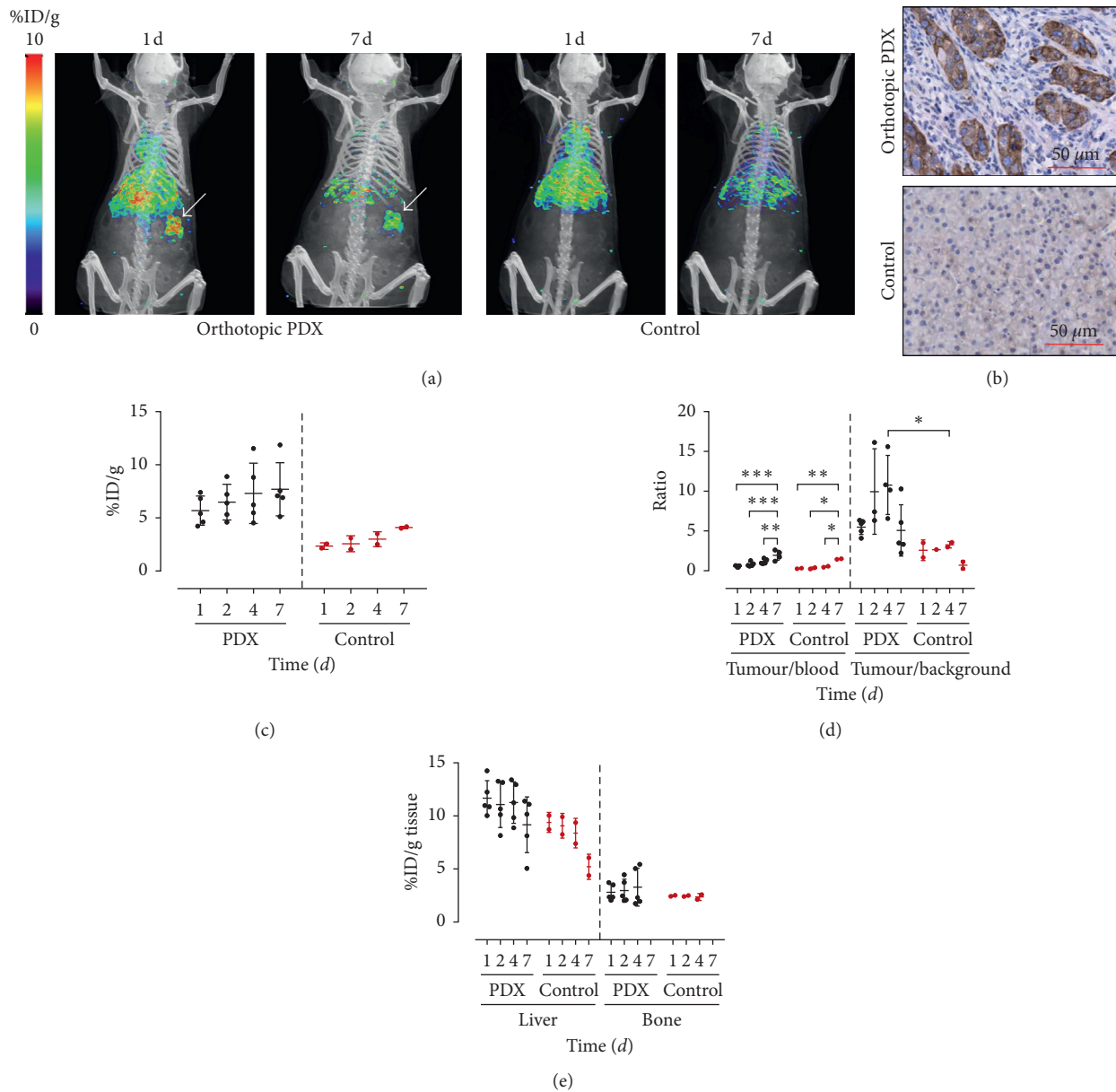


FIGURE 5: Orthotopic patient-derived xenografted mice injected with ^{89}Zr -DFO-LEM2/15. (a) Representative PET/CT images of orthotopic PDX and control mice injected with ^{89}Zr -DFO-LEM2/15 acquired at 1 and 7 days after injection. Tumour locations are indicated by white arrows. (b) Immunohistochemistry studies of pancreas tissues derived from orthotopic PDX and control mice. MT1-MMP was detected using LEM2/15 antibody. Scale bar: 50 μm . (c) Tumour uptake (expressed as %ID/g) of ^{89}Zr -DFO-LEM2/15 as quantified by PET imaging. (d) Tumour-to-blood and tumour-to-background ratios derived from PET images. (e) Liver and bone uptake of ^{89}Zr -DFO-LEM2/15 as quantified by PET imaging at different times after injection in PDX and control mice.

increased over time, from $5.7 \pm 1.4\%$ ID/g at 1 d to $7.7 \pm 2.5\%$ ID/g at 7 d in PDX mice, whereas the accumulation in pancreas of control mice increased from $2.3 \pm 0.3\%$ ID/g at 1 d to $4.1 \pm 0.1\%$ ID/g at 7 d (Figure 5(c)); thus, ^{89}Zr -DFO-LEM2/15 uptake in tumours of PDX mice was about twice higher than in the pancreas of control mice. The tumour-to-blood ratios were at all time points higher in PDX mice than in control ones, 0.56 ± 0.10 , 0.81 ± 0.28 , 1.15 ± 0.32 , and 1.95 ± 0.63 versus 0.28 ± 0.05 , 0.31 ± 0.13 , 0.51 ± 0.09 , and 1.47 ± 0.05 at 1, 2, 4, and 7 days, respectively (Figure 5(d)). Tumour-to-background ratios were also around 2–7 times higher in PDX

mice than in control mice (Figure 5(d)). The mean values of radioimmunoconjugate tumour uptake, tumour-to-blood, and tumour-to-background ratios in PDX mice were similar to those found in CAPAN-2-tumour-bearing mice. As for the liver and bone uptake of ^{89}Zr -DFO-LEM2/15 in mice bearing orthotopic PDX tumours (Figure 5(e)), the mean values were also similar to those shown in Figure 4(e).

We also assessed by immunochemistry techniques the expression of MT1-MMP in tumours of PDAC patient-derived xenograft mice (Figure 5(b)). As expected, whereas MT1-MMP was highly expressed in tumour cells but not in

stromal cells, verified by immunostaining using LEM2/15, no immunostaining was observed in the pancreas of control mice. This is in good agreement with studies showing that MT1-MMP is overexpressed in pancreatic tumours relative to normal pancreas [39].

Our preclinical studies with MT1-MMP overexpressing CAPAN-2 cells and PDAC patient-derived tumours demonstrate that ^{89}Zr -DFO-LEM2/15 constitutes a promising radiotracer for noninvasive immunoPET measurements of MT1-MMP expression *in vivo*. Given the crucial role that MT1-MMP plays in both physiologic and pathologic conditions, MT1-MMP overexpression is seen in a number of different tumours, including PDACs as shown herein and in earlier reports [39–41]. Pancreatic ductal adenocarcinoma is the most common form of pancreatic cancer and accounts for ~90% of all pancreatic tumours [42]. It is associated with an overall 5-year survival rate of <8%, exhibiting the poorest prognosis of all solid tumours [43]. One of the reasons for this poor prognosis is the high resistance of PDAC to conventional chemotherapy treatments [44]. Following the initial success of gemcitabine in the treatment of advanced PDAC, combination therapies with gemcitabine were administered with limited success to tackle locally advanced and metastatic disease. This failure is attributable to many factors, including extrinsic or intrinsic resistance to gemcitabine [45]. Notably, PDAC is a tumour characterized by the development of extensive fibrosis termed desmoplasia. Interestingly, MT1-MMP overexpression was particularly prominent in areas of the tumour with intense fibrotic reaction, suggesting that type I collagen-enriched desmoplastic reaction may also contribute to MT1-MMP expression in the *in vivo* setting [40]. Dangi-Garimella et al. [6] showed that MT1-MMP expression associates to an increased HMGA2 expression (a nonhistone DNA-binding nuclear protein involved in chromatin remodelling and gene transcription) in human PDAC tumours, suggesting that the marked fibrotic reaction may contribute to gemcitabine resistance through increased MT1-MMP-HMGA2 signalling. Therefore, owing to the central role that MT1-MMP plays in collagen-induced gemcitabine resistance [45], this metalloproteinase emerges as a good predictive biomarker of the response to gemcitabine in patients with pancreatic cancer; thus, PET imaging probes such as ^{68}Ga -DOTA-AF7p or ^{89}Zr -DFO-LEM2/15, with the modifications that our research has highlighted so as to increase the affinity of ^{68}Ga -DOTA-AF7p and/or obtain miniaturized derivatives of the LEM2/15 mAb, could be used for the early prediction of resistance to gemcitabine in PDAC patients. Targeting MT1-MMP with these probes could furthermore also be a novel approach to sensitizing pancreatic tumours to gemcitabine.

4. Conclusions

We have in this report radiolabelled two molecules, an anti-MT1-MMP monoclonal antibody (LEM2/15) and a MT1-MMP-specific binding peptide (MT1-AF7p) with ^{89}Zr and ^{68}Ga , respectively. We assessed and compared their *in vivo* properties for use as new MT1-MMP-targeted PET imaging probes in several models of pancreatic cancer. Both tracers

highly accumulated in MT1-MMP-expressing tumours and were able to visualise clearly subcutaneously and orthotopically implanted xenografts, although the ^{89}Zr -DFO-LEM2/15 probe exhibited much greater specific uptake compared to the ^{68}Ga -labelled peptide. The results of our study highlight the relevance of MT1-MMP as a suitable biomarker for noninvasive PET imaging of pancreatic cancer. Also, our results suggest that the ^{89}Zr -DFO-LEM2/15 probe may have potential application in PDAC detection and follow-up and can be a lead for further tracer optimization. In fact, miniaturization of LEM2/15 and radiolabelling with ^{68}Ga to enhance its radiopharmacological properties are in progress and may facilitate translation in the clinical setting for the improvement of the clinical management of PDAC patients.

Data Availability

The data used to support the findings of this study are available from the corresponding author upon request.

Disclosure

The present address of Pedro Pablo López-Casas is Bionotech Therapeutics S.L, Valencia, Spain. The present address of Manuel Hidalgo is Beth Israel Deaconess Medical Center, Harvard Medical School, Boston, Massachusetts, USA.

Conflicts of Interest

The authors declare that they have no conflicts of interest.

Acknowledgments

The authors are grateful to Dr. Luis E. Donate for critical reading of the manuscript. They thank the staff of the Histopathology Core Unit of CNIO for excellent technical support. This work was partially supported by a grant from the Regional Government of Madrid (CAM), Spain (S2017/BMD-3867 RENIM-CM), and cofinanced by European Structural and Investment Fund.

References

- [1] D. P. Ryan, T. S. Hong, and N. Bardeesy, "Pancreatic adenocarcinoma," *New England Journal of Medicine*, vol. 371, no. 11, pp. 1039–1049, 2014.
- [2] L. C. Chu, M. G. Goggins, and E. K. Fishman, "Diagnosis and detection of pancreatic cancer," *Cancer Journal*, vol. 23, pp. 333–342, 2017.
- [3] D. V. Sahani, P. A. Bonaffini, O. A. Catalano et al., "State-of-the-art PET/CT of the pancreas: current role and emerging indications," *RadioGraphics*, vol. 32, no. 4, pp. 1133–1158, 2012.
- [4] K. Mimori, T. Fukagawa, Y. Kosaka et al., "A large-study of MT1-MMP as a marker for isolated tumor cells in peripheral blood and bone marrow in gastric cancer cases," *Annals of Surgical Oncology*, vol. 15, no. 10, pp. 2934–2942, 2008.
- [5] J. Y. Perentes, N. D. Kirkpatrick, S. Nagano et al., "Cancer cell-associated MT1-MMP promotes blood vessel invasion and

- distant metastasis in triple-negative mammary tumors," *Cancer Research*, vol. 71, no. 13, pp. 4527–4538, 2011.
- [6] S. Dangi-Garimella, S. B. Krantz, M. R. Barron et al., "Three-dimensional collagen-I promotes gemcitabine resistance in pancreatic cancer through MT1-MMP-mediated expression of HMGA2," *Cancer Research*, vol. 71, no. 3, pp. 1019–1028, 2011.
- [7] S. Pahwa, M. J. Stawikowski, and G. B. Fields, "Monitoring and inhibiting MT1-MMP during cancer initiation and progression," *Cancers*, vol. 6, no. 1, pp. 416–435, 2014.
- [8] C. M. Overall and C. López-Otín, "Strategies for MMP inhibition in cancer: innovations for the post-trial era," *Nature Reviews Cancer*, vol. 2, no. 9, pp. 657–672, 2002.
- [9] R. Kaimal, R. Aljumaily, S. L. Tressel, and A. Agarwal, "Selective blockade of matrix metalloproteinase-14 with a monoclonal antibody abrogates invasion, angiogenesis, and tumor growth in ovarian cancer," *Cancer Research*, vol. 73, no. 8, pp. 2457–2467, 2013.
- [10] K. A. Botkjaer, H. F. Kwok, M. G. Terp et al., "Development of a specific affinity-matured exosite inhibitor to MT1-MMP that efficiently inhibits tumor cell invasion *in vitro* and metastasis *in vivo*," *Oncotarget*, vol. 7, no. 13, pp. 16773–16792, 2016.
- [11] L. Devy, L. Huang, L. Naa et al., "Selective inhibition of matrix metalloproteinase-14 blocks tumor growth, invasion, and angiogenesis," *Cancer Research*, vol. 69, no. 4, pp. 1517–1526, 2009.
- [12] S. Ingvarsen, A. Porse, C. Erpicum et al., "Targeting a single function of the multifunctional matrix metalloproteinase MT1-MMP: impact on lymphangiogenesis," *Journal of Biological Chemistry*, vol. 288, no. 15, pp. 10195–10204, 2013.
- [13] B. G. Gálvez, S. Matías-Román, J. P. Albar, F. Sánchez-Madrid, and A. G. Arroyo, "Membrane type 1-matrix metalloproteinase is activated during migration of human endothelial cells and modulates endothelial motility and matrix remodeling," *Journal of Biological Chemistry*, vol. 276, no. 40, pp. 37491–37500, 2001.
- [14] Y. Udi, M. Grossman, I. Solomonov et al., "Inhibition mechanism of membrane metalloproteinase by an exosite-swiveling conformational antibody," *Structure*, vol. 23, no. 1, pp. 104–115, 2015.
- [15] L. Zhu, H. Wang, L. Wang et al., "High-affinity peptide against MT1-MMP for *in vivo* tumor imaging," *Journal of Controlled Release*, vol. 150, no. 3, pp. 248–255, 2011.
- [16] N. Kondo, T. Temma, Y. Shimizu et al., "Radioiodinated peptidic imaging probes for *in vivo* detection of membrane type-1 matrix metalloproteinase in cancers," *Biological & Pharmaceutical Bulletin*, vol. 38, no. 9, pp. 1375–1382, 2015.
- [17] K. Min, B. Ji, M. Zhao et al., "Development of a radiolabeled peptide-based probe targeting MT1-MMP for breast cancer detection," *PLoS One*, vol. 10, no. 10, Article ID e0139471, 2015.
- [18] T. Temma, K. Sano, and Y. Kuge, "Development of a radiolabeled probe for detecting membrane type-1 matrix metalloproteinase on malignant tumors," *Biological & Pharmaceutical Bulletin*, vol. 32, no. 7, pp. 1272–1277, 2009.
- [19] A. G. de Lucas, A. J. Schuhmacher, M. Oteo et al., "Targeting MT1-MMP as an ImmunoPET-based strategy for imaging gliomas," *PLoS One*, vol. 11, no. 7, Article ID e0158634, 2016.
- [20] L. R. Perk, M. J. W. D. Vosjan, G. W. M. Visser et al., "p-Isothiocyanatobenzyl-desferrioxamine: a new bifunctional chelate for facile radiolabeling of monoclonal antibodies with zirconium-89 for immuno-PET imaging," *European Journal of Nuclear Medicine and Molecular Imaging*, vol. 37, no. 2, pp. 250–259, 2010.
- [21] M. J. W. D. Vosjan, L. R. Perk, G. W. M. Visser et al., "Conjugation and radiolabeling of monoclonal antibodies with zirconium-89 for PET imaging using the bifunctional chelate p-isothiocyanatobenzyl-desferrioxamine," *Nature Protocols*, vol. 5, no. 4, pp. 739–743, 2010.
- [22] E. Romero and M. A. Morcillo, "Inorganic oxides with potential application in the preparation of a $^{68}\text{Ge}/^{68}\text{Ga}$ generator system," *Applied Radiation and Isotopes*, vol. 119, pp. 28–35, 2017.
- [23] E. Romero, A. Martinez, M. Oteo et al., "Preparation of ^{68}Ga -labelled DOTA-peptides using a manual labelling approach for small-animal PET imaging," *Applied Radiation and Isotopes*, vol. 107, pp. 113–120, 2016.
- [24] B. Rubio-Viqueira, A. Jimeno, G. Cusatis et al., "An *in vivo* platform for translational drug development in pancreatic cancer," *Clinical Cancer Research*, vol. 12, no. 15, pp. 4652–4661, 2006.
- [25] M. Hidalgo, E. Bruckheimer, N. V. Rajeshkumar et al., "A pilot clinical study of treatment guided by personalized tumorgrafts in patients with advanced cancer," *Molecular Cancer Therapeutics*, vol. 10, no. 8, pp. 1311–1316, 2011.
- [26] P. A. Yushkevich, J. Piven, H. C. Hazlett et al., "User-guided 3D active contour segmentation of anatomical structures: significantly improved efficiency and reliability," *Neuroimage*, vol. 31, no. 3, pp. 1116–1128, 2006.
- [27] V. Ellenrieder, B. Alber, U. Lacher et al., "Role of MT-MMPs and MMP-2 in pancreatic cancer progression," *International Journal of Cancer*, vol. 85, pp. 14–20, 2000.
- [28] L. Zhang, S. Bhatnagar, E. Deschenes, and G. M. Thurber, "Mechanistic and quantitative insight into cell surface targeted molecular imaging agent design," *Scientific Reports*, vol. 6, no. 1, article 25424, 2016.
- [29] N. Gengenbacher, M. Shingal, and H. G. Augustin, "Pre-clinical mouse solid tumour models: status quo, challenges and perspectives," *Nature Reviews Cancer*, vol. 17, no. 12, pp. 751–765, 2017.
- [30] M. M. Jensen, J. T. Jorgensen, T. Binderup et al., "Tumor volume in subcutaneous mouse xenografts measured by microCT is more accurate and reproducible than determined by ^{18}F -FDG-microPET or external caliper," *BMC Medical Imaging*, vol. 8, no. 1, article PMC2575188, 2008.
- [31] E. A. Fragozeorgi, C. Zikos, E. Gourni et al., "Spacer site modifications for the improvement of the *in vitro* and *in vivo* binding properties of (99m)Tc-N(3)S-X-bombesin2-14 derivatives," *Bioconjugate Chemistry*, vol. 20, no. 5, pp. 856–867, 2009.
- [32] D. J. Buchsbaum, V. K. Langmuir, and B. W. Wessels, "Experimental radioimmunotherapy," *Medical Physics*, vol. 20, no. 2, pp. 551–567, 1993.
- [33] A. R. Jalilian and J. A. Osso, "Production, applications and status of zirconium-89 immunoPET agents," *Journal of Radioanalytical and Nuclear Chemistry*, vol. 314, no. 1, pp. 7–21, 2017.
- [34] S. Heskamp, R. Raavé, O. Boerman et al., " ^{89}Zr -immuno-positron emission tomography in oncology: state-of-the-art ^{89}Zr radiochemistry," *Bioconjugate Chemistry*, vol. 28, no. 9, pp. 2211–2223, 2017.
- [35] D. M. McDonald and P. L. Choyke, "Imaging of angiogenesis: from microscope to clinic," *Nature Medicine*, vol. 9, no. 6, pp. 713–725, 2003.
- [36] M. A. Deri, B. M. Zeglis, L. C. Francesconi et al., "PET imaging with ^{89}Zr : from radiochemistry to the clinic," *Nuclear Medicine and Biology*, vol. 40, no. 1, pp. 3–14, 2013.

- [37] R. Chakravarty, S. Goel, and W. Cai, "Nanobody: the "magic bullet" for molecular imaging?," *Theranostics*, vol. 4, no. 4, pp. 386–398, 2014.
- [38] A. Krasniki, M. D'Huyvetter, N. Devoogdt et al., "Same-day imaging using small proteins: clinical experience and translational prospects in oncology," *Journal of Nuclear Medicine*, vol. 59, no. 6, pp. 885–891, 2018.
- [39] T. Imamura, G. Ohshio, M. Mise et al., "Expression of membrane-type matrix metalloproteinase-1 in human pancreatic adenocarcinomas," *Journal of Cancer Research and Clinical Oncology*, vol. 124, no. 2, pp. 65–72, 1998.
- [40] S. R. Bramhall, J. P. Neoptolemos, G. W. Stamp et al., "Imbalance of expression of matrix metalloproteinases (MMPs) and tissue inhibitors of the matrix metalloproteinases (TIMPs) in human pancreatic carcinoma," *Journal of Pathology*, vol. 182, no. 3, pp. 347–355, 1997.
- [41] A. J. Ottaviano, L. Sun, V. Ananthanarayanan et al., "Extracellular matrix-mediated membrane-type 1 matrix metalloprotease expression in pancreatic ductal cells is regulated by transforming growth factor- β 1," *Cancer Research*, vol. 66, no. 14, pp. 7032–7040, 2006.
- [42] H. Ying, P. Dey, W. Yao et al., "Genetics and biology of pancreatic ductal adenocarcinoma," *Genes & Development*, vol. 30, no. 4, pp. 355–385, 2016.
- [43] R. L. Siegel, K. D. Miller, and A. Jemal, "Cancer statistics," *CA: A Cancer Journal for Clinicians*, vol. 67, no. 1, pp. 7–30, 2017.
- [44] I. Garrido-Laguna and M. Hidalgo, "Pancreatic cancer: from state-of-the-art treatments to promising novel therapies," *Nature Reviews Clinical Oncology*, vol. 12, no. 6, pp. 319–334, 2015.
- [45] C. Liang, S. Shi, Q. Meng et al., "Complex roles of the stroma in the intrinsic resistance to gemcitabine in pancreatic cancer: where we are and where we are going," *Experimental & Molecular Medicine*, vol. 49, no. 12, p. e406, 2017.

Research Article

Early Imaging Biomarker of Myocardial Glucose Adaptations in High-Fat-Diet-Induced Insulin Resistance Model by Using ^{18}F -FDG PET and $[\text{U-}^{13}\text{C}]$ glucose Nuclear Magnetic Resonance Tracer

Yi-Hsiu Chung,¹ Kuan-Ying Lu,^{2,3} Shao-Chieh Chiu,¹ Chi-Jen Lo,⁴ Li-Man Hung,^{5,6,7} Jiung-Pang Huang,⁵ Mei-Ling Cheng,^{3,4,5} Chao-Hung Wang ,⁸ Cheng-Kun Tsai,³ Yu-Chun Lin ,² Shang-Hung Chang,⁵ and Gigin Lin ^{2,3}

¹Center for Advanced Molecular Imaging and Translation (CAMIT), Linkou Chang Gung Memorial Hospital, Taoyuan, Taiwan

²Department of Medical Imaging and Intervention, Imaging Core Lab, Institute for Radiological Research, Linkou Chang Gung Memorial Hospital and Chang Gung University, Taoyuan, Taiwan

³Clinical Metabolomics Core Laboratory, Linkou Chang Gung Memorial Hospital, Taoyuan, Taiwan

⁴Metabolomics Core Laboratory, Healthy Aging Research Center, Chang Gung University, Taoyuan, Taiwan

⁵Department and Graduate Institute of Biomedical Sciences, College of Medicine, Chang Gung University, Taoyuan, Taiwan

⁶Healthy Aging Research Center, Chang Gung University, Taoyuan, Taiwan

⁷Kidney Research Center, Linkou Chang Gung Memorial Hospital, Taoyuan, Taiwan

⁸Heart Failure Center, Division of Cardiology, Department of Internal Medicine, Chang Gung Memorial Hospital, Keelung, Taiwan

Correspondence should be addressed to Gigin Lin; giginlin@cgmh.org.tw

Received 9 March 2018; Revised 31 May 2018; Accepted 4 June 2018; Published 12 July 2018

Academic Editor: Anxo Fernández-Ferreiro

Copyright © 2018 Yi-Hsiu Chung et al. This is an open access article distributed under the Creative Commons Attribution License, which permits unrestricted use, distribution, and reproduction in any medium, provided the original work is properly cited.

Background. High-fat diet (HFD) induces systemic insulin resistance leading to myocardial dysfunction. We aim to characterize the early adaptations of myocardial glucose utility to HFD-induced insulin resistance. **Methods.** Male Sprague–Dawley rats were assigned into two groups, fed a regular chow diet or HFD ad libitum for 10 weeks. We used *in vivo* imaging of cardiac magnetic resonance (CMR), ^{18}F -FDG PET, and ex vivo nuclear magnetic resonance (NMR) metabolomic analysis for the carbon-13-labeled glucose ($[\text{U-}^{13}\text{C}]\text{Glc}$) perfused myocardium. **Results.** As compared with controls, HFD rats had a higher ejection fraction and a smaller left ventricular end-systolic volume ($P < 0.05$), with SUV_{max} of myocardium on ^{18}F -FDG PET significantly increased in 4 weeks ($P < 0.005$). The $[\text{U-}^{13}\text{C}]\text{Glc}$ probed the increased glucose uptake being metabolized into pyruvate and acetyl-CoA, undergoing oxidative phosphorylation via the tricarboxylic acid (TCA) cycle, and then synthesized into glutamic acid and glutamine, associated with overexpressed LC3B ($P < 0.05$). **Conclusions.** HFD-induced IR associated with increased glucose utility undergoing oxidative phosphorylation via the TCA cycle in the myocardium is supported by overexpression of glucose transporter, acetyl-CoA synthase. Noninvasive imaging biomarker has potentials in detecting the metabolic perturbations prior to the decline of the left ventricular function.

1. Introduction

Diabetes mellitus (DM) is a pandemic metabolic problem characterized by hyperglycemia due to defects in secretion or action of insulin, namely, type 1 or type 2 diabetes mellitus

(T2DM), respectively. In 2015, 415 million people had DM in the world, and the number will grow to 522 million in 2030 with the conservative estimation [1, 2]. High-fat diet (HFD) is one leading cause of T2DM [3, 4], causing resistance to insulin in multiple organs [5]. The relatively

subtle metabolic changes, such as moderate hyperglycemia and increased plasma triglyceride (TG) levels, can gradually lead to structural changes and heart failure [6, 7]. Some previous reports have shown that the myocardium of humans and animals with T2DM might switch energy production from glucose utilization to fatty acid oxidation [8–10], which may play a critical role in the pathogenesis of T2DM. The presence of hyperinsulinemia, obesity, and impaired glucose tolerance in the rats with HFD has been characterized as the prediabetic T2DM rat model in the literature [11]. The Randle cycle (glucose fatty-acid cycle), a metabolic process involving the switch between glucose and fatty acids for substrates [12], is theorized to play a role in explaining T2DM and IR [13, 14]. Although the energy balance from differing macronutrient composition is equal, the glucose and fat balances that contribute to the overall energy balance are supposed to change reciprocally with dietary composition [15]. Monitoring the metabolic switch in myocardium would help in early detection and treatment of the myocardial changes in T2DM.

Cardiac magnetic resonance (CMR) imaging is a non-invasive assessment of both ischemic and nonischemic heart disease and heart failure [16]. CMR has become the gold standard for evaluating the left ventricular (LV) function, providing objective structural and detailed functional readouts [17–19]. However, the measurement of myocardial metabolism remains a challenge for CMR. ^{18}F -fluorodeoxyglucose (^{18}F -FDG) is a glucose analog which has been extensively used in positron emission tomography (PET) in clinical oncological diagnosis and assessment of the treatment response [20]. ^{18}F -FDG is taken up by cells and trapped in the cytoplasm as ^{18}F -FDG-6-phosphate by hexokinase once it enters into cells through glucose transporters (Glut) [21]. Normal myocardium also actively uptakes ^{18}F -FDG due to high expression of hexokinase 2 [22, 23], providing the opportunity of using ^{18}F -FDG to probe the first command step of myocardium glucose utilization by the *in vivo* noninvasive micro-PET study. The Langendorff system perfused with carbon-13-labeled glucose ($[\text{U-}^{13}\text{C}]\text{Glc}$) can potentially probe the downstream metabolic activities further to ^{18}F -FDG-6-phosphate in the myocardium [5]. High-resolution nuclear magnetic resonance (NMR) technology can identify the following metabolic products of $[\text{U-}^{13}\text{C}]\text{Glc}$ to precisely characterize the myocardial glucose utilization in the HFD-induced insulin resistance (IR). However, noninvasive detection of early myocardial changes of the prediabetic T2DM rat model has not been investigated yet.

We aim to characterize the metabolic changes associated with myocardial glucose utilization in a rat model of HFD-induced IR as an early diabetic onset model using the noninvasive imaging of cardiac MRI, ^{18}F -FDG micro-PET, and $[\text{U-}^{13}\text{C}]\text{Glc}$ NMR corroboration.

2. Methods

2.1. Animal Model and Experiment Design. We purchased male Sprague–Dawley (SD) rats (age 6 weeks) from BioLASCO Taiwan Co., Ltd. (Taipei, Taiwan). The SD rats were maintained in a climate-controlled facility on a 12 h light/12 h dark cycle with access to water and food ad libitum. All experimental

procedures were conducted according to the Guide for the Care and Use of Laboratory Animals and were approved by the Institutional Animal Care and Use Committee of Chang Gung University and Chang Gung Memorial Hospital, Taiwan (IACUC: CGU13-051). After two weeks of acclimation, the SD rats were randomly assigned to 2 groups, fed a regular chow diet (control, C; $n = 9$) or high-fat diet (HFD; $n = 9$) ad libitum for 10 weeks. As our previous research, the regular chow diet consisted of 23.5% protein, 5.1% fat, and 50.3% carbohydrates (g %, LabDiet® 5001, St. Louis, MO); the HFD consisted of 24% protein, 24% fat, and 41% carbohydrates (g %, Research Diets D12451I, New Brunswick, NJ) [24]. We recorded their body weight and food intake weekly. In the SD rats (C, $n = 9$; HFD, $n = 9$), blood from the tail vein was withdrawn under fasting status for insulin-resistant testing. The insulin level was determined manually through Ultra-sensitive Mouse Insulin ELISA Kit (Crystal Chem Inc., IL, USA). Briefly, a $5\ \mu\text{l}$ aliquot of plasma was applied in the ELISA kit. Then, the OD excitation wavelength 450 nm/emission wavelength 630 nm was used in detection. The sensitivity of Ultrasensitive Mouse Insulin ELISA Kit is 0.05 ng/mL. The glucose level in whole blood was measured by ONETOUCH® ULTRA® (Johnson & Johnson) with a drop test in a test strip. The biochemistry indexes, such as triacylglycerol (TG), total cholesterol (T-CHO), and high-density lipoprotein (HDL-C), were detected by Fujifilm NX500i (Japan) with $10\ \mu\text{l}$ of plasma following the ELISA kit protocol. The measurement ranges of glucose, TG, T-CHO, and HDL-C are 19.62–600 mg/dL, 10–500 mg/dL, 50–450 mg/dL, and 10–110 mg/dL, respectively. Homeostasis model assessment-insulin resistance (HOMA-IR) was calculated using HOMA2 calculator [25] and has been reported as a useful tool for diagnosing insulin resistance [26]. We carried out cardiac MRI weekly for 10 weeks (Control, $n = 9$; HFD, $n = 9$) and ^{18}F -FDG PET on week 1, week 4, and week 7 (Control, $n = 3$; HFD, $n = 3$) after HFD feeding. We further analyzed the heart by using the $[\text{U-}^{13}\text{C}]\text{Glc}$ Langendorff perfusion study, NMR, and western blotting at 18 weeks of age (Control, $n = 2$; HFD, $n = 3$). In comparison to the early phase of pre-DM status, we analyzed the hearts with and without Langendorff perfusion by NMR and western blotting at 32 weeks of age (Control, $n = 3$; HFD, $n = 3$), as detailed below. The flow chart of the performing animal and tissue experiments was summarized in Figure 1.

2.2. CMR. CMR was performed with ECG and respiratory gating on the ClinScan 7T MRI (Bruker BioSpin, Germany). Short-axis CINE with the bright-blood technique was chosen to capture myocardial wall motion and thickness between end-systole and end-diastole phases. Specific parameters of CINE using FLASH sequence are TR/TE 12/1.67 ms, slice thickness 1 mm, three averages, flip angle 15° , the field of view $45 \times 45\ \text{mm}^2$, and 144×192 matrix, which gives rise to in-plane resolution $0.312 \times 0.234\ \text{mm}^2$. Such CINE scans were acquired sequentially and evenly from the base to the apex, yet the slice numbers to cover the whole heart and the corresponding acquisition time per incidence slightly varied among different animals and ECG

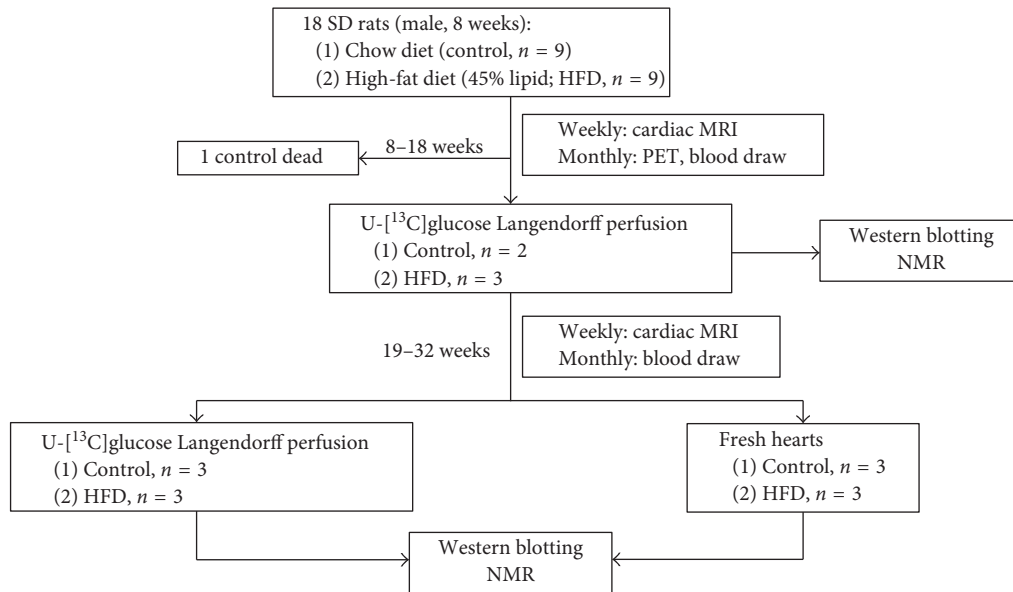


FIGURE 1: Flow chart of animal experiments. The age and number of animals used in each experiment are displayed. Rats were divided into two groups by the high-fat diet and regular chow diet, following the biochemical assessment, *in vivo* imaging study, Langendorff perfusion NMR, and western blotting.

stability. All CINE frames were quantitatively analyzed using QMass (Medis, the Netherlands), with manual delineation of the myocardium for left ventricular volume, ejection fraction, wall motion, and wall thickness.

2.3. Micro-PET. The SD rats were imaged using an InveonTM system (Siemens Medical Solutions Inc., Malvern, PA, USA) at Chang Gung Memorial Hospital, Taiwan. All rats were fasted for 12 hours before micro-PET but allowed ad libitum to access water. Although the blood glucose level of each rat was not measured before the micro-PET study, in the previous reports, there is no significant difference in glucose levels of the control and HFD rats with 12-hour fasting [27]. The rats underwent a 30 min image acquisition in the prone position 90 min after receiving 22.49 ± 0.17 (standard deviation, SD) MBq of ^{18}F -FDG via tail vein injection. The rats were anesthetized with 3% isoflurane, and the heart of the rat was positioned near the center of the field of view where the spatial resolution is approximately 1.2 mm. The regions of interest (ROIs) of the myocardium were analyzed in the PET images manually. The ^{18}F -FDG uptakes of the myocardium were expressed as the maximum standardized uptake value (SUV_{max}) [28]. All image analyses were conducted by using PMOD version 3.2 image analysis software (PMOD Technologies Ltd., Zurich, Switzerland).

2.4. Isolated Heart Perfusion. Rats were anesthetized with sodium pentobarbitone (50 mg/kg, intraperitoneal injection, IP) and given heparin (300 units/kg, IP), following a cervical dislocation. Immediately, hearts were isolated in ice-cold Krebs–Henseleit buffer [21], cannulated via the aorta, and perfused in Langendorff mode at a constant perfusion pressure of 100 mmHg at 37°C [29]. Hearts were perfused with KH buffer (137.0 mM NaCl, 5.4 mM KCl, 1.22 mM

MgSO_4 , 1.8 mM CaCl_2 , 1.2 mM KH_2PO_4 , 11.0 mM dextrose, and 6.0 mM HEPES, pH 7.4), gassed with 95% O_2 and 5% CO_2 in steady perfusion for 10 min. Then, the dextrose in KH buffer was replaced with $[\text{U}-^{13}\text{C}]\text{Glc}$, following 2 min perfusion. The hearts were removed from the Langendorff perfusion system after completing the perfusion, and each compartment of the heart was separated at the saline cooling bath. Each compartment of the hearts was wrapped in an aluminum foil and stored in liquid nitrogen for further usage.

2.5. NMR Metabolomic Study and Data Analysis. NMR spectra were acquired using a Bruker Avance III HD 600 MHz spectrometer operating at 600.13 MHz and equipped with a TXI CryoProbe at 300 K. Two types of ^1H NMR spectra were acquired: NOESY and Carr–Purcell–Meiboom–Gill (CPMG) pulse sequence. The analyzed aqueous metabolites were glucose, lactate, acetate, glutamine, and glutamate; the analyzed lipophilic metabolite was a long-chain lipid component (CH_2) $_n$. Using the Bruker TopSpin 3.2 software and Chenomx Profiler 8.0, we integrated the NMR spectra for the HFD and control groups. The ratio of the metabolic concentrations of HFD and control groups at 18 and 32 weeks was determined, respectively. The metabolic levels of the NMR spectra were computed by the internal reference of sodium 3-trimethylsilyl-2,2,3,3-tetradeuteriopropionate (TSP) in the aqueous phase and of tetramethylsilane (TMS) in the lipophilic phase. The sum of ^{13}C resonances at the 4th and 5th positions of glutamate was compared with the sum of ^{13}C resonances at the 1st, 2nd, and 3rd positions (Glu45/Glu123 ratio).

2.6. Western Blotting. Myocardium lysates were analyzed by western blotting, as described previously [30]. The myocardium lysate protein was transferred onto Immun-Blot PVDF membranes (Bio-Rad, USA). PVDF membranes were

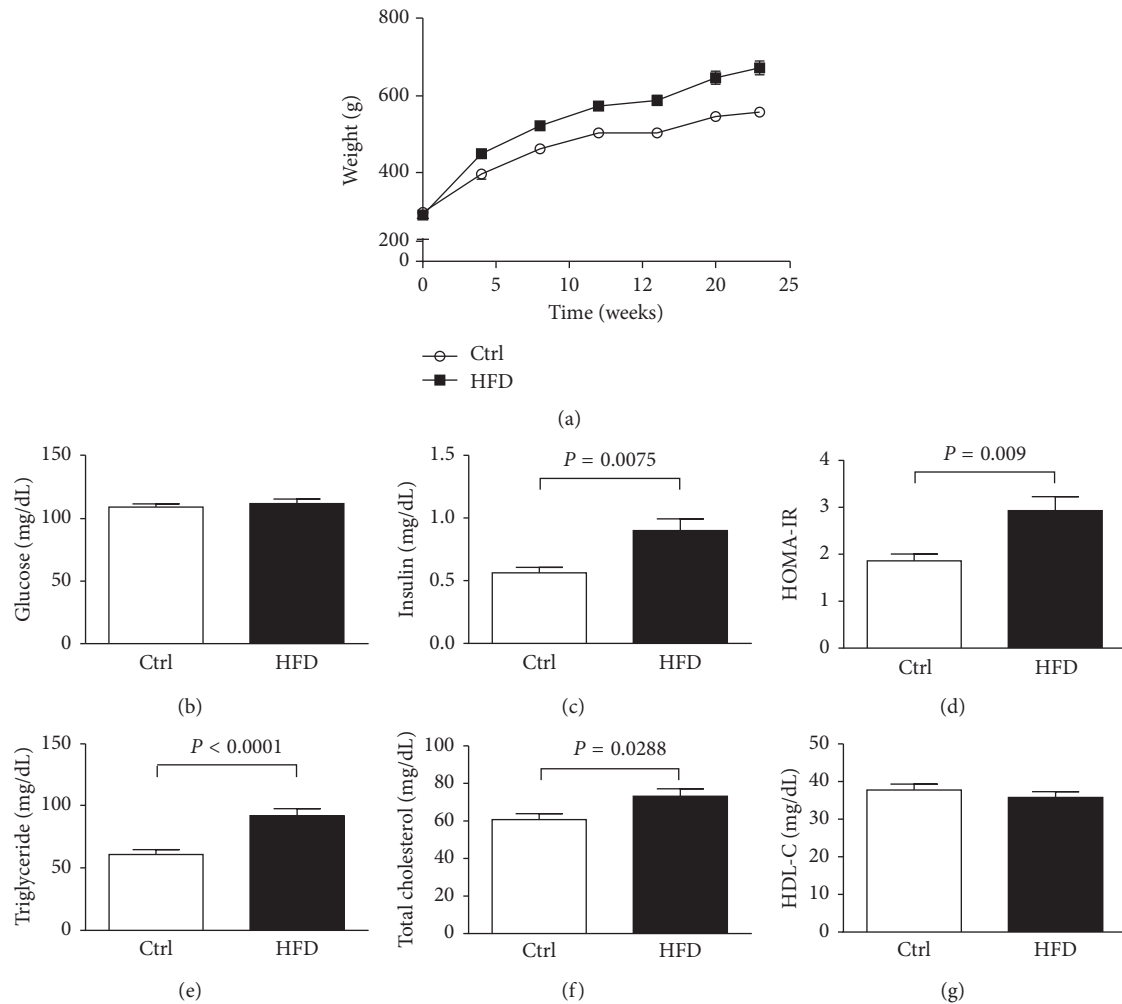


FIGURE 2: Characterization of HFD-induced obesity model. Rats fed high-fat diet became significantly obese in the time course of body weight (a). Slightly increased glucose concentration in plasma in the HFD group after 10 weeks of high-fat diet feeding (b). Significantly increased insulin (c), HOMA-IR (d), triglyceride (e), and total cholesterol (f) concentration in the HFD group after 10 weeks of high-fat diet feeding. Slightly decreased HDL-C in the HFD group after 10 weeks of high-fat diet feeding (g). Taken together, the HFD rats developed insulin resistance in 10 weeks after high-fat diet feeding. * $P < 0.05$; ** $P < 0.01$; *** $P < 0.001$ versus control.

incubated with Glut4 (1F8) Mouse mAb, AceCS1 (D19C6) antibody (Cell Signaling, MA, USA), caspase-3 antibody (Cell Signaling, MA, USA), PARP antibody (Cell Signaling, MA, USA), LC3B antibody (Cell Signaling, MA, USA), and β -actin (as a loading control; Sigma-Aldrich, Israel). The membranes were then incubated with the anti-rabbit or anti-mouse secondary antibody (Sigma-Aldrich, Israel). Specific binding antibody-target protein interactions were rinsed with ECL (BioRad, USA) and detected under the chemiluminescence system (BioSpectrum UVP, CA, USA). Each blotting band was normalized with its loading control and quantitated utilizing ImageJ 1.49t.

2.7. Relative Gene Expression Analysis for *Slc2a4* (*Glut4*) and *Acs2* (*AceCS1*). First, total RNA of each sample was extracted using Aurum™ Total RNA Fatty and Fibrous Tissue Kit (Bio-Rad, USA) and was quantified by NanoDrop 1000 Spectrophotometer (Thermo Scientific, USA). Reverse transcription was then demonstrated via iScript™ cDNA

Synthesis Kit (Bio-Rad, USA) by adding 1 μ g of total RNA on CFX96 Touch™ Real-Time PCR Detection System (Bio-Rad, USA). Real-time PCR was performed by means of SsoFast™ EvaGreen® Supermixes (Bio-Rad, USA) on CFX96 Touch™ Real-Time PCR Detection System (Bio-Rad, USA) through adding an equal volume (2 μ l) of cDNA products of each sample. The target genes were *Slc2a4* (for *Glut4*; Bio-Rad, qRnoCID0001996, USA) and *Acs2* (for *AceCS1*; Bio-Rad, qRnoCID0005949, USA), β -actin was selected as an internal control (forward primer sequence: 5'-CGGTCAGGTCATCACTATC-3'; reverse primer sequence: 5'-TGCCA-CAGGATTCCATAC-3'). Further Δ Cq of the target gene expression was calculated and normalized with β -actin by the equation Δ Cq = Cq(target) - Cq(β -actin).

2.8. Statistical Analysis. Values are expressed as means \pm SD (standard deviation). Statistical analyses were performed using Prism Software (version 6; GraphPad). Data were not normally distributed based on the Kolmogorov-Smirnov test.

Therefore, the cardiac uptakes in the control and HFD groups were compared using Kruskal–Wallis analysis followed by the nonparametric Tukey test. In other experimental data, the comparison of control and HFD groups was done by Student's *t*-test with nonparametric Mann–Whitney test. A *P* value of 0.05 or less was considered statistically significant.

3. Results

3.1. Physiological and Hemodynamics Remodeling in HFD-Induced IR Hearts. After diet alteration for 10 weeks, rats fed HFD developed a phenotype of IR syndrome, which is characterized by hyperlipidemia and hyperinsulinemia and impaired fasting glucose and homeostasis model assessment–insulin resistance (HOMA-IR), as shown in Figure 2. The values of HOMA-IR were obtained by means of the HOMA2 calculator. The body weight, blood insulin concentration, HOMA-IR, triglyceride, and total cholesterol significantly increased in the HFD group ($P < 0.05$), as compared with the control group.

3.2. Morphological Effect of HFD on CMR. The representative short axis of CMR images in end-systolic and end-diastolic phases in the control and the HFD rats at 16 weeks of age is demonstrated in Figure 3. *In vivo* cardiac function of control and HFD groups was summarized by CMR with QMass analysis and pool analysis comparison in Table 1. Rats with HFD have a higher ejection fraction, smaller left ventricular end-systolic volume (LVESV), and thicker end-systolic wall thickness than the control group ($P < 0.05$).

3.3. Metabolic Effect of HFD on ^{18}F -FDG PET. HFD rats have altered *in vivo* myocardial ^{18}F -FDG uptakes. The SUV_{max} of the left ventricular myocardium was significantly increased in the HFD group than that in the control group over time periods. (SUV_{max} , 1.71 ± 0.36 versus 1.22 ± 0.16 at week 1; 2.18 ± 0.39 versus 0.92 ± 0.05 at week 4, $P = 0.0049$; 2.00 ± 0.93 versus 1.10 ± 0.08 at week 7), as shown in Figure 4. ^{18}F -FDG can be taken up by glycolytic cells and phosphorylated by hexokinase but was trapped in the cells in its phosphorylated form, due to lacks of a 2' hydroxyl group needed for subsequent metabolism [31]. Therefore, we used $[\text{U-}^{13}\text{C}]$ Glc NMR to further study the downstream metabolism of myocardium glucose utilization.

3.4. High-Resolution NMR Analysis of $[\text{U-}^{13}\text{C}]$ Glc Perfused Myocardium. There is a list of the steady-state aqueous metabolites associated with the glucose metabolic pathway of the HFD and control rat hearts by ^1H NMR spectrum analyses in Supplementary Material 1. The majority of myocardial metabolites maintained stable as compared with controls, except levels of acetate, butyrate, glutamine, O-acetylcarnitine, propionate, taurine, and uridine significantly decreased in the HFD groups compared to the control group ($P < 0.05$). Those altered levels of metabolites such as acetate, butyrate, and glutamine were associated with the pathways of glucose metabolism. Other altered levels of

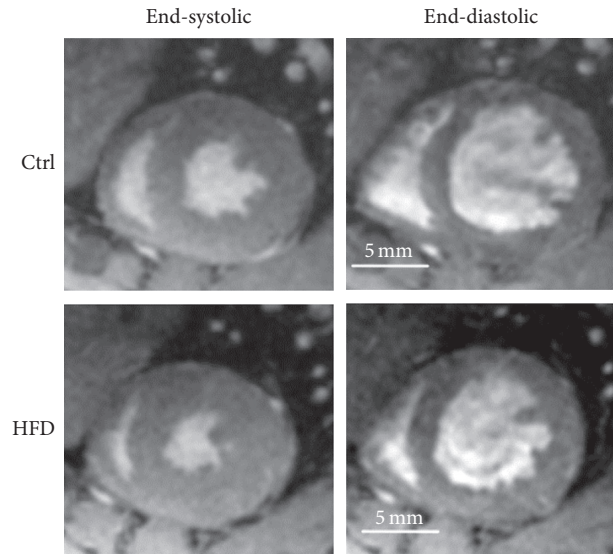


FIGURE 3: The representative short axis of CMR images in end-systolic and end-diastolic phases. The myocardium CMR images of control and HFD rats in end-systolic and end-diastolic phases are shown. The ejection fraction of the HFD rats significantly increased, and the left ventricle volume of the HFD rats significantly decreased, as compared with control rats based on the QMass analysis.

metabolites, O-acetylcarnitine, propionate, taurine, and uridine were related to the pathway of fatty acid metabolism. To further interrogate the increased glucose uptake demonstrated on ^{18}F -FDG PET, glucose tracers labeled at each carbon position $[\text{U-}^{13}\text{C}]$ Glc was infused into the Langendorff perfusion system, to analyze the glucose utility of the HFD. Figure 5 reveals the glucose metabolic network identified by the $[\text{U-}^{13}\text{C}]$ Glc NMR system. In myocardium glucose utilization, the ^{13}C -carbon of glucose was metabolized to glycine (Gly), lactate, and pyruvate as well as acetyl-CoA. The ^{13}C -carbon from acetyl-CoA was contained in citrate, isocitrate, and α -ketoglutarate (αKG), which synthesizes glutamic acid and glutamine (Gln). The ^{13}C -carbon at the 4th and 5th positions of glutamine indicates the utility of $[\text{U-}^{13}\text{C}]$ Glc undergoing oxidative phosphorylation via the TCA cycle. The Glu45/Glu123 ratio of labeled ^{13}C -carbon in glucose metabolic substances of HFD groups is significantly higher than that of control groups (18 weeks of age: 0.38 ± 0.03 versus 0.33 ± 0.01 ; 32 weeks of age: 1.06 ± 0.28 versus 0.39 ± 0.07 , $P = 0.017$).

3.5. Myocardial Overexpression of Glut4, PARP, and LC3B in HFD-Induced IR. Interestingly, we found the protein expression of Glut4 increased in accordance with the change on the ^{18}F -FDG PET ($P < 0.05$). The mRNA levels for Glut4 (*Slc2a4* gene) were also altered ($P < 0.05$). The different trends in mRNA and protein expression might indicate a complex feedback mechanism and warrant further study. The AceCS1 protein and ACSS2 mRNA expression were not significantly changed during both the early and late HFD feeding. However, in 18 weeks of age rat myocardium, the PARP expression was significantly increased as compared with the control ($P < 0.05$), following to 32 weeks of age, the PARP expression was decreased (early versus late, $P < 0.05$).

TABLE 1: Comparison of the cardiac function of control and HFD rats.

Cardiac function	Control ($n = 9$)	HFD ($n = 9$)	P value
Ejection fraction (%)	73.32 ± 0.8229	79.50 ± 1.799	0.0096*
Stoke volume (μl)	322.2 ± 24.22	317.7 ± 23.52	0.8953
LV volume of ED (μl)	439.9 ± 32.71	399.0 ± 26.79	0.3415
LV volume of ES (μl)	117.7 ± 9.545	81.33 ± 7.833	0.0081**
Cardiac output ($\mu\text{l}/\text{min}$)	133.7 ± 10.06	131.9 ± 9.765	0.8987
ED segmented wall thickness (mm)	3.061 ± 0.068	3.391 ± 0.098	0.0168*

Values are expressed as mean \pm SD. The cardiac function of the control and HFD rats was measured from CMR images and QMass Software; * $P < 0.05$ and ** $P < 0.01$ versus control; LV = left ventricle; ED = end-diastolic volume; ES = end-systolic volume.

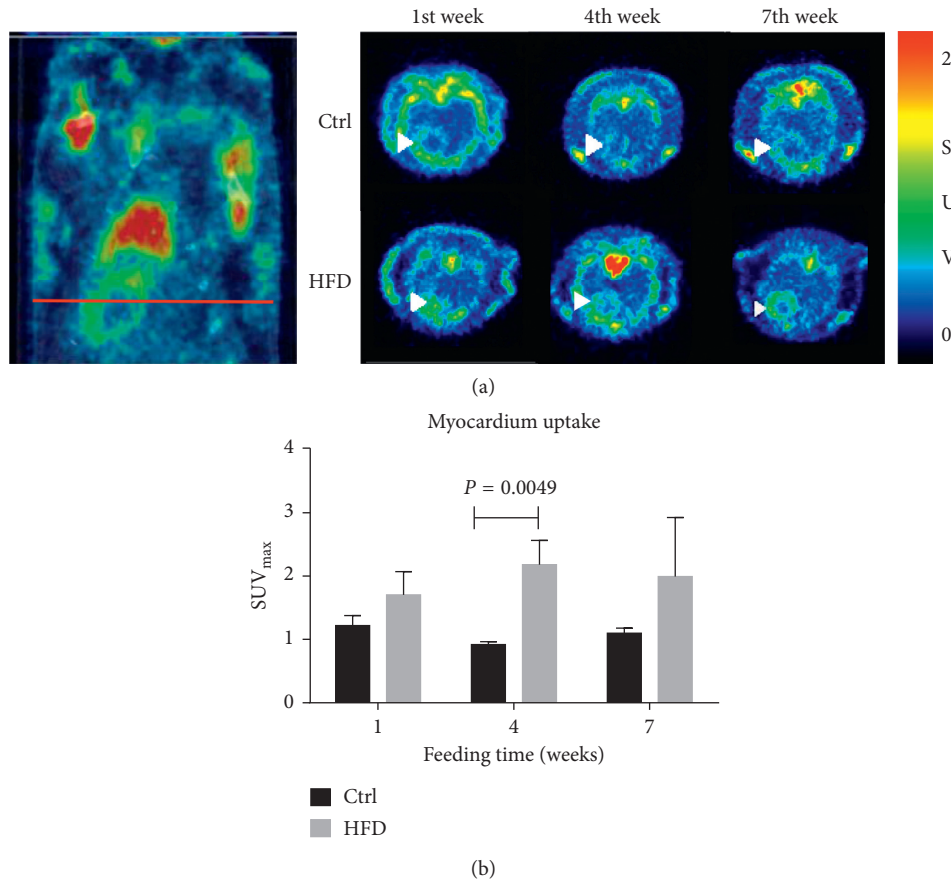


FIGURE 4: ^{18}F -FDG PET/CT imaging. (a) Representative midventricular transversal images in a time course. The right image is a corresponding coronal plane ^{18}F -FDG PET/CT. (b) Quantitative myocardial glucose uptake by micro-PET after intravenous injection of ^{18}F -FDG in the control ($n = 3$) and HFD ($n = 3$) rats. Significantly increased myocardial ^{18}F -FDG uptake in 4 weeks after HFD feeding is noted. * $P < 0.05$ versus control. Ctrl = control.

Notably, the expression of LC3B, an autophagy activation protein, was higher in the 32 weeks of age HFD group compared with the control ($P < 0.05$) (Figure 6).

4. Discussion

In the present study, we found the HFD rats in 10 weeks high-fat diet feeding results in mild hyperglycemia, hypercholesterolemia, hyperinsulinemia, and homeostasis model assessment-IR (HOMA-IR), as determined by the biochemical and physiological analysis, with a significant increase in body weight. The significantly increased EF and decreased LVEDV was measured in the HFD rats, indicating that the ten-week HFD fed rats

might develop the myocardial hypertrophy, observed as the thicker myocardium wall by CMR. Corresponding to ^{18}F -FDG PET study, the myocardium walls of the HFD rats show significant ^{18}F -FDG uptake among seven weeks, implying that the HFD rats need amounts of glucose to acquire the energy to support the hypertrophic myocardium activities under glucose utilization in the early stage. Also, with increased glucose metabolite, for example, glutamine and glutamate, and Glut4 expression in late stage, the highly increased myocardium glucose utilization in HFD rats should fully be demonstrated as taking the results together.

We noticed that blood glucose levels between control and high-fat diet groups did not different significantly,

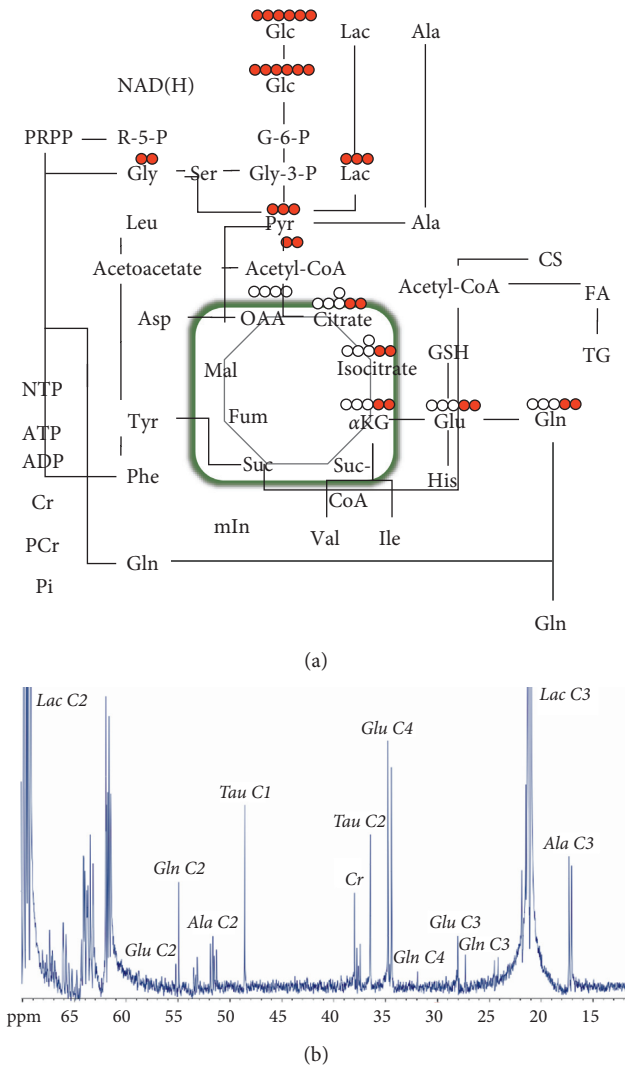


FIGURE 5: [U-¹³C]-labeled downstream glucose metabolism. (a) The measurement of downstream glucose metabolism by [U-¹³C]-labeled glucose and NMR technique. The carbon atoms of glutamine (Glu₄₅) are from the upstream of glucose metabolism. (b) The ¹³C NMR full spectrum of the myocardium in the HFD rats is demonstrated. After the citric acid cycle, the 4th labeled carbon position in glutamate showed a higher signal than that of the other positions.

which might be attributed to our fasting procedure that is not strict. Even though we removed their food from cages, rats still could eat the bedding materials, fests, and food debris remaining in the cages. Our observations were in line with reports showing no significant difference in glucose levels between control and high-fat diet feeding rats for 9 weeks [32] and 16 weeks [33].

Our results detailed how the Randel cycle replenishes the intermediates of the citric acid cycle. The hemodynamic stress of HFD-induced myocardium overrides fatty acid inhibition of glucose metabolism, which is presumably associated with activation of AMP-activated protein kinase (AMPK), an immediate metabolic adaption and protects the heart from ischemic stress [34]. Interestingly, some previous studies reported that myocardial IR induced by HFD feeding

preserves the cardiac contractile function in mild to moderate heart failure rats [35]. Histopathological analysis of the cross-sectional area of myocardium showed significantly increased thickness in HFD rats [24]. We showed that the myocardial hypertrophy induced by HFD needs to consume more energy to support its activity and function by glucose utilization. In line with our results, the increase in myocardial glucose utilization rate compensates the poor fatty acid uptake in the rats with spontaneously hypertension or myocardial infarction [36, 37]. Due to the disturbance in cardiac metabolism, the HFD results in the hyperinsulinemia and hemodynamics remodeling in the pre-T2DM rat model. On the contrary, the cardiomyocytes cross-sectional area increased in the long-term HFD feeding mice [38]. In another mice study with a prolonged HFD for 20 weeks, there was a 40% increase in fatty acid oxidation in the myocardium, whereas glucose oxidation was decreased to 30% of the control [39]. Contrary to our pre-T2DM rat model, the diabetic mouse model appears to be a different metabolic phenotype of cardiopathology.

Some previous reports have demonstrated the alteration of myocardial metabolism in the various diabetic rat models [11]. Shoghi et al. found the decreased myocardial glucose uptake rate in PET images and lower expression of glucose transporters (Glut1 and Glut4) in 20-week-old Zucker Diabetic Fatty (ZDF) rats (fa/fa) but did not show significant difference in morphological changes in the echocardiography measurements [40]. Feeding Wistar rats with high-fat and high-fructose diet for 16 weeks with a small dose of streptozotocin, Menard et al. reported altered myocardium energy metabolism as well as increased myocardial non-esterified fatty acid uptake in the 14 (R, S)-¹⁸F-fluoro-6-thiaheptadecanoic acid (¹⁸F-FTHA) micro-PET images [41]. The above evidence supports the metabolic alterations in the myocardium during the development of T2DM.

¹⁸F-FDG PET demonstrated an early alternation of myocardium glucose utilization in 4-week HFD, whereas the myocardium dysfunction of HFD rats was detected by CMR after 18-week HFD. It seems to be reasonable that the perturbation of myocardium metabolism is followed by the myocardium dysfunction over the progression of the insulin-induced cardiopathological diseases. We have shown the myocardium glucose utilization by *in vivo* glucose analogs PET tracer and *ex vivo* labeling [U-¹³C]Glc NMR. More recent reports suggested the glutamine as a vital biomarker of metabolic syndromes and insulin-resistant phenotypes [42, 43]. The mice fed oral supplementation of glutamine leading to reduced glucose concentration, indicating glutamine, may play a critical role in the metabolic disease pathways. In our study, we showed that the ratio of labeled C4-5 to C1-3 in glutamine in HFD mice hearts increases, implying either increased Glu₄₅ or decreased Glu₁₂₃. Glu₄₅ is from [U-¹³C]Glc; Glu₁₂₃ can be from glutamine uptake, which did not occur in our study. The increased glutamine concentration in HFD mice myocardium could be a positive feedback mechanism as the myocardium suffers from the metabolic problem. The further mechanism of glutamine feedback warrants validations in the future. Furthermore, the myocardium fatty acid is considered to predominate the metabolism in the diabetic heart diseases prevailing, which has not been discussed in our study.

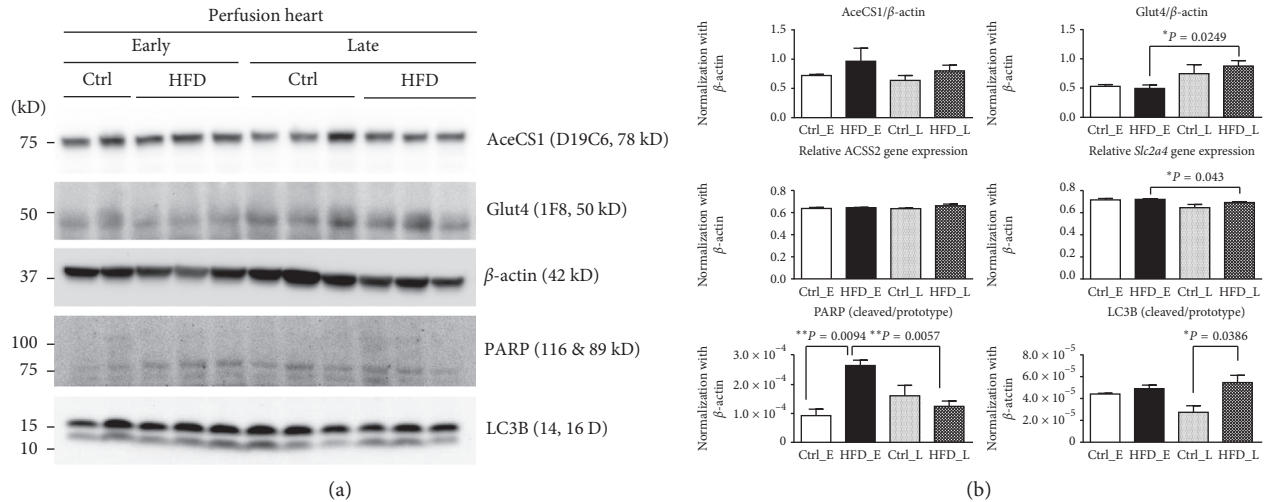


FIGURE 6: Western blotting and mRNA analysis of myocardium: AceCS1, Glut4, PARP, and LC3B protein expression and *Slc2a4* and *Acss2* gene expression in the perfusion hearts in HFD and control rats in 18 weeks and 36 weeks after high-fat diet feeding. AceCS1 protein expression and *Acss2* gene expression did not show a significant difference between control and HFD in early and late stages. However, mRNA levels change in Glut4, albeit different in trend. Nonetheless, the protein expression of Glut4 increases in accordance with the ^{18}F -FDG PET/CT. Decreased cleaved/prototype PARP and increased LC3B-autophagy activation in the myocardium of the HFD rats are noted.

Even so, several published literature have investigated the myocardium energy utilization by PET radiopharmaceuticals such as carbohydrate metabolism (^{18}F -FDG, ^{11}C -acetate, and ^{11}C -glucose) and fatty acid metabolism (^{11}C -palmitate and fatty acid analogs) [44]. The multiple metabolic substrates PET tracers could be our further study direction to investigate the myocardium energy utilization and metabolism.

Cardiac health relies on the heart's ability to utilize different substrates to support overall oxidative metabolism to generate ATP. We demonstrated overexpressed Glut4 and associated changes in mRNA levels in the HFD group, which linked to an increased autophagy activity protein that might intent to generate the additional ATP to support the excessed myocardium activities from the cardiac hypertrophy of HFD rats. The switch from glucose to fatty acid oxidation leads to a less-efficient oxidative phosphorylation because more electrons transported to complex 2 rather than complex 1 in the mitochondrial respiratory chain, hence increasing the production of ROS. Our study represented the early metabolic adaptation of myocardium induced by HFD. The identification of the metabolic phenotypes of chronic diseases including diabetics and heart failure in an early period facilitates the improvement of therapeutic impact [34]. The presence of pre-DM IR associated with a higher reliance on myocardial glucose metabolism. The perturbations in myocardial metabolism may precede an eventual decline of the left ventricular function. Future research should explore the influence of pre-DM status on clinical cardiac ^{18}F -FDG PET imaging to better stratify patients for suitable therapeutic intervention.

5. Limitations

There are limitations to this study. First, the obese and T2DM heart is less adaptable to myocardial substrate metabolism under anesthesia, known as anesthesia-induced cardioprotection [45]. Anesthesia is unavoidable during in

vivo imaging study, and the impact to experimental results still under debate [45, 46]. Therefore, a minimum dose of anesthesia was considered as a concession in our study. Instead of using a continuous dynamic scan, our micro-PET study was acquired 30 min as a static scan, not only keeping conscious during the uptake period but also less time-consuming to adapt clinical situation. For this purpose, we had decided to omit the metabolic rate of glucose with ^{18}F -FDG derived from dynamic PET scan and Patlak analysis. Nevertheless, we used a clinical standard quantitative SUV of the myocardium to reflect analog glucose uptake in the regional organs [28].

The glucose utilization is increased in the early HFD-induced myocardial adaptation in the pre-T2DM model, in contrast to the glucose metabolism transit to fatty acid metabolism for energy utility in the myocardium in the late T2DM. Although the preliminary report demonstrated the potential to quantify the myocardial triglyceride content using CMR spectroscopy [47], CMR spectroscopy suffered from the limited sensitivity to detect the glycolysis pathway and was not chosen in this study. ^{18}F -FDG, although being transported into the myocardium and phosphorylated by hexokinase as the first step toward glycolysis, is trapped intracellularly as ^{18}F -FDG-6-phosphate, thus cannot track down the downstream glycolytic pathway. Therefore, we applied a combination approach of ^{18}F -FDG and $[\text{U}-^{13}\text{C}]\text{Glc}$ NMR metabolomic analysis trying to understand the whole metabolic landscape. Nevertheless, it is the first time that the downstream metabolic products of pyruvate can be monitored by imaging the augmented form of CMR-hyperpolarized $[\text{U}-^{13}\text{C}]\text{pyruvate}$ in real time, and hopefully, these promising results found in this study will have clinical applications in the near future [48].

6. Conclusions

In conclusion, HFD-induced IR induces cardiac morphological changes, with a higher ejection fraction, smaller

LVESV, and thicker end-systolic wall thickness than the control group. The prediabetic myocardium increased glucose utility undergoing oxidative phosphorylation via the TCA cycle, supported by overexpression of glucose transporters and acetyl-CoA synthase. Noninvasive imaging biomarker has potentials in detecting the metabolic perturbations prior to the decline of the left ventricular function.

Abbreviations

HFD:	High-fat diet
T2DM:	Type 2 diabetes mellitus
CMR:	Cardiac magnetic resonance
¹⁸ F-FDG:	¹⁸ F-fluorodeoxyglucose
PET:	Positron emission tomography
NMR:	Nuclear magnetic resonance
[U- ¹³ C]Glc:	Carbon-13-labeled glucose
HOMA-IR:	Homeostasis model assessment-IR
IR:	Insulin resistance
SUV _{max} :	Maximum standardized uptake values.

Data Availability

The NMR, western blot, and mRNA data used to support the findings of this study are available from the corresponding author upon reasonable request. The CMR and PET scan images data used to support the findings of this study are available from Yi-Hsiu Chung upon reasonable request.

Conflicts of Interest

The authors declare that there are no conflicts of interest regarding the publication of this article.

Acknowledgments

The authors thank the Metabolomics Core Laboratory, Healthy Aging Research Center (HARC), Chang Gung University, Clinical Metabolomics Core Laboratory, Chang Gung Memorial Hospital (CGMH), for carrying out metabolomic analysis using NMR spectroscopy. The authors also thank Chiu-Han from the Center for Advanced Molecular Imaging and Translation (CAMIT), CGMH, for excellent assistance in animal imaging studies and Dr. Thomas Eykyn, Kings College London, United Kingdom, for providing useful advice. The authors received the funding support from the Chang Gung Medical Foundation with Grant nos. CIRPG3E0022, CMRPG3C1873, CPRPG3G0021, CRRPG3E0013, and CMRPG3D1821.

Supplementary Materials

Supplementary Material 1: the majority of myocardial metabolites maintained stable as compared with controls, except levels of acetate, butyrate, glutamine, and O-acetylcarnitine. (*Supplementary Materials*)

References

- [1] K. G. Alberti and P. Zimmet, "Global burden of disease—where does diabetes mellitus fit in?," *Nature Reviews Endocrinology*, vol. 9, no. 5, pp. 258–260, 2013.
- [2] L. Guariguata, "By the numbers: new estimates from the IDF diabetes Atlas update for 2012," *Diabetes Research and Clinical Practice*, vol. 98, no. 3, pp. 524–525, 2012.
- [3] E. Dirkx, R. W. Schwenk, J. F. Glatz, J. J. Luiken, and G. J. van Eys, "High-fat-diet-induced diabetic cardiomyopathy," *Prostaglandins, Leukotrienes and Essential Fatty Acids*, vol. 85, no. 5, pp. 219–225, 2011.
- [4] W. Zhang, M. Wu, T. Kim et al., "Skeletal muscle TRIB3 mediates glucose toxicity in diabetes and high-fat-diet-induced insulin resistance," *Diabetes*, vol. 65, no. 8, pp. 2380–2391, 2016.
- [5] M. A. Schroeder, H. J. Atherton, D. R. Ball et al., "Real-time assessment of Krebs cycle metabolism using hyperpolarized ¹³C magnetic resonance spectroscopy," *FASEB Journal*, vol. 23, no. 8, pp. 2529–2538, 2009.
- [6] A. Aneja, W. H. Tang, S. Bansilal, M. J. Garcia, and M. E. Farkouh, "Diabetic cardiomyopathy: insights into pathogenesis, diagnostic challenges, and therapeutic options," *American Journal of Medicine*, vol. 121, no. 9, pp. 748–757, 2008.
- [7] M. R. MacDonald, M. C. Petrie, N. M. Hawkins et al., "Diabetes, left ventricular systolic dysfunction, and chronic heart failure," *European Heart Journal*, vol. 29, no. 10, pp. 1224–1240, 2008.
- [8] C. Capirci, D. Rubello, F. Chierichetti et al., "Long-term prognostic value of ¹⁸F-FDG PET in patients with locally advanced rectal cancer previously treated with neoadjuvant radiochemotherapy," *American Journal of Roentgenology*, vol. 187, no. 2, pp. W202–W208, 2006.
- [9] S. Boudina and E. D. Abel, "Diabetic cardiomyopathy revisited," *Circulation*, vol. 115, no. 25, pp. 3213–3223, 2007.
- [10] T. S. Larsen and E. Aasum, "Metabolic (in)flexibility of the diabetic heart," *Cardiovascular Drugs and Therapy*, vol. 22, no. 2, pp. 91–95, 2008.
- [11] S. Skovso, "Modeling type 2 diabetes in rats using high fat diet and streptozotocin," *Journal of Diabetes Investigation*, vol. 5, no. 4, pp. 349–358, 2014.
- [12] S. Bevilacqua, G. Buzzigoli, R. Bonadonna et al., "Operation of Randle's cycle in patients with NIDDM," *Diabetes*, vol. 39, no. 3, pp. 383–389, 1990.
- [13] A. R. Shuldiner and J. C. McLenithan, "Genes and pathophysiology of type 2 diabetes: more than just the Randle cycle all over again," *Journal of Clinical Investigation*, vol. 114, no. 10, pp. 1414–1417, 2004.
- [14] J. Delarue and C. Magnan, "Free fatty acids and insulin resistance," *Current Opinion in Clinical Nutrition and Metabolic Care*, vol. 10, no. 2, pp. 142–148, 2007.
- [15] K. N. Frayn, "The glucose-fatty acid cycle: a physiological perspective," *Biochemical Society Transactions*, vol. 31, no. 6, pp. 1115–1119, 2003.
- [16] M. W. Hansen and N. Merchant, "MRI of hypertrophic cardiomyopathy: part I, MRI appearances," *American Journal of Roentgenology*, vol. 189, no. 6, pp. 1335–1343, 2007.
- [17] P. Elliott, B. Andersson, E. Arbustini et al., "Classification of the cardiomyopathies: a position statement from the European society of cardiology working group on myocardial and pericardial diseases," *European Heart Journal*, vol. 29, no. 2, pp. 270–276, 2008.
- [18] R. A. Noureldin, S. Liu, M. S. Nacif et al., "The diagnosis of hypertrophic cardiomyopathy by cardiovascular magnetic resonance," *Journal of Cardiovascular Magnetic Resonance*, vol. 14, p. 17, 2012.

- [19] A. G. Rose, "Evaluation of pathological criteria for diagnosis of hypertrophic cardiomyopathy," *Histopathology*, vol. 8, no. 3, pp. 395–406, 1984.
- [20] G. L. Cascini, A. Avallone, P. Delrio et al., "18F-FDG PET is an early predictor of pathologic tumor response to preoperative radiochemotherapy in locally advanced rectal cancer," *Journal of Nuclear Medicine*, vol. 47, no. 8, pp. 1241–1248, 2006.
- [21] N. K. Monakhov, E. L. Neistadt, M. M. Shavlovskil, A. L. Shvartsman, and S. A. Neifakh, "Physicochemical properties and isoenzyme composition of hexokinase from normal and malignant human tissues," *Journal of the National Cancer Institute*, vol. 61, no. 1, pp. 27–34, 1978.
- [22] S. P. Mathupala, A. Rempel, and P. L. Pedersen, "Glucose catabolism in cancer cells: identification and characterization of a marked activation response of the type II hexokinase gene to hypoxic conditions," *Journal of Biological Chemistry*, vol. 276, no. 46, pp. 43407–43412, 2001.
- [23] Y. Shinohara, K. Yamamoto, K. Kogure, J. Ichihara, and H. Terada, "Steady state transcript levels of the type II hexokinase and type I glucose transporter in human tumor cell lines," *Cancer Letters*, vol. 82, no. 1, pp. 27–32, 1994.
- [24] J. P. Huang, M. L. Cheng, C. H. Wang, M. S. Shiao, J. K. Chen, and L. M. Hung, "High-fructose and high-fat feeding correspondingly lead to the development of lysoPC-associated apoptotic cardiomyopathy and adrenergic signaling-related cardiac hypertrophy," *International Journal of Cardiology*, vol. 215, pp. 65–76, 2016.
- [25] HOMA Calculator, January 2018, <http://www.dtu.ox.ac.uk/homacalculator/>.
- [26] E. Bonora, G. Targher, M. Alberiche et al., "Homeostasis model assessment closely mirrors the glucose clamp technique in the assessment of insulin sensitivity: studies in subjects with various degrees of glucose tolerance and insulin sensitivity," *Diabetes Care*, vol. 23, no. 1, pp. 57–63, 2000.
- [27] R. A. K. Langah, K. M. Spicer, R. Chang, and M. Rosol, "Inhibition of physiologic myocardial FDG uptake in normal rodents: comparison of four pre-scan preparation protocols," *Advances in Molecular Imaging*, vol. 2, no. 3, p. 10, 2012.
- [28] B. Quintana-Villamandos, M. J. Delgado-Martos, C. Fernandez-Riveira et al., "Can 18F-FDG-PET show differences in myocardial metabolism between Wistar Kyoto rats and spontaneously hypertensive rats?," *Laboratory Animals*, vol. 47, no. 4, pp. 320–323, 2013.
- [29] M. Skrzypiec-Spring, B. Grotthus, A. Szelag, and R. Schulz, "Isolated heart perfusion according to Langendorff—still viable in the new millennium," *Journal of Pharmacological and Toxicological Methods*, vol. 55, no. 2, pp. 113–126, 2007.
- [30] G. Lin, D. K. Hill, G. Andrejeva et al., "Dichloroacetate induces autophagy in colorectal cancer cells and tumours," *British Journal of Cancer*, vol. 111, no. 2, pp. 375–385, 2014.
- [31] A. Zhu, D. Lee, and H. Shim, "Metabolic positron emission tomography imaging in cancer detection and therapy response," *Seminars in Oncology*, vol. 38, no. 1, pp. 55–69, 2011.
- [32] J. Yu, J. Zheng, X. F. Liu et al., "Exercise improved lipid metabolism and insulin sensitivity in rats fed a high-fat diet by regulating glucose transporter 4 (GLUT4) and musclin expression," *Brazilian Journal of Medical and Biological Research*, vol. 49, no. 5, article e5129, 2016.
- [33] C. Marques, M. Meireles, S. Norberto et al., "High-fat diet-induced obesity rat model: a comparison between Wistar and Sprague-Dawley rat," *Adipocyte*, vol. 5, no. 1, pp. 11–21, 2016.
- [34] L. Hue and H. Taegtmeier, "The Randle cycle revisited: a new head for an old hat," *American Journal of Physiology-Endocrinology and Metabolism*, vol. 297, no. 3, pp. E578–E591, 2009.
- [35] B. A. Christopher, H. M. Huang, J. M. Berthiaume et al., "Myocardial insulin resistance induced by high fat feeding in heart failure is associated with preserved contractile function," *American Journal of Physiology-Heart and Circulatory Physiology*, vol. 299, no. 6, pp. H1917–H1927, 2010.
- [36] T. Hajri, A. Ibrahim, C. T. Coburn et al., "Defective fatty acid uptake in the spontaneously hypertensive rat is a primary determinant of altered glucose metabolism, hyperinsulinemia, and myocardial hypertrophy," *Journal of Biological Chemistry*, vol. 276, no. 26, pp. 23661–23666, 2001.
- [37] J. M. Berthiaume, M. E. Young, X. Chen, T. A. McElfresh, X. Yu, and M. P. Chandler, "Normalizing the metabolic phenotype after myocardial infarction: impact of subchronic high fat feeding," *Journal of Molecular and Cellular Cardiology*, vol. 53, no. 1, pp. 125–133, 2012.
- [38] Z. Wang, L. Li, H. Zhao, S. Peng, and Z. Zuo, "Chronic high fat diet induces cardiac hypertrophy and fibrosis in mice," *Metabolism*, vol. 64, no. 8, pp. 917–925, 2015.
- [39] J. Yan, M. E. Young, L. Cui, G. D. Lopaschuk, R. Liao, and R. Tian, "Increased glucose uptake and oxidation in mouse hearts prevent high fatty acid oxidation but cause cardiac dysfunction in diet-induced obesity," *Circulation*, vol. 119, no. 21, pp. 2818–2828, 2009.
- [40] K. I. Shoghi, R. J. Gropler, T. Sharp et al., "Time course of alterations in myocardial glucose utilization in the Zucker diabetic fatty rat with correlation to gene expression of glucose transporters: a small-animal PET investigation," *Journal of Nuclear Medicine*, vol. 49, no. 8, pp. 1320–1327, 2008.
- [41] S. L. Menard, E. Croteau, O. Sarrhini et al., "Abnormal in vivo myocardial energy substrate uptake in diet-induced type 2 diabetic cardiomyopathy in rats," *American Journal of Physiology-Endocrinology and Metabolism*, vol. 298, no. 5, pp. E1049–E1057, 2010.
- [42] S. Cheng, E. P. Rhee, M. G. Larson et al., "Metabolite profiling identifies pathways associated with metabolic risk in humans," *Circulation*, vol. 125, no. 18, pp. 2222–2231, 2012.
- [43] S. H. Shah, W. E. Kraus, and C. B. Newgard, "Metabolomic profiling for the identification of novel biomarkers and mechanisms related to common cardiovascular diseases: form and function," *Circulation*, vol. 126, no. 9, pp. 1110–1120, 2012.
- [44] L. R. Peterson and R. J. Gropler, "Radionuclide imaging of myocardial metabolism," *Circulation: Cardiovascular Imaging*, vol. 3, no. 2, pp. 211–222, 2010.
- [45] C. E. van den Brom, C. S. Bulte, S. A. Loer, R. A. Bouwman, and C. Boer, "Diabetes, perioperative ischaemia and volatile anaesthetics: consequences of derangements in myocardial substrate metabolism," *Cardiovascular Diabetology*, vol. 12, p. 42, 2013.
- [46] H. Toyama, M. Ichise, J. S. Liow et al., "Evaluation of anesthesia effects on [18F]FDG uptake in mouse brain and heart using small animal PET," *Nuclear Medicine and Biology*, vol. 31, no. 2, pp. 251–256, 2004.
- [47] P. A. Liao, G. Lin, S. Y. Tsai et al., "Myocardial triglyceride content at 3 T cardiovascular magnetic resonance and left ventricular systolic function: a cross-sectional study in patients hospitalized with acute heart failure," *Journal of Cardiovascular Magnetic Resonance*, vol. 18, p. 9, 2016.
- [48] C. H. Cunningham, J. Y. Lau, A. P. Chen et al., "Hyperpolarized ¹³C metabolic MRI of the human heart: initial experience," *Circulation Research*, vol. 119, no. 11, pp. 1177–1182, 2016.

Research Article

Positron Emission Tomography Imaging of Macrophages in Atherosclerosis with ^{18}F -GE-180, a Radiotracer for Translocator Protein (TSPO)

Sanna Hellberg ¹, Heidi Liljenbäck,^{1,2} Olli Eskola,¹ Veronique Morisson-Iveson,³ Matthew Morrison,³ William Trigg,³ Pekka Saukko,⁴ Seppo Ylä-Herttuala ^{5,6}, Juhani Knuuti,^{1,7} Antti Saraste,^{1,7,8} and Anne Roivainen ^{1,2}

¹Turku PET Centre, University of Turku, Kiinamyllynkatu 4-8, 20520 Turku, Finland

²Turku Center for Disease Modeling, University of Turku, Kiinamyllynkatu 10, 20520 Turku, Finland

³GE Healthcare Ltd., White Lion Road, Amersham, Buckinghamshire HP7 9LL, UK

⁴Department of Pathology and Forensic Medicine, University of Turku, Kiinamyllynkatu 10, 20520 Turku, Finland

⁵A.I. Virtanen Institute for Molecular Sciences, University of Eastern Finland, Neulaniementie 2, 70210 Kuopio, Finland

⁶Science Service Center, Kuopio University Hospital, Puijonlaaksontie 2, 70210 Kuopio, Finland

⁷Turku PET Centre, Turku University Hospital, Kiinamyllynkatu 4-8, 20520 Turku, Finland

⁸Heart Center, Turku University Hospital, Hämeentie 11, 20520 Turku, Finland

Correspondence should be addressed to Anne Roivainen; anne.roivainen@utu.fi

Received 17 January 2018; Revised 26 March 2018; Accepted 8 April 2018; Published 22 May 2018

Academic Editor: Charalampos Tsoumpas

Copyright © 2018 Sanna Hellberg et al. This is an open access article distributed under the Creative Commons Attribution License, which permits unrestricted use, distribution, and reproduction in any medium, provided the original work is properly cited.

Intraplaque inflammation plays an important role in the progression of atherosclerosis. The 18 kDa translocator protein (TSPO) expression is upregulated in activated macrophages, representing a potential target to identify inflamed atherosclerotic plaques. We preclinically evaluated ^{18}F -GE-180, a novel third-generation TSPO radioligand, in a mouse model of atherosclerosis. *Methods.* Nine hypercholesterolemic mice deficient in low density lipoprotein receptor and apolipoprotein B48 (LDLR^{-/-}-ApoB^{100/100}) and six healthy C57BL/6N mice were injected with 10 MBq of ^{18}F -GE-180. Specificity of binding was demonstrated in three LDLR^{-/-}-ApoB^{100/100} mice by injection of nonradioactive reference compound of ^{18}F -GE-180 before ^{18}F -GE-180. Dynamic 30-minute PET was performed followed by contrast-enhanced CT, and the mice were sacrificed at 60 minutes after injection. Tissue samples were obtained for ex vivo biodistribution measurements, and aortas were cut into serial cryosections for digital autoradiography. The presence of macrophages and TSPO was studied by immunohistochemistry. The ^{18}F -GE-180 retention in plaque areas with different macrophage densities and lesion-free vessel wall were compared. *Results.* The LDLR^{-/-}-ApoB^{100/100} mice showed large, inflamed plaques in the aorta. Autoradiography revealed significantly higher ^{18}F -GE-180 retention in macrophage-rich plaque areas than in noninflamed areas (count densities 150 ± 45 PSL/mm² versus 51 ± 12 PSL/mm², $p < 0.001$). Prominent retention in the vessel wall without plaque was also observed (220 ± 41 PSL/mm²). Blocking with nonradioactive GE-180 diminished the difference in count densities between macrophage-rich and noninflamed areas in atherosclerotic plaques and lowered the count density in vessel wall without plaque. *Conclusion.* ^{18}F -GE-180 shows specific uptake in macrophage-rich areas of atherosclerotic plaques in mice. However, retention in atherosclerotic lesions does not exceed that in lesion-free vessel wall. The third-generation TSPO radioligand ^{18}F -GE-180 did not show improved characteristics for imaging atherosclerotic plaque inflammation compared to previously studied TSPO-targeting tracers.

1. Introduction

Atherosclerosis is a disease of the vessel wall involving both systemic and local inflammatory processes. Macrophages

have a central role in the development of atherosclerosis, from initiation of the inflammatory process to plaque progression and even plaque rupture [1, 2]. Detection of the level of inflammation in atherosclerosis would have high

TABLE 1: Characteristics of studied animals.

	LDLR ^{-/-} ApoB ^{100/100}	C57BL/6N	LDLR ^{-/-} ApoB ^{100/100} , block
Number of mice	6	6	3
Weight (g)	39.5 ± 6.2	34.6 ± 3.6	30.9 ± 6.3
Age (months)	6.8 ± 0.3	5.7 ± 0.5	7.0 ± 0.2
High-fat diet (months)	4.6 ± 0.1	—	5.0 ± 0.2
Injected radioactivity (MBq)	10.0 ± 0.2	10.1 ± 0.5	10.3 ± 0.2

The data are given in mean ± standard deviation. Block: excess amount of nonradioactive GE-180 given intravenously 5 minutes before administration of ¹⁸F-GE-180.

value in assessing disease activity. An imaging method for that purpose would also advance the development of anti-inflammatory drugs for atherosclerosis, since it would allow following up the treatment efficacy.

Positron emission tomography/computed tomography (PET/CT) imaging is a sensitive and quantitative method for detecting biological processes. Glucose analogue 2-deoxy-2-[¹⁸F]-fluoro-*D*-glucose (¹⁸F-FDG) PET/CT is a sensitive method for detecting inflammatory activity in vascular wall based on uptake in inflammatory cells [3, 4]. ¹⁸F-FDG, however, is not specific for inflammation, and therefore, new imaging tracers for a more specific inflammation detection and therapy evaluation are needed. The 18kDa translocator protein (TSPO), previously known as peripheral benzodiazepine receptor, is an evolutionarily conserved and ubiquitously expressed protein mainly localized in the outer mitochondrial membrane. It is involved in steroid biosynthesis as well as in mitochondrial cholesterol transport. It has been studied both as a potential therapeutic target and as a target for imaging purposes [5–8]. Imaging of TSPO has been studied mainly in neuroinflammatory diseases, since TSPO is highly expressed in activated microglial cells. The prototypic TSPO PET tracer ¹¹C-(*R*)-PK11195 and many new-generation tracers have been evaluated for that purpose [9]. Since TSPO is expressed in active macrophages, there has also been attempts to image atherosclerotic inflammation with TSPO-targeting tracers, both in preclinical [10–12] and clinical [13, 14] settings. Imaging with ¹¹C-(*R*)-PK11195 is limited by a low target-to-background ratio, and for many second-generation TSPO radioligands, a genetic polymorphism affects their binding [15]. Therefore, novel tracers would be desirable to overcome these limitations.

S-*N,N*-diethyl-9-[2-¹⁸F-fluoroethyl]-5-methoxy-2,3,4,9-tetrahydro-1*H*-carbazole-4-carboxamide (Flutriclamide, ¹⁸F-GE-180) is a novel, third-generation TSPO radioligand with high affinity and specific binding [16–18]. We aimed at evaluating ¹⁸F-GE-180 in the imaging of atherosclerotic plaque inflammation in a LDLR^{-/-}ApoB^{100/100} mouse model. We studied the tissue distribution and retention of the radiotracer by *in vivo* PET/CT imaging and *ex vivo* biodistribution. *Ex vivo* autoradiography was performed to assess the tracer retention in plaque areas with different macrophage densities. The specificity of the ¹⁸F-GE-180 binding was studied in mice with preinjection of excess of nonradioactive reference compound of ¹⁸F-GE-180 (non-radioactive GE-180). The presence of TSPO and macrophages in aorta was studied by immunohistochemistry.

2. Materials and Methods

2.1. Animals. All mice were housed in animal facilities of University of Turku Central Animal Laboratory under standard conditions with lights on from 6.00 am to 6.00 pm. The mice had *ad libitum* access to water and food throughout the study. All studies were conducted with approval from the Lab-Animal Care & Use Committee of the State Provincial Office of Southern Finland (Reference number ESAVI/1583/04.10.03/2012) and in compliance with the European Union directives relating to the conduct of animal experimentation.

Hypercholesterolemic mouse model deficient in the LDL receptor and apoB48 (LDLR^{-/-}ApoB^{100/100}) was utilized. The lipid profile of these mice resembles human familial hypercholesterolemia, and they develop large, inflamed plaques in the aortas. Nine male LDLR^{-/-}ApoB^{100/100} mice were fed with Western-type diet (TD.88137, Harlan Teklad, consisting of 42% of calories from fat and 0.2% from cholesterol, no sodium cholate, Harlan Laboratories, Madison, WI, USA) for 4–5 months, starting at the age of two months. Six male 6–7-month-old C57BL/6N mice fed with regular chow diet were utilized as healthy controls. The details of studied mice are presented in Table 1.

2.2. Radiosynthesis of ¹⁸F-GE-180. ¹⁸F-GE-180 was synthesized according to the previously described protocol [19]. The molar activity was 1800 ± 740 GBq/μmol at the end of synthesis, and the radiochemical purity was >97% in each tracer batch. The nondecay-corrected radiochemical yield was 53% ± 3%.

2.3. *In Vivo* Imaging. The mice were anaesthetized with 2–2.5% isoflurane inhalation and kept on a heating pad. They were first imaged with CT for attenuation correction (Inveon Multimodality PET/CT, Siemens Medical Solutions, Knoxville, TN, USA). After CT, approximately 10 MBq of ¹⁸F-GE-180 was administered as an intravenous bolus injection via a tail vein cannula, and a 30-minute dynamic PET was started at the same time with the injection. After PET, 100 μl of intravenous contrast agent (eXIA160XL, Binitio Biomedical Inc., Ottawa, ON, Canada) was injected, and a high-resolution CT was performed as described in [20]. The PET images were reconstructed with 2D ordered-subset expectation maximization (OSEM2D) algorithm with two iterations into 2 × 30 s, 4 × 60 s, and 5 × 300 s time frames, and CT images were reconstructed with a Feldkamp-based

algorithm. The radioactivity concentration in tissues was analysed by defining regions of interest (ROIs) with Carimas 2.9 program (Turku PET Centre, Turku, Finland). The ROI for blood was placed in the left jugular vein. The results were extracted as mean standardized uptake values (SUV) and were plotted as time-activity curves. Mean SUVs at 20–30 min after injection were utilized in numerical calculations.

2.4. Blocking Study. For three LDLR^{-/-}ApoB^{100/100}, an *in vivo* blocking study was performed to demonstrate the specificity of ¹⁸F-GE-180. These mice were injected with excess amount (3 mg/kg) of nonradioactive GE-180 (GE Healthcare Ltd., Amersham, United Kingdom) 5 minutes before the injection of radioactive ¹⁸F-GE-180. Nonradioactive GE-180 was dissolved in 20% ethanol, 20% dimethyl sulfoxide (DMSO), and 60% sterile water, and the injection volume was 2 ml/kg. After that, we followed the same protocol as in the other mice in the study.

2.5. Tissue Sampling and Ex Vivo Biodistribution. At 60 min after injection of ¹⁸F-GE-180, the mice were sacrificed. Under deep isoflurane anesthesia, the blood was collected by cardiac puncture into heparinized tubes and mice were euthanized with cervical dislocation. Samples of blood and various tissues were collected and weighed, and the radioactivity was measured using a gamma counter (Triathler 3", Hidex, Turku, Finland) cross-calibrated with a dose calibrator (VDC-202, Veenstra Instruments, Joure, Netherlands). Radioactive decay was corrected to the time of injection, and the dose remaining in the injection site was subtracted. The radioactive concentration measured in the tissue samples was expressed as SUV. For the radioactivity measurements, the aorta from ascending aorta to the level of diaphragm was dissected and blood was removed with saline. The aortic roots of mice were preserved in formalin and embedded in paraffin for histological analyses.

2.6. Autoradiography of Aortic Cryosections. The distribution of radioactivity in aorta was studied with digital autoradiography in LDLR^{-/-}ApoB^{100/100} mice. The saline-rinsed aorta was frozen, and sequential longitudinal sections of 8 and 20 μ m were cut with a cryomicrotome at -15°C and thaw-mounted onto microscope slides. The sections were air-dried and opposed to an imaging plate (Fuji Imaging Plate BAS-TR2025, Fuji Photo Film Co., Ltd., Tokyo, Japan). After an exposure time of 16 h, the imaging plates were scanned with a Fuji Analyser BAS-5000 (Fuji Photo Film Co., Ltd., Tokyo, Japan; internal resolution 25 μ m).

2.7. Histology and Immunohistochemistry. The 20 μ m aortic sections were stained with hematoxylin and eosin for morphology. The 8 μ m aortic sections were stained with anti-Mac-3 antibody (Clone M3/84, 1:5000, BD Pharmingen, Franklin Lakes, NJ, USA) to detect the macrophages in plaques. For the aortic roots, serial paraffin sections from the level of the aortic sinus were cut and stained with either

anti-Mac-3 or anti-TSPO antibody (NBPI-95674, 1:10,000, Novus Biologicals, Littleton, CO, USA) or with Movat's pentachrome stain. The detailed methods for immunohistochemistry have been described previously [11]. The plaque burden was quantitated from the Movat's pentachrome stained aortic root sections as intima-to-media ratio (IMR). The quantitation was performed with ImageJ (NIH, Bethesda, MD, USA).

2.8. Autoradiography Analyses. The autoradiographs of 8 μ m sections were analysed for count densities (photo-stimulated luminescence per unit area, PSL/mm²) with Tina 2.1 software (Raytest Isotopenmessgeräte GmbH, Straubenhardt, Germany). The ROIs were defined to plaques and lesion-free vessel wall according to the histology. The ROIs in plaques were divided to three groups (low, intermediate, and high macrophage infiltration) based on the percentage of Mac-3 positive staining in the plaque area measured by ImageJ (NIH, Bethesda, MD, USA). The radioactivity retention in plaque areas with different macrophage densities and lesion-free vessel wall were compared. The background counts were subtracted, and the retention was normalized to the injected radioactivity dose per gram of mouse weight as well as the proportion of tracer decayed during the exposure time [11].

2.9. Statistical Analyses. The results are expressed as mean \pm SD. Statistical analyses were conducted with IBM SPSS Statistics 23 (IBM Corp., Armonk, NY, USA). *p* values of less than 0.05 were considered statistically significant. The sample size was evaluated by performing power calculation based on the previous study evaluating aortic PET tracer uptake in LDLR^{-/-}ApoB^{100/100} and C57BL/6N mice [20]. According to the power calculation, assuming the average tracer uptake (SUV) to be 1.5 \pm 0.11, 5 mice per group would be needed to detect 15% difference in the uptake at 90% probability with the alpha value being 0.05. To compare the tissue radioactivity concentrations of LDLR^{-/-}ApoB^{100/100} mice to those of C57BL/6N and blocked LDLR^{-/-}ApoB^{100/100} mice in the *in vivo* PET and ex vivo biodistribution analyses, ANOVA with Dunnett's post hoc correction was performed. In autoradiography, the count densities in areas with different macrophage percentages and lesion-free vessel wall were analysed by ANOVA and Tukey's correction. Comparisons between LDLR^{-/-}ApoB^{100/100} mice and blocked LDLR^{-/-}ApoB^{100/100} mice in autoradiography were performed by Student's *t*-test.

3. Results

3.1. Histology and Immunohistochemistry. Histological and immunohistochemical stainings of the aortic root in LDLR^{-/-}ApoB^{100/100} mice and C57BL/6N mice are shown in Figure 1. All LDLR^{-/-}ApoB^{100/100} mice showed extensive atherosclerosis in the aorta, whereas C57BL/6N mice had lesion-free arteries. The IMR in the aortic root was 2.0 \pm 0.6 for LDLR^{-/-}ApoB^{100/100} mice reflecting significant plaque burden. The atherosclerotic plaques in LDLR^{-/-}ApoB^{100/100} mice contained various amounts of macrophages (Mac-3

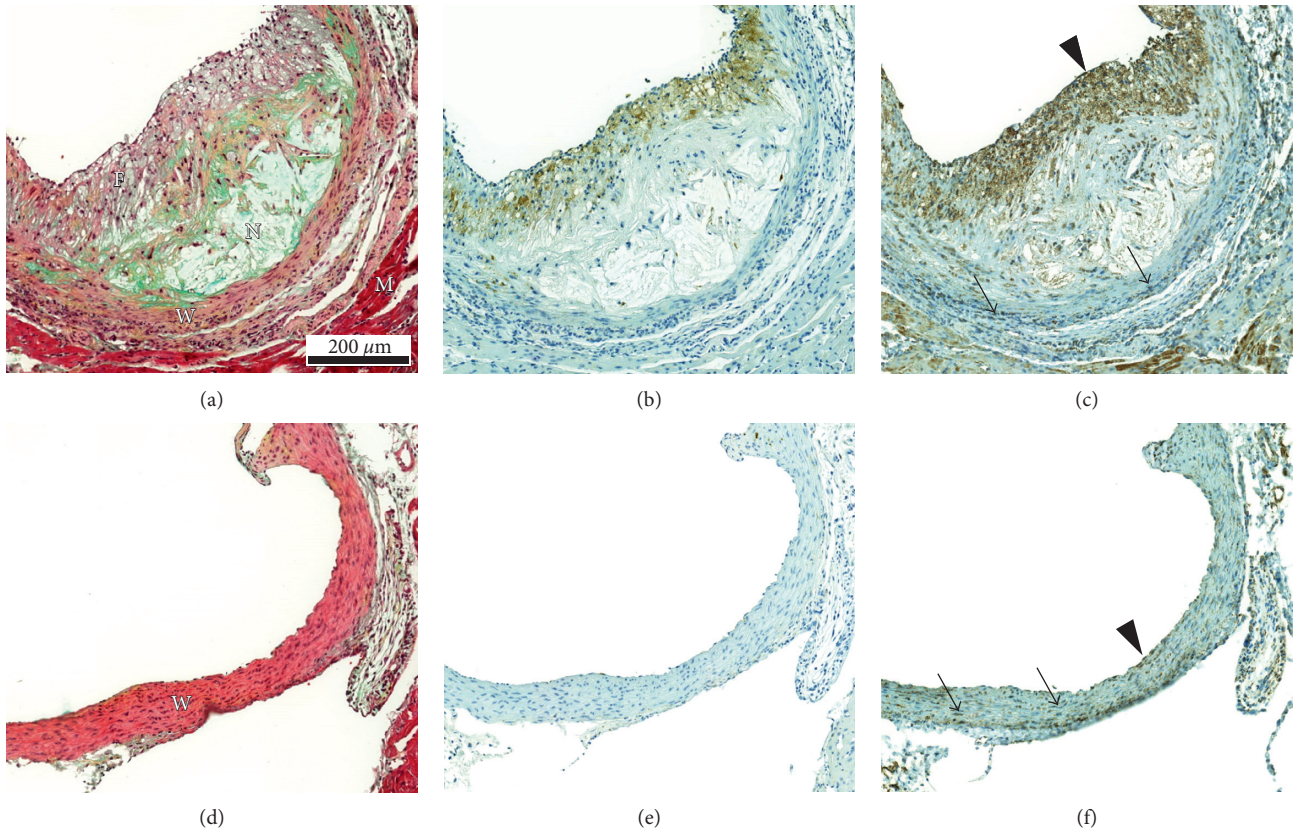
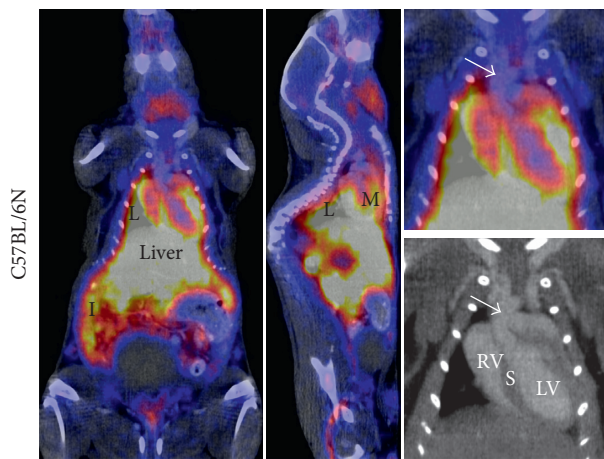
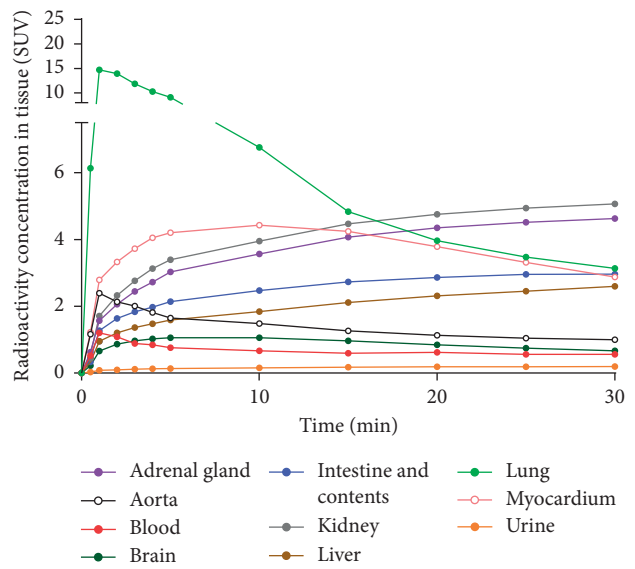


FIGURE 1: Visualisation of the vascular morphology and the presence of macrophages and TSPO in $LDLR^{-/-}ApoB^{100/100}$ and C57BL/6N mice. (a) Movat's pentachrome stained section of $LDLR^{-/-}ApoB^{100/100}$ aortic root shows large and cell-rich plaque with necrotic core (N) and fibrous cap (F). W = vessel wall (vascular smooth muscle cells) and M = myocardium. (b) Macrophage immunostaining (Mac-3) of the same plaque. Positive staining (brown colour) is present in the fibrous cap area. (c) TSPO immunostaining. Positive staining (brown colour) is present in the same areas as Mac-3 positive staining and additionally in vascular smooth muscle cells (arrow), endothelial cells (arrowhead), and in the myocardium. (d) Movat's pentachrome stained aortic root section of C57BL/6N mouse shows lesion-free vessel wall lined by endothelium. (e) Mac-3 staining is negative. (f) Positive TSPO staining is seen in both smooth muscle cells (arrows) and endothelial cells (arrowhead).



(a)



(b)

FIGURE 2: Continued.

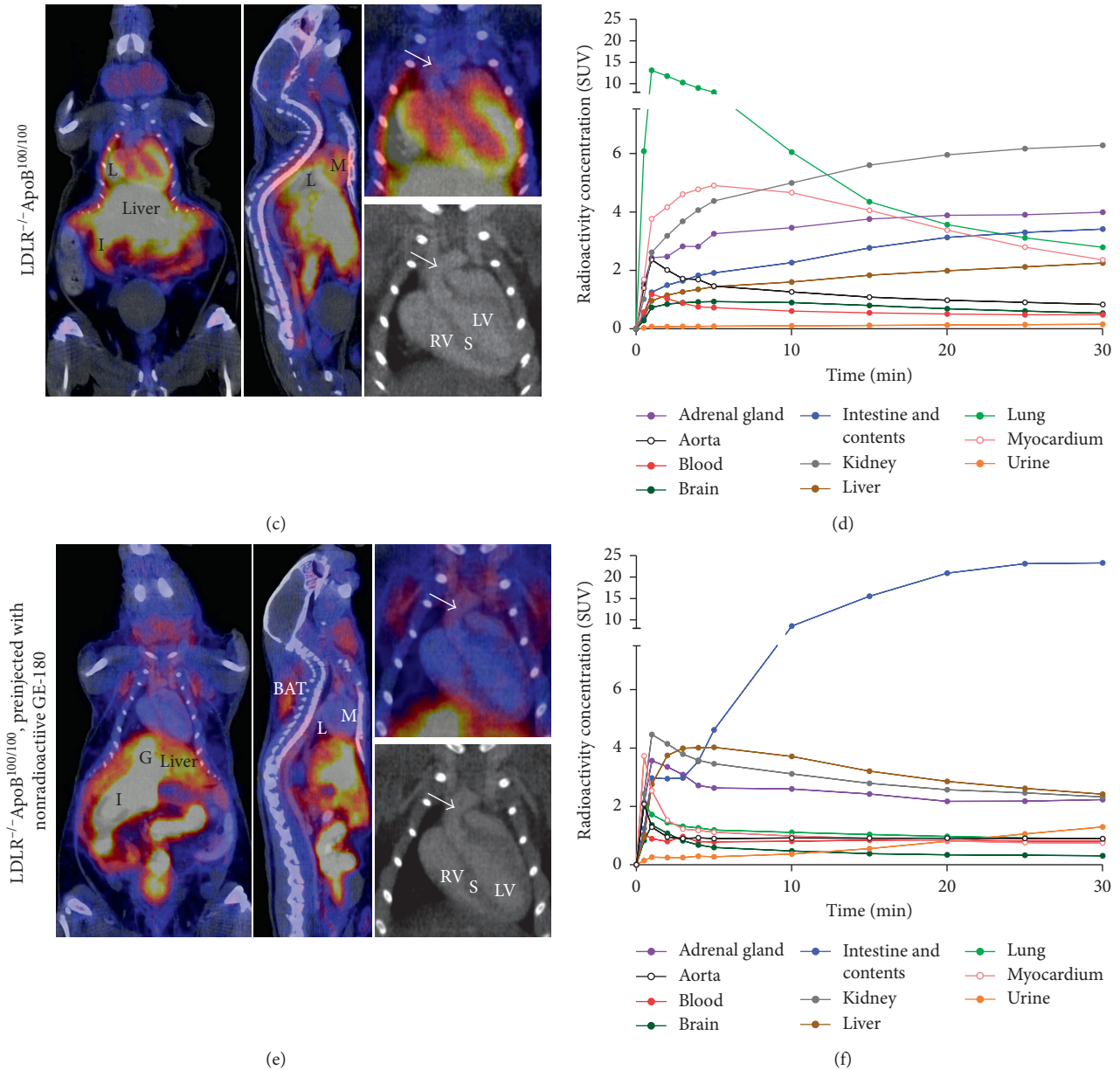


FIGURE 2: Representative *in vivo* PET/CT images. (a) Coronal PET/CT image shows the sum of ^{18}F -GE-180 radioactivity within 0–30 minutes after injection in a healthy C57BL/6N mouse. High radioactivity concentration is seen in the lungs (L), myocardium (M), and in the intestine and its contents (I). Close-up of the thoracic area is shown, with an arrow pointing to the aortic arch. Left and right ventricles as well as septum (LV, RV, and S) are annotated in the CT image. (b) Mean time-activity curves derived from six C57BL/6N mice show rapid peaking in the lung radioactivity concentration. (c) PET/CT in $\text{LDLR}^{-/-}\text{ApoB}^{100/100}$ mice. In the thoracic close-up, the arrow points to a plaque in the aortic arch. (d) Mean time-activity curves derived from six $\text{LDLR}^{-/-}\text{ApoB}^{100/100}$ mice. (e) The effect of preinjection with nonradioactive GE-180 to the ^{18}F -GE-180 distribution. Radioactivity concentration is increased in the gallbladder (G), intestine and its contents, and brown adipose tissue (BAT) and decreased in the lungs and myocardium. Close-up of the thoracic area is shown, with an arrow pointing to plaque in the aortic arch. (f) Mean time-activity curves derived from three $\text{LDLR}^{-/-}\text{ApoB}^{100/100}$ mice preinjected with nonradioactive GE-180. Highest radioactivity concentration is observed in the intestine and its contents.

positive staining ranging from 3.7% to 53% of the plaque area). A colocalisation of TSPO staining and Mac-3 staining was detected in the plaque intima (Figures 1(b) and 1(c)). However, TSPO staining was also seen in some Mac-3 negative cells. The medial layer of vessel wall was generally devoid of Mac-3 staining in both $\text{LDLR}^{-/-}\text{ApoB}^{100/100}$ and C57BL/6N mice (Figures 1(b) and 1(e)), whereas TSPO

staining in the vessel wall was intense in both strains (Figures 1(c) and 1(f)).

3.2. *In Vivo* PET/CT Imaging. *In vivo* PET/CT imaging showed rapid clearance of ^{18}F -GE-180 from the blood circulation and high, transient retention in the lungs. The

TABLE 2: ^{18}F -GE-180 *in vivo* PET/CT imaging results at 20–30 minutes after injection.

	LDLR ^{-/-} ApoB ^{100/100} (n = 6)	C57BL/6N (n = 6)	p value	LDLR ^{-/-} ApoB ^{100/100} , block (n = 3)	p value
Adrenal gland	3.95 ± 0.71	4.58 ± 0.58		2.21 ± 0.44	0.003
Aorta	0.87 ± 0.18	1.02 ± 0.12		0.90 ± 0.13	
BAT	0.37 ± 0.12	0.37 ± 0.12		1.37 ± 0.29	<0.001
Blood	0.48 ± 0.10	0.56 ± 0.10		0.81 ± 0.16	0.003
Bone	0.56 ± 0.15	0.45 ± 0.11		0.51 ± 0.24	
Brain	0.57 ± 0.10	0.71 ± 0.08	0.028	0.32 ± 0.02	0.002
Intestine and its contents	3.36 ± 0.88	2.96 ± 0.22		23.21 ± 10.85	<0.001
Kidney	6.23 ± 0.85	5.01 ± 0.84	0.038	2.40 ± 0.47	<0.001
Liver	2.19 ± 0.68	2.53 ± 0.32		2.52 ± 0.44	
Lung	2.95 ± 0.54	3.30 ± 0.72		0.91 ± 0.37	0.001
Muscle	0.27 ± 0.13	0.34 ± 0.07		0.41 ± 0.06	
Myocardium	2.58 ± 0.51	3.10 ± 0.46		0.75 ± 0.09	<0.001
Pancreas	1.86 ± 0.48	1.87 ± 0.24		1.90 ± 0.45	
Spleen	3.65 ± 0.65	3.69 ± 0.86		1.44 ± 0.35	0.002
Thymus	1.02 ± 0.28	1.29 ± 0.14		1.02 ± 0.08	
Urine	0.15 ± 0.03	0.19 ± 0.17		1.18 ± 0.47	<0.001
WAT	0.12 ± 0.02	0.15 ± 0.05		0.48 ± 0.41	0.022

The results are expressed as mean standardized uptake values ± standard deviation extracted from the PET/CT images. *p* values are derived from ANOVA with Dunnett's correction, LDLR^{-/-}ApoB^{100/100} mice as the control group. Blank cell in column indicates insignificant *p* value (>0.05). Block: excess amount of nonradioactive GE-180 given intravenously 5 minutes before administration of ^{18}F -GE-180.

TABLE 3: ^{18}F -GE-180 *ex vivo* biodistribution at 60 minutes after injection.

	LDLR ^{-/-} ApoB ^{100/100} (n = 6)	C57BL/6N (n = 6)	p value	LDLR ^{-/-} ApoB ^{100/100} , block (n = 3)	p value
Adrenal gland	20.79 ± 5.08	33.87 ± 5.24	0.001	4.12 ± 2.12	0.001
Aorta	2.03 ± 0.45	2.52 ± 0.40		1.37 ± 0.20	
BAT	0.84 ± 0.25	0.56 ± 0.18		3.37 ± 0.49	<0.001
Blood	0.23 ± 0.05	0.16 ± 0.02	0.046	0.38 ± 0.08	0.001
Bone	0.99 ± 0.26	0.88 ± 0.18		0.75 ± 0.19	
Brain	0.48 ± 0.05	0.51 ± 0.07		0.31 ± 0.05	0.004
Intestine	6.13 ± 1.44	5.76 ± 1.21		3.14 ± 1.50	0.017
Kidney	15.71 ± 10.27	9.97 ± 3.32		2.53 ± 0.29	0.037
Liver	3.20 ± 0.71	5.14 ± 1.07	0.005	2.50 ± 0.68	
Lung	13.93 ± 9.21	9.85 ± 3.14		2.55 ± 0.74	0.046
Muscle	0.35 ± 0.09	0.38 ± 0.05		0.32 ± 0.02	
Myocardium	2.54 ± 0.47	2.31 ± 0.34		0.71 ± 0.13	<0.001
Pancreas	3.07 ± 0.69	2.46 ± 0.44		0.80 ± 0.11	<0.001
Spleen	6.85 ± 3.44	6.48 ± 2.11		1.94 ± 0.53	0.039
Thymus	1.36 ± 0.39	2.03 ± 0.37	0.011	1.42 ± 0.13	
Urine	0.14 ± 0.06	0.20 ± 0.14		3.61 ± 2.60	0.001
WAT	0.22 ± 0.19	0.14 ± 0.09		0.36 ± 0.09	

The results are expressed as standardized uptake values ± standard deviation. *p* values are derived from ANOVA with Dunnett's correction, LDLR^{-/-}ApoB^{100/100} mice as the control group. Blank cell in column indicates insignificant *p* value (>0.05). Block: excess amount of nonradioactive GE-180 given intravenously 5 minutes before administration of ^{18}F -GE-180.

highest retention was observed at 1-minute time point (SUV 13 ± 2.6), which lowered to SUV 2.8 ± 0.45 at 30 minutes. High retention of radioactivity was seen in the kidneys, adrenal glands, intestine and its contents, and myocardium (Figure 2(a)). Radioactivity concentration in the aorta was similar in LDLR^{-/-}ApoB^{100/100} mice and C57BL/6N mice (SUV 0.87 ± 0.18 versus 1.0 ± 0.12). At 20–30 minutes after injection, LDLR^{-/-}ApoB^{100/100} mice had significantly lower radioactivity concentration in the brain compared to the C57BL/6N mice (SUV 0.57 ± 0.10 versus 0.71 ± 0.08, *p* = 0.028) and higher retention in the kidneys (6.23 ± 0.85 versus 5.01 ± 0.84, *p* = 0.038). In the other analysed tissues, no differences between the strains were observed (Table 2). Preinjection of excess nonradioactive GE-180 had no effect on

the radioactivity concentration measured in the aorta in LDLR^{-/-}ApoB^{100/100} mice (SUV 0.90 ± 0.13). However, it resulted in reduced radioactivity concentration in the adrenal glands, brain, kidneys, lungs, myocardium, and spleen and increased radioactivity concentration in brown and white adipose tissue, blood, intestine and its contents, and urine (Figure 2(b), Table 2).

3.3. Ex Vivo Biodistribution. The *ex vivo* biodistribution of ^{18}F -GE-180 at 60 minutes after injection was in line with the results obtained from the PET/CT imaging with few exceptions (Table 3). The radioactivity concentration in the aorta was similar between the LDLR^{-/-}ApoB^{100/100} and the C57BL/6N mice (SUV 2.0 ± 0.45 versus 2.5 ± 0.40). Preinjection of

nonradioactive GE-180 in LDLR^{-/-}ApoB^{100/100} mice had no significant effect (SUV 1.4 ± 0.20). The radioactivity concentration in the intestine was not increased by preinjection of nonradioactive GE-180 in the ex vivo measurements. On the contrary, it caused reduction in the radioactivity concentration in the pancreas in the ex vivo measurements, which was not seen in the PET/CT results.

3.4. Autoradiography. In autoradiography images, ¹⁸F-GE-180 retention in aortic atherosclerotic plaques was assessed in the areas with low, intermediate, and high macrophage densities as well as in lesion-free vessel wall. In the plaques, the count density was most prominent in the areas with high and intermediate macrophage density (150 ± 38 PSL/mm² and 150 ± 45 PSL/mm², resp.) (Figure 3). The percentages of macrophage staining were $33\% \pm 8.1\%$ and $24\% \pm 6.0\%$ in those areas. The count density in the areas of low macrophage infiltration ($8.9\% \pm 3.3\%$ macrophages) was significantly lower to both intermediate and high macrophage density areas (51 ± 12 PSL/mm², $p < 0.001$). However, the retention in the vessel wall without lesion formation was even more prominent (220 ± 41 PSL/mm², $p < 0.001$, $p = 0.013$, and $p = 0.017$ to areas of low, intermediate, and high macrophage density, resp.). Preinjection with nonradioactive GE-180 significantly increased the count density in the areas with lowest macrophage density (81 ± 2.5 PSL/mm², $p = 0.002$) and decreased the count density in the lesion-free vessel wall (100 ± 18 PSL/mm², $p = 0.002$). Preinjection of nonradioactive GE-180 tended to decrease the count density in the plaque areas with highest and intermediate macrophage densities (110 ± 0.93 PSL/mm², $p = 0.091$ and 100 ± 12 PSL/mm², $p = 0.11$, resp.). In the mice preinjected with nonradioactive GE-180, the percentages of macrophage staining were $43\% \pm 8.8\%$, $26\% \pm 8.8\%$, and $9.3\% \pm 4.7\%$ in plaque areas with high, intermediate, and low macrophage infiltration, respectively. Thus, no significant difference in the macrophage percentages between preinjected and the other LDLR^{-/-}ApoB^{100/100} mice was observed.

4. Discussion

Several different targets for PET imaging of inflammation in atherosclerosis have been studied [21]. As an imaging target for atherosclerosis, TSPO is attractive since it is highly expressed in macrophages [14]. In the PET imaging of vascular inflammation with TSPO-targeting tracers, ¹¹C-(R)-PK11195 has shown great potential especially in imaging vasculitis [8, 22]. In imaging atherosclerosis, where the inflammatory process is not as prominent, ¹¹C-(R)-PK11195 has shown lower target-to-background ratio [13]. Novel TSPO-targeting tracers have been studied in preclinical settings to overcome this problem. For example, ¹⁸F-FEDAA1106 has been evaluated in the imaging of the carotid artery cuff model in mice [23] and ¹¹C-PBR28 in a rat model of aortic aneurysm [24]. Both of these studies showed noticeable tracer uptake in lesion areas. However, the models represent an induced, intense local inflammation in the vessel wall, which might not translate to the clinical situation in atherosclerotic patients. The model used in the current study might mimic the clinical

atherosclerotic disease better, since there is variable inflammatory activity in the plaques. In previous studies with the same model, both ¹¹C-(R)-PK11195 [10] and a novel TSPO tracer ¹⁸F-FEMPA [11] have shown uptake in macrophage-rich plaques, but high tracer retention has been observed in the lesion-free vessel wall.

The third-generation TSPO radioligand ¹⁸F-GE-180 evaluated in the current study showed similar binding characteristics. It showed uptake in macrophage-rich areas within atherosclerotic lesions as well as in lesion-free vessel wall. Tracer retention was most prominent in tissues with high TSPO expression, such as the lungs and adrenal glands [25]. Preinjection with nonradioactive GE-180 tended to reduce the count density in macrophage-rich plaque areas. In addition, it reduced the retention in tissues with high expression of TSPO, such as the lungs and myocardium, and increased the proportion of tracer remaining in the circulation and taken up in adipose tissue. The kinetics of the tracer were favorable for *in vivo* imaging, since the blood clearance was rapid. However, no differences in aortic radioactivity concentration were observed between atherosclerotic and healthy mice, and the prominent retention in lesion-free vessel wall as well as in the lungs and myocardium might cause limitations.

In addition to high retention in macrophage-rich plaque areas, the ¹⁸F-GE-180 retention in the vessel wall without lesion formation was prominent. Therefore, the aortic radioactivity concentration, measured both *in vivo* and *ex vivo*, showed no difference between LDLR^{-/-}ApoB^{100/100} and C57BL/6N mice. As shown by immunohistochemistry, macrophages as well as smooth muscle cells and endothelial cells in the aortic wall were positive for TSPO in both mouse strains. High TSPO radioligand uptake to vessel wall has been observed in the same model as in the current study [10, 11] and in a rat model of aortic aneurysm [26]. However, similar vessel wall uptake of TSPO radioligands was not reported in another rat or mouse models [23, 24], nor in the previous studies with ¹¹C-(R)-PK11195 in patients [13, 22]. The reason for this might be differences in the TSPO expression or differences between the studied radioligands. TSPO is expressed in various cell types of the circulatory system, such as vascular smooth muscle cells and endothelial cells, and its expression shows variation depending on the physiological state [27]. For example, the expression of TSPO in vascular endothelial cells is suggested to be reactive to proinflammatory stimuli [28]. The expression of TSPO in vascular smooth muscle cells also shows variation between species [29, 30]. Despite TSPO is expressed in various cells of vessel wall, its expression in macrophages is significantly higher than in the other cell types present in the vascular wall in humans [14]. Therefore, the observed high retention in lesion-free vessel wall in mice might not preclude the use of ¹⁸F-GE-180 in vascular imaging in patients. The observed high uptake of TSPO-targeting tracers in the lesion-free vessel wall seen in the current study and previous studies in the same mouse model [10, 11], however, suggest that other animal models should be chosen for future studies with TSPO-targeting tracers.

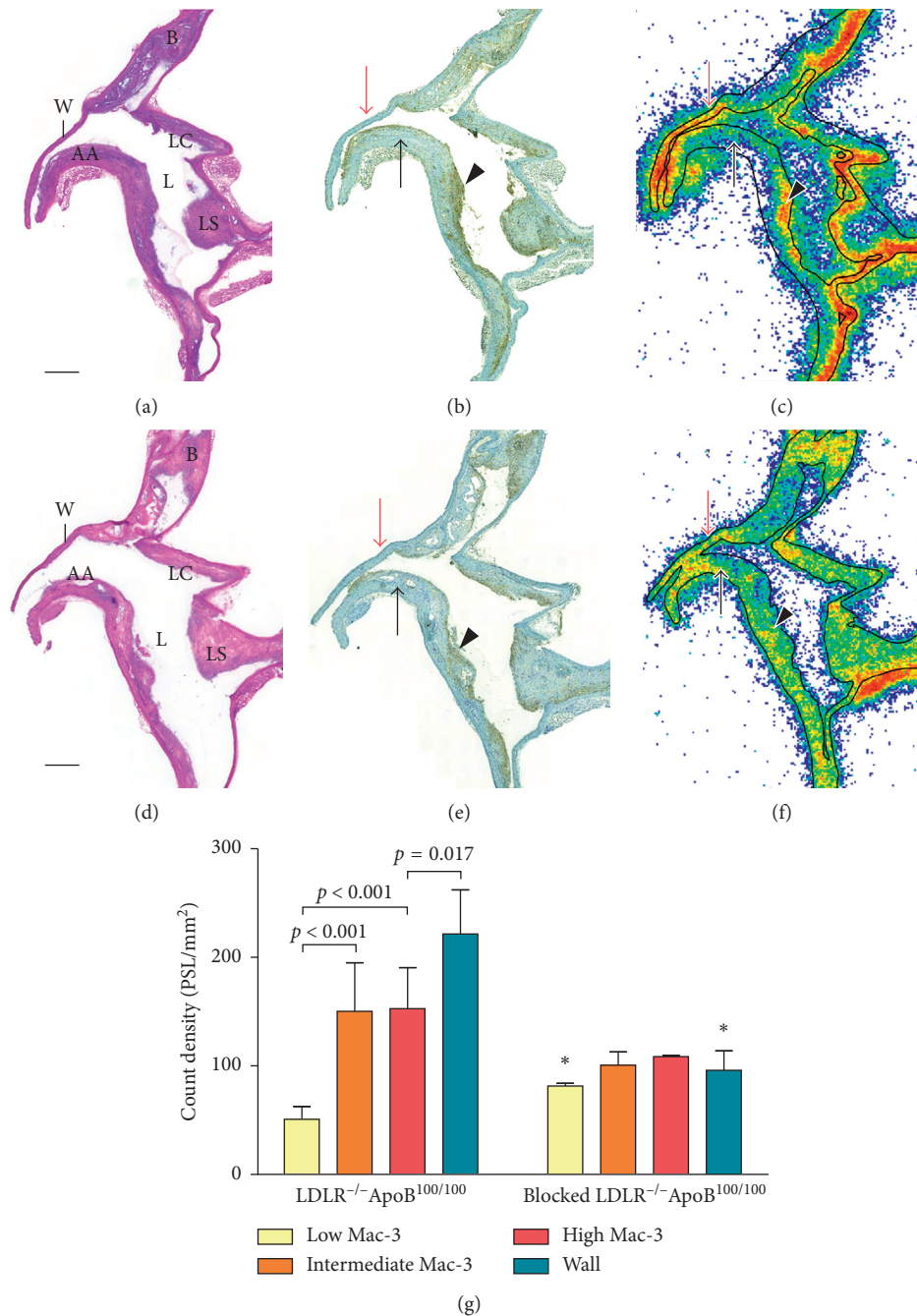


FIGURE 3: Ex vivo autoradiography of aortic sections in LDLR^{-/-} ApoB^{100/100} mice. Longitudinally cut aortic arch stained with hematoxylin-eosin (a, d) shows large atherosclerotic plaques in the inner curvature of the arch and its all branches. Scale bar is 1 mm. AA = aortic arch, B = brachiocephalic trunk, LC = left common carotid artery, LS = left subclavian artery, L = lumen, and W = lesion-free vessel wall. Macrophage immunostainings (b, e) show areas of high (arrowhead) and low (black arrow) macrophage infiltration in the plaques. Lesion-free vessel wall is indicated with a red arrow. (c) Autoradiography shows high ¹⁸F-GE-180 count density (red colour) in the macrophage-rich areas in plaques as well as in the lesion-free vessel wall. Plaque areas with low macrophage infiltration show low count density (blue to green). (f) Autoradiography in mice preinjected with nonradioactive GE-180 shows similar level of count density in lesion-free vessel wall and all plaque areas. (g) Quantitative results of the autoradiography. ANOVA with Tukey's correction were used in assessing differences between analysed areas within each mouse group. Asterisk indicates statistically significant difference to nonblocked LDLR^{-/-} ApoB^{100/100} mice in Student's *t*-test.

The aortic ¹⁸F-GE-180 radioactivity concentration in LDLR^{-/-} ApoB^{100/100} mice was not significantly affected by blocking with nonradioactive GE-180; however, the pattern of uptake in the vessel components altered significantly.

Without the preinjection, the ¹⁸F-GE-180 count density was very focused on plaque areas with intermediate or high macrophage infiltration, and the count density was very low in the areas with low number of macrophages. This reflects

well the previously observed high ^{18}F -GE-180 uptake in microglial cells and low retention in the noninflamed brain areas [31, 32]. Count density in lesion-free vessel wall was also prominent. Preinjection with GE-180 tended to decrease the count density in plaque areas with intermediate and high macrophage infiltration, whereas it actually increased the count density in areas with low macrophage infiltration. This supports the specificity of ^{18}F -GE-180 uptake to macrophages in the plaques, since preinjection with nonradioactive GE-180 increased the nonspecific retention in lipid-rich, acellular areas of the plaques. This may be caused by increased availability of circulating tracer, since the ^{18}F -GE-180 SUV in blood was higher in the preinjected mice. The retention of ^{18}F -GE-180 in lesion-free vessel wall was also significantly lowered by the preinjection, which was expected due to prominent TSPO staining seen in the histology.

The nonradioactive GE-180 was administered in vehicle containing 20% DMSO and 20% ethanol due to limited solubility of the compound. DMSO is known to have anti-inflammatory properties [33]. Therefore, it is possible that the effects of preinjection with nonradioactive GE-180 might also be mediated by the vehicle. The prominent decrease of ^{18}F -GE-180 radioactivity concentration in highly TSPO-expressing tissues, such as the adrenal glands, however, suggests occupation of TSPO by nonradioactive GE-180. Additionally, no difference in the amounts of Mac-3 positive macrophages was seen between preinjected and the other mice. Due to the limitation of having Mac-3 as an only marker of inflammatory cells, the potential acute effect of DMSO to the inflammatory phenotype cannot be ruled out. The lack of more detailed analysis of macrophages and other inflammatory cells is acknowledged as a limitation in this study. Notably, the mouse plaque burden was measured from the aortic root, while the radioactivity measurements and autoradiography were performed from thoracic aorta. This limits the available information on the severity of atherosclerosis in the aortic areas studied for radioactivity.

The high and specific lung uptake of TSPO radioligands has been considered as a potential limiting factor in using TSPO as an imaging target in vascular imaging [34]. The lung uptake is most likely caused by resident inflammatory cells with high TSPO expression [25]. In the current study, we observed a high radioactivity concentration in lungs peaking rapidly and decreasing during the 30-minute dynamic *in vivo* PET/CT imaging. The optimal imaging time frame for ^{18}F -GE-180 in neuroinflammatory disease imaging was shown to be 90 minutes or more in previous first-in-man-studies [17, 18]. At later time points, the lung uptake may have decreased to such a level that it does not preclude imaging blood vessels in close proximity. In contrast to the tracer retention in the lungs, the myocardial radioactivity concentration did not show clearance during the 30-minute dynamic imaging. This may cause limitations for imaging of the coronary arteries.

The *in vivo* imaging of small targets, especially in rodents, has certain limitations. Analysing small targets, such as the aortic arch or adrenal glands, is subject to partial volume effects, which lead to lower SUVs *in vivo* than ex vivo.

Generally, the SUVs measured from the *in vivo* PET/CT images at 20–30 minutes after injection and the ex vivo SUVs measured at 60 minutes after injection were in line. The observed discrepancy in the intestinal radioactivity concentration between *in vivo* and ex vivo SUVs is probably caused by technical reasons, since analysed intestinal uptake *in vivo* contains both the intestinal tissue and its contents, but for the ex vivo measurement, the contents were removed. The preinjection with nonradioactive GE-180 decreased pancreatic radioactivity concentration in the ex vivo measurements but that was not seen in the *in vivo* results. This could be explained by spillover from surrounding intestinal radioactivity in the *in vivo* images, which was high in the GE-180 preinjected mice.

5. Conclusion

^{18}F -GE-180 showed specific uptake in macrophages not only in atherosclerotic plaques but also in the lesion free vessel wall in mice. Overall, retention in atherosclerotic lesions did not exceed that in lesion-free vessel wall in this model of atherosclerosis. The third-generation TSPO radioligand ^{18}F -GE-180 did not show improved characteristics for imaging atherosclerotic plaque inflammation compared to the previously studied TSPO-targeting tracers.

Abbreviations

^{18}F -FDG:	2-deoxy-2- ^{18}F -fluoro- <i>D</i> -glucose
CT:	Computed tomography
DMSO:	Dimethyl sulfoxide
^{18}F -GE-180:	<i>S</i> - <i>N,N</i> -diethyl-9-[2- ^{18}F -fluoroethyl]-5-methoxy-2,3,4,9-tetrahydro-1 <i>H</i> -carbazole-4-carboxamide
IMR:	Intima-to-media ratio
PET:	Positron emission tomography
PSL/mm ² :	Photo-stimulated luminescence per square millimeter
ROI:	Region of interest
SUV:	Standardized uptake value
TSPO:	18 kDa translocator protein.

Data Availability

All data supporting the results can be found at Turku PET Centre, Turku, Finland, or from the corresponding author upon request.

Disclosure

Only a portion of the data has been presented in World Congress on Inflammation 2013 (Natal, Brazil; poster) and in Turku PET Symposium 2014 (Turku, Finland; poster). Data collection and analysis were performed independent of the funding sources.

Conflicts of Interest

Veronique Morisson-Iveson, Matthew Morrison, and William Trigg were employed by GE Healthcare Ltd. at the time of the study. The other authors declare no conflicts of interest.

Acknowledgments

The tissue sectioning and stainings were performed in Turku Center for Disease Modeling, Histology Unit by Erica Nyman, Duyen Le, and Minna Grönroos. Liisa Lempiäinen is acknowledged for the aortic root sectioning. Aake Honkaniemi is acknowledged for the assistance in PET/CT imaging, and Timo Kattelus and Mia Stähle are acknowledged for assistance with the figures. The study was conducted within the Finnish Centre of Excellence in Cardiovascular and Metabolic Diseases supported by the Academy of Finland, University of Turku, Turku University Hospital, and Åbo Akademi University. Grants for research were obtained from Turku University Contrast Media & Molecular Imaging 9 Hospital, Finnish Cultural Foundation, Ida Montin Foundation, Emil Aaltonen Foundation, Aarne Koskelo Foundation, Turku University Foundation, Finnish Foundation for Cardiovascular Research, and Sigrid Jusélius Foundation. Funding for salaries, project costs, and the cassettes for radiosynthesis were received from GE Healthcare Ltd. GE Healthcare Ltd. had a role in planning of the study, interpretation of the data, and in writing the manuscript.

References

- [1] K. J. Moore and I. Tabas, "Macrophages in the pathogenesis of atherosclerosis," *Cell*, vol. 145, no. 3, pp. 341–355, 2011.
- [2] G. K. Hansson, P. Libby, and I. Tabas, "Inflammation and plaque vulnerability," *Journal of Internal Medicine*, vol. 278, no. 5, pp. 483–493, 2015.
- [3] J. H. F. Rudd, K. S. Myers, S. Bansilal et al., "¹⁸F-fluorodeoxyglucose positron emission tomography imaging of atherosclerotic plaque inflammation is highly reproducible. Implications for atherosclerosis therapy trials," *Journal of the American College of Cardiology*, vol. 50, no. 9, pp. 892–896, 2007.
- [4] A. Tawakol, Z. A. Fayad, R. Mogg et al., "Intensification of statin therapy results in a rapid reduction in atherosclerotic inflammation: results of a multicenter fluorodeoxyglucose-positron emission tomography/computed tomography feasibility study," *Journal of the American College of Cardiology*, vol. 62, no. 10, pp. 909–917, 2013.
- [5] L. Lecanu, Z. X. Yao, A. McCourty et al., "Control of hypercholesterolemia and atherosclerosis using the cholesterol recognition/interaction amino acid sequence of the translocator protein TSPO," *Steroids*, vol. 78, no. 2, pp. 137–146, 2013.
- [6] J. M. W. Taylor, A. Allen, and A. Graham, "Targeting mitochondrial 18 kDa translocator protein (TSPO) regulates macrophage cholesterol efflux and lipid phenotype," *Clinical Science*, vol. 127, no. 10, pp. 603–613, 2014.
- [7] X. Qi, J. Xu, F. Wang, and J. Xiao, "Translocator protein (18 kDa): a promising therapeutic target and diagnostic tool for cardiovascular diseases," *Oxidative Medicine and Cellular Longevity*, vol. 2012, article 162934, 9 pages, 2012.
- [8] F. Lamare, R. Hinz, O. Gaemperli et al., "Detection and quantification of large-vessel inflammation with ¹¹C-(R)-PK11195 PET/CT," *Journal of Nuclear Medicine*, vol. 2012, Article ID 162934, 9 pages, 2012.
- [9] F. Chauveau, H. Boutin, N. Van Camp, F. Dollé, and B. Tavitian, "Nuclear imaging of neuroinflammation: a comprehensive review of [¹¹C]PK11195 challengers," *European Journal of Nuclear Medicine and Molecular Imaging*, vol. 35, no. 12, pp. 2304–2319, 2008.
- [10] I. Laitinen, P. Marjamäki, K. Nägren et al., "Uptake of inflammatory cell marker [¹¹C]PK11195 into mouse atherosclerotic plaques," *European Journal of Nuclear Medicine and Molecular Imaging*, vol. 36, no. 1, pp. 73–80, 2009.
- [11] S. Hellberg, J. M. U. Silvola, M. Kiugel et al., "18-kDa translocator protein ligand ¹⁸F-FEMPA: biodistribution and uptake into atherosclerotic plaques in mice," *Journal of Nuclear Cardiology*, vol. 24, no. 3, pp. 862–871, 2017.
- [12] C. A. Foss, D. Bedja, R. C. Mease et al., "Molecular imaging of inflammation in the ApoE^{-/-} mouse model of atherosclerosis with IodoDPA," *Biochemical and Biophysical Research Communications*, vol. 461, no. 1, pp. 70–75, 2015.
- [13] O. Gaemperli, J. Shalhoub, D. R. J. Owen et al., "Imaging intraplaque inflammation in carotid atherosclerosis with ¹¹C-PK11195 positron emission tomography/computed tomography," *European Heart Journal*, vol. 33, no. 15, pp. 1902–1910, 2012.
- [14] J. L. E. Bird, D. Izquierdo-Garcia, J. R. Davies et al., "Evaluation of translocator protein quantification as a tool for characterising macrophage burden in human carotid atherosclerosis," *Atherosclerosis*, vol. 210, no. 2, pp. 388–391, 2010.
- [15] D. R. Owen, A. J. Yeo, R. N. Gunn et al., "An 18-kDa Translocator Protein (TSPO) polymorphism explains differences in binding affinity of the PET radioligand PBR28," *Journal of Cerebral Blood Flow and Metabolism*, vol. 32, no. 1, pp. 1–5, 2012.
- [16] H. Wadsworth, P. A. Jones, W. F. Chau et al., "GE-180: a novel fluorine-18 labelled PET tracer for imaging translocator protein 18 kDa (TSPO)," *Bioorganic and Medicinal Chemistry Letters*, vol. 22, no. 3, pp. 1308–1313, 2012.
- [17] Z. Fan, V. Calsolaro, R. A. Atkinson et al., "Flutriciclamide (¹⁸F-GE180) PET: First-in-human PET study of novel third-generation in vivo marker of human translocator protein," *Journal of Nuclear Medicine*, vol. 57, no. 11, pp. 1753–1759, 2016.
- [18] C. Feeney, G. Scott, J. Raffel et al., "Kinetic analysis of the translocator protein positron emission tomography ligand [¹⁸F]GE-180 in the human brain," *European Journal of Nuclear Medicine and Molecular Imaging*, vol. 43, no. 12, pp. 2201–2210, 2016.
- [19] T. Wickstrøm, A. Clarke, I. Gausemel et al., "The development of an automated and GMP compliant FASTlab™ Synthesis of [¹⁸F]GE-180; a radiotracer for imaging translocator protein (TSPO)," *Journal of Labelled Compounds and Radiopharmaceuticals*, vol. 57, no. 1, pp. 42–48, 2014.
- [20] S. Hellberg, J. M. U. Silvola, M. Kiugel et al., "Type 2 diabetes enhances arterial uptake of choline in atherosclerotic mice: an imaging study with positron emission tomography tracer ¹⁸F-fluoromethylcholine," *Cardiovascular Diabetology*, vol. 15, no. 1, p. 26, 2016.
- [21] J. M. Tarkin, F. R. Joshi, and J. H. F. Rudd, "PET imaging of inflammation in atherosclerosis," *Nature Reviews Cardiology*, vol. 11, no. 8, pp. 443–457, 2014.
- [22] F. Pugliese, O. Gaemperli, A. R. Kinderlerer et al., "Imaging of vascular inflammation with [¹¹C]-PK11195 and positron emission tomography/computed tomography angiography," *Journal of the American College of Cardiology*, vol. 56, no. 8, pp. 653–661, 2010.
- [23] S. Cuhlmann, W. Gsell, K. Van Der Heiden et al., "In vivo mapping of vascular inflammation using the translocator

- protein tracer ^{18}F -FEDAA1106,” *Molecular Imaging*, vol. 13, no. 6, pp. 1–11, 2014.
- [24] S. J. English, J. A. Diaz, X. Shao et al., “Utility of ^{18}F -FDG and ^{11}C -PBR28 microPET for the assessment of rat aortic aneurysm inflammation,” *EJNMMI Research*, vol. 4, no. 1, p. 20, 2014.
- [25] E. Bribes, D. Carriere, C. Goubet, S. Galiegue, P. Casellas, and S.-L. Joelle, “Immunohistochemical assessment of the peripheral benzodiazepine receptor in human tissues,” *Journal of Histochemistry and Cytochemistry*, vol. 52, no. 1, pp. 19–28, 2004.
- [26] L. Sarda-Mantel, J. M. Alsac, R. Boisgard et al., “Comparison of ^{18}F -fluoro-deoxy-glucose, ^{18}F -fluoro-methyl-choline, and ^{18}F -DPA714 for positron-emission tomography imaging of leukocyte accumulation in the aortic wall of experimental abdominal aneurysms,” *Journal of Vascular Surgery*, vol. 56, no. 3, pp. 765–773, 2012.
- [27] L. Veenman and M. Gavish, “The peripheral-type benzodiazepine receptor and the cardiovascular system. Implications for drug development,” *Pharmacology and Therapeutics*, vol. 110, no. 3, pp. 503–524, 2006.
- [28] H. K. Joo, Y. R. Lee, G. Kang et al., “The 18-kDa translocator protein inhibits vascular cell adhesion molecule-1 expression via inhibition of mitochondrial reactive oxygen species,” *Molecules and Cells*, vol. 38, no. 12, pp. 1064–1070, 2015.
- [29] J. C. W. Mak and P. J. Barnes, “Peripheral type benzodiazepine receptors in human and guinea pig lung: characterization and autoradiographic mapping,” *Journal of Pharmacology and Experimental Therapeutics*, vol. 252, no. 2, pp. 880–885, 1990.
- [30] J. F. French and M. A. Matlib, “Identification of a high-affinity peripheral-type benzodiazepine binding site in rat aortic smooth muscle membranes,” *Journal of Pharmacology and Experimental Therapeutics*, vol. 247, no. 1, pp. 23–28, 1988.
- [31] H. Boutin, K. Murray, J. Pradillo et al., “ ^{18}F -GE-180: a novel TSPO radiotracer compared to ^{11}C -R-PK11195 in a pre-clinical model of stroke,” *European Journal of Nuclear Medicine and Molecular Imaging*, vol. 42, no. 3, pp. 503–511, 2014.
- [32] A. M. Dickens, S. Vainio, P. Marjamäki et al., “Detection of microglial activation in an acute model of neuroinflammation using PET and radiotracers ^{11}C -(R)-PK11195 and ^{18}F -GE-180,” *Journal of Nuclear Medicine*, vol. 55, no. 3, pp. 466–472, 2014.
- [33] M. Colucci, F. Maione, M. C. Bonito, A. Piscopo, A. Di Giannuario, and S. Pieretti, “New insights of dimethyl sulphoxide effects (DMSO) on experimental in vivo models of nociception and inflammation,” *Pharmacological Research*, vol. 57, no. 6, pp. 419–425, 2008.
- [34] L. L. Johnson, “Targeting activated macrophages to identify the vulnerable atherosclerotic plaque,” *Journal of Nuclear Cardiology*, vol. 24, no. 3, pp. 872–875, 2017.